Sede Amministrativa

UNIVERSITA' DEGLI STUDI DI PADOVA

DIPARTIMENTO DI INGEGNERIA INDUSTRIALE

SCUOLA DI DOTTORATO DI RICERCA IN INGEGNERIA
INDUSTRIALE
INGEGNERIA CHIMICA, DEI MATERIALI E DELLA PRODUZIONE
CICLO XXVI

PHASE STABILITY
IN DUPLEX STAINLESS STEELS

Direttore della Scuola: Ch.mo Prof. Paolo Colombo
Coordinatore d'indirizzo: Prof. Enrico Savio
Supervisore: Prof.ssa Irene Calliari

Dottorando: Marco Breda

Eadem mutata resurgo

SUMMARY

This thesis summarizes the work performed during the research activities developed in the three-years course of scientific training for the attainment of the Doctor of Philosophy degree. The research was mainly focused on the study of the physical metallurgy of Duplex stainless steels, a particular class of stainless steels having a biphasic austeno-ferritic microstructure, with the aim to characterize their microstructural stability as a consequence of heat treatments and cold plastic deformation.

The choice of the research topic was dictated by the increasing use of these steels for industrial applications, being able to provide high-strength features and elevated performances against corrosive attacks, making them particularly suitable and competitive in aggressive environments, also as structural materials. However, there are limitations to the use of Duplex steels, owing to the occurrence of microstructural modifications, either during high-temperature exposures or as a result of cold working, which can compromise their interesting features.

The thesis is organized into three main parts; the first chapter is focused on properties, problems and applications of Duplex stainless steels, providing a general introduction about these materials and in which particular emphasis was given to those metallurgical variables that affect the production process and the microstructural stability. In Chapter 2 and 3, the research activities concerning the effects of heat treatments (Chapter 2) and cold rolling (Chapter 3) the on the Duplex properties are presented and discussed. It was considered appropriate to report a brief summary of literature at the beginning of the second chapter, aimed to provide the reader with the "state of art" on the effects of thermal cycles on Duplex steels properties, whereas the remaining sections of the chapter are a constitutive part of the research activities. In addition, the experimental part discussed in Chapters 2 and 3 has been integrated with a section devoted to the study of Duplex application at an industrial scale (Appendix A), aimed to the employment of these materials in marine environment. Finally, Appendix B reports the results concerning

archaeometallurgical studies, which has contributed to the scientific training of the candidate, even if it was not related to the main research topic.

Experiments and training courses were mainly carried out in facilities and laboratories pertaining to the Industrial Engineering Department (DII) of the University of Padua – and particularly those belonging to the DII "metallurgy group" – under the supervision of Prof. Irene Calliari and Prof . Emilio Ramous. However, certain specific activities have required the involvement of other structures external to the University of Padua; among these, the neutron diffraction measurements were carried out in the INES diffractometer, located at the ISIS facility in the Rutherford Appleton Laboratory (Didcot, UK), in collaboration with Dr. Antonella Scherillo and Dr. Francesco Grazzi (CNR of Florence), while the magnetic measurements were performed in the laboratories of the University of Budapest (BME), in collaboration with Prof. István Mészáros. Moreover, the EBSD analysis on the deformed materials were executed by Dr. Paola Bassani (CNR of Lecco), while the mechanical impact tests were carried out in collaboration with Dr. Cinzia Menapace (University of Trento), in the university laboratories, and with Eng. Marco Pizzo (Unilab Laboratori Industriali srl), in the Exova CTR srl laboratories.

The results of the studies pertaining to the research period and reported in this thesis have contributed to enhance the knowledge about Duplex stainless steels, in relation to the effects that microstructural modifications can induce on the materials properties, and were of appropriate scientific relevance to allowing their presentation in international conferences and their publication in scientific journals.

INTRODUZIONE

La presente tesi riassume il lavoro eseguito durante l'attività di ricerca svolta nel corso del triennio di formazione scientifica per il conseguimento del titolo di Dottore di Ricerca. L'obiettivo principale è stato lo studio della metallurgia fisica degli acciai inossidabili Duplex, una particolare categoria di acciai inossidabili a struttura bifasica austeno-ferritica, con lo scopo di caratterizzarne la stabilità microstrutturale a seguito di trattamenti termici e deformazione plastica a freddo.

La scelta del tema di ricerca è stata dettata dal sempre più crescente utilizzo di questi acciai in ambito industriale, grazie alle loro elevate caratteristiche meccaniche e di resistenza agli attacchi corrosivi che li rendono particolarmente adatti e competitivi per applicazioni in ambienti aggressivi, anche come materiali ad uso strutturale. Tuttavia, esistono delle limitazioni all'impiego degli acciai Duplex, dovute a trasformazioni microstrutturali che possono insorgere durante l'esposizione del materiale a temperature elevate o che possono verificarsi a seguito di deformazioni a freddo, compromettendone le interessanti caratteristiche.

La tesi è suddivisa in tre parti principali. Nel primo capitolo è riportata un'introduzione generale sugli acciai Duplex, focalizzata sulle loro proprietà, problematiche e applicazioni, in cui è stata data particolare enfasi alle variabili metallurgiche che ne influenzano il processo produttivo e la stabilità microstrutturale. Nei Capitoli 2 e 3, invece, sono presentate e discusse le attività oggetto di ricerca riguardanti lo studio degli effetti dei trattamenti termici (Capitolo 2) e della laminazione a freddo (Capitolo 3) sulle caratteristiche dei Duplex. Si è ritenuto opportuno esporre all'inizio del secondo capitolo un breve riassunto di lavori presenti in letteratura, con lo scopo di fornire al lettore lo "stato dell'arte" in merito alle conoscenze sugli effetti dei cicli termici sulle proprietà dei Duplex, mentre le restanti sezioni del capitolo sono parte costitutiva dell'attività di ricerca svolta dal candidato. Inoltre, la parte sperimentale discussa nei Capitoli 2 e 3 è stata integrata con una sezione dedicata allo studio dei Duplex in ambito industriale (Appendice A) e riguardante le applicazioni di questi materiali in ambiente marino. Infine, in Appendice B si riportano i risultati ottenuti da uno studio archeometrico di carattere

metallurgico, sviluppato nel corso del periodo di Dottorato e che ha contribuito alla formazione scientifica del candidato, seppure il tema in oggetto non sia strettamente correlato all'attività di ricerca principale.

Le attività di ricerca, sperimentali e di formazione, sono state principalmente svolte presso i locali e i laboratori del Dipartimento di Ingegneria Industriale (DII) dell'Università degli Studi di Padova, ed in particolare in quelli pertinenti al gruppo di metallurgia del DII, sotto la supervisione della Prof.ssa Irene Calliari e del Prof. Emilio Ramous. Tuttavia, alcune attività hanno richiesto il coinvolgimento di altre strutture esterne all'Università di Padova. Nella fattispecie, le misurazioni di diffrazione di neutroni sono state effettuate nella stazione diffrattometrica INES, situata presso la struttura ISIS nel Rutherford Appleton Laboratory (Didcot, UK) in collaborazione con la Dott.ssa Antonella Scherillo ed il Dott. Francesco Grazzi del CNR di Firenze, mentre le misure magnetiche sono state condotte presso i laboratori dell'Università di Budapest (BME), in collaborazione con il Prof. István Mészáros. Le analisi EBSD sui materiali deformati sono invece state realizzate dalla Dott.ssa Paola Bassani del CNR di Lecco, mentre le prove meccaniche di tenacità ad impatto sono state effettuate in collaborazione con la Dott.ssa Cinzia Menapace dell'Università di Trento, presso i laboratori universitari, e con l'Ing. Marco Pizzo (Unilab Laboratori Industriali srl), presso i laboratori Exova CTR srl.

I risultati riportati nella presente tesi hanno contribuito ad ampliare la conoscenza degli effetti delle modificazioni microstrutturali sulle caratteristiche e proprietà degli acciai Duplex e, pertanto, presentano una rilevanza scientifica tale da averne permesso la presentazione in convegni internazionali e la pubblicazione in riviste scientifiche di settore.

CONTENTS

CHAPTER 1

DUPLEX STAINLESS STEELS

1.1. INTRODUCTION

Duplex Stainless Steels (DSS) represent a particular category of stainless steels, characterized by a biphasic (namely Duplex) microstructure, composed by ferrite and austenite. The presence of almost equal volume fractions of the two phases allow for the achievement of a very favourable combination of mechanical and corrosion resistance properties, making DSS suitable for particular applications. Due to their properties, these steels play a role of great interest and, moreover, the relatively limited cost further makes DSS highly competitive against the standard ferritics and austenitics grades [1-5].

These steels are known since the thirties but, owing to the provided interesting features together with the costs saving, their development was of great industrial and commercial relevance especially in the last forty years. The remarkable growth in nickel cost, associated with an increasing demand by the petrochemical industry, have eased the improvement of DSS, in order to obtain materials of limited cost, employable in aggressive environments also as structural materials. Moreover, the introduction of steels manufacturing production systems such as VOD (Vacuum Oxygen Decarburization) and AOD (Argon Oxygen Decarburization) have permitted the attainment of decreased carbon contents and reduced presences of inclusions together with a more strict control of the nitrogen amount in alloys, making the DSS manufacturing ever more reliable [5].

DSS are high-alloyed steels (Table 1.1) and their composition must be carefully balanced in order to obtain a microstructure of approximately 50% austenite and 50% ferrite. They mainly contain chromium (20–29%), nickel (1–7%), molybdenum (4% maximum) and nitrogen (up to 0.4%), while the carbon content is maintained around 0.03% or below. The most common grade is the SAF 2205, with 22%-Cr and 5%-Ni, but

in the last years increasing efforts were made to develop other alternative grades, either of lower cost or higher performances. Recently, DSS with lower Ni and Mo contents – the so-called Lean grades – were produced, owing to the increased cost of these elements, for which a further addition of Mn and N is needed to balance the microstructure [6]. Conversely, the achievement of a highly superior corrosion resistance, particularly against pitting and stress corrosion, and a further mechanical strengthening was accomplished by the design of other new categories – the so-called Super- and Hyper-DSS (SDSS and HDSS, respectively) – containing W, Cu and higher amounts of Cr, Mo and N; for these latter grades, the increased cost is justified by the attainment of extraordinary properties.

Table 1.1 – Chemical compositions of common Duplex Stainless Steels [wt.%].

Grade	UNS	EN	C	Cr	Ni	Mo	N	Mn	Cu	W
Lean										
2101	S32101	1.4162	0.04	21.0–22.0	1.4–1.7	0.1–0.8	0.20–0.25	4–6	0.1–0.8	-
-	S32202	1.4062	0.03	21.5–24.0	1.0–2.8	0.45	0.18–0.26	2.00	-	-
2304	S32304	1.4362	0.03	21.5–24.5	3.0–5.5	0.1–0.6	0.05–0.20	2.50	0.1–0.6	-
Standard										
2205	S31803	1.4462	0.03	21.0–23.0	4.5–6.5	2.5–3.5	0.08–0.20	2.00	-	-
2205	S32205	1.4462	0.03	22.0–23.0	4.5–6.5	3.0–3.5	0.14–0.20	2.00	-	-
Super										
2507	S32750	1.4410	0.03	24.0–26.0	6.0–8.0	3.0–5.0	0.24–0.32	1.20	0.5	-
-	S32760	1.4501	0.03	24.0–26.0	6.0–8.0	3.0–4.0	0.20–0.30	1.00	0.5–1.0	0.5–1
-	S32906	-	0.03	28.0–30.0	5.8–7.5	1.5–2.6	0.30–0.40	1–1.5	0.8	-
Hyper										
-	S32707	-	0.03	26.0–29.0	5.5–9.5	4.0–5.0	0.30–0.50	1.50	1.0	-
-	S33207	-	0.03	29.0–33.0	6.0–9.0	3.0–5.0	0.40–0.60	1.50	1.0	-

In several applications DSS are preferred against other stainless steels, especially when the risk of stress corrosion limits the use of austenitics and when generalized corrosion restricts the use of ferritics. As the others stainless steels, DSS can be classified according to their resistance to pitting corrosion, assessed by the PRE_N index (Pitting Resistance Equivalent Number), a parameter which is intimately related to the composition of the steel

and frequently used as comparison term between different grades. The expression normally employed to define PRE_N is the following:

$$PRE_N = Cr(\%) + 3.3 \cdot Mo(\%) + k \cdot N(\%) \tag{1.1}$$

where the symbol (%) indicates the weight percentage of the considered element, while k is a constant that varies between 10 and 30, and for which the most widely used value is 16. If DSS are tungsten-alloyed grades, the contribution of such element must be taken into account and the previous relation is modified as follows:

$$PRE_W = Cr(\%) + 3.3 \cdot [Mo(\%) + 0.5 \cdot W(\%)] + k \cdot N(\%) \tag{1.2}$$

The use of PRE_N (or PRE_W) is qualitative, because it refers to the average alloy composition and does not consider the influence of phases morphology and microstructural inhomogeneities at local level, such as a not uniform elements partitioning within the two phases. However, by means of this index is still possible to draft a classification of DSS in four different main categories:

1. Lean DSS (including SAF 2101 and SAF 2304), which are characterized by a PRE_N value of about 25 and by a low content of Ni and Mo; these steels can in most cases replace the austenitics AISI 304 and 316;

2. Standard DSS (SAF 2205), with a PRE_N of about 35 and which possess a good compromise between cost and both mechanical and corrosion resistance properties;

3. Super DSS (such as SAF 2507 and Zeron®100), which are highly-alloyed SDSS having PRE_N and PRE_W indexes around 40–42 and offering a corrosion resistance equivalent to that of super-austenitics containing 5–6% of Mo;

4. Hyper DSS (SAF2707), having PRE_N higher than 45, combining very high Cr-Mo-W additions with a significant nitrogen content (up to 0.4%) and for which higher solution-annealing temperatures are needed.

Nevertheless, although PRE_N is easily obtainable from the average alloy composition, a more useful parameter to classify DSS against pitting corrosion is the Critical Pitting Temperature (CPT), defined as the temperature below which the steel is indefinitely

resistant to localized attacks and which is intimately related to the real microstructural conditions of the steel. Similarly, the Critical Crevice Temperature (CCT) can be defined as a ranking index against crevice corrosion but, due to the dependence of such localized attack on the particular geometry of the interested components, the difficulty to achieve reproducible practice tests restrains it use.

After the forming operations, all DSS are necessarily solution-annealed and water quenched, in order to obtain the characteristic biphasic microstructure. The treatment temperature is strongly dependent on steels composition and on the previous thermo-mechanical process at which the steels were subjected, and is performed in the temperature range where the two phases coexist in approximately comparable volume fractions.

Besides the interesting properties provided by the biphasic microstructure, DSS can be efficiently employed only within a limited temperature range (-50–250°C), since at lower temperatures the material exhibit a not negligible drop in toughness, whereas precipitation of secondary phases can occur at higher temperatures [1]. The sub-zero toughness reduction is due to the presence of the BCC ferrite, which exhibits cleavage as the temperature is lowered, and also the precipitation of undesired phases is caused by the ferritic phase, which is thermodynamically unstable at high temperatures and may decompose. In fact, the high alloying elements content eases decomposition reactions in ferrite, making DSS particularly prone to phases precipitation after (relatively) prolonged exposures at high temperature. In practice, the onset of these phases is due to inefficient cooling or improper heat treatments during the manufacturing process, but can also be encountered during the product lifecycle, for example after incorrect welding operation.

Secondary phases may precipitate in a wide temperature range (250–1000°C) and those of greater interest are formed above 600°C, because the decomposition kinetics are enhanced by the high temperature and their formation rate is greater (the precipitation can occur after few minutes in the higher-alloyed DSS grades). The presence of these secondary phases (intermetallic compounds, nitrides, carbides) affect the excellent characteristics of DSS, promoting localized corrosion and markedly reducing their impact toughness, also for very low volume fractions. In fact, the most relevant phases possess Cr and Mo contents which are higher than in ferrite from which are formed, causing a depletion in such elements and promoting the risk of localized corrosion; moreover, since these phases are structural discontinuities, they act as preferential sites for cracks

nucleation. For these reasons, DSS must be produced as "free from intermetallics". For this purpose, the solution-annealing treatment not only allow for the achievement of the biphasic microstructure, but also is necessary to re-dissolve any precipitate formed during the manufacturing operation, ensuring a clean and balanced microstructure [1-5].

In the present chapter, an overview of the DSS features is given, considering different aspects concerning their physical metallurgy and their properties, both mechanical and against corrosion, in order to give a better comprehension on the involved topics during the whole Ph.D. research work.
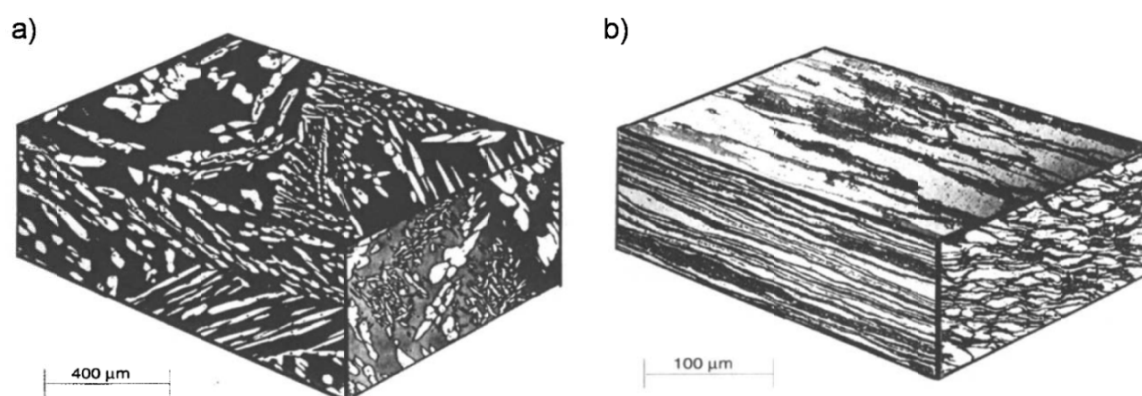

Fig 1.1 – 3D views of typical Duplex microstructures: a) cast and b) hot-rolled [4].

1.2. PHYSICAL METALLURGY

The biphasic microstructure of DSS, composed by austenitic grains surrounded by a ferritic matrix (Fig. 1.1), is the key element of this class of steels, giving them the favourable combination of mechanical and corrosion-resistance properties and making them very interesting materials. On the other hand, owing to this particular microstructure, DSS can undergo significant microstructural modifications as a consequence of either thermo-mechanical treatments in the high-temperature range or plastic deformation at room temperature, causing a drastic reduction in their advantageous properties [1-5]. As a matter of fact, the instability of the ferritic matrix at high temperatures and the presence of the metastable austenitic phase may lead to the formation of new phases, which are strictly related to chemical composition, microstructure, heating temperature and strain associated to the involved process. Thus, depending on the different conditions to which the steel is subjected, ferrite decomposition (which causes σ- and χ-phase formation), carbides/nitrides

precipitation and Strain-Induced Martensite (SIM or α'-martensite) formation from austenite may occur. Therefore, in DSS, the control of the microstructure during the solidification process and after the hot-working operations is of essential importance and depends on both composition of the steel and thermo-mechanical processes.
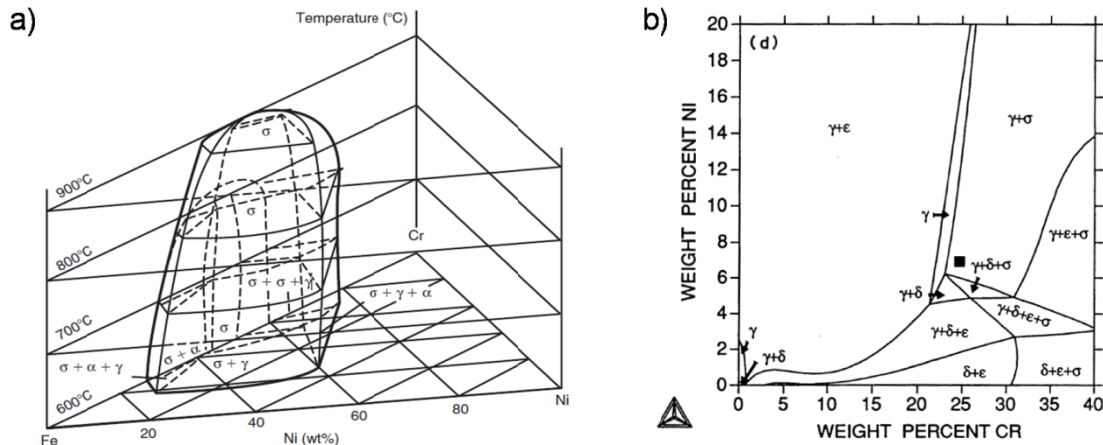

Fig 1.2 – DSS phase diagrams: a) ternary system Fe-Cr-Ni and b) simulated isothermal section of multi-component system Fe-Cr-Ni-Mo-N [1].

These materials are high-alloyed special steels, containing 6–7 main elements; hence, their behaviour in relation to temperature variation cannot be described by ordinary phase diagrams. Even though DSS are employed in a non-equilibrium state, the knowledge of their equilibrium conditions is of fundamental importance to define those parameters which can provide the optimal microstructure and which can limit their operating conditions. Therefore, since DSS are based on complex systems, the study of their physical metallurgy involves either pseudo-binary diagrams or sections of the Fe-Cr-Ni ternary system (Fig. 1.2a); unfortunately, due to the presence of a not negligible amount of other alloying elements, such representations are not completely exhaustive and may only provide information of qualitative character [5]. However, during the last years, the progress in computational systems and material science have permitted the development of thermodynamic simulation software based on the minimization of the Gibbs free energy in different conditions, allowing to adequately describe the DSS equilibrium microstructure in a wide compositional range, in terms of both phases type and amount (Fig. 1.2b) [5]. The computations provided by these programs are, obviously, not free of errors, but can give important information on the microstructural evolutions in DSS when thermally-

treated; moreover, these computations are also often employed in design for the development of new grades.

Nevertheless, while the high-temperature precipitations were widely studied during the past years, only little attention was paid to the possibility of a strain-induced martensitic transformation in this class of steel. Therefore, it is of fundamental importance to define those parameters which affect the formation of dangerous phases arising from either diffusive or diffusionless processes, in order to avoid their occurrence during the manufacturing operations and during the lifecycle of the final products. Among the previously mentioned phase transformations, the products of ferrite decomposition and the high-temperature precipitations are, in general, of greater interest. Thus, the present paragraph firstly deals with the understanding of both the effect of the alloying elements and the physical metallurgy of DSS in relation to the exposition of the materials at high temperatures, while a description of the strain-induced phase transformation is given in Paragraph 1.2.4.4, even though it must be underlined that the room temperature behaviours are ever conditioned by the high-temperature processes.

1.2.1. Effects of alloying elements

DSS are high-alloyed steels containing considerable amounts of several elements. As a premise, it is necessary to underline that the study of the influences of individual elements in alloys becomes increasingly complicated as the number of such elements increases, although the preliminary study of the individual influence assumes relevance in order to supervise and orient the obtainable properties from the applicative point of view.

Table 1.2 – Partition coefficients of some Duplex grades (α/γ).

Grade	Cr	Ni	Mo	N	Si	Mn
2304	1.19	0.61	1.65	0.18	1.16	0.89
2205	1.20	0.58	1.72	0.20	-	-
2507	1.13	0.70	1.30	0.13	-	-

The alloying elements may be divided in α- and γ-promoting elements. The firsts have the aptitude to broaden the stability field of ferrite (α- or δ-phase), while the seconds extend the stability range of austenite (γ-phase). For this purpose, it is useful to identify the

so-called partition coefficients, defined as the ratio between the amounts of the element solubilised in each phase, intimately relate to the bulk composition of the alloy. Since partitioning is a diffusive process, these ratios strictly depend on the particular cooling conditions at which the alloy is subjected. Slow cooling rates can correctly redistribute the elements between the two phases on the basis of their thermodynamic characteristics, whereas high rates tend to inhibit such process, making the composition of austenite and ferrite more homogeneous and giving rise to partition coefficients close to the unit. In Table 1.2 the partition coefficients of some DSS grades are reported, while the partitioning process is further discussed in Paragraph 1.2.3.
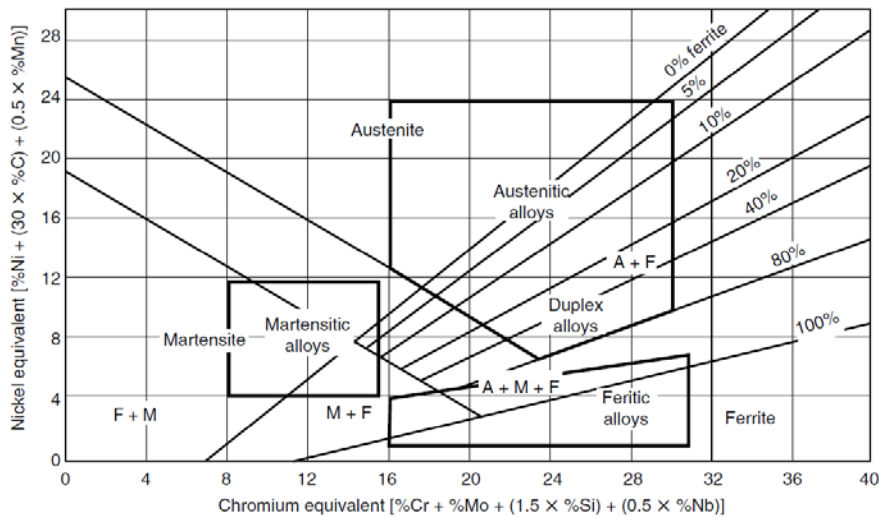

Fig 1.3 – Schaeffler diagram.

As already reported, DSS are characterized by a typical biphasic microstructure consisting of ferrite and austenite, usually present in almost equal volume fraction, which is achieved by an adequate balancing of the alloying elements. However, the adjustment of the microstructure is complicate, because not only depends on the alloy composition.

The identification of the obtainable stainless steels microstructure can be made by means of the Schaeffler diagram (Fig. 1.3), originally developed for the evaluation of welded microstructures resulting from non-equilibrium rapid cooling. This diagram is based on the relation between the elements and their specific attitude to stabilize the BCC- or the FCC-iron lattice structures (α- or γ-promoting elements). Therefore, the obtainable steels microstructures are plotted as a function of chromium-equivalent (Cr_{eq}) and nickel-

equivalent (Ni_{eq}) parameters, which are commonly calculated using the following expressions:

$$Cr_{eq} = Cr(\%) + 1.5 \cdot Si(\%) + Mo(\%) + 0.5 \cdot Nb(\%) + 2 \cdot Ti(\%) + 5 \cdot V(\%) + 3 \cdot Al(\%) \qquad (1.3)$$

$$Ni_{eq} = Ni(\%) + 30 \cdot C(\%) + 0.87 \cdot Mn(\%) + a \cdot [N(\%) - 0.045] \qquad (1.4)$$

An increased content of alloying elements will suppress the martensitic transformation which may occur during quenching, resulting in an austenitic (high Ni_{eq}) or ferritic (high Cr_{eq}) structure. If the austenite-stabilizing elements are present in an adequately content, the austeno-ferritic (Duplex) microstructure is formed.

Chromium

Chromium is a strong α-promoting element, and therefore stabilize ferrite; it is also the main alloying element and, as a matter of fact, a minimum of 10.5% of Cr is required to make the steels "stainless". The main advantage of adding chromium is indeed to improve the resistance to localised corrosion (pitting, crevice), owing to the formation of the protective passive Cr-rich oxy-hydroxide layer. Even though Cr increases the nitrogen solubility in ferrite, there is a limit in the amount that can be added to the steel, as the beneficial effect of higher contents is negated by enhancing the precipitation of detrimental intermetallic phases, such as the σ-phase [4].

Molybdenum

Molybdenum has a similar effect on ferrite stability owing to its α-promoting character and also increases the nitrogen solubility in the ferritic phase. As for Cr, its beneficial influence concerns the extension of the passive potential range and the reduction of the corrosion current density in the active range, enhancing pitting and crevice corrosion resistance in chloride solutions. The corrosion resistance was also found to be improved by suppressing the active sites via formation of an oxy-hydroxide or molybdate ion. In high temperature seawater, the addition of at least 3% of Mo is recommended to prevent crevice corrosion, while an upper limit of about 4% Mo has been quoted, due to the tendency of enhancing σ-phase formation in the hot-working temperature range. This element not only increases the

rate of intermetallic precipitation, but also extends the stability range to higher temperatures [4].

Nickel

In order to maintain about 40–60% ferrite, the steel composition must be balanced with austenite stabilisers; for this reason, the level of nickel addition depends on the Cr content. Excessive Ni contents cause an increase in austenite level that can be well above 50%, resulting in a Cr and Mo enrichment of the remaining ferrite, and therefore enhancing the intermetallic phases formation. Ni retards the σ-phase precipitation, but too higher contents accelerate the α' formation in the range 300–600°C, another embrittling phase. Ni does not have some direct effect on corrosion properties and its main role is to control phase balance and element partitioning [4].

Nitrogen

Nitrogen is a strong γ-promoting elements and has a multiple effect by increasing pitting resistance, austenite content and steel strength. The influence on pitting is similar to that of Cr and Mo, moving the passivation potential toward the noble direction and thus increasing the passive potential range. This effect is enhanced in the presence of Mo and it has been suggested that Mo and N have a synergistic influence on pitting characteristics. Nitrogen preferentially dissolves into austenite due to the increased solubility in that phase and also concentrates at the metal-passive film interface. Nitrogen has also been noted to increase the crevice corrosion resistance due to the altering of the crevice solution chemistry or by segregating to the surface, which is in keeping with the mechanism for enhanced pitting resistance. Another important property of N is the ability to stabilise DSS against the intermetallic phases precipitation by retarding the precipitation kinetics, since it reduces Cr partitioning [4].

The increasing in nitrogen level can reduce the risk of nitride formation; this may appear contradictory, but is due to an increase in austenite content and thus to a reduction in the distance between austenite islands. The addition of C and N strengthens both ferrite and austenite by interstitial solid solution but, as carbon is undesirable due to the risk of sensitisation, the addition of nitrogen is preferred [4]. Nitrogen also reduces the stacking fault energy of austenite and increases its work-hardening rate.

Manganese

Manganese is an austenite stabiliser but has little effect on DSS phase balance, especially at the normally encountered levels. Nevertheless, it increases N solubility but seems that can increase temperature range and formation rate of σ-phase. Its additions is useful against abrasion and wear resistance and also the tensile properties are improved without loss of ductility. However, Mn additions in excess of 3–6%, for nitrogen levels of 0.1–0.25%, significantly decrease the critical pitting temperature (CPT), probably due to the increased likelihood of MnS inclusions which can act as initiation sites for pits and to the destabilization of the passive layer [4].

Copper

Copper additions to high alloyed austenitic stainless steel are recognised to reduce the corrosion rate in non-oxidising environments, such as sulphuric acid. In general, the addition of Cu to DSS is limited to about 2%, since higher levels reduce hot ductility and can lead to precipitation hardening. Under high velocity conditions, where cavitation erosion in H_2S-contaminated seawater prevail, Cu appears to be beneficial, due to the formation of a Cu-rich layer on the surface during active dissolution. Further, copper has been found to improve machinability in low oxygen and sulphur materials and can lead to hardening after exposure to the 300–600°C temperature range, apparently due to the precipitation of tiny Cu-rich precipitates. These precipitates do not significantly reduce corrosion resistance or toughness and have been exploited for improving abrasion-corrosion resistance in DSS pump castings [4].

Tungsten

Tungsten additions of up to 2% improve pitting resistance, by extending the passive potential range and reducing the passivation current. Similarly, W increases crevice corrosion resistance in heated chloride solutions, due to its adsorption into the passive layer without modification of the oxide state. However, in acid chloride solutions W appears to pass from the substrate into the passive film by interaction with water to form insoluble WO_3, increasing the oxides stability and bonding to the substrate.

Tungsten is known to promote intermetallic formation in the 600–1000°C temperature range and it is believed to be thermodynamically, but not kinetically, equivalent to

molybdenum with respect to σ-phase formation. However, levels between 1–3% have been shown to restrict the formation of σ-phase at the grain boundaries and, on the contrary, precipitation occurs at intragranular sites [4].

Silicon

Silicon is beneficial for concentrated nitric acid service and also enhances the high temperature oxidation resistance. Nevertheless, since Si is generally considered to enhance σ-phase formation, it is generally preferred to limit its addition to 1% [4].

Carbon, sulphur and phosphorus

The carbon content of most wrought duplex stainless steels is limited to 0.02–0.03%, primarily to suppress the precipitation of Cr-rich carbides, which can act as initiation sites for pitting corrosion and intergranular attack. Similarly, S and P contents are controlled, although not eliminated, as the presence of some sulphur is important for weld bead penetration [4].

1.2.2. Solidification

The solidification of high-alloyed stainless steels can proceed in different ways, primarily as a function of the specific chemical composition of the alloy (Fig. 1.4a). If the percentage of the α-promoting elements is high, the material will solidify at the Cr-rich side of the eutectic field in Fig. 1.4b, the solidification is completely ferritic and austenite arises after further cooling as product of a diffusion-controlled solid-state reaction. The second possibility route is the so-called flip-flop solidification, which occur in the eutectic valley at very low cooling rates and with an increased amount of γ-promoting elements. In this case, after a primary crystallization of the α-phase, the equilibrium is shifted toward the three-phase valley, due to the melt depletion of α-promoting elements, therefore promoting the γ-crystals nucleation [7-9].

In general, due to the great amount of ferrite-stabilizing elements, DSS solidify as fully ferritic and δ-ferrite is formed as first solidification product, with a liquidus temperature of about 1400–1500°C and which varies in relation to the chemical composition of the steel, while the austenitic phase (γ) forms afterwards through a partial solid-state phase transformation process. The so-obtained ferrite/austenite Duplex structure is stable only

within a definite temperature range, in which phase ratio and the respective compositions are proper for a given grade and vary with temperature, with the high temperature stability of the Duplex structure being influenced more by nitrogen content, than by Cr or Mo [4]. Generally, in DSS, the Cr_{eq}/Ni_{eq} ratio is maintained between 2.25 and 3.5; higher Ni and N contents reduce this ratio, allowing the austenite formation at higher temperature and a more rapid genesis of the γ-phase during cooling [9].
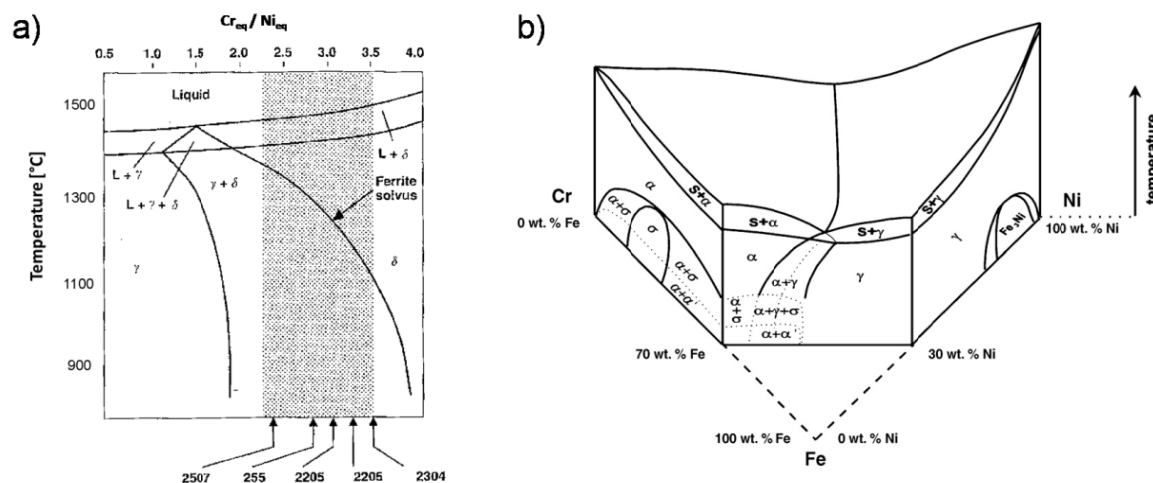

Fig 1.4 – Phase diagrams: a) pseudobinary system for DSS [9] and b) ternary system Fe-Cr-Ni [7].

As cooling continues, for temperature lower than 1000°C the solidifying alloy pass through a first (high-temperature) critical range in which other phases are formed in replacement of δ-ferrite, since at those temperatures the phase is unstable and sensitive to eutectoidic decomposition. These new forming phases are principally intermetallic compounds, nitrides and carbides, among which the most important (and dangerous) is the intermetallic σ-phase, which is often accompanied by another intermetallic compound, the χ-phase. The formation of such phases is strongly time-dependent and can be avoided by passing through the critical range at a proper cooling rate. Despite their harmful effects, these phases are not structural anomalies but belong to the DSS equilibrium microstructure (Fig. 1.5) and, in isothermal conditions, gradually replace ferrite, which is totally transformed at the equilibrium [5].

The solidification process proceeds with the gradual disappearing of austenite, which is stable only within a high-remperatures range, and α-ferrite is formed around 700°C down to room temperature. Below 600°C another (low-temperature) critical temperature range is encountered and, if the time at which the alloy remains in temperature is sufficiently long,

the formation of other secondary phases and the spinoidal decomposition of ferrite can also occur. However, due to the low temperature, the kinetics involved to allow ferrite decomposition are rather slow and thus the formation of such secondary phases can be easily avoided.
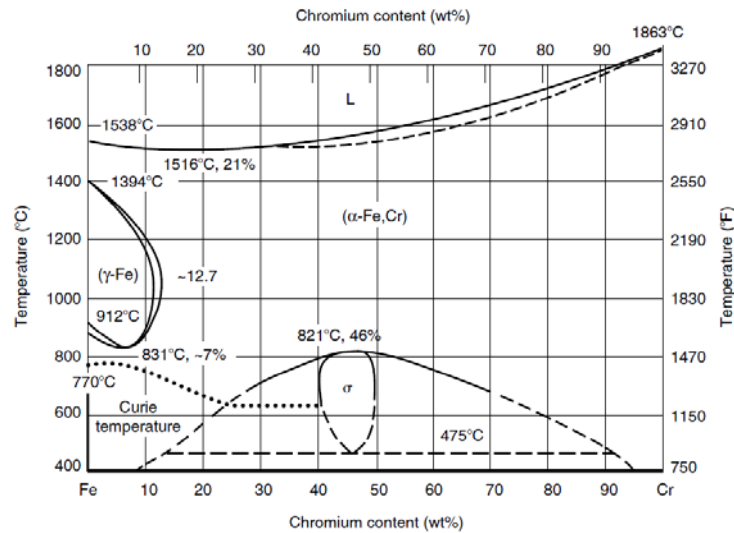

Fig 1.5 – Binary Fe-Cr phase diagram.

As a consequence of this complex solidification process, DSS require a particular and careful solution-annealing treatment, in order to guarantee a balanced microstructure and avoid the secondary phases formation, due to the severe detrimental effects on DSS properties (Paragraph 1.2.4.4 and Chapter 2).

1.2.3. Solution-annealing treatment (solubilisation)

This treatment is mandatory in all DSS, because it allows for the formation of a balanced austeno-ferritic microstructure free from intermetallics, and it consists in a solution-annealing treatment at a proper temperature for a certain soaking time, followed by water-quenching. The solubilisation temperature, always above 1040°C, is primarily related to the particular grade – and therefore to the alloy composition – and is chosen within the ferrite/austenite stability field, in order to achieve an equal volume fraction of the phases. The soaking time must instead take into account the previous manufacturing process and should be adequately long both to guarantee an adequate elements partitioning and to re-dissolve the secondary phases, if presents. Finally, the water quenching must be as rapid as

possible, in order to avoid the precipitation of undesirable phases. Hence, through this treatment, the high-temperature microstructure is frozen at room temperature and the final DSS microstructure is then composed by a ferritic matrix in which the austenitic grains are dispersed (Fig. 1.1). As a result, the two phases have different compositions, due to the different solid solubility potential of alloying elements in BCC and FCC lattices – especially for interstitial atoms – and which are also related to solubilisation temperature and cooling rate [10].

It must be notice that the so-obtained ferritic phase is the high-temperature δ-ferrite and is sometimes improperly called α-phase, which is instead the low-temperature ferrite. Both ferrites have the same BCC crystal structure but their composition and stability range are different; the real α-ferrite forms during the complete solidification of the alloy at about 700°C in DSS and, since the composition is different and suffer from the disappearing of the γ phase during the solidification process, must be considered different from the δ-phase. However, the ferritic phase obtained from solubilisation is often called α-ferrite, but is only a denomination.

The annealing conditions (solubilisation temperature and soaking time) affect both miscrostructure and elements partitioning inside the phases, and depend on the previous thermo-mechanical processes. If the DSS are annealed at a temperature near the ferrite solvus, the phase balance will be high in ferrite while, reducing the temperature, a progressive amount of austenite is expected (Fig. 1.6a). In equilibrium conditions, the α- and γ-promoting elements are correctly distributed inside the phases, with Cr-Mo-W concentrated in ferrite and Ni-C-N-Mn in austenite, and, with falling temperature, the equilibrium compositions of both phases are continually changing, according to the ferrite solvus line composition [9]. At the same time, diffusion is slowing with decreasing temperature and if the soaking time is too short the elements will not correctly partition inside the two phases (Fig. 1.6b). Furthermore, hot working speeds diffusion, so that a lower effective quenching temperature is more easily obtained for wrought DSS than for casts and welds [9]. Practically, the annealing temperature must be as lower as possible and should be chosen in order to re-dissolve any precipitates and to achieve the desired Duplex microstructure – and this also minimizes the amount of nitrogen remaining in the ferritic phase. Nevertheless, although the 50/50 ferrite/austenite phase ratio is the ideal value for a

Duplex microstructure, in reality the phase fractions cover a slightly wider range, which is between 40/60 and 60/40.
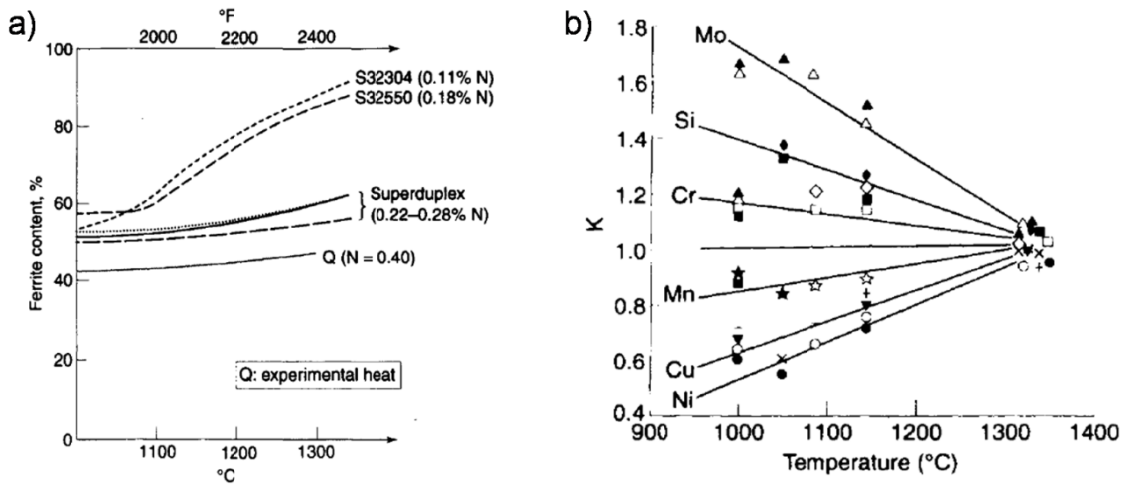

Fig 1.6 – a) variation in ferrite content with temperature and b) temperature dependence of elements partitioning coefficients (K = α/γ) [4].

The ideal structure of DSS is of course purely ferritic-austenitic. However, in practice, this is quite difficult to achieve, particularly when the dimensions of the final product are large or during welding operations, when the cooling rates cannot be fully controlled. Moreover, if the steel is an high-alloyed grade, the situation is aggravated. The cooling rates must be properly chosen because, while σ-phase tends to be a problem during slow coolings, chromium nitrides behave in an opposite way; in particular, non-equilibrium intragranular nitrides are likely to form when the cooling is so rapid that there is insufficient time for nitrogen to escape from ferrite [11].

Thus, after solubilisation, both ferrite and austenite are forced to exist at room temperature from a high-temperature equilibrium condition and this has different implications on the phases stability, owing to the peculiar character of each phase. In fact, while the allotropic nature of iron allow the existence of the BCC δ-ferrite at room temperature, in a Duplex microstructure austenite is instead in metastable conditions, owing to the FCC iron structure which pertains to higher temperature. This metastability can cause other types of solid-state phase transformation, which are no more related to the effect of thermal cycles but which are diffusionless, possessing a strain-induced character (Paragraph 1.2.4.2).

1.2.3.1. Elements partitioning

The phase diagrams related to DSS [1,7,9] point out the strong relationships among solubilisation temperature, phase balance and elements partitioning inside the phases. Ferrite and austenite have different compositions but the partition coefficients – defined in Paragraph 1.2.1 – for a given substitutional alloying element do not significantly vary among different DSS grades. This is because the solubility limits for these elements in never exceeded for the concentrations and annealing temperatures concerned. Ferrite is enriched in P-W-Mo-Si-Cr while austenite in N-Ni-Cu-Mn even though, for the most highly alloyed grades (SDSS), it has been proposed that the partition coefficients tend more towards unity, apparently due to the use of higher solubilisation temperatures [4].

On the contrary, regarding the interstitial nitrogen, its partition coefficient is seen to vary markedly among alloys and is highly dependent on composition. In particular, Cr and Mn increase nitrogen solubility (Fig. 1.7a), which is also governed by temperature (Fig. 1.7b). An increasing in solubilisation temperature may increase a little the nitrogen solubility in ferrite but also causes a marked decrease in austenite volume fraction, leading to an enrichment in nitrogen in the remaining austenite, thus modifying the partition coefficients.
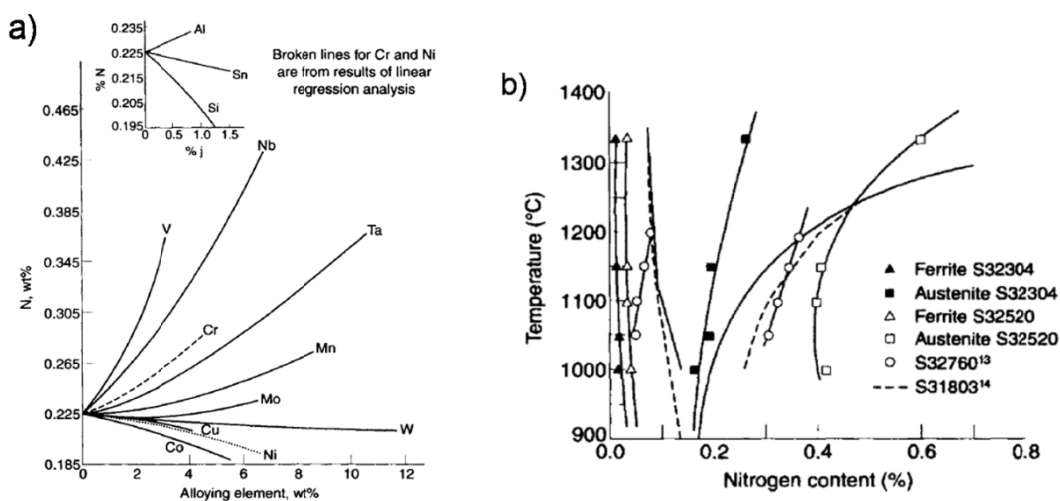
Fig 1.7 – a) effect of alloying elements on N solubility at 1600°C in Fe-18%Cr-8%Ni alloys and b) nitrogen content in ferrite and austenite as a function of temperature for different alloys [4].

However, on cooling, austenite formation occurs and the ferrite becomes rapidly saturated in nitrogen, with the excess nitrogen diffusing into the austenite. Further additions of nitrogen to the bulk alloy composition, as in SDSS, lead to nitrogen enrichment in the austenite, being 0.03–0.05% N the equilibrium solubility limit in ferrite

at room temperature. Nitrogen addition has a significant influence on pitting corrosion resistance, especially in austenite, which is the weakest phase against pitting, balancing the preferential partitioning of Cr and Mo in ferrite and leading to a similar pitting resistance of the two phases [4].

1.2.4. Solid-state phase transformations

Numerous microstructural changes can occur in DSS during isothermal or continuous cooling heat treatments and most of them are concerned with ferrite, which is unstable at high temperatures. However, as reported at the beginning of this paragraph, the metastable condition of austenite can cause other types of phase transformation, which do not involve thermal activation, but which are related to the plastic response to the FCC phase during cold working. Hence, if the interesting properties of DSS are precisely achieved from the simultaneous presence of the two phases, in the other hand their favourable features are mined by the instability of the phases in different temperature ranges.

The difference between the two phases is primarily site in their different crystal structure: austenite is characterized by a FCC lattice while ferrite is a BCC phase. This implies different responses to plastic deformation and different behaviours when diffusion mechanisms are involved. Both phases form interstitial and substitutional solid solutions with the alloying elements but ferrite favours diffusion processes at high temperature owing to the BCC crystal structure. On the other hand, FCC austenite is more deformable and posseses a low stacking fault energy, which can ease lattice rearrangements and diffusionless phase transformations.

1.2.4.1. Ferrite stability

Austenite from ferrite is only the first solid-state phase transformation which occur in DSS during solidification, whereas other secondary phases are formed by decreasing/increasing temperature within a wide temperature range. Ferrite is unstable at high temperatures and the precipitation mechanisms related to such phases formation are also enhanced by the diffusion rates of the involved elements, which are approximately 100 times faster in ferrite than in austenite, due to the less compact lattice of the BCC structure. Moreover, as already mentioned, ferrite is enriched in Cr and Mo, which are known to promote the

formation of intermetallic phases, and their solubility in ferrite falls with decreasing temperature, increasing the probability of precipitation during heat treatments. [4].
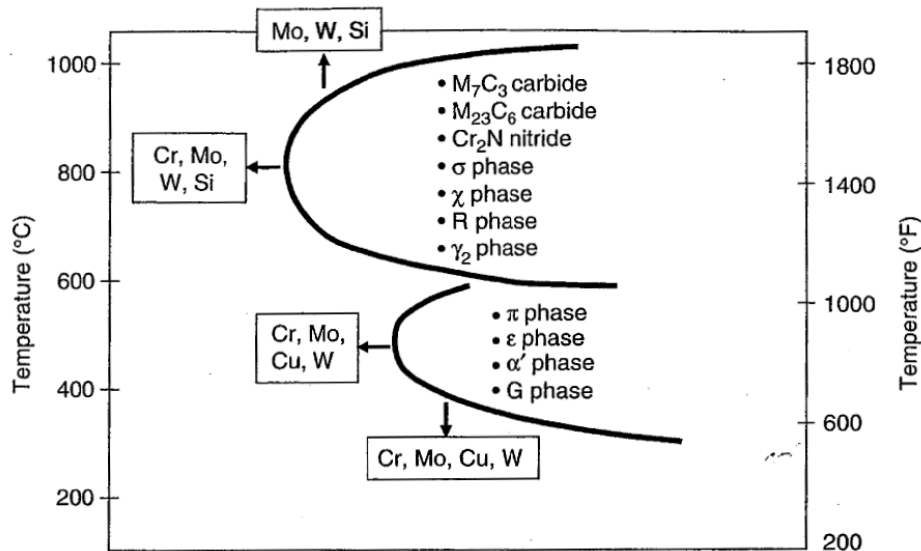

Fig 1.8 – Secondary phases in DSS and influence of alloying elements
on precipitation kinetics [9].

Isothermal heat treatments

The precipitation of these phases, can be subdivided in two main categories, in relation to the concerned temperature range (Fig. 1.8). The investigation of the susceptibility of different grades to secondary phases formation is usually carried out by the determination of the Time-Temperature Transformation (TTT) diagrams, produced after isothermal heat treatment followed by water quenching. These diagrams are often called Time-Temperature-Precipitation (TTP) diagrams and are aimed to define the critical ranges in which the precipitation can occur in terms of precipitation kinetics. Thus, from the TTP curves, three main temperature ranges concerning the ferrite solid-state phase transformations can be defined, and can considered valid for all the DSS grades [1-5]:

1. 300–600°C. This "low-temperature" range is the so-called "*475°C embrittlement*", because at this temperature the ferrite transformation is (relatively) faster and the forming phases can cause severe embritteling effects. This range is primarily characterized by the spinoidal decomposition of ferrite in Cr-rich α' and Fe-rich α domains with slight different lattice parameters. Furthermore, other precipitation processes have been found to occur in this range and, among these, the most

important is certainly relative to the precipitation the G-phase, containing high levels of Ni, Mo and Si.

2. 600–1050°C. This "high-temperature" range is characterized by the formation of several secondary phases, whose precipitation kinetics and incubation times are strongly affected by the chemical composition. These phases, discussed in detail in Paragraph 1.2.4.3, are identified as σ-phase, χ-phase, Cr_2N nitrides, carbides (M_7C_3, $M_{23}C_6$), π-phase, ε-phase, secondary austenite (γ_2) and R-phase, and mainly originates from the eutectoidic decomposition of ferrite. Their precipitation occurs in significantly shorter times respect to the low-temperature range and is enhanced in the high-alloyed grades. Each alloying element has a characteristic effects of phases formation (Paragraph 1.2.1) and the composition must be balanced also in terms of elements inter-mechanisms. These phases can cause a strong decreasing in both mechanical and corrosion resistance properties, as discussed in Paragraph 1.2.4.4 and in Chapter 2.

3. Above about 1050°C: for normal cooling rates DSS solidify as fully ferritic and, during cooling, part of this ferrite transformed into austenite. This transformation is naturally reversible and, therefore, an increasing in temperature results in a greater volume fraction of ferrite, also causing a reduction in the partition of substitutional elements between the phases[4].

Both in high- and low-temperature ranges (1) and (2), can be identified a temperature at which the precipitation kinetics are favoured and where ferrite decomposition occurs faster (hereinafter called "nose"). As reported, in range (1) the decomposition is promoted at about 475°C and this temperature is almost the same for all DSS, while in range (2) the "nose" is strongly composition-dependent and therefore varies among DSS grades (Fig. 1.9a) [4,7]. As expected, SDSS grades show the greatest propensity for intermetallic precipitation, due to their higher contents of Cr, Mo and W, and especial care is required during the manufacturing operations. However, it should be emphasised that the precipitation kinetics in these high-alloyed DSS are, at worst, equivalent to the super-austenitic or super-ferritic stainless steels [4].

For the low-alloyed DSS (*i.e.* Lean DSS or Mo-free grades), intermetallics precipitation need much more holding time (several 10 hours) and nitrides precipitations, particularly in

high-N grades, could be the primarily cause in reducing corrosion and toughness properties when heated at 600–950°C. Lean DSS may be considered as very stable in terms of microstructure, when standard heat treatments – including solution-annealing – are performed. Air cooling can even be considered for some applications and very thick products can be quenched from the solubilisation temperature [12].

All the precipitating phases re-dissolve during the solution-annealing treatment, and in some cases it happens just after few minutes. Nevertheless, the solubilisation treatment must be well designed, in order to achieve the desired Duplex microstructure.
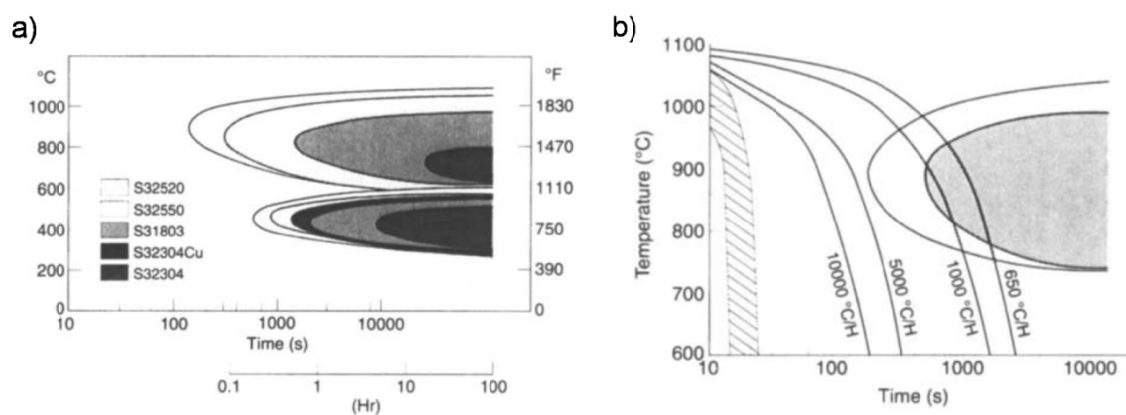

Fig 1.9 – a) TTT and b) CCT diagrams of DSS [4].

Continuous cooling

Similar TTP diagrams can be obtained in continuous cooling conditions and, while the isothermal TTP curves are mainly aimed to investigate the precipitation kinetics and the stability fields of the secondary phases, these precipitation-CCT curves are of large industrial interest because allow for the determination of the critical cooling rate for the secondary phases formation.

At temperatures near the ferrite solvus, the nucleation of precipitates is slow and their growth is fast, whereas the opposite is true at lower temperatures, near the "nose" of the transformation curve. A considerable shift in time can be seen in the position of the precipitation "nose" between the TTT and CCT diagrams (Fig. 1.9b). Cooling rates as low as about 2000°C per hour are possible without precipitation, for solution annealing at 1080°C. However, more rapid cooling is recommended for higher annealing temperatures, since the risk of nitride precipitation is increased [4].

1.2.4.2. Austenite stability

Austenite is the paramagnetic FCC allotropic form of iron and its existence competes to high temperature; thus, at room temperature, austenite is in a metastable condition and the occurrence of proper deformation mechanisms could generate lattice rearrangements involving stress- or strain-induced phase transformations. Austenite is (partially) stabilized by adding a suitable amount of γ-promoting elements in DSS compositions, and this stabilization is further effective by increasing the content of such elements. However, being DSS biphasic, the composition must be well-balanced and limited values of the Cr_{eq}/Ni_{eq} ratio must be maintained, in order to achieve the Duplex microstructure and to avoid harmful precipitations. As previously mentioned, if austenite is not well stabilized, its metastable conditions at room temperature could give rise to a difusionless solid-state phase transformation during plastic deformation, leading to the appearance of the so-called Strain-Induced Martensite (SIM or α'-martensite).

The stability of the austenitic phase depends on the amount of the solubilised alloying elements, and the involved deformation mechanisms can be associated to its Staking Fault Energy (SFE), which is related to the phase chemical composition at a fixed temperature [13]. SFE is an important parameter in the definition of the plastic behaviour of a phase, owing to its relationship to the dislocation configuration; high-SFE materials, exhibiting more cross-slip, form cellular dislocation structures while low-SFE materials usually form planar array of dislocations in which the absence of significant cross-slip promotes work-hardening [14]. The tendency to SIM formation increases with the decreasing of the SFE value [15] and is primarily related to plastic strain rather than to the acting stress [16]. As a matter of fact, in Lean and Standard DSS grades, austenite is differently alloyed respect to austenite in austenitic stainless steels, since the amount of the strong γ-promoting Ni is lower – and thus requiring higher amounts of N and the presence of Mn. This leads to lower SFE values of austenite in DSS and therefore to a more or less metastable condition of the phase at room temperature, depending on the considered grade.

Strain-Induced Martensite

The strain-induced martensitic transformation is generally observed in metastable austenitic stainless steels, where austenite evolves toward the thermodynamically more stable α'-martensite as a consequence of the cold plastic deformation. The process is

diffusionless (*i.e.* do not require thermal activation), even though it is enhanced by low temperatures, and involves interactions among micro-defects generated during cold working in the austenitic grains. The martensitic transformation takes place with a cooperative movements of atoms and is promoted by dislocations and twins accumulations, creating a very precise orientation relationship between the parent austenite and the product martensite.
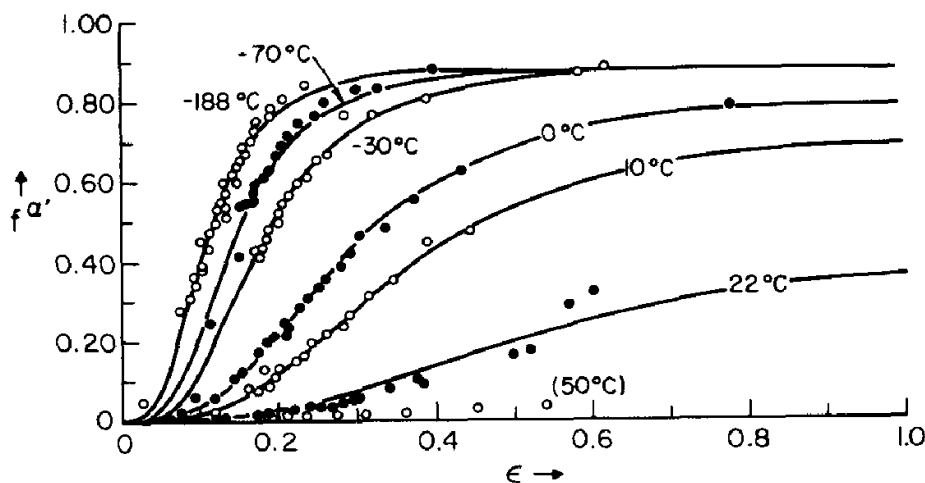

Fig 1.10 – Influence of temperature in the kinetics of SIM in a AISI 304 stainless steel [22].

Conversely to stress-assisted mechanisms, the nucleation sites for SIM formation are created during plastic deformation [16,17] and the shear bands intersections, promoted by low SFE, were found to be the preferential active sites [18,19]. These intersections are planar defects, which are associated to the overlapping of stacking faults on {111} planes; twins form when stacking faults overlap on successive {111} planes, ε-martensite forms when the overlapping occurs on alternate {111} planes, whereas stacking faults bundles arises from irregular overlapping. These various type of overlapping can act as embryos and the generated SIM, having a lath-like morphology [19], is commonly formed via two possible transformation sequences, either $\gamma \rightarrow \varepsilon \rightarrow$ SIM or $\gamma \rightarrow$ SIM, depending on SFE of austenite (ε-martensite is proper of lowest SFE alloys) [16]. In fact, although ε-martensite plays a fundamental role on the strain-induced nucleation, it is not necessary for the achievement of the full transformation, since SIM can nucleate independently, especially when ε is not even thermodynamically stable [16]. Nevertheless, the genesis of SIM and the amount of transformed austenite not only depend on SFE, but must also be related to

other parameters, such as strain rate, temperature and stress-type, which can modify the phase response to the plastic deformation (Fig. 1.10) [16-26].

SIM may enhance the work hardening rate of the steel, influencing the uniform elongation – which is good for formability – and the mechanical strength is also increased. However, it can cause delayed cracking in deep drawn components [27] and can affect the pitting corrosion resistance, due the presence of residual stresses caused by the $\gamma \rightarrow$ SIM volume change and owing to the increasing in the number of active anodic sites in the surface [28-30]. SIM is a BCC ferromagnetic phase, having nearly the same lattice parameter to that of ferrite (a $\approx$ 0.287 nm [23]), while ε-martensite is paramagnetic (as austenite) and possesses a HCP crystal structure. Hence, SIM identification in austenitic stainless steels by x-rays diffraction techniques is very easy to achieve, owing to the solely presence of the FCC-austenite; on the contrary, the concurrent presence of ferrite and austenite renders this method unhelpful in DSS. Nevertheless, due to the magnetic behaviour of SIM, a change in magnetic properties of DSS occurs after its formation, allowing its detection throughout magnetic measurements, even though these methods require an appreciable volume fraction of martensite.

The Strain-Induced Martensite was extensively studied in metastable austenitc stainless steels – especially in types AISI 304L and 316L [13-26] – in which it occurs at relatively low strains in a wide range of temperatures, but a few attention was paid on such possibility in DSS [31-33]. In Chapter 3, the effects of cold rolling in DSS are presented and the onset of SIM formation is discussed, pointing out that the Duplex microstructure can play a not negligible role on such transformation, modifying the mechanisms of deformation and the kinetics of SIM formation owing to its biphasic character.

1.2.4.3. Secondary phases

As previously reported, DSS may undergo a series of significant phase transformation, especially at high temperatures. In Paragraph 1.2.4.1 the precipitation of secondary phases was generally described, attributing the genesis of such phases to the instability of the ferritic matrix and to the chemical composition of the steel, and a subdivision of the critical temperature range (300–1000°C) was presented.

This section describes the different precipitates affecting DSS after isothermal exposition at high temperature, but which can also arise if the cooling rate is too slow. A summary of these phases is given in Table 1.3, together with crystallographic information and temperature range of precipitation; among these, the σ-phase is the most important one and must be absolutely avoided, owing to its principal dangerous contribution on both embrittling effects and loss in corrosion resistance.

Table 1.3 – Phases observed in Duplex Stainless Steels [1].

Phase	Chemical formula	Temperature range [°C]	Space group	Lattice parameter [nm]
Ferrite (α or δ)	-	-	*Im3m*	$a = 0.286–0.288$
Austenite (γ)	-	-	*Fm3m*	$a = 0.358–0.362$
Sigma (σ)	Fe–Cr–Mo	600–1000	*P4$_2$/mnm*	$a = 0.879$, $c = 0.454$
Chi (χ)	$Fe_{36}Cr_{12}Mo_{10}$	700–900	*I43m*	$a = 0.892$
Chromium nitride	Cr_2N	700–900	*P31m*	$a = 0.480$, $c = 0.447$
Chromium nitride	CrN	-	*Fm3m*	$a = 0.413–0.447$
R	Fe–Cr–Mo	550–650	*R3*	$a = 1.090$, $c = 1.934$
π	$Fe_7Mo_{13}N_4$	550–600	*P4$_1$32*	$a = 0.647$
Metal carbides	M_7C_3	950–1050	*Pnma*	$a = 0.452$, $b = 0.699$, $c = 1.211$
Metal carbides	$M_{23}C_6$	600–950	*Fm3m*	$a = 1.056–1.065$

Sigma (σ) phase

This is the intermetallic phase of greatest interest, both for the high volume fraction that may precipitate and for the deleterious effects on corrosion resistance and impact toughness, even when present in very small amounts. The σ-phase is a complex phase and was found for the first time in the Fe-Cr system (Fig 1.5); it possesses a tetragonal-close-packed (TCP) structure with an elemental cell of 32 atoms and 5 crystallographically different atom sites; is composed by transition metals and is stable only within a certain composition range [34]. This intermetallic compound precipitates at triple points and α/γ grain boundaries in the temperature range 600–1000°C, with the faster precipitation rate at around 800–900°C, grows toward ferrite and is enriched in Fe, Cr and Mo, as shown in Table 1.4 [35].

In DSS, this phase is not the consequence of errors in the manufactoring cycle, but pertains to the equilibrium structure of (almost) all DSS. The σ-phase forms by ferrite decomposition, according to the sequence σ → ferrite + austenite, even though in many cases the precipitation sequence is more complex and involves the formation of other compounds, such as χ-phase, nitrides, etc. This decomposition is very similar to an eutectoid decomposition and the forming austenite is indicated as "tertiary" (γ_3) – even if it is often improperly called γ_2. The ferrite transformation follows this mechanism because the growing of σ causes a depletion in Cr and Mo of the surrounding ferrite and a concurrent enrichment in Ni, leading to the formation of austenite from ferrite; at the same time, the formation of this austenite causes an enrichment in Cr and Mo of the adjacent ferrite, which becomes a suitable nucleation site for σ and so on. The result is the occurrence of alternate areas of austenite and σ-phase. This mechanism also justifies the preferential formation of σ at the α/γ grain boundaries and at the triple points, instead of inside the ferritic grains [5].

Table 1.4 – Compositional ranges of the σ-phase [wt.%].

Cr	Ni	Mo	W
29–34	3–5	3–9	0–7

The formation of σ is mainly favoured by Cr and Mo – but also by W and Si – which enlarge its stability field and enhance both the precipitation rate and its volume fraction, and can occur in very few minutes in the higher-alloyed DSS grades. A high solubilisation temperature tends to increase the volume fraction of ferrite and will suppress σ precipitation, owing to a greater dilution of the ferrite-stabilizing elements, but the cooling rate is also a vital factor. However, whereas sigma is avoided by cooling from higher temperatures, the conditions for chromium nitrides will instead become more favourable [1].

The σ -phase is a hard and brittle phase; its unit cell does not possess easy-slip planes, therefore causing significant embrittling effects, which are enhanced by the coalescence of the particles. The disadvantages induced by σ also derive from its composition, because its formation causes a depletion in Cr of the surrounding ferritic matrix, whose composition

drops below the passivation threshold, facilitating the corrosion mechanisms in the area adjacent to the precipitated particles.

Chi (χ) phase

This is another intermetallic compound, enriched in Cr and especially in Mo (Table 1.5); it possesses a cubic structure and mainly precipitates within the temperature range 700–900°C, with the fastest rate around 850°C. Also in this case, the precipitates nucleate and grow at the interfaces, decorating the grain boundaries, and can be either of elongated or globular shape [2]. For these reasons, the harmful effects of χ-phase on mechanical and corrosion resistance properties are hardly separable from those produced by σ [1]. Moreover, the kinetics of χ-phase formation are enhanced by tungsten, and this is especially evident in SDSS grades.

Table 1.5 – Compositional ranges of the χ-phase [wt.%].

Cr	Ni	Mo	W
20–28	3–5.5	9–22	0–16

The nucleation of χ- phase from ferrite is very easy, owing to the cube-cube orientation relationship between the phases in combination with small coherency strains; it causes a depletion in Mo in the surrounding area and a destabilization of the ferritic matrix, which tends to be replaced by austenite. Some authors asserted that χ-phase is a metastable precursor of the σ-phase [11,35], because after isothermal heat treatments at 750–850°C it appears by first and vanishes for long soaking times, apparently in favour of σ. However, a more accurate study on the precipitation kinetics of both phases within the critical temperature range revealed that the mechanism of formation can be addressed to a "*competitive precipitation*" [36]. This type of precipitation occurs because to the concurrent presence of different mechanisms, which are controlled by temperature, diffusion and coherency between lattices; different combinations of these factors cause the suitable condition for easing the precipitation of one phase rather than the other. Nevertheless, the two phases are almost always present at the same time, but χ precipitates in smaller volume fractions than σ, also due to the limited Mo alloy content, which restrains the precipitating amount.

Chromium nitrides (Cr₂N and CrN)

The nitrogen levels generally present in DSS are well above the solubility limit in ferrite for temperatures around 1000°C but, on the contrary, are below of that in austenite (Fig. 1.11). This difference in solubility has important implications on the precipitation of nitrides. Nitrides precipitation causes a local depletion of chromium, making the steel more susceptible to localized corrosion and the presence of such microstructural discontinuities also increases the number of preferential sites for the cracks initiation, compromising the resistance characteristics of the steel. In DSS, the predominating chromium nitride is the Cr_2N type, with a hexagonal structure, while CrN nitrides with a cubic structure has been less frequently observed, taking apart in the heat affected zone of the weldments in a SAF 2205 [37].
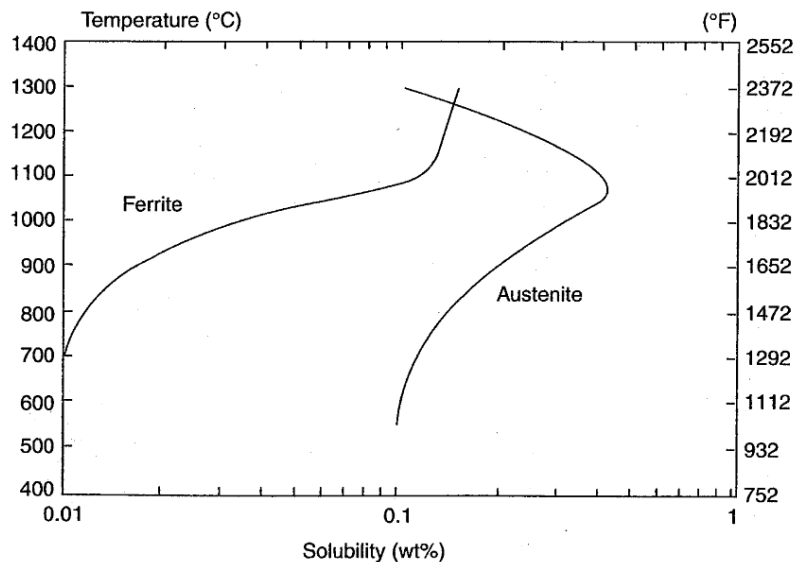

Fig 1.11 – Nitrogen solubility in ferrite and austenite [9].

The formation of Cr_2N can occur by two distinct ways, in relation to the thermal process at which the DSS are subjected. They can precipitate either intragranularly, as a result of a too quick cooling from the solution-annealing temperatures (1050–1100°C), or intergranularly, during isothermal heat treatments at lower temperatures. The intragranular nitrides is formed because, at the solubilisation temperatures, the nitrogen solubility in ferrite reaches comparables values to that in austenite and a quick cooling to low temperatures, where the solubility in ferrite decreases, causes an incomplete diffusion and redistribution of nitrogen into austenite, resulting in a ferrite nitrogen-supersaturated solid solution. The consequence is the precipitation of nitrides with elongated shape inside the

ferrite. These nitrides are ever present after any solubilisation treatment, in various extent depending on the cooling conditions, but the their precipitation is not as dangerous as the intergranular ones, since their position is not favourable for cracks initiation and doesn't contribute to embritteling effects.

On the contrary, the intergranular nitrides form as a result of isothermal heat treatments carried out within the DSS critical temperature range (700–950°C). These nitrides can be related to the supersaturation conditions of ferrite, precipitate in globular form and decorate both the ferritic grain boundaries and the austenite/ferrite interfaces [1]. In some DSS grades, the nitrides precipitation during isothermal heating is accompanied by the formation of secondary austenite (γ_2) [38].
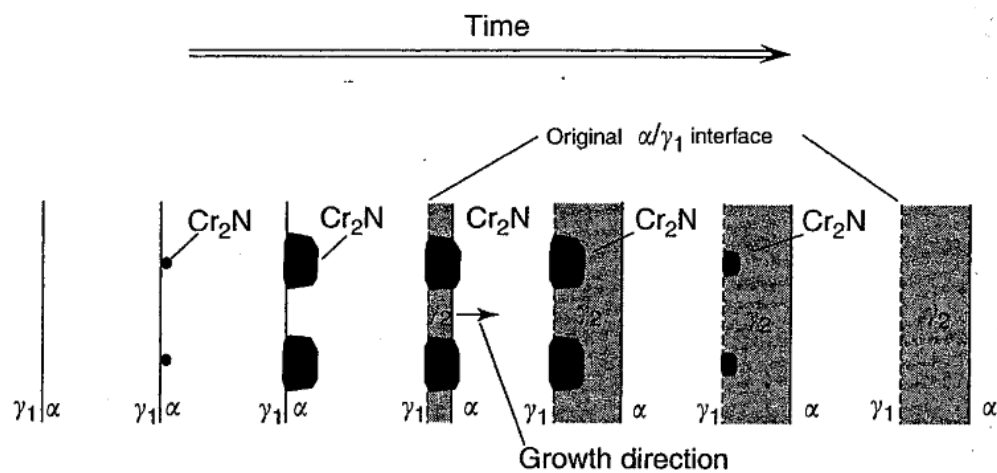

Fig 1.12 – Mechanism for secondary austenite formation [9].

Secondary austenite (γ_2)

The austenitic component in DSS may be called "primary austenite" and it can form during the solidification of the alloy via three different mechanisms – eutectoidic reaction, martensitic shear process and Widmannstätten precipitation, depending on cooling conditions [1]. However, austenite may also form at relatively low temperature, for example in both multi-pass weldings and during isothermal ageing within the critical range; in these cases the duplex structure is re-heated, causing the formation of "secondary austenite" (γ_2) [11]. This nucleation was found to be strictly related to the presence of Cr_2N chromium nitrides (Fig 1.12) [38] and can significantly alter the microstructure balance. Secondary austenite contains less amount of N, Cr and Mo than primary austenite,

increases the toughness of the material but it is deleterious for the corrosion resistance, particularly against pitting.

The formation of secondary austenite can be addressed to two different mechanisms. The first concerns the increasing of the primary austenite grains, while the second takes into account the nucleation within the ferrite grains and is associated to the pre-existing precipitation of chromium nitrides. Considering the latter mechanism, the intergranular position of the precipitated Cr_2N nitrides causes a local depletion of Cr and Mo which, during the heating, allows for the nucleation of γ_2 at the grain boundaries and its subsequent growth [38]. Its appearance is much more frequent in multiple-pass weldings, due to the re-heating of the welding zone, and a more accurate description between secondary austenite and intra- and intergranular chromium nitrides can be found in [38].

Carbides ($M_{23}C_6$ and M_7C_3)

Carbides are interstitial phases composed by a transition metal and carbon. Their precipitation occur at high temperatures when a too high carbon content (generally >0.03%) is present in the bulk composition and make the material susceptible to intergranular corrosion. Among these, chromium carbides are the more harmful ones because they cause a depletion in Cr of the matrix.

In DSS, the $M_{23}C_6$ and M_7C_3 are the most frequently observed carbides [1], which precipitate at α/γ and α/α interfaces. The $Cr_{23}C_6$ carbides, having a HCP crystal structure, are the first precipitating ones, due to the high mobility of carbon in ferrite at high temperatures and their formation increases the risk of intergranular corrosion. However, the low carbon content in DSS makes difficult the carbides precipitation and the nitrides formation is favoured.

Spinoidal decomposition (α')

This precipitation occurs by spinoidal decomposition of ferrite in the temperature range 300–600°C, leading to the formation of two Cr-rich (α') and Fe-rich (α) phases, which cause a decrease in toughness and a hardness increase. Since this decomposition occurs more rapidly at 475°C, it is also known as "*475°C embrittlement*" and also causes a decrease in corrosion resistance, particularly against pitting [39].

This phenomenon takes place after long soaking times, because the diffusivity of the involved elements is low, and is due to the miscibility gap in the Fe-Cr system, which cause the free energy exhibits two minima and which involves the diffusion against the concentration gradient (the so-called "up-hill" diffusion) [7]. This phase decomposition can even occur at temperatures below 300°C, but the required times to achieve the process is of the order of thousands of hours.

G phase

This phase precipitates in the temperature range 300–600°C and contains high amounts of Ni, Si and Mo; these particles are characterized by reduced dimensions (usually 1–10 nm and sometimes up to 50 nm) and precipitate within the ferrite grains, with a uniformity which depends on the chemical composition (*e.g.* those DSS containing high Mo are characterized by a more uniform precipitation if compared to low-Mo DSS). In any case, these particles preferentially precipitate in correspondence of dislocations and at α/γ interfaces, with chemical composition and dimensions which vary according to the steel composition and to the ageing conditions [40] .

R phase

This is a metallic phase possessing rhombohedral crystal structure and irregular shape; the R-phase, precipitates both within and between the ferritic grains, usually in the temperature range 550–700°C after very long soaking times and often coexists with σ-phase. Depending on the exposure time, this phase precipitates in variable dimensions, related to certain elements in the alloy composition (particularly Cr and Mo). It makes DSS prone to localized corrosion attack owing to the very high molybdenum content and also causes a decrease in toughness [41,42].

Other phases

Other phases may precipitate in DSS: among these, of some importance there are the π-phase, a Mo-rich nitride which nucleates between 550°C and 600°C and which causes embrittlement and decreasing in pitting resistance, and the Laves phase (or μ-phase) having HCP crystal structure of variable composition and which forms at high temperatures for long soaking times.

1.2.4.4. Effects of secondary phases on DSS properties

As already reported, the high percentage of alloying elements makes DSS particularly prone to phases precipitation after prolonged exposure at high temperature, rendering these steels sensitive to embrittlement phenomena and to localized corrosion attack. For this reasons, the temperature range within which these steels can be efficiently employed is from -50°C to 250°C, since at lower temperatures all DSS present a relevant drop in toughness, due to the ductile-to-brittle transition, while for temperatures higher than 250°C the instability of ferrite causes the precipitation of secondary phases [1-12]. In the present work, major attention is paid to the possibility of nitrides and intermetallics precipitation in DSS after isothermal heat treatment in the high-temperature critical range (above 600°C) and, in the following, the term "secondary phases" especially refers to the intermetallics σ- and χ-phases and to Cr_2N nitrides.

The intermetallics are characterized by high hardness and fragility. These phases can increase both hardness and tensile strength but, at the same time, can also significantly lower the impact toughness of the material, making DSS unacceptably brittle even at room temperature. Moreover, intermetallics contain significant percentages of Cr and Mo, causing a depletion in such elements of the surrounding matrix and making DSS susceptible to localized corrosion. The same effects can also be caused by intergranular nitrides which, being Cr-rich structural discontinuities as the intermetallics, ease pitting attacks and promote both crack nucleation and propagation.

Therefore, the mechanical and corrosion resistance properties are strongly influenced from the precipitation of undesired secondary phases after solidification or after improper/uncorrect heat treatments. This problem is of particular interest in welding process, especially in the heat affected zone of thick sections, where temperature and cooling rate are not easily controllable and phases nucleation is facilitate. If possible, DSS are always placed in operating condition after a solution-annealed treatment.

Influence on mechanical properties

The presence of σ- and χ-phases in the Duplex microstructure, which form in the range 700–950°C, lead to a reduction in ductility and to a disastrous loss of toughness [1-4,43-46]. This is due both to the fragility of such phases and to their intergranular position, thus becoming stress-intensification sites having low deformability and where crack nucleation

is promoted. Experimental results showed that the above-mentioned detrimental loss of toughness is evident at all temperatures (Fig. 1.13) and only the 1% volume fraction of intermetallics is sufficient to reduce the room temperature impact toughness to a third of the value in the solution-annealed material [44-46].
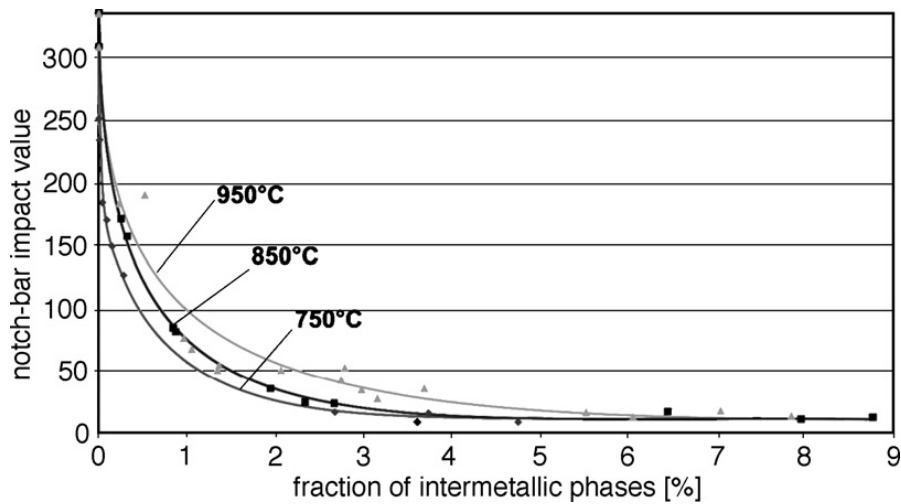

Fig 1.13 – Influence of σ-phase precipitation on DSS impact toughness [34].

Furthermore, distribution and morphology of the precipitates affect the impact response and it was evidenced that the lower the precipitation temperature, the more brittle the behaviour [46]. This primarily depends on the morphology of the sigma phase, and even little deformations cause transcrystalline, finely structured brittle fractures of σ-phase particles, due to its TCP structure. In the more net-like morphology precipitated at lower temperatures, cracks are enabled to run through σ-phase particles over long distances and the narrow fields of surrounding ferrite are forced to cleave, whereas in the bigger and more bulk σ-phase at higher precipitation temperatures, the bigger portion of ferrite and austenite enhances the surrounding ferrite to a more ductile failure mode [46]. This phenomenon is particularly important in the SDSS grades, in which the precipitation is the most rapid and therefore special care is required throughout the thermo-mechanical process, including correct solution-annealing temperature, component thickness and quenching rate [4].

Conversely, the influence of intermetallics on tensile strength has a different character. Tensile and yield strengths generally grow with the amount of precipitated intermetallic phases and a influence of morphology can also be recognized. The increase in strength can mainly attributed to strength of the intermetallic particles in combination with their cross-

linking in ferrite (*i.e.* the phases has not a bulk-island character but are interconnected within ferrite). However, σ-phase preferentially brakes after 3–4% of tensile strain, while χ-phase follows the movement of the matrix without cracking [46].
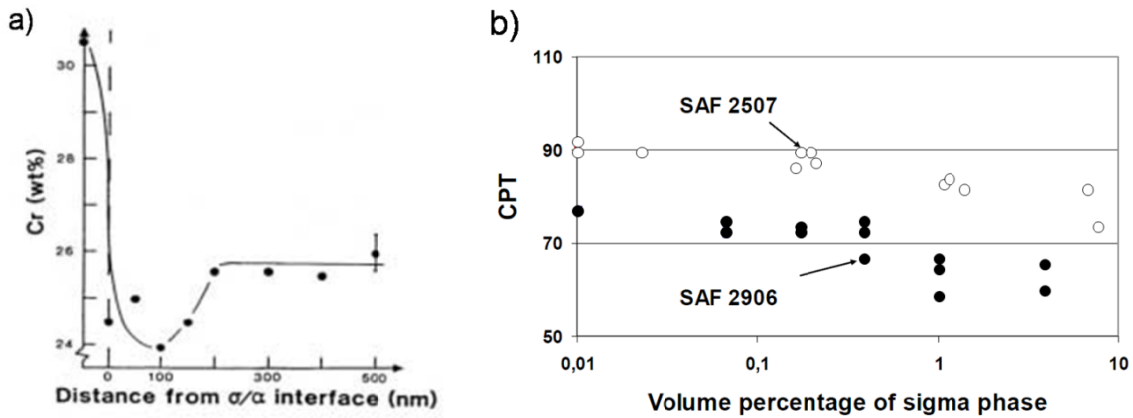

Fig 1.14 – a) Chromium depletion at σ/α phase boundary [5]
and b) influence of sigma-phase on DSS critical pitting temperature [11].

Influence on corrosion properties

When secondary phases precipitation occurs at grain boundaries, such as in presence of σ, χ and Cr_2N, the passivity breakdown conditions are more readily reached, due to the depletion of the matrix in Cr and Mo and to the associated local compositions gradients (Fig. 1.14a). The simultaneous precipitation of these harmful phases was found to initiate a large number of pits close to the boundaries and can be associated to the lowering in Cr content below the passivation threshold in the vicinity of the precipitates [11]. For example, SAFs 2507 and 2906 can tolerate 0.1–0.5% of σ-phase without noticeable effects on pitting corrosion resistance (Fig 1.14b).

As previously reported, in some DSS grades the precipitation of intermetallics and nitrides can be accompanied by the formation of secondary austenite; this austenite is depleted in Cr and Mo, becoming prone to corrosion and, moreover, the neighbourhood of the more noble phases causes an enhancement of the anodic dissolution of γ_2 [46].

1.3. MECHANICAL PROPERTIES

The mechanical properties of DSS (Table 1.6) – and not only the mechanical ones – are generally influenced by the interactions between ferrite and austenite, and by the different

single-phase behaviour in presence of the other phase, resulting in enhanced features which render this class of steels very interesting materials. Nevertheless, while ferrite is stable at room temperature, austenite suffers of a metastable condition due to its allotropic nature, which pertains to higher temperatures, and the onset of phase transformation due to plastic deformation are then possible, as discussed in Chapter 3.

Table 1.6 – Typical mechanical properties of Austenitic, Ferritic and Duplex alloys.

Alloy	0.2% proof stress [MPa]	Ultimate tensile strength [MPa]	Elongation A5 (min) [%]	RT impact toughness [J]
AISI 304	210	515–690	45	>300
AISI 430	205	450	20	-
SAF 2304	400	600–820	25	300
SAF 2205	450	680–880	25	250
SAF 2507	550	800–1000	20–25	250–300

As reported in Paragraph 1.2.2, DSS solidify as fully ferritic while austenite is subsequently formed through solid-state phase transformation; austenite is then the second-phase inside the final Duplex microstructure and possesses a grains size which is of the same order of the matrix grains. Therefore, the mechanisms of deformation in DSS are modified by the presence of such second phase and, since the Duplex microstructure is produced by equilibrium methods, the existence of austenite ensures maximum solid-solution hardening, because its presence results from supersaturation of the ferritic matrix. The presence of such kind of second phase in a continuous matrix results in localized internal stresses which modify the matrix plastic properties. The extent of these modifications depend on several factors such as size, shape, number and distribution of the particles, strength, ductility and strain-hardening behaviour of the phases, crystallographic mismatch among the phases, and is also related to interfacial bonding and interfacial energy between the matrix and the second phase.

The understanding of the fracture resistance in DSS requires firstly careful investigations of the mechanisms of crack nucleation in ferrite due to elastic and plastic incompatibilities between the phases, and secondly of the way in which plastic flow in austenite can control the propagation of a crack in ferrite. Austenite and ferrite show the Kurdjumov-Sachs orientation relatioships $\{111\}\gamma \parallel \{100\}\alpha$ and, in this plane, $<110>\gamma \parallel$

<111>α, resulting in either one common slip system or two nearly-common slip systems. Hence, the interface is a complex semicoherent interface. It has been shown that, during compression tests in cast DSS alloys, deformation takes place homogeneously in both phases and the slip traces were found to be continuous from one phase to the other. In austenite plastic deformation is quite homogeneous in the whole phase, even if slip has a rather plane character, while deformation in ferrite starts from the interfaces and seems to be correlated to deformation started in austenite [47].

The tensile properties of DSS are influenced by plate thickness, becoming increasingly anisotropic with thickness reduction. The anisotropy, and concomitant strengthening, are due to refinement of the structure, with the ferrite/austenite structure being elongated parallel to the principal strain axis (banded-like or pancake grains displacement), but there is no fibre-strengthening effect due to plastic deformation, since the phases have similar hardness values. In a previous work [4], a marked and unusual texture was reported to developed in the two phases, with a major orientation of the type (100)[011] to (211)[011] for ferrite and (110)[223] for austenite, whereas more recent studies have pointed out that in SAF 2205 cold-rolled sheets the developed texture are (100)[001] in ferrite and {110}<112> in austenite [48]; however, a more detailed description on textures development in DSS is reported in Chapter 3. In any case, a strong anisotropy in DSS mechanical properties is expected as a consequence of the plastic deformation, owing to the formation of a heavily-banded microstructure, especially in the cold rolled conditions.

Finally, a very interesting property of these steels is the so-called superplasticity, which enable DSS to be considerably plastically deform under moderate stress at appropriate temperatures, making possible the achievement of very complex shapes.

1.3.1. Tensile characteristics

Austenite and ferrite have similar Young's modules, but the yield stress is smaller in the former phase than for the latter [47]. This difference, coupled with a different deformation hardening rate of the individual phases, causes a different load sharing between the phases and therefore strong inter-phase reactions result in the formation of microstresses that maintain their equilibrium among subsets of grains of different orientations [11]. These residual microstresses have a great effect on DSS yielding and, consequently, affect

deformation and fracture behaviour. However, the resulting yield strength of DSS is usually two or three times greater than in AISI 304 and the high elastic limit, combined with their good ductility, allow for a weight reduction of structures, leading to consequent savings in raw materials and manufacturing costs [49].

The strength in DSS is essentially controlled by ferrite and strongly depends on grain size; the fine microstructure usually achieved in Duplex allow for the attainment of a considerable contribution to the strength, as described by the well known Hall-Petch relation [1]. Besides that, the mechanical properties of DSS can be also related to the beneficial synergistic effect given by the two-phase structure and to the contribution of both substitutional and interstitial solid solutions which are formed with the alloying elements. Hence, the high mechanical resistance of DSS is the result of a combination of several simultaneous mechanisms [4]:

- interstitial solid solution hardening (C, N);
- substitutional solid solution hardening (Cr, Mo, Ni, etc.);
- strengthening by grain refinement;
- presence of the biphasic microstructure;
- strengthening due to ferrite, since, for a similar composition, this phase is harder than the austenitic structure;
- strain induced by differential contraction of the two phases on cooling from annealing temperatures.

About the first strengthening mechanism, a raising in N content preferentially strengthens austenite by interstitial solid solution hardening, till it becomes stronger than ferrite. Indeed, for low nitrogen contents (<0.1%) austenite has the lower yield strength, while at higher levels (>0.2%) ferrite becomes the weaker phase; this explains why macroscopic hardening is most pronounced for small nitrogen additions, becoming less marked beyond a certain level (*i.e.* 0.12% for 2205), where only a moderate hardening occurs [4].

The variation in mechanical strength for DSS alloys with temperature is essentially controlled by ferrite. Strengthening is accentuated at low temperatures, with some significant drops over the temperature range 20–300°C; an increase in wall thickness may be necessary when operating at 100°C, as compared to 20°C [4].

The work hardening rate in DSS is similar to other types of stainless steel. Only 304-304L grades show higher work-hardening rate, owing to the Strain-Induced Martensite transformation, a phenomenon which may also occur in low-alloyed DSS and which was also found to be possible in the medium-alloyed grades, such as the 2205 [31-33] (Chapter 3). The capacity to work-harden up to tensile strengths of 1200 MPa or above is exploited in the manufacture of wirelines and surgical.

Further, the addition of Cu enables considerable hardening to be obtained, without excessive loss of ductility, provided that the heat treatment has been optimised; therefore it is not surprising that the use of copper is particularly appreciated for applications requiring both abrasion and corrosion resistance [4].

1.3.2. Impact toughness

Despite their high strength, DSS exhibit good ductility and toughness which, however, are lower than austenitic steels. These materials retain a good toughness even to low temperatures (*e.g.* -40°C) and, if compared to carbon and ferritic steels, the ductile-to-brittle transition is more gradual. The low temperature toughness behaviour of DSS is, in fact, between that of ferritics and austenitics, due to the combined effect of the two phases, and can be ascribed to the presence of austenite, which retards the cleavage fracture of ferrite [1]. High impact energies can be achieved in SDSS (*e.g.* over 100 J, at -100°C [50]) in solution-annealed and unwelded conditions. As it happens in all materials, a marked scatter in the toughness values should be expected during the transition, owing to alloy composition and thermomechanical history, which in turn affect microstructure and texture. Moreover, the impact strength can be improved by reducing the oxygen content, and by controlling the aluminium leve1, to avoid the formation of AlN [4].

Cold working reduces the room temperature impact strength in DSS and increases the ductile to brittle transition temperature. The textures developed during cold rolling in the two phases alter the impact response in DSS, leading to higher value in transverse than in longitudinal direction relative to the banded structure [1]. The combination of cold working and ageing in the range 300–400°C causes a great drop in impact toughness at room temperature and the ductile to brittle transition can be raised above ambient temperature [4].

1.4. CORROSION RESISTANCE

The corrosion properties of stainless steels are generally defined by the ability to passivate and to remain in the passive state in the service environment. However, there are fundamental differences in alloy design of Duplex and austenitic grades, which leads to significant variations in their corrosion behaviour, especially in environments where general corrosion is taking place. On the other hand, austenitic and DSS alloys with equivalent PRE_N often exhibit similar critical pitting and crevice corrosion temperatures in chloride media [4].

DSS exhibit a high level of corrosion resistance in most environments where the austenitic stainless steels are normally employed; the high Cr content, which is beneficial in oxidizing acids, coupled with Mo and N, give DSS a superior resistance in mildly-reducing acid environments and the relatively high amount of these three elements also provides very good resistance to chloride induced pitting and crevice corrosion. Ferrite is, however, susceptible to hydrogen embrittlement which causes a decreasing in resistance in environments or applications where H may be charged into the metal. As a matter of fact, if compared to standard austenitics grades, DSS possess a greater resistance to localized corrosion attacks, such as stress corrosion cracking (SCC), crevice and pitting corrosion, and also have a better resistance against generalized corrosion than ferritics. Therefore, the realization of these steels is related to the possibility to obtain materials of limited cost, employable in such environments where the risk of stress corrosion does not allow the use of austenitics and where the generalized corrosion restricts the use of ferritics [4].

1.4.1. Pitting corrosion

In chlorinated solutions, the pitting phenomenon occurs when the intervention of Cl^- ions cause the destruction of the passive film, as their specific action results in the reduction of the stability field of the passive potential and in increasing the corrosion current. The role of chloride ions in pitting initiation is related to a local destabilization of the passive film, together with an effect which counteract the formation of a new protective layer. Cr-Mo-N-W are the main beneficial elements against pitting attacks and a qualitative quantification of DSS resistance is given by the PRE_N index, obtained by Relations (1.1) and (1.2).

However, it is necessary to consider that pitting resistance of ferrite and austenite is different, due to the partitioning of the alloying elements between the phases, and especially if the heat treatment is not optimised. In fact, an alloy with a high nominal PRE_N may produce a lower pitting resistance than expected if one of the phases is depleted in one of the characterizing elements compared to the other phase (*i.e.* it has a lower localised PRE_N value). In particular, the effect of different partitioning on corrosion resistance assumes relevance in relation to weldments. In DSS, austenite is the weakest phase towards pitting resistance, owing to its lower PRE_N (or PRE_W) index, and the only manner to increase its resistance is to increase the nitrogen content, which is not even possible. For this purpose, a greater volume fraction of ferrite can increase the austenite resistance by allowing the solubilisation of a greater amount of Cr , Mo and N inside the γ-phase, at expenses of mechanical resistance.

In general, the pitting resistance is significantly influenced by metallurgical parameters such as composition, inclusions or second phases, heat treatments, size of grains and cold working, which are not taken into account in the PRE_N ranking. However, for a given chlorinated environment, each stainless steel can be characterized with a temperature below which pitting does not occur, even after indefinitely long times. This temperature is defined as the Critical Pitting Temperatures (CPT) and represents a parameter of highly interest, because it takes into account the influence of both the microstructure and the elements distribution inside the phases and, therefore, the real conditions of the steel. Indeed, a steel with a high nominal PRE_N value can be characterized by a low CPT value, if one of the phases is depleted of Cr, Mo, W or N – *i.e.* whether the local value of the PRE_N is, for any reason, low. The CPT is usually determined in discreetly chlorinated solutions, but its value was found to be independent of both chlorides concentration, in the range 0.01–5 M, and pH, in the range of 1–7 [51,52]. On the contrary, the surface roughness of the material can affect the measured CPT value [53], which decreases as the roughness increased.

In general, the Duplex CPT are comparable to that of austenitics (Fig. 1.15a) and those of SDSS are slightly superior to that of 6%Mo super-austenitics. SAF 2205 can be used at very high temperatures, while in chlorinated seawater only superduplex or superaustenitic steels can be successfully applied. SAF 2205 is also resistant to pitting up to about 80°C in 1.5% NaCI (0.90% CI⁻) solution, while superduplex grades are immune up to the boiling

point. On the other hand, in more aggressive media (*i.e.* higher potential and chloride levels), lower critical pitting temperatures are obtained [4]. Nevertheless, if the environment is sufficiently aggressive, localized attack preferentially occurs at austenite/ferrite phase boundaries, because these are preferential sites for segregation of impurities [1].
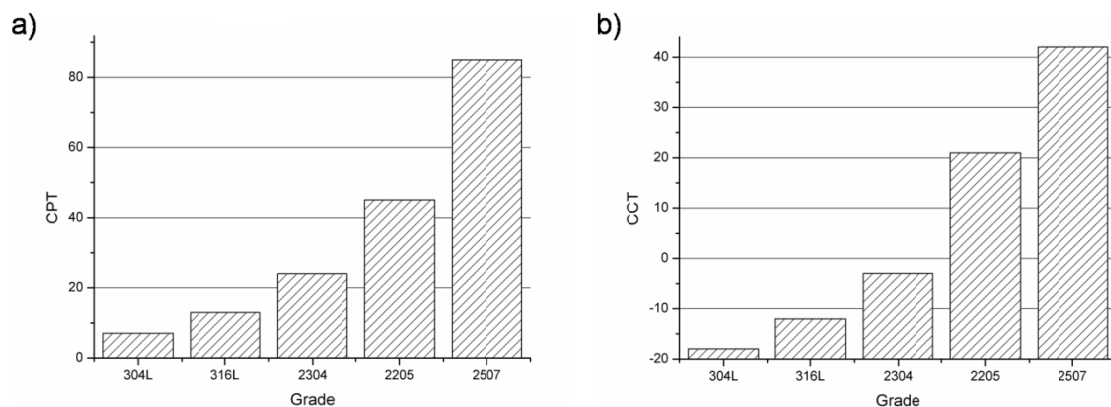

Fig 1.15 – Critical temperatures for DSS corrosion resistance in seawater: a) pitting (CPT) and b) crevice (CCT).

1.4.2. Crevice corrosion

Crevices can be formed at flanged joints, beneath weld spatter etc. and, as a rule, the tighter the gap the more likely that crevice corrosion will occur for a given bulk environment. For instance, soft non-metallic materials, which can mould to the metal surface are considered severe crevice formers. The crevice corrosion resistance of stainless steels can be related to the pitting resistance, since the Critical Crevice Temperatures (CCT) are roughly related to the CPT [4] (Fig. 1.15b).

Several experments in chlorinated seawater have shown that grades SAF 2205 and 2505 can suffer from crevice attack in 1 ppm chlorine at 16°C and 0.8 ppm at 10°C, while SDSS grades are resistant at 45°C in sea water with 0.8 ppm chlorine; moreover, it has been stated that Zeron®100 SDSS has a 50% chance of suffering from crevice corrosion during upset conditions (say 24 hours at 70°C) while repassivation will occur when the temperature is dropped to 30–40°C; in this respect, SDSS alloys perform better than 6% Mo superaustenitic alloys [4].

1.4.3. Stress Corrosion Cracking (SCC)

If compared to austenitic grades with similar pitting and crevice corrosion resistance, DSS exhibit significantly better Stress Corrosion Cracking (SCC) resistance, owing to the presence of ferrite, which is immune to this type of failure [54]. However, they are susceptible to this type of corrosion under certain conditions, such as at high temperatures, in chloride environments or when the circumstances favour hydrogen-induced cracking (*e.g.* boiling 42%-Mg, pressurized aqueous chloride systems and drop evaporation at high temperatures) and, moreover, they are sensitive to Sulphide-induced Stress Corrosion Cracking (SSCC).

In *chloride environments*, cracking can preferentially occur in ferrite or through both phases; this may seem surprising as the resistance of ferritic stainless steels is normally considered high, while the susceptibility of austenitic grades is renowned, due to the higher Ni contents. However, the ferrite in a DSS contains at least 3% of Ni, in comparison to common nickel-free ferritic grades, and this makes the ferrite phase in DSS susceptible to SCC [4].

The resistance of DSS to stress corrosion cracking in the presence of H_2S and chloride is reduced, if compared to similar environments where only chloride is present, owing to the effect of *hydrogen sulphide*, which may be evolved in oil wells or polluted waters due to bacterial activity. Reduced sulphur species are known to catalyse the anodic dissolution of Fe and Ni, and therefore can be assumed to control the kinetics of localised corrosion. The presence of H_2S in a solution will remove oxygen to form elemental sulphur and water; the removal of oxygen restricts the cathodic reaction to hydrogen evolution or, to a lesser extent, reduction of sulphur to a sulphide; thus, the surface of the steel becomes enriched in atomic hydrogen, which enhances hydrogen diffusion into the steel, leading to the possibility of hydrogen-induced cracking [4].

1.4.4. Resistance to acids and caustics

Duplex 2205 and 2507 outperform many high-Ni austenitics steels in sulphuric acid solutions containing up to about 15% acid, and they are better than types 316 or 317 through at least 40% acid. DSS do not have sufficient Ni to resist the strong reducing conditions of mild-concentration sulphuric acid solutions or hydrochloric acid. At wet/dry

interfaces in reducing environments, where acid concentrates, corrosion – especially of ferrite – may be activated and proceeds rapidly. The resistance to oxidizing conditions makes DSS good candidates for nitric and strong-organic acid services.

In *sulphuric acid*, the beneficial effect of copper, as an active alloying element in reducing acids, leads to the improved performance of alloys 2505 and Zeron®100 – containing between 0.5% and 2% of Cu – if compared to 2507 without copper. In *hydrochloric acid*, grade 2205 offers similar resistance to 316L at low temperatures, although the resistance is better at higher temperatures, while SDSS show improved resistance and are similar to austenitic alloys; the best performance in HCl is observed in Zeron®100, with Cu and W additions, which has been shown to be acceptable in a number of applications previously thought unsuitable for stainless steels. However, under highly oxidising conditions, like *concentrated nitric acid*, DSS exhibit dramatically different behaviours because Mo has a strong negative effect, while Cr is beneficial. For this reason, a limit of 2%Mo has been recommended.

DSS, and in particular SDSS, have shown remarkably good passivation properties in pure and contaminated *organic acids*; modern Duplex are resistant in acetic acid whereas the austenitic grade 304L corrodes at high temperatures and may also crack at high concentrations; in formic acid – the most aggressive of the organic acids – most stainless steels and titanium corrode heavily at intermediate concentrations and high temperatures, but SDSS were found to be resistant almost to the boiling point [4].

The high Cr content and the presence of ferrite provide good performances of DSS also in caustics environments. In presence of *sodium hydroxide*, as in pulp and paper industry, DSS have shown much lower corrosion rates at moderate temperatures than standard austenitic grades in white liquors, and their beneficial is more marked in synthetic white liquors, where chlorides are present [4].

1.5. APPLICATIONS

DSS were firstly introduced onto the market as alternatives to the standard austenitic grades AISI 304 and 316 in aggressive environments, especially owing to the improved corrosion resistance and to cost-savings due to the lower Ni amount. Enhanced corrosion performances, in combination with toughness, mechanical strength and good weldability,

render these steels very suitable for several applications in chlorides-containing media [12].

Nowadays, DSS gained a considerable interest in the great welded constructions and as container ships for highly-aggressive chemicals products; however, their use in construction of large welded bridges is limited due to the fact that there is not a considerable amount of experimental data on DSS fatigue resistance, comparable to that existing for conventional carbon steels [49]. Hence, due to their favourable combinations of properties, DSS can be successfully employed in different aggressive environments:

- Chemical, petrochemical and nuclear plants

- Oil and gas offshore applications (piping, flowlines, bolting, etc.)

- Pulp and paper industries

- Desalination plants

- Buildings and bridges

- Power generation (seawater cooling below 300°C)

- Mining/extraction

- Food manufacture

- Implantation material in human bodies (biocompatibility for high PRE_N)

Chemical and petrochemical

Among the various DSS grades, SAF 2205 is preferred against the 300-series austenitic stainless steels, owing to its higher corrosion and stress-corrosion resistance in many environments, together with considerable higher tensile properties and only a moderate increase in price. SAF 2304 has been used for clean duties, replacing austenitic grades in hot aqueous chloride media; today, this grade is selected for exchanger tubing in natural gas preheaters, where low grade steam is used for heating purposes. For applications where higher chloride contents are present, *e.g.* brackish water and hot coastal conditions, both tubing and tubesheets are made in SAF 2205. This grade has also been used for reactors, heat exchangers and storage tanks in the production of detergent.

For many years, cast J93370 DSS has found applications in phosphoric (and sulphuric) acid production, where chlorides and fluorides are present combined with erosion and wear conditions, such as in pumps, agitator blades and shafts. More recently, this grade has been

employed for stud bolts in ammonia injectors; valve internals in urea recycle lines and pumps and valves in sulphuric and nitric acid duties [4].

Oil&Gas offshore applications

The use of DSS for offshore applications predominantly started in the early days of the North Sea developments. The corrosive conditions which were encountered in this region negated the use of carbon steels and led to the selection of stainless steels. DSS have been successfully supplied for down hole equipment and wellheads, flow lines, umbilical, process piping, vessels and mechanical components, such as pump parts, compressors and valves. In particular, due to their high strength and good corrosion resistance, they have become ever more employed in high pressure systems, topside equipment, pipework, and blast walls, which lead to a reduction in the topside weight in offshore facilities. Presently, DSS are used with thicknesses up to 100 mm and with design temperatures down to -50°C and, generally, they can provide many years of trouble-free service [4].

Several extended papers issued from Oil&Gas companies underline the very satisfactory behaviour of 22- and 25-Cr DSS which have been experienced in a large set of applications (*i.e.* top side, subsea pipings, manifolds, umbilical, wells applications, fire systems). Some failures have been observed but most of them are related to unintended service conditions, including poor design, high local stresses, overloaded conditions, unexpected microstructure defects (σ-phase), local saturated brine solutions (evaporation/condensation phenomenon's associated with high temperature), and some Hydrogen-Induced Stress Cracking (HISC) cases [12].

Other experiences underline the possible benefits of the uses of lean DSS in structural applications for platforms; pipe racks, pipe supports, architectural walls, insulation claddings, cable trays could be typical applications where carbon steel is replaced by lean DSS, with a typical cost savings of 20–40%. Nevertheless, special care should be made in material selection, taking in to account the in service conditions since, among Lean DSS, a wide range of chemistries are proposed (PRE$_N$ from 23 to 28) [12].

Pulp and paper

One of the first applications involved grade S31500 (3RE60) for suction rolls. In this steel, the combination of high-Cr and low-Ni contents seemed to be beneficial against attack in

such media and, similarly, SDSS clad plates of SAF 2507 have been successfully used for chip prestreaming vessels in continuous digesters. Generally, DSS find many applications in this industry sector, including chemical pulping, bleaching, chemi-thermomechanical pulping (CTMP), pulp storage tanks, paper machines, recovery and steam plants [4].

Desalination and severe chloride containing environments

Some companies have completely shifted from austenitic to duplex grades. SAF 2205 is the cost-saver material, bringing weight reductions and low maintenance costs due to the excellent corrosion resistance properties; more recently SAF 2304 has been introduced for the less severe conditions. Conversely, for the most severe conditions the classical SDSS are to be considered and the newly Hyper DSS grades seem to offer improved properties [12]. Thus, DSS evaporators can be built with thinner plates, requiring less material and less welding.

Building and construction/bridges

Due to their cost advantages when considering weight savings aspects and maintenance cost savings (21-23% Cr providing more corrosion resistance than 304 grades), Lean DSS are more and more considered for structural applications; reinforced Duplex bars are now specified for corrosion free bridge even in marine environments [12].

Experimental works have confirmed that duplex grades can be used in the most critical cases for design and construction; the cost calculation for solid Duplex bridges, compared to carbon steel, resulted in an increase of 20% of the erection and building costs (including the welds), whereas savings are expected from lower maintenance costs. Furthermore, more recent investigations confirm the advantages of DSS in fire conditions; higher temperature can be considered without damages as well as more safety margins [12].

REFERENCES

[1]   J. O. Nilsson. *Mater Sci Tech Ser* 8 (1992) 685.
[2]   J. Charles. Proc. Conf. *Duplex Stainless Steels '91*. Les Ulis, France (1991) 185.
[3]   J. Charles. Proc. Conf. *Duplex Stainless Steel '94*. Glasgow, Scotland (1994) 41.

[4]   R. N. Gunn. *Duplex Stainless Steels: Microstructure, Properties and Applications.* Abington Publishing, Cambridge, England (1997).

[5]   E. Ramous. *La Metallurgia Italiana* 4 (2004) 37.

[6]   I. Calliari, M. Dabalà, E. Ramous and G. Staffellini. *Mater Sci Forum* 604–605 (2009) 419.

[7]   M. Knyazeva and M. Pohl. *Metallogr Microstruct Anal* 2 (2013) 113.

[8]   J. Charles. *La Metallurgia Italiana* 2 (1995) 83.

[9]   J. C. Lippold and D. J. Kotecki. *Welding Metallurgy and Weldability of Stainless Steels.* John Wiley & Sons, Hoboken, New Jersey (2005).

[10]   G. Melotti, R. Bertelli, M. Zanesco, I. Calliari, E. Ramous. *La Metallurgia Italiana* 4 (2005) 39.

[11]   J. O. Nilsson, G. Chai. Proc. Conf. *Duplex 2007 International Conference & Expo*. Grado, Italy (2007).

[12]   J. Charles. *A review after DSS '07 held in Grado* (2007).

[13]   R. E. Schramm and R. P. Reed. *Metall Trans A* 6A (1975) 1345.

[14]   R. E. Schramm and R. P. Reed. *Metall Trans A* 7A (1976) 359.

[15]   P. Seetharaman and J. Krishnan. *J Mater Sci* 16 (1981) 523.

[16]   G. B. Olson and M. Cohen.. *J Less-Common Met* 28 (1972) 107.

[17]   S. S. Hecker, M. G. Stout, K. P. Staudhammer and J. L. Smith. *Metall Trans A* 13A (1982) 619.

[18]   R. Lagenborg. *Acta Metall* 12 (1964) 823.

[19]   P. L. Mangonon and G. Thomas. *Metall Trans* 1 (1970) 1577.

[20]   F. Lecroisey and A. Pineau. *Metall Trans* 3 (1972) 387.

[21]   K. Spencer, M. Véron, K. Yu-Zhang and J. D. Embury. *Mater Sci Tech* 25 (2009) 7.

[22]   G. B. Olson and M. Cohen. *Metall Trans A* 6A (1975) 791.

[23]   P. Haušild, V. Davydov, J. Drahokoupil, M. Landa, P. Pilvin. *Mater and Design* 31 (2010) 1821.

[24]   A. Das, S. Sivaprasad, M. Ghosh, P. C. Chakraborti, S. Tarafder. *Mat Sci Eng A* 486 (2008) 283.

[25]   J. Talonen, H. Hänninen. *Acta Mater* 55 (2007) 6108.

[26]   A. Hedayati, A. Najafizadeh, A. kermanpur, F. Forouzan. *J Mat Proc Tech* 210 (2010) 1017.

[27]   K. H. Lo, C. H Shek, J. K. L. Lai. *Mat Sci Eng R* 65 (2009) 39.

[28]   G. F. Vander Voort. *Metallography: Priciples and Practice*. ASM International (2007).

[29]   A. Randak and F. W. Trautes. *Werkstoffe und Korrosion* 21 (1970) 97.

[30]   K. Elaylperumal, P. K. De, J. Balachandra. *Corrosion* 28 (1972) 269.

[31]   W. Reick, M. Pohl and A. F. Padilha. *Steel Res* 67 (1996) 253–256.

[32]   S. S. M. Tavares, M. R. da Silva, J. M. Pardal, H. F. G. Abreu, A. M. Gomes. *J Mater Process Tech* 180 (2006) 318.

[33]   P. Bassani, M. Breda, K. Brunelli, I. Mészáros, F. Passaretti, M. Zanellato and I. Calliari. *Microsc Microanal* 19 (2013) 988.

[34]   M. Pohl, O. Storz, T. Glogowski. *Mater Charact* 58 (2007) 65–71.

[35]   L. Karlsson, L. Bengtsson, U. Rolander, S. Pak. Proc. Conf. *Application stainless steels '92*. Stockholm, Sweden (1992) 335.

[36]   I. Calliari, M. Breda, M. Pellizari and E. Ramous. *The χ-phase in duplex stainless steels* (in press).

[37]   S. Hertzman, W. Roberts and M. Lindenmo, Proc. conf. *Duplex Stainless steels*. The Hague, The Nederlands (1986) 257.

[38]   A. J. Ramirez, J. C. Lippold and S. D. Brandi. *Metall Mater Trans A* 34A (2003) 1575.

[39]   S. S. M. Tavares, R. F. de Noronha, M. R. da Silva, J. M. Neto, S. Pairis. *Material Research* 4 (2001) 237.

[40]   M. Guttmann. Proc. Conf. *Duplex Stainless Steels '91*. Beaune, France (1991) 79.

[41]   B. Joeffson, J. O. Nilsson, A. Wilson. Proc. Conf. *Duplex Stainless Steels '91*. Beaune, France (1991) 67.

[42]   L. Karlsson, L. Ryen, S. Pak. *Welding Research Supplement* 74 (1995) 28.

[43] J. O. Nilsson, A. Wilson. *Mater Sci Tech* 9 (1993) 545.

[44] I. Calliari, M. Zanesco, E. Ramous. *J Mater Sci* 41 (2006) 7643.

[45] I. Calliari, M. Breda, E, Ramous, K. Brunelli, M. Pizzo, C. Menapace. *J Mater Eng Perform* 21 (2012) 2117.

[46] M. Pohl, O. Storz, T. Glogowski. *Int J Mater Res* 99 (2008) 1163.

[47] B. Verhaeghe, F. Louchet, B. Doisneau-Cottignies, Y, Bréchet. *Philos Mag* 76 (1997) 1079.

[48] W. B. Hutchinson, K. Ushioda and G. Runnsjö. *Mater Sci Tech Ser* 1 (1985) 728.

[49] S. Bernhardsson. Proc. Conf. *Duplex Stainless Steels '91*. Beaune, France (1991) 185.

[50] M. Breda, I. Calliari, E. Ramous, M. Pizzo, L. Corain, G. Straffelini. *Mater Sci Eng A* 585 (2013) 57.

[51] R. Qvarfort. *Corros Sci* 29 (1989) 987.

[52] N. J. Laycock, M. H. Moayed, R. C. Newman. *J Electrochem Soc* 145 (1998) 2622.

[53] M. H. Moayed, N. J. Laycock, R. C. Newman. Corrosion Science 45 (2003) 1203.

[54] H. Bhadeshia and R. Honeycombe. *Steels: Microstructures and Properties*. Butterworth-Heinemann, Oxford, England (2006).

CHAPTER 2

ISOTHERMAL HEAT TREATMENTS

2.1. INTRODUCTION

In the present chapter, the effects of isothermal heat treatments (or ageing treatments) on DSS microstructures and impact properties are discussed. As reported in Chapter 1, owing to the instability of the ferritic matrix at high temperatures, DSS are sensitive to secondary phases precipitations, which can cause not negligible implications, especially during the manufacturing process and in welding operations, due to the detrimental effects on properties of the new generated phases.

The chapter deals with the solid-state phase transformations pertaining to the DSS high-temperature critical range, where the diffusion kinetics are enhanced and where the precipitation may occur for very short soaking times, as happens in SDSS. The intermetallics σ- and χ-phases and chromium nitrides are the phases of major interest, causing local Cr-depletions in the matrix, compromising the resistance to localized attack and highly worsening the impact toughness of the materials.

The intermetallics are known to be generated by the eutectoidic decomposition of ferrite, where the metastable α-phase is replaced by a more stable mixture of phases following the reaction α → σ(χ) + γ$_2$. However, the formation of intermetallics seems to interest only the higher-alloyed grades, rather than low-alloyed Lean DSS, which are instead mainly subjected to nitrides formation. The main difference between high- and low-alloyed grades is the different elements amount in and, in particular, the molybdenum content, as will be discussed in the following sections. DSS are biphasic steels at room temperature but, owing to the allotropic nature of iron, if the temperature is raised above 700°C, and especially within the high-temperature critical range, ferrite does no more belong to the equilibrium microstructure. This causes its decomposition, and the high

content of alloying elements further affect its stability, leading to the formation of secondary phases. The eutectoidic reaction involves the formation of phases with different composition to the parent matrix and long-range diffusion mechanisms are required, both of substitutional and interstitial elements [1].

The precipitation phenomenon in DSS involves diffusion mechanisms and takes place in solid-state conditions. Therefore, besides the obvious effect of temperature on promoting atoms mobility, the kinetics of reactions are also conditioned by the particular microstructure of the steel. A large number of grain boundaries and defects inside the matrix may enhance secondary phases formation, because, under certain circumstances, diffusion may preferentially occur along such high-diffusivity paths, rather than through the lattice, thus becoming the dominant diffusion mechanism [1]. Secondary phases is known to preferentially nucleate at triple points and grain boundaries, within a temperature range where grain boundaries diffusion is preferred (*i.e.* below 0.75–$0.8 \cdot T_M$, being T_M the equilibrium melting temperature), and their growth proceed toward the unstable ferrite, subtracting elements to the matrix and causing its decomposition. Comparing DSS having the same nominal chemical composition but different microstructures, a different responses to phases precipitation can be achieved. For example, if the number of triple points is increased due to recrystallization processes occurred during solubilisation, or if a greater number of dislocations is present, the precipitation kinetics can be substantially altered and phases formation can be enhanced. These facts underline the importance of the thermo-mechanical history of the steels on the precipitation behaviour, which cannot be neglected, even though a comparison among different DSS grades overcomes these microstructural effects, being the precipitation mainly influenced by the alloying grade.

Although the effects of secondary phases on DSS properties are clearly related to the microstructural damage after ageing, in this chapter the topics are presented separately. First of all, a description of the precipitation kinetics within the critical temperature range is presented. This can give an understanding on the entity of such damage induced by the secondary phases precipitation at a microstructural level in terms of volume fraction of such phases, which varies among different DSS grades, and is of fundamental importance in order to design reliable manufacturing processes and to know the limits of these steels. Then, the effects on mechanical properties, and in particular on impact toughness, are discussed, with the aim to fully characterize the DSS behaviour after phases precipitation.

This separation in two sections can provide a better description of the overall implications due to secondary phases in DSS, pointing out different important aspects.

Ageing treatments

All the isothermal heat treatments were carried out by introducing the samples inside a muffle furnace set at the soaking temperature, allowing the heating of the material from room temperature. The various ageing temperatures were chosen on the basis of previous works reported in literature and, in the case of new materials, either considering critical temperatures ranges in similar DSS or after the analysis of the equilibrium phase diagrams. Each set of treatments, followed by water quenching, has involved different annealing times, in order to fully characterize the precipitation kinetics in the steels under examination.

This procedure was designed for the determination of the precipitation kinetics inside the critical temperature range, or the range itself, in the investigted DSS. This is also suitable for a reproduction of industrial applications, allowing the simulation of such conditions at which the material may be subjected, as the heat-affected zone during welding operations.

Table 2.1 – Chemical composition of the investigated Duplex Stainless Steels.

Grade	C	Si	Mn	Cr	Ni	Mo	Cu	W	P	S	N
SAF 2101	0.028	0.69	3.82	21.72	1.13	0.10	0.34	-	0.028	0.0025	0.16
LDX 2101	0.025	0.65	5.13	21.57	1.56	0.28	0.30	-	0.019	0.0010	0.23
SAF 2304	0.030	0.56	1.43	23.17	4.29	0.18	0.16	-	0.027	0.0010	0.13
LDX 2404	0.022	0.33	2.83	24.41	3.34	1.54	0.42	-	0.021	0.0004	0.25
SAF 2205	0.030	0.56	1.46	22.75	5.04	3.19	-	-	0.025	0.0020	0.16
SAF 2507	0.015	0.24	0.83	24.80	6.89	3.83	0.23	-	0.023	0.0010	0.27
SAF 2510	0.020	0.44	0.37	25.30	9.90	4.00	-	-	0.018	0.0010	0.275
Zeron®100	0.014	0.25	0.88	25.23	6.89	3.67	0.72	0.62	0.023	0.0010	0.28

Materials

The investigated DSS are reported in Tables 2.1 and 2.2, together with their relative chemical composition, product type and PRE_N index. All the materials were treated in the

as-received conditions; this means that, after the forming operations, they were all subjected to a solubilisation treatment at the proper temperature and subsequently water quenched.

The materials were of different shape (rods, bars, plates, billets or sheets), hence with different starting microstructures, which can in some extent alter the precipitation behaviour at the early stages of precipitation, as explained in the following sections. Thus, the presented results may not to be consider as absolute, but can give in any case a significant overview of the precipitation phenomenon which affect DSS and permit to underline the different existing behaviours among different DSS grades.

Table 2.2 – Product type and PRE_N indexes of the investigated Duplex Stainless Steels.

Grade	Product type	Size	PRE_N (PRE_W) index
SAF 2101	bar	10x40 mm (cross-section)	25
LDX 2101	sheet	3 mm (thickness)	26
SAF 2304	billet	60x60 mm (cross-section)	26
LDX 2404	sheet	2 mm (thickness)	33.5
SAF 2205	bar	10x30 mm (cross-section)	36
SAF 2507	plate	15x1250 mm (cross-section)	42
SAF 2510	rod	45 mm (diameter)	43
Zeron®100	plate	14.5x1350 mm (cross-section)	43

Investigation methods

The microstructures were investigated by means of classical metallographic techniques. Optical Microscopy (OM) by using a Leica DMRE was only performed on the as-received samples after chemical etching (Beraha's reagent), whereas a Leica Cambridge Stereoscan 440 Scanning Electron Microscopy (SEM), coupled with Energy Dispersive Spectrometry (EDS) for the composition analysis, was employed to investigate the microstructural features of the treated samples. The OM and SEM micrographs were used to estimate the volumetric fraction of the phases, by means of an image-analysis software.

The use of SEM does not require any samples etching, because the observations in backscattered-electron mode (BSE) at 29 kV permit to distinguish the phases according to their different average atomic number. Austenite appears brighter than ferrite, while the

secondary phases (such as σ and χ) are more brilliant due to the higher content of Cr and Mo, and therefore to the higher average atomic number; nitrides and carbides can instead be observed as small black particles, whose shape and location depend on the process from which are generated.

Some samples were also examined by X-Ray Diffraction (XRD), using a Siemens D500 diffractometer (CrKα radiation, step 0.05° and 3 sec of acquisition time) in the angular range 2θ = 55–145°, in order to unambiguously identify the present phases.
The equilibrium phase diagrams were obtained by thermodynamic simulations, using the Thermo-Calc software [2] based on the CALPHAD method [3] and employing the thermodynamic database TCFe6.

The study of DSS mechanical properties was focused on the determination of impact toughness. For these tests, different Charpy pendulums were employed on V-notched specimens, having available energies of 300–450 J, as reported in the specific sections. The fracture surfaces were investigated by means of SEM, in secondary-electron mode (SE) at 15 kV, and by using a Stereo Microscope, in order to investigate the fracture surfaces at macro- and microstructural levels.

2.2. EFFECTS ON MICROSTRUCTURE

The main effect of the DSS exposure at high temperature is the decomposition of the ferritic matrix, which can occur in a wide temperature range. In the present thesis, only the high-temperature decomposition of ferrite is considered, which occurs in the temperature range 600–1000°C and in different extent depending on the examined grade. In this range, the decomposition may lead to the formation of the secondary (intermetallic) χ- and σ-phases, via eutectoidic reaction, and also to the precipitation of chromium nitrides.

As previously reported, the microstructural conditions can strongly affect the steel behaviour during the ageing treatments. In this paragraph the effect of different microstructures is (partially) taken into account by separately considering the materials in the as-received and cold-worked conditions. These cases are obviously completely different, because cold working introduces an increased number of defects inside the microstructures, altering the diffusion kinetics at high temperatures and, therefore, the precipitation behaviours, which is a diffusive phenomenon.

However, the as-received microstructures in the investigated DSS cannot be considered as equals, in terms of precipitation behaviour. As a matter of fact, the manufacturing operations are not the same for all the final products and, if it were, it is possible that were not performed in the same extent in all materials. Moreover, if different products are taken into account, the solution-annealing treatments, aimed to restore the microstructures after the forming operations, are not even accomplished at the same manner, and the particular conditions at which are carried out cause the onset of different microstructures. Therefore, besides the compositions of different DSS grades, microstructure can play a fundamental role on the precipitation kinetics, since ferrite decomposition preferentially occur at grain boundaries and interfaces, which are intimately connected to microstructure achieved during the manufacturing process.

2.2.1. As-received materials

The materials presented in this section are final products coming from different manufacturing cycles and thus of various forms and with different microstructures. As previously pointed out, different microstructures may lead to peculiar responses to the ageing treatments, but a comparison between different DSS grades can be made in any case, because the composition effect overcomes the microstructural effect in terms of precipitation kinetics.

In the first section of this paragraph, an overview on the effects of heat treatments on DSS microstructures is presented and a brief review of literature papers is reported. These works mainly belong to the various activities performed in the researcher's department on as-received (or as-delivered) materials, but were not performed by the researcher. However, it was thought be useful to give a comprehension of the "state of art" on what is known about phases precipitations in DSS. All the others sub-sections of this paragraph are instead an integral part of the Ph.D. research work and describe the results obtained from isothermal heat treatments in various DSS grades.

2.2.1.1. State of Art: secondary phases in DSS

In this paragraph a brief review of previous works is presented, concerning the effect of isothermal heat treatments on microstructures in various DSS grades. The following results

are a summary of already published researches [4-28], which can be found in literature and which are not part of the author thesis, but are useful to provide a starting point for the reader and are indeed necessary to give a comprehension of the precipitation phenomena affecting DSS.

It is well known that the precipitation kinetics are determined by nucleation and growth rates, *i.e.* thermodynamic driving forces and diffusion. This results in the typical C-curves in a time-temperature-precipitation (TTP) diagram for intermetallic phases (Fig. 2.1a) [8]. Besides microstructural effects, all DSS are subjected to a more or less rapid formation of secondary phases, which is intimately connected to the chemical composition of the steel. The higher the alloying elements content, the faster the precipitation, and the prevention of intermetallics formation is commonly achieved by applying appropriate annealing temperatures and cooling rates [8]. Therefore, the extraordinary properties achieved in SDSS, owing to the higher contribution of substitutional and interstitial solution hardening, are severely mined by the possibility of phases precipitation for very short times. Lean DSS are instead only subjected to nitrides formation in the whole critical range and the intermetallics are not generally observed, due to the lower content of Cr and Mo. In the standard grades, such as SAF 2205, the precipitation occur for longer times than SDSS, but the higher content of secondary phases promoting elements respect to Lean DSS causes the appearance of both the intermetallics.
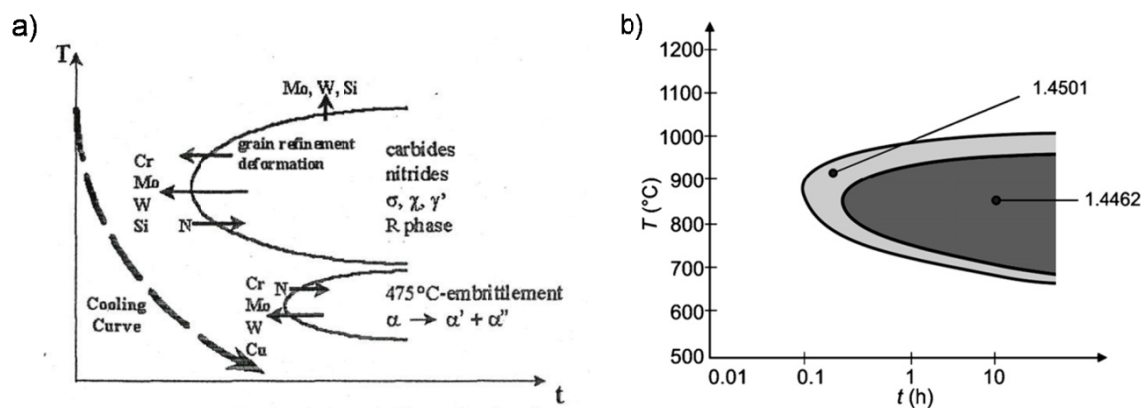
Fig. 2.1 – a) general TTP diagram of DSS [8] and b) TTP diagram of two Duplex grades [9].

In Standard and Super DSS grades, also called Cr-Ni-Mo DSS, both σ- and χ-phases precipitation occurs in isothermal and continuous cooling conditions. The intermetallics preferentially precipitate at triple junctions and α/γ interfaces; χ is usually the first

precipitating one during ageing [4-6,9,10,16], but in continuous cooling treatments this phase only appears at the lower cooling rates [16,17]. Different alloying elements contents lead to different stability field of the intermetallic phases, shifting the nose of the TTP curves toward higher temperatures and lower times (850–900°C in SAF 2205 and around 950°C in SAF 2507, as shown in Fig. 2.1b [9,16]).

In DSS, the positive influence of nitrogen on the kinetics of intermetallic precipitation is less evident than in austenitic grades, owing to the change in ferrite-austenite phase ratio occurring in the DSS case, which causes a less important effect of N on reducing the Cr activity. However, the higher the nitrogen content, the lower the σ-phase content [23]. Compositional effects are more visible in SDSS, which are tungsten-alloyed DSS. SDSS displayed a more rapid growth of intermetallics, due to the similar effects of W and Mo, having both similar diffusion coefficients in the critical temperature range and enhancing the driving force for the intermetallics formation [24]. Nevertheless, whereas simple addition of W makes DSS more prone to phases precipitation, the partial substitution of W for Mo is beneficial for delaying the precipitation [25].
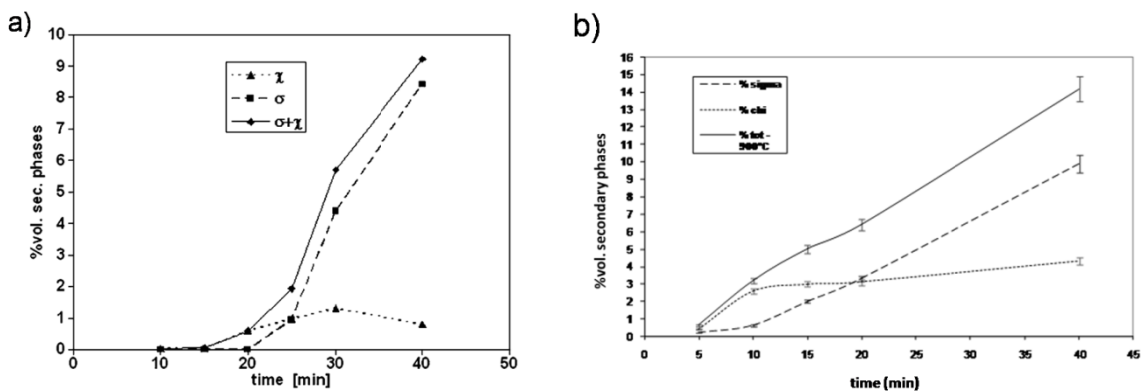
Fig. 2.2 – Precipitation kinetics of σ- and χ-phase at 900°C: a) SAF 2205 [13] and b) Zeron®100 SDSS [14].

The effect of the alloying grade on the precipitation kinetics in Cr-Ni-Mo DSS is clearly visible from Fig. 2.2, considering for both steels a fixed temperature of 900°C, where the diffusion rates are comparable. It must be notice that a reliable phases quantification is largely dependent on the phases content, and it became particularly difficult at the early stages of precipitation, but the differences between the two steels are clearly evident. An increased content of intermetallics-promoting elements causes a faster occurrence of the precipitation phenomena. The composition also conditions the precipitation during

continuous cooling treatments, causing an increasing of the critical cooling rate for secondary phases formation from 0.35°C/s in SAF 2205 to 0.8–0.9°C/s in SAF 2507 [16,17].

The precipitation kinetics in DSS were extensively studied and the reported observations, also in the same grade, were not free of discrepancies, as pointed out by different authors in the SAF 2205 aged at 850°C [8,9,13]. However, the stability field of χ-phase, and the relative nose of the TTP diagram, is at slightly lower temperatures than σ [12,19] and its presence is strongly affected by compositional effects. Moreover, in previous works, χ-phase was erroneously stated to be a metastable precursor of the more thermodynamically stable σ-phase, whereas recent studies have pointed out that its presence can be addressed to a competitive precipitation phenomenon between the two intermetallics [7], as reported in Chapter 1. In equilibrium conditions, the χ-phase seems to disappear in favour of σ, which tends to substitute ferrite and, after ageing, the ferrite-austenite 50/50 microstructure tends to be replaced by a sigma/austenite microstructure, for which the relative volume fraction is found to be assessed in a proportion of 75/25 for the SAF 2205, as shown in Fig. 2.3.
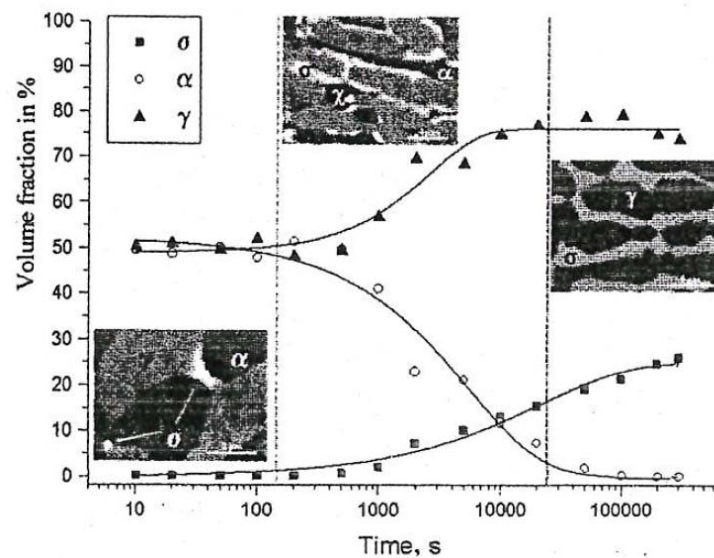
Fig. 2.3 – Evolution of α, γ and σ-phase volume fractions at 850°C
in a 2205 DSS [8].

According to the precipitation temperature, the morphology of the σ-phase changes (Fig. 2.4). At the lowest precipitation temperatures (750°C), a coral-like structure of σ-phase can be found. The amount of single σ nuclei at the beginning of the precipitation is

rather high, depending on the shorter diffusion distances at lower precipitation temperatures. Hence, lower diffusion velocity causes higher local supersaturation and leads to a higher density of precipitations. A different precipitation behaviour can be observed at 950°C. Here, the σ-phase is bigger and more compact, and the linking between single σ crystals is marginal, resulting from a lower nucleation formation force but a high diffusion rate at elevated temperatures [9].
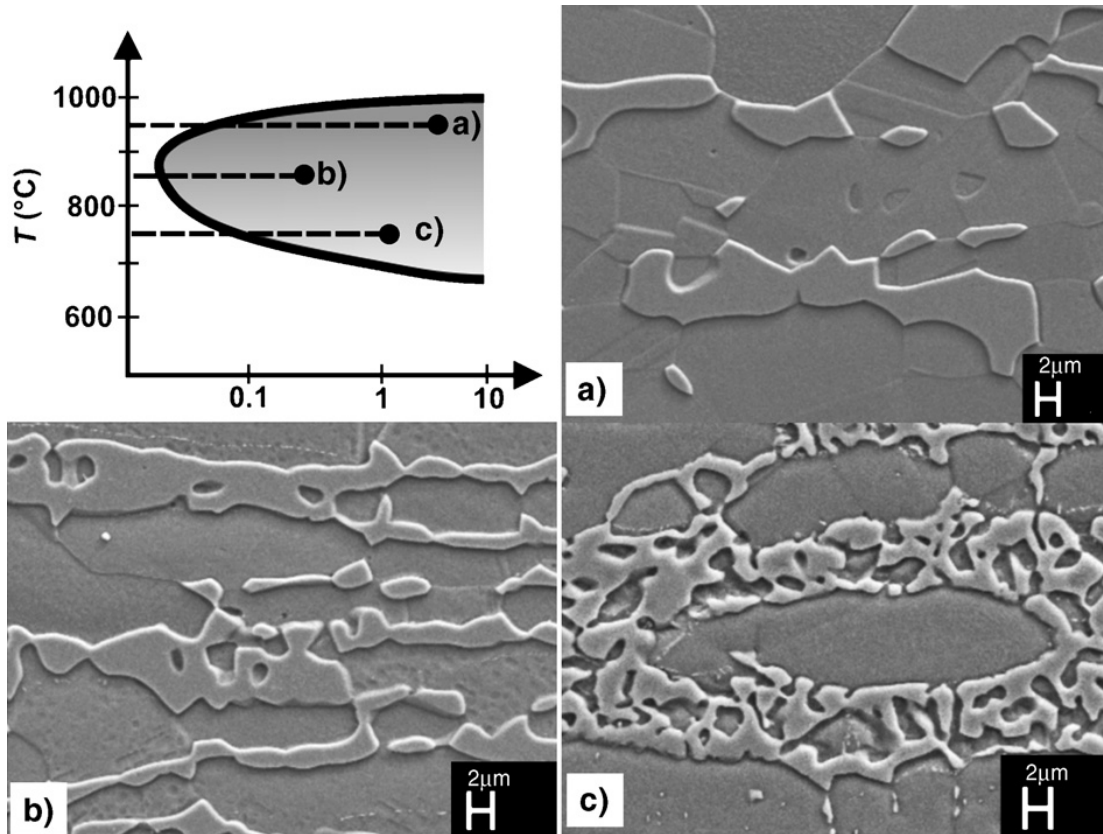

Fig. 2.4 – Influence of temperature in the σ-phase morphology: a) 950°C, b) 850°C and c) 800°C [9].

On the opposite side, despite what is foreseen by the thermodynamic calculations, in Lean DSS – which are or Cr-Mn grades – the ageing treatments usually don't cause the precipitation of χ- and σ-phases, also for very long treatment times exceeding the 750 hours [16,26]. Beside the reduced Mo content, the lack of intermetallics could be justified by the effect of the significant content of nitrogen, which reduces the activity of Cr and Mo, thus lowering the driving force for σ- and χ-phase precipitation. This precipitation delay probably can derive from the lowering of the partitioning ratio for Cr and Mo in the ferrite [27].

It must be noticed that, in SAF 2304, nitrides precipitation is accompanied by the formation of secondary austenite (γ_2). The appearance of γ_2 involves a rearrangement of the austenitic grains, whose boundaries move toward ferrite entrapping nitrides within them and, if the soaking time is sufficiently long, can be dissolved therein. On the contrary, the absence of secondary austenite in SAF 2101 could be explained by the low Ni content, and the precipitated nitrides always remain at the ferrite-austenite grain boundaries. This fact has evident implications on the impact toughness of the aged materials. After isothermal treatments, SAF 2304 maintains its ductility, because nitrides are located far from grain boundaries, and the toughness is never less than 60 J [28]; on the contrary, SAF 2101 grade has evidenced that the presence of nitrides at the grain boundaries decreases its toughness to values lower than 20 J [28] (Paragraph 2.2.1.2).

2.2.1.2. Nitrides in DSS

In Paragraph 2.2.1.1, the decomposition of ferrite in terms of intermetallic phases is discussed. However, almost all DSS contain significant percentages of nitrogen (typically in the range 0.1–0.3%), which represents an important alloying element since, together with nickel and manganese, allows the stabilization of the austenitic phase [4,29] and also gives to the steel a higher resistance to pitting corrosion. For this reason, the content of nitrogen in DSS can be up to ten times higher than carbon, making possible and easier the formation of nitrides, which are mainly of chromium, the principal alloying element. The chemical compositions of the investigated DSS (SAFs 2101, 2304, 2205, 2507, 2510 and Zeron®100 SDSS) are reported in the previous Table 2.1.

The formation of nitrides in DSS has been attested in Cr-Ni DSS [30-32], although in these steels the main undesired effects are due to other secondary compounds, such as σ- and χ-phase. However, the presence of nitrides seems to be more important and conditioning in Cr-Ni SDSS and in Cr-Mn DSS (or Lean Duplex) and, as already observed for the other secondary phases [16], mechanisms and conditions of their precipitation are different and peculiar for each grade.

Equilibrium data

From the phase diagrams calculated by Thermo-Calc (Fig. 2.5), it is possible to note that

nitrides are equilibrium phases in all DSS and are foreseen at the thermodynamic equilibrium for temperatures below 950–1000°C. The amount of nitrides depends on the alloy nitrogen concentration and on the overall composition of the steel, ranging from a minimum of about 1.5–2% of the volume fraction in 2205 DSS to about 4–5% in the high-alloyed Cr-Ni grades. As expected, nitrogen is mainly dissolved in austenite, while in ferrite nitrogen is present at lower concentrations, mainly at elevated temperature. Consequently, in the non-equilibrium microstructure obtained by rapid cooling from the solubilisation temperature, the ferrite is generally supersaturated in nitrogen.
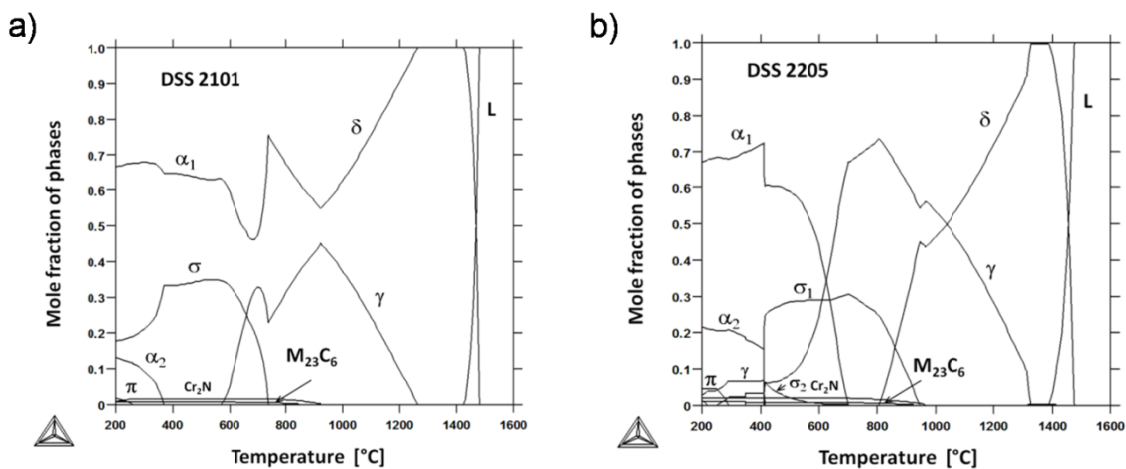
Fig. 2.5 – Calculated phase diagrams: a) SAF 2101 and b) SAF 2205.

Cr-Mn grades: SAF 2101 and SAF 2304

In these steels, the balanced microstructure is obtained by adding high contents of the γ-promoting Mn in replacement of Ni, while the low content of Mo allows for a significant reduction in χ- and σ-phase precipitation.

The 2101 DSS, isothermally heat treated in the temperature range 600–950°C, was only characterized by nitrides precipitation, located at the ferritic grain boundaries and between ferrite and austenite. The precipitates, analyzed by means of EDS (close to the resolution limit), appeared to be enriched in chromium and were identified as chromium nitrides (Cr_2N), but the presence of chromium carbides ($M_{23}C_6$) cannot be excluded, since an accurate distinction by SEM-BSE investigation is not guaranteed. At 600–650°C and for ageing times shorter than 40 minutes, the precipitation has not occurred, but for longer times small nitrides began to appear at the ferritic grain boundaries. On the contrary, at 750°C the precipitation occurred after only 20 minutes and nitrides continued to be present

also after 20 hours of treatment. Rising the temperature, the particles became coarser and also precipitated at ferrite/austenite grain boundaries. In Fig. 2.6 a schematic of the precipitation kinetics of these particles and a SEM-BSE micrograph are reported. In 2101 DSS, Cr-nitrides at the grain boundaries represented the only secondary phases, which mainly formed for temperatures above 750°C, and which were responsible for serious embrittling effects, causing a decrease in impact toughness of more than 100 J [28].
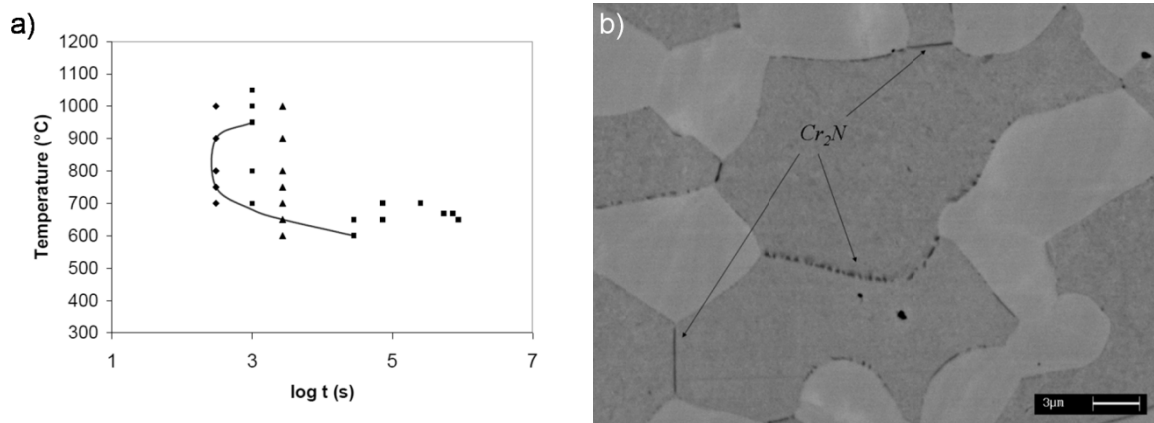
Fig. 2.6 – 2101 Lean DSS: a) nitrides precipitation kinetics and b) microstructure at 900°C for 45 min (SEM-BSE).
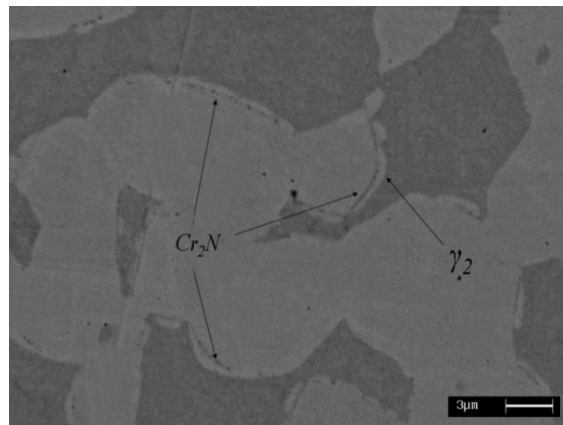
Fig. 2.7 – Nitrides precipitation in SAF 2304 treated at 750°C for 90 min accompanied by secondary austenite formation (SEM-BSE).

The 2303 DSS, after isothermal treatments at 550–650°C, did not show any nitrides formation, while a moderate precipitation of these particles was detected after 40–45 min of permanence at 750°C and 850°C. Here, the precipitation of nitrides required higher temperatures and longer times than in the 2101 grade. The precipitates were mainly located near the grain boundaries between ferrite and austenite, but were also identified within the austenitic grains (Fig. 2.7). This can be justified by the formation of secondary austenite

which, in this grade, occurred together with nitrides precipitation [33]. The process involved in the γ_2 formation seemed to be characterized by a depletion of Cr by nitrides formation and a concurrent enrichment in Ni of those regions which underwent the transformation, as discussed in Chapter 1.

Cr-Ni grades: SAF 2205, SAF 2507, Zeron®100 and 2510

As reported in Paragraph 2.2.1.1, in these grades, the main effect of the isothermal heat treatments in the critical temperature range was the precipitation of σ- and χ-phase, which substantially reduced toughness and corrosion resistance of DSS. However, as they are nitrogen-alloyed grades, higher amounts of nitrides are foreseen on the equilibrium data.

In the 2205 DSS, the amount of nitrides is lower than in the other grades, also in the equilibrium microstructure, and was estimated less than 1.5% of the volume fraction. After isothermal treatments at 700–900°C [13] and after continuous cooling from the solution-annealing temperature [17], the nitrides precipitation was very limited and not easily detectable by means of conventional metallographic techniques. Nitrides always accompanied the precipitation of σ- and χ-phases which, being in larger amounts, can be considered as the only phases which can affect the material properties.
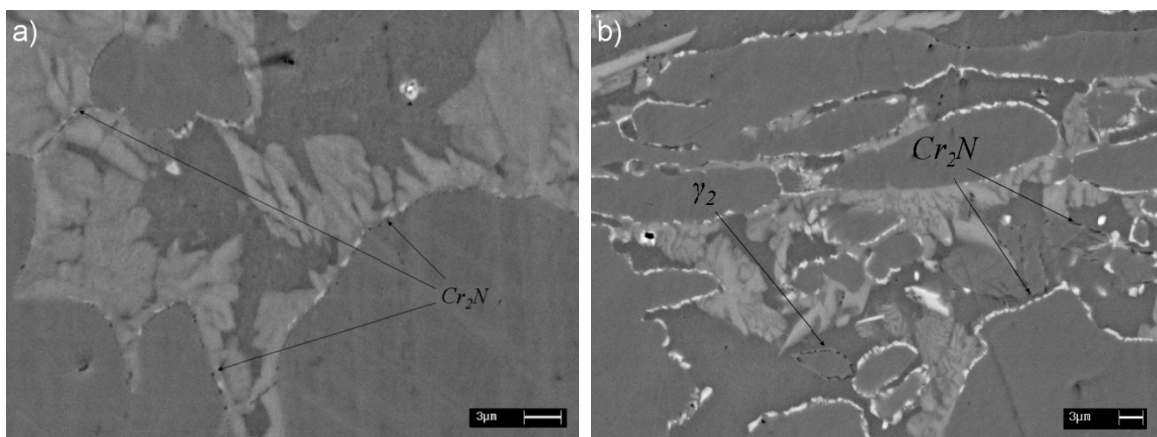

Fig. 2.8 – Cr-Ni Super DSS (SEM-BSE): a) 2510 treated at 900°C for 15 min and
b) Zeron®100 treated at 850°C for 25 min.

2507, Zeron®100 and 2510 SDSS are Cr-Ni DSS, higher alloyed than SAF 2205. The isothermal treatments at 700–950°C allowed a rapid precipitation of both σ- and χ-phases after few minutes (3–5 min) [14,34] and the concurrent precipitation of chromium nitrides was observed (Fig. 2.8). In these steels, the Cr_2N initially precipitated as particles at the

grain boundaries, coarser than in 2205, and afterwards as fine precipitates inside the supersaturated ferritic matrix. In all the SDSS, the amount of nitrides increased with the treatment time but always remained within 1% of the volume fraction, while the other phases exceeded the 10% after 10 minutes of treatment. Nitrides also precipitate during the continuous cooling tests, when the times for diffusion are obviously lower than in the isothermal treatments. In these conditions, the precipitation sequences which characterize the appearance of the intermetallic phases were different and σ-phase appeared by first, followed by χ and nitrides, by decreasing the cooling rate [18].

Nitrides contributed to the embrittlement of all Cr-Ni DSS and SDSS when exposed to isothermal heat treatment in the critical temperature range, and this effect was particularly evident in those samples with a limited amount of intermetallic phases (1–2%), where the greatest decreasing in toughness was observed. Therefore, those samples which were slightly affected by nitrides precipitation must be considered as the most critical ones, whereas the effect of nitrides may be almost negligible in presence of a higher volume fractions of intermetallic compounds, because the toughness resistance resulted already worsened.

Concluding remarks

The investigation on nitrides formation mechanism in DSS indicated that precipitation and its effect on both microstructure and toughness were different and peculiar of various DSS grade. In the Cr-Ni grades, the 2205 steel exhibited a very limited nitrides formation (below 1.5%), owing to the lowest nitrogen content, and therefore its toughness can be mainly worsened by the other secondary phases, when present. In the high-alloyed Cr-Ni grades (SDSS), having the highest nitrogen content, the nitrides amount can instead be greater, but the worsening in toughness is primarily due to the intermetallics.

Nitrides can give an effective contribution to the toughness decrease only at the early stages of precipitation phenomena, when the amounts of the all precipitating phases can already produce an harmful toughness decrease. On the contrary, when the amounts of the intermetallic phases became higher, the nitrides contribution is limited, being overcame by their effects. Finally, in the Cr-Mn DSS, nitrides are the main precipitating phase. In 2101 DSS nitrides appeared as intergranular small precipitates which produced an abrupt decrease in toughness, while in 2304 DSS, the nitrides formation occurred together with

the formation of significant amounts of secondary austenite. In this latter case, nitrides remained embedded within the enlarged austenitic grains and this different location reduced their harmful effects on toughness which was instead weakly reduced.

2.2.1.3. New Lean DSS: LDX 2101 and LDX 2404

Previous studies have shown that the precipitation of the two intermetallic compounds χ- and σ-phase only interests the high-alloyed DSS grades, due to the higher content of alloying elements, while the low-alloyed Lean DSS seemed only interested by the formation of nitrides [16]. In this paragraph, the microstructural modifications resulting from isothermal treatments in two Lean DSS steels is discussed, with the aim to examine their microstructural stability for a relatively short soaking times and in conditions close to equilibrium.

Table 2.3 – Chemical composition of the Lean Duplex Stainless Steels.

Grade	C	Si	Mn	Cr	Ni	Mo	Cu	P	S	N	PRE$_N$
LDX 2101	0.025	0.65	5.13	21.57	1.56	0.28	0.30	0.019	0.0010	0.23	26
LDX 2404	0.022	0.33	2.83	24.41	3.34	1.54	0.42	0.021	0.0004	0.25	33.5

The investigated Lean Duplex steels were two new-developed grades (LDX 2101 and LDX 2404), whose composition is reported in Table 2.3 together with the corresponding PRE$_N$ index. As can be seen, the composition of LDX 2101 is not so far from that of SAF 2101, whereas LDX 2404 differs from the steels of the same category for a higher amount of molybdenum.

The two Lean DSS were in the form of sheet, obtained from cold rolling with a maximum thickness reduction of 50%, solubilised at the proper temperature and subsequently water quenched. The materials were then subjected to the same isothermal heat treatments, at different temperatures within the whole DSS critical temperature range (600–1000°C) and for various soaking times (from 10 minutes to 100 hours), in order to compare the obtained results in terms of atomic mobility and diffusion mechanisms, which are strongly temperature-dependent.

Microstructures and equilibrium phase diagrams

The microstructures of the steels in the as-received conditions are shown in Fig. 2.9 and, as expected, exhibited the classical grain fragmentation due to the previous rolling process, with a partial recrystallization of the austenitic grains due to the subsequent solution-annealing treatment. In this regard, comparing nominally equal DSS grades – having nearly the same chemical composition – the role of microstructure achieved after the forming process cannot be neglected, and the grain fragmentation induced by the cold rolling process can condition in some extent the precipitation kinetics in the steels under investigation, especially in the first stages of precipitation. The image-analysis performed on the OM micrographs confirmed that the phases of both steels were well balanced, with a about 52% ferrite and 48% austenite.
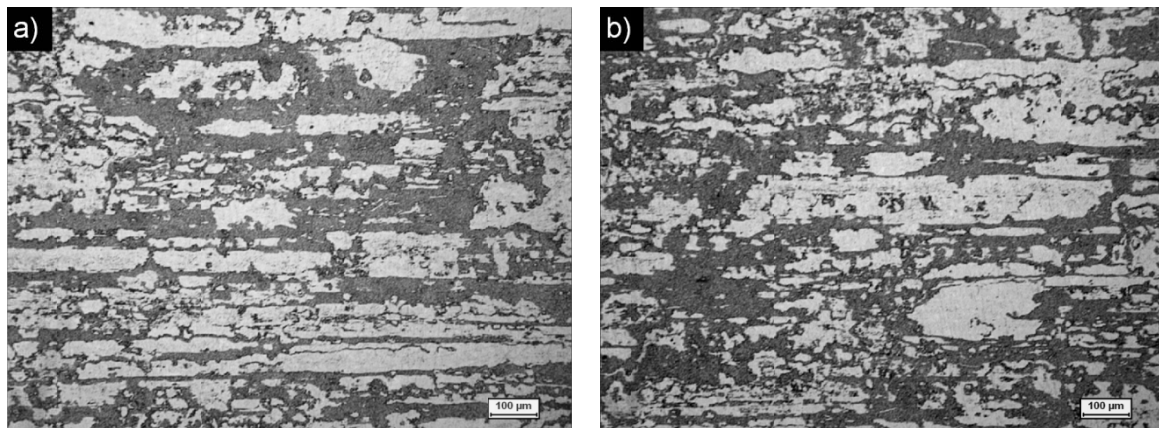
Fig. 2.9 – Microstructures of the as-received samples (OM): a) LDX 2101 and b) LDX 2404.

The ageing temperatures were chosen after the analysis of the equilibrium phase diagrams obtained by thermodynamic simulations, which can provide indications on the equilibrium microstructure and therefore on those temperatures at which the formation of certain phases may be favoured. The performed treatments are summarized in Table 2.4, where the names of the two DSS (2101 and 2404) are placed in correspondence of the time-temperature combinations.

The analysis of the phase diagrams shown in Fig. 2.10, highlighted the prediction of σ-phase at equilibrium in both the steels, with a stability field slightly more enlarged toward higher temperatures in 2404, probably due to the higher content of the alloying elements that promote its formation (in particular Cr and Mo). On the contrary, the χ-phase was not foreseen, as it instead happens for the highly alloyed DSS [*6-LEAN*], and this can be

ascribed to the low Mo content of the steels, if compared to Standard and Super DSS grades. Besides the presence of σ-phase, the equilibrium diagrams also predict a significant quantity of chromium nitrides (Cr_2N), which in both cases is maintained close to 2–4% of the volume fraction, and the presence of a very small quantity of $M_{23}C_6$ carbides (<1%).

Table 2.4 – Isothermal heat treatments.

Temperature [°C]	Time [min]								
	5	10	30	60	120	480	1440	3000	6000
600	-	-	2101	-	-	-	-	-	2101 2404
650	-	2101	2101	-	-	-	-	-	-
700	-	2101 2404	2101	-	-	-	-	-	-
750	-	2101 2404	2101	-	-	-	-	-	-
800	2101 2404	2101 2404	2101 2404	2101 2404	2101 2404	2101 2404	2101 2404	2101 2404	-
850	-	2101 2404	2101	-	-	-	-	-	-
900	-	2101 2404	-	-	-	-	-	-	-
950	-	2404	-	-	-	-	-	-	-
1000	-	2404	-	-	-	-	-	-	-
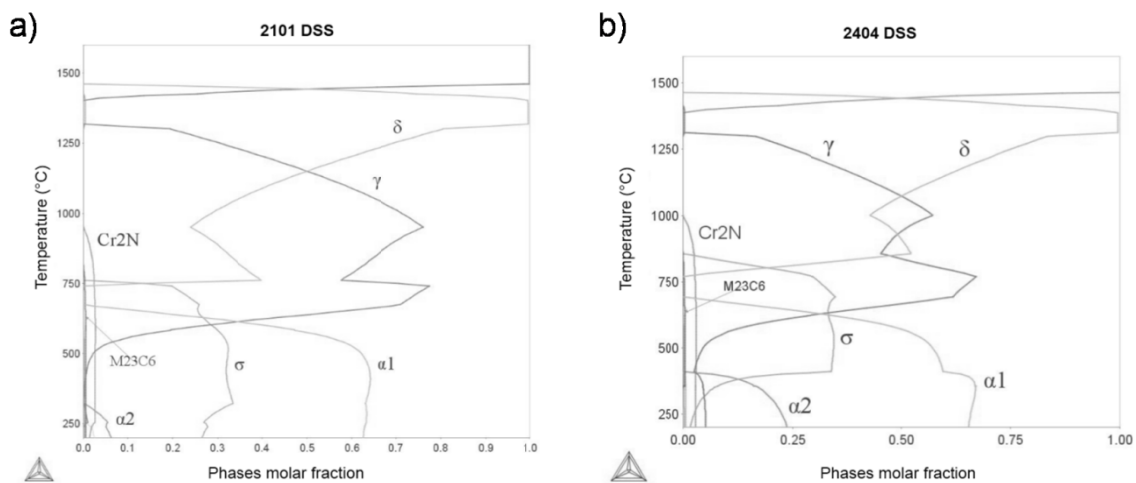
Fig. 2.10 – Equilibrium phase diagrams: a) LDX 2101 and b) LDX 2404.

In both diagrams, at 600°C, it is possible to notice appreciable quantities of σ-phase (approximately 30% of the volume fraction) but, if one considers the kinetics governing the diffusion processes, this temperature is very low and the required time to reach the equilibrium conditions is very long. At 800°C, diffusion is faster and the thermodynamic equilibrium condition may be reached in shorter time but, while for 2404 this temperature falls in the σ-phase stability field, in 2101 it falls outside of that range.

600°C isothermal heat treatments

As previously reported, at 600°C the calculations provide the presence of the σ-phase in both steels. However, after a 100 hours treatment, only small dark precipitates were detected, preferentially arranged at ferritic grain boundaries and in greater quantities in 2101 than in 2404 (Fig. 2.11).
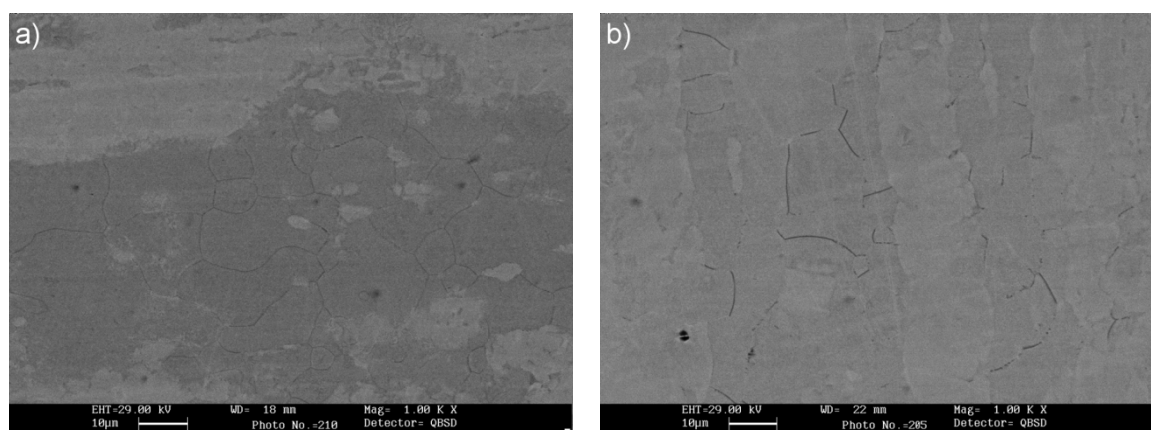
Fig. 2.11 – Microstructures after isothermal treatments at 600°C for 100 hours (SEM-BSE):
a) LDX 2101 and b) LDX 2404.

These particles were identified by XRD as Cr_2N chromium nitrides (hexagonal structure), but their size was below the EDS detection limit. However, even if the EDS spectra acquired on such particles included the signal from the surrounding matrix, a significant enrichment in Cr was detected.

Comparing the diffraction spectra obtained on the treated materials with those in the as-received conditions (Fig. 2.12), it is possible to notice, just before the $\gamma(111)$ austenitic peak, the Cr_2N principal peak ($2\theta \approx 65.4°$). The low volume fraction of nitrides justified the solely presence of the main peak, whose intensity was very low but whose position allowed to attribute it to this class of nitrides.
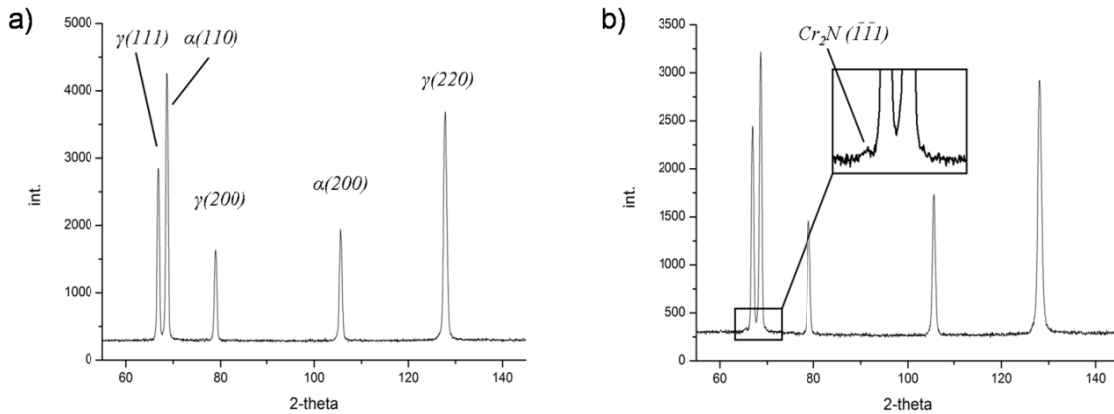
Fig. 2.12 – Diffraction spectra of LDX 2101: a) as-received and b) treated at 600°C for 100 ore.

At 600°C the diffusivity of those elements involved in the secondary phases formation is very low and only the precipitation of Cr_2N nitrides seemed to be favoured, since chromium is the main alloying element. The low value of the diffusion coefficients, together with the low content of molybdenum, did not allow the precipitation of χ- and σ-phase, even though the soaking time always plays a fundamental role and the 100 hours treatment may be not enough to their formation.
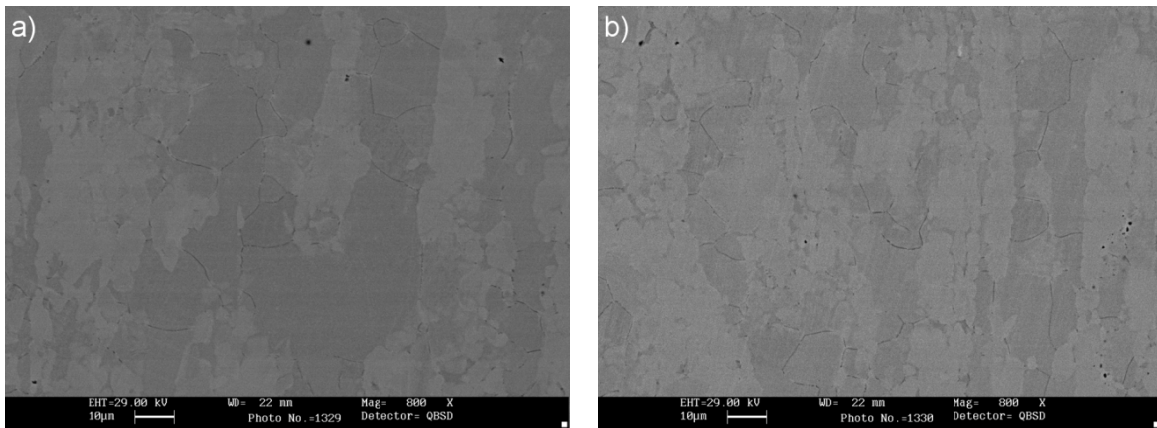
Fig. 2.13 – Microstructures of LDX 2404 treated at 800°C (SEM-BSE): a) for 10 min and b) for 30 min.

LDX 2404: 800°C isothermal heat treatments

In this steel, the 5 minutes exposure did not permit the formation of any precipitates, while, after 10 minutes of treatment, dark particles similar to the Cr_2N identified at 600°C were detected at ferrite grain boundaries and rarely at the ferrite/austenite interfaces (Fig. 2.13). Also in this case the precipitates were too small to allow an EDS analysis and also their volume fraction was below the XRD detection limit. Increasing the treatment time (30

min), any substantial growth in particles size was not observed, whereas their quantity noticeably increased (Fig. 2.13), remaining however not identifiable by means of EDS and XRD.

Table 2.5 – Chemical composition of σ-phase in LDX 2404 (1 hour at 800°C) [wt.%].

Cr	Mo	Ni	Mn	Fe
30	3	2	3.5	bal

Nevertheless, the steel's behaviour as a result of longer treatment times was different. Conversely to what happens to other Lean DSS, after 1 hour of permanence at 800°C a new phase was observed. The EDS analysis confirmed it to be σ-phase (Table 2.5), significantly enriched in Cr and Mo if compared to ferrite and austenite and whose composition was within the provided ranges for this intermetallic compound (see Chapter 1). After 2 hours treatment (Fig. 2.14), the volume fraction of σ increased, but not in a significantly extent to enable its detection by XRD analysis.
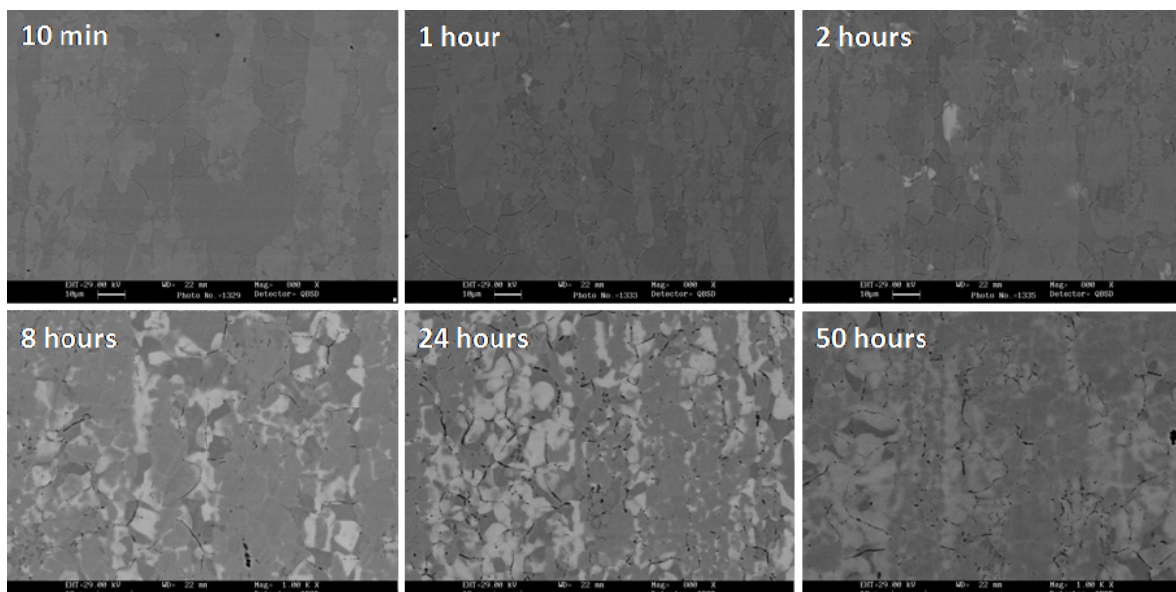

Fig. 2.14 – Microstructural evolution of LDX 2404 treated at 800°C (SEM-BSE).

Increasing the soaking time, a progressive increase in σ-phase amount was observed and the almost total decomposition of ferrite was reached after 50 hours of treatment (Fig. 2.14), highlighting that such transformation occurred very slowly if compared to the high-alloyed DSS. Again, the EDS analysis and the XRD spectrum (Fig. 2.15) confirmed that

such phase was the intermetallic compound. Moreover, it is possible to notice that the very long treatment times also caused the coalescence of the Cr_2N particles, changing from continuous chains at the grain boundaries to a more fragmented displacement, probably due to the formation of σ.
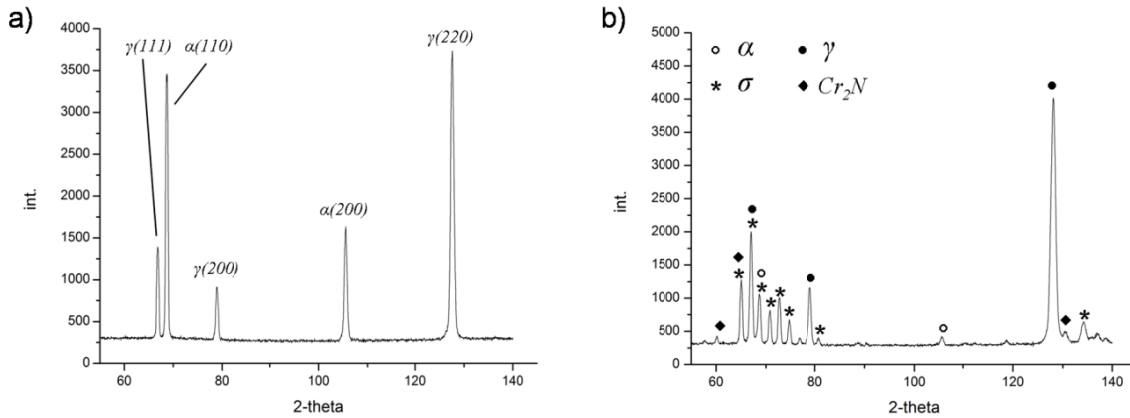

Fig. 2.15 – Diffraction spectra of LDX 2404: a) as-received and b) treated at 800°C for 50 hours.

The slower ferrite decomposition observed in the LDX 2404 can be attributed to compositional factors. Comparing this steel to the high-alloyed DSS, where nucleation and growth of σ are favoured [16], the lowest alloying elements content necessary to the formation of the intermetallic compound retarded the precipitation. If compared to similar grades, the peculiarity of the 2404 under analysis lies in the higher molybdenum content in the alloy, which therefore can be considered as the discriminating factor for the σ-phase formation, controlling the diffusion processes and the precipitation kinetics involved in the genesis of the intermetallic phase. Molybdenum, in fact, possesses the highest value of the diffusivity coefficient at any temperature within the critical range [8] and its contribution is essential in increasing the driving force for the formation of σ [12]. As expected, no χ-phase was detected; in this case, the low molybdenum content of the steel, although high if compared to other Lean Duplex, was not sufficient to allow for the formation of such intermetallic compound.

LDX 2101: 800°C isothermal heat treatments

Also for this steel, the 10 minutes treatment at 800°C only caused the precipitation of chromium nitrides. These particles were slightly smaller than those observed in 2404, due to the lower Cr content, but were in a comparable volume fraction. Increasing the treatment

time, the number of such particles increased and the phases coarsened, but still remaining below the EDS and XRD detection limits. After 2 hours treatment, nitrides are again the only precipitates, roughly maintaining the same size but in a greater volume fraction.
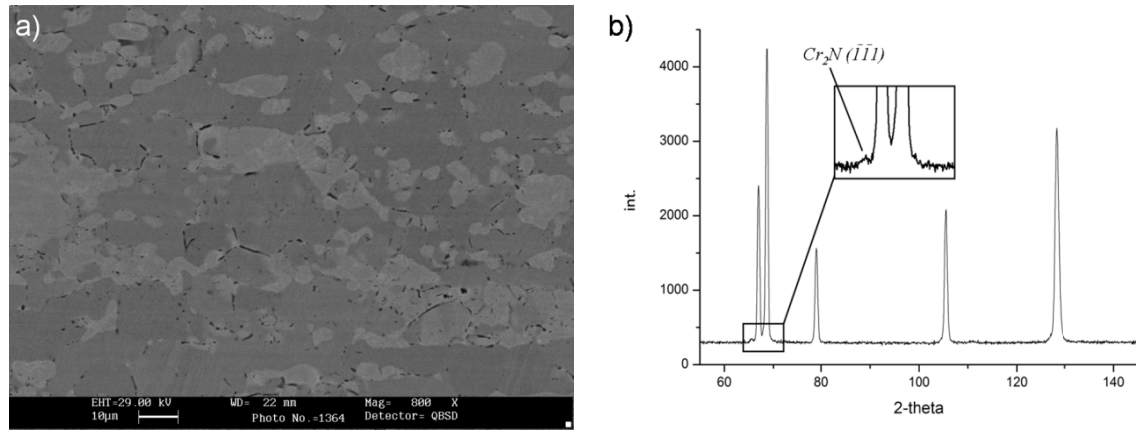

Fig. 2.16 – LDX 2101 treated at 800°C for 50 hours: a) microstructure (SEM-BSE)
and b) corresponding diffraction spectrum.

As expected, after 50 hours, SEM and XRD measurements revealed that there was not precipitation of any intermetallic compounds and that Cr_2N chromium nitrides were the only secondary phases within the microstructure (Fig. 2.16). Also for this steel, the 50 hours treatment caused nitrides coalescence and the precipitation at the grain boundary resulted more fragmented than for shorter times.
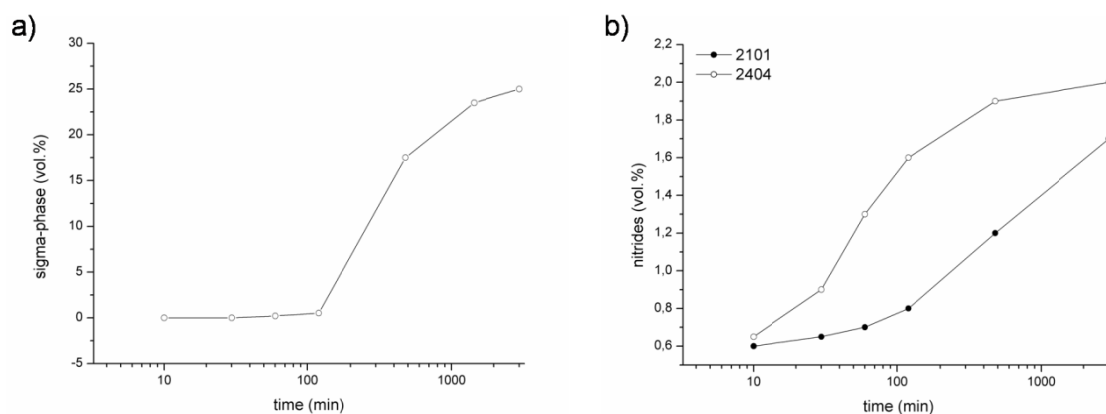

Fig. 2.17 – Precipitation kinetics: a) σ-phase in LDX 2404 and b) Cr_2N nitrides in both steels.

Precipitation kinetics

As previously discussed, only the LDX 2404 was affected by σ-phase precipitation. In Fig. 2.17a, the estimated volume fraction of the intermetallic compound as a function of the treatment time are presented. Due to the lower content of alloying elements, in 2404 the precipitation kinetics were very slow if compared to that observed in the higher-alloyed DSS and, after 50 hours of treatment, the equilibrium conditions were not totally reached, since ferrite was not completely transformed.

At all temperatures and for all the considered soaking times, Cr_2N were observed in both steels and the related precipitation kinetics are reported in 2.17b. For short treatment times (10 min), both steels were affected by a comparable amount of precipitates, whereas for longer times the highest Cr content in the 2404 DSS conditioned the precipitation by favouring the formation of a greater volume fraction of nitrides. However, after 50 hours treatments the quantity of precipitates was settled on close values in both steels. This can be explained considering that, in 2404, the decomposition of ferrite was very slow in the initial stages and the treatment primarily caused the nitrides precipitation; the subsequent appearance of σ altered the precipitation kinetics causing a reduction in nitrides formation. The precipitation of σ-phase, which was favoured for longer soaking times, subtracted Cr to the matrix, inhibiting the precipitation of a greater amount of nitrides.
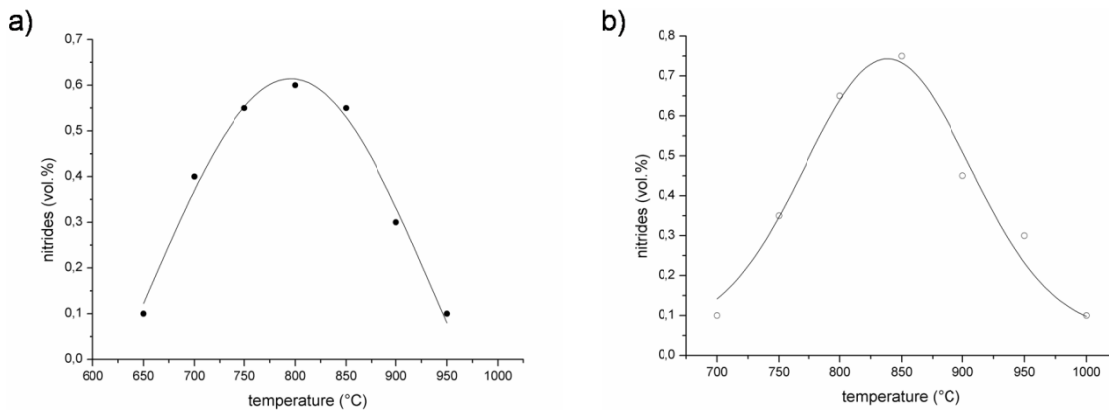

Fig. 2.18 – Precipitation pseudo-kinetics: a) LDX 2101 and b) LDX 2404.

After the results obtained from the 600°C and 800°C treatments, further isothermal treatments of 10 minutes were performed in the whole critical temperature range (Table 2.4), in order to determine the temperature at which the nitrides formation may be favoured, according to the observed amount of precipitates. The data in Fig. 2.18 suggest

that such temperatures are in the range 800–850°C for LDX 2404 and 750–850°C for LDX 2101.

In the previous Paragraph 2.2.1.2, the nitrides precipitation kinetics in a rod-shaped SAF 2101 DSS are presented; this steel has a chemical composition which is not so far from the LDX 2101 examined in the present section, except for a three times lower Mo content (about 0.1% in SAF and 0.3% in LDX). Comparing these two Lean DSS, it can be noticed an anticipated precipitation in the LDX steel respect to the SAF grade, although the estimated critical temperature range (750–850°C) was found to be the same. This fact can be explained considering the influence of both compositional effects and microstructural differences. Besides the higher content of Mo, which promotes phases precipitation Chapter 1), in LDX 2101 the microstructure was rather fragmented, owing to the rolling process. Thus, the presence of an increased number of triple points and grain boundaries, and the induced residual stresses may act as enhancing factor for the precipitation kinetics, moving the occurrence of nitrides formation towards lower treatment times.

Concluding remarks

In LDX 2101 and LDX 2404, at all temperatures within the critical range and for all the treatment times, Cr_2N chromium nitrides were detected in intergranular position, although the precipitation occurred with different kinetics in each steel. Such particles represent a problem for the favourable characteristics of these steels, compromising the interesting combination of corrosion resistance and mechanical strength. Presence and position of the nitrides, in fact, cause a local depletion of chromium at the grain boundary, favouring the localized corrosive attack, and make DSS weaker from the mechanical point of view, facilitating the initiation of fracture mechanisms.

2.2.2. Cold rolled materials

Ferrite decomposition is a diffusion process and, as introduced in Paragraph 2.1, the precipitation kinetics involved during the formation of secondary phases are affected by the amount of the diffusivity paths and therefore by crystal disorder and dislocations density. It is known that cold deformation increases the number of defects inside the grains and the crystal disorder is strictly related to the achieved deformation degree.

The sheets manufacturing processes, as recently introduced for the fabrication of water tanks and heat exchange panels [35], can induce several microstructural modifications which affect the formability properties. The influences of manufacturing processes on the tensile properties of DSS sheet, and especially elongation at room temperature, have been studied by few researchers, but it was evidenced that the elongation is related to the hot-rolling texture, as well as to the annealing temperature after both hot- and cold-rolling [35]. On the contrary, there are no data on mechanisms and kinetics of phases precipitation in the cold rolled samples after heat treatments.

In the present paragraph, the effect of cold rolling on phases precipitation in two DSS is presented. Even though the examined steels have different TTP curves, the heat treatment were performed at the same temperature, in order to compare the results in terms of atomic mobility and diffusion mechanisms, which are strongly temperature-dependent. The solution annealing temperature, the relative elements concentration and their partitioning contribute to regulate both the activation energy for the precipitation and the flux of atoms through the different phases. Thus, supposing that the mechanisms which regulate the diffusion processes are almost the same, treatments at same temperatures will similarly condition the precipitation.

2.2.2.1. SAF 2205 and SAF 2507 cold rolled and heat treated

In this section, the SAFs 2205 and 2507 DSS presented in Paragraph 2.1 – and whose chemical compositions are reported in Table 2.6 – were examined. The steels were cold rolled at various deformation degrees, from 5% to 85% thickness reduction, in the same direction of the previous hot working, then isothermically heat treated in a muffle furnace at 900°C for 10 and 30 minutes and finally water quenched. For a comparison, the as-received materials were treated at the same conditions.

Table 2.6 – Chemical composition of the investigated DSS.

Grade	C	Si	Mn	Cr	Ni	Mo	Cu	P	S	N
SAF 2205	0.030	0.56	1.46	22.75	5.04	3.19	-	0.025	0.0020	0.16
SAF 2507	0.015	0.24	0.83	24.80	6.89	3.83	0.23	0.023	0.0010	0.27

Cold rolled microstructures

The effects of cold rolling on the DSS microstructures concerning the mechanisms of deformation and the phases behaviour are detailed discussed in Chapter 3 of the present thesis, while in this paragraph only a short description is presented.

The cold worked samples were characterized by a band-like microstructure which gradually developed as the deformation degree increased, exhibiting grains elongation toward the rolling direction. During the cold deformation, the two phases exhibited different plastic behaviours and, as the thickness reduction increases, the ferrite bands were more reduced than the austenitic grains. Even though this difference in thickness between the two phases was not very pronounced at the early stages of deformation, it was rather evident from thickness reduction that exceeded the 50%.

Since the solid-state phase transformation during the isothermal heat treatment involves the ferritic matrix, only the effects of the cold rolling in this phase will be discussed. The deformation process induces an increase of the dislocations density inside the grains, leading to an increasing of the number of interfaces and defects within the matrix. These features, being areas of higher energy, are to be considered as preferential sites for the precipitation of secondary phases.
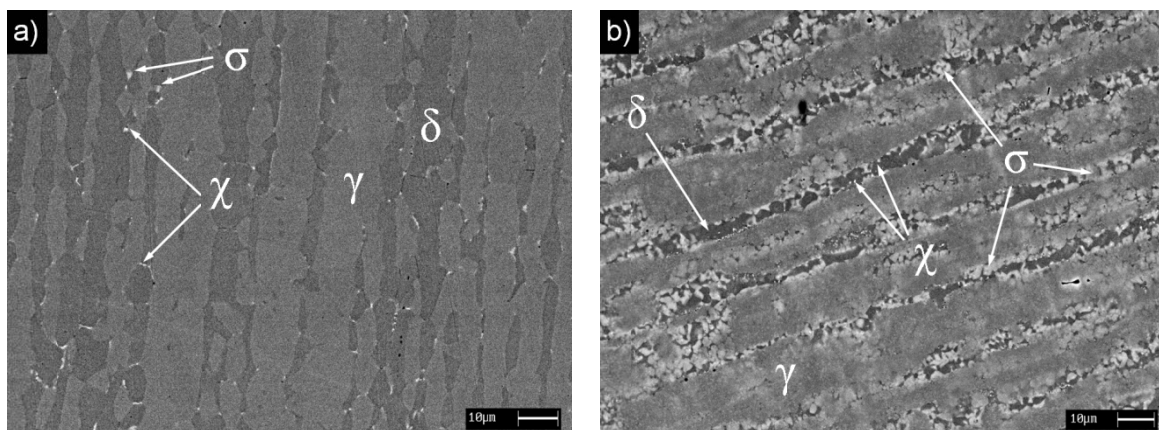

Fig. 2.19 – Secondary phases precipitation in SAF 2205 treated for 10 minutes (SEM-BSE):
a) undeformed material and b) 85% thickness reduction.

2205 DSS cold rolled and heat treated

After the 10 minutes treatment, the secondary phases precipitation in the as-received material was very slight and it mainly consisted in χ-phase, estimated around 1% of the volume fraction (Fig. 2.19a), even though some σ particles were seldom detected. Plastic

deformation enhanced the amount of the precipitating phases; as the thickness reduction increased, the χ-phase was gradually substituted by the σ-phase and, at the maximum thickness reduction, it was almost fully replaced, reaching about the 18% of volume fraction (Fig. 2.19b).

As can be seen from Fig. 2.20, the precipitation kinetics of the material treated for 10 minutes can be described by an exponential-type law and the SEM examination has evidenced an irregular increasing of the precipitation amount for deformation which exceeding 15%. On the contrary, the exposure of the material for 30 minutes generated a progressive and steady increase of the precipitating phases by increasing the deformation degree, and the relation between the volume fraction of secondary phases against the deformation can be considered almost linear.
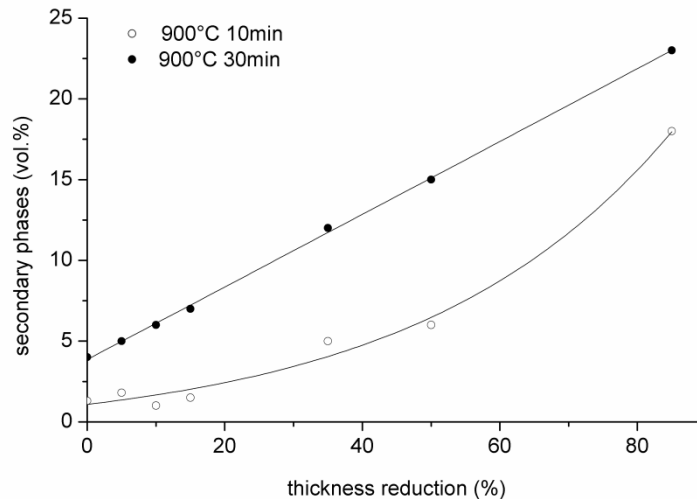

Fig. 2.20 – Precipitation kinetics in the cold rolled 2205 DSS.

From the plot in Fig. 2.20, the effect of the plastic deformation on the treated sample is clearly evident, especially for the shortest times. For the 10 minutes treatment, the increasing of the crystal defects and the generation of micro-strain gradients of progressive higher entity strongly affected the precipitation behaviour. Thus, the material passed from a slight-affected condition – in terms of secondary phases amount – for lower thickness reductions to a strongly-damaged microstructure at 85% of deformation. This situation could be explained considering that, up to 15% of deformation, the dislocation density and the number of defects were not very high, even though a certain amount of surplus energy was stored, and the distortion energy of crystals was not sufficient to act as discriminating

factor in order to reduce the time for the precipitation. On the contrary, over 35%, the distortional energy stored inside the grains was enough to significantly promote the precipitation.

In the samples treated for 30 minutes the deformation also caused an increasing of the precipitation entity, but without the strong drop observed in the previous case for deformations over 15%. In this case the increasing of the precipitates amount was more regular because the exposure time at the soaking temperature was higher (Fig. 2.21). In fact, the precipitation process is a diffusive transformation and is strongly time-dependant, thus a greater time at the treatment temperature promoted the entire diffusion process.
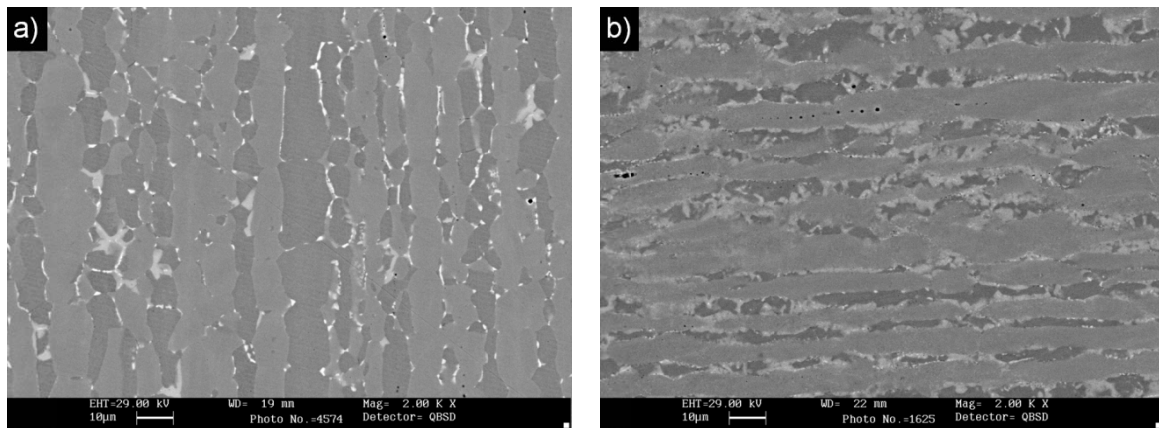
Fig. 2.21 – Secondary phases precipitation in the 2205 grade treated for 30 minutes (SEM-BSE): a) undeformed material and b) 50% thickness reduction.
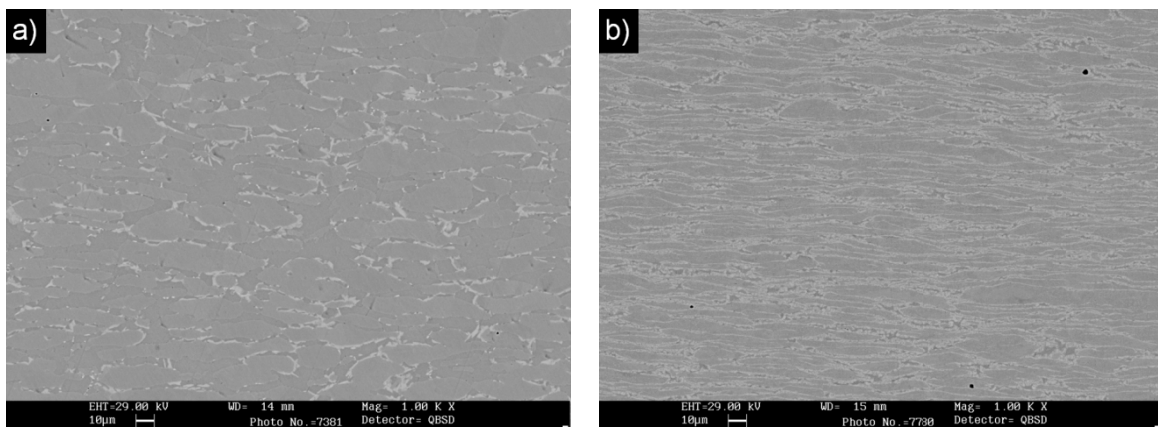
Fig. 2.22 – Secondary phases precipitation in the SAF 2507 treated for 10 minutes (SEM-BSE): a) undeformed material and b) 65% thickness reduction.

2507 DSS cold rolled and heat treated

This steel exhibited a different behaviour respect to the 2205 grade, since the soaking temperature of the treatment is critical for this steel and causes a very fast precipitation. Thus, after 10 minutes of exposure, in the base material the precipitation was around 10% of the volume fraction and rapidly increased as the deformation proceeded, reaching about the equilibrium value for the 85% of deformation (Fig. 2.22).

The results obtained in the 2507 DSS are plotted in Fig. 2.23. Also in this case, the effect of the deformation was more pronounced for the 10 minutes treatment, while after 30 minutes the rising of the secondary phases amount with the deformation was quite slight, although the microstructural damage was wider. However, in both cases, for the 85% of deformation the equilibrium volume fraction of secondary phases was approximately reached and the ferrite was almost completely transformed.
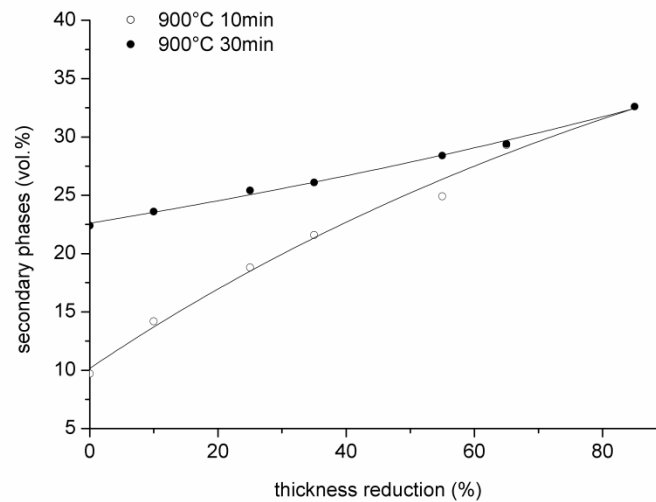

Fig. 2.23 – Precipitation kinetics in the cold rolled 2507 DSS.

Isothermal heat treatments and phase precipitation

In the as-received materials the kinetics of the precipitation at these temperatures is well known and the nucleation of intermetallic compounds mainly occurs at the triple points and at the grain boundaries, because of the high interfacial energy. The high distortional energy associated to these regions, which arises from the misfit between the different phase lattices or due to the misorientation of two crystals of the same phase, lowers the activation energy for phases nucleation. The secondary phases formation and their growth occur by diffusion mechanisms and these regions must be considered as high diffusivity paths,

where the initiation of the process and the phases growth are facilitated. In the deformed DSS, cold rolling modified the grains shape, implying an increase of the distortion at the interfaces and making these regions more reactive.

Thus, plastic deformation rendered the interfaces more prone to the nucleation of new phases by giving to the whole structure a surplus of internal energy, which promots the entire process (nucleation and growth). After cold rolling, the χ-phase formation was particularly favoured, due to the low misfit between the crystal structures of such phase and ferrite, especially in correspondence of the dislocations, since both phases are BCC. Moreover, the treatments were carried out below the theoretical limit value of 0.75–0.8·T_M, causing a predominant diffusion along grain boundaries and dislocations respect the diffusion through the crystal lattice [1].

The precipitation sequences in the deformed samples were not different from that observed in the as-received materials. The χ-phase appears always by first and was followed by the σ-phase, but the precipitation occurred not only at the interfaces but also inside the ferritic grains, due to the presence of dislocations agglomerates, and the kinetics of the phenomenon were modified. In the deformed samples, the nucleation sites were much more than in the as-received material, reducing the time for the precipitation depending on the degree of deformation degree.

Concluding remarks

Cold working modified the microstructure by increasing the crystals disorder. As expected, the number of defects and interfaces were higher than in the as-received materials and the grains were increasingly fragmented as the thickness reduction proceeded. This gave to the entire microstructure a surplus of internal energy, in terms of distortional energy of the interfaces and strain gradients at the local level, making the ferritic phase more prone to phase transformation. Grain boundaries and dislocations must be considered as high diffusivity paths and thus an increasing of them and of their interfacial energy promoted the diffusional processes as the secondary phase precipitation.

Plastic deformation at room temperature significantly enhanced the precipitation kinetics, leading to a substantial damage even for short soaking time at the critical temperature. Thus, after any degrees of cold deformation a further solution-annealing treatment is recommended, in order to allow for the relaxation of the microstructure and

the reduction of the internal defects. The solubilisation after cold deformation must be well designed, taking into account the composition of the steel, the size of the product and the deformation degree. The temperature and the time also must be well chosen, in order to guarantee approximately the 50/50 phase ratio and the greatest reduction of internal defects and stresses. Moreover, the soaking time must avoid an excessive grains polygonalization during annealing because it causes the generation of a major number of triple points, which are preferential precipitation sites.

2.3. EFFECTS ON IMPACT RESISTANCE

Secondary phases are hard structural discontinuities inside the Duplex microstructure and, since preferentially precipitate at the interfaces, can give rise to serious embritteling effect. The enhanced mechanical properties of DSS are achieved from the biphasic microstructure and, as observed in SDSS, an increased amount of alloying elements allow for a further mechanical strengthening by solid solution hardening (Chapter 1). However, increasing the alloying content will render the material more prone to phases precipitation, implying a very careful control of the microstructure after forming and welding operations, in order to avoid precipitation phenomena. The results presented in this paragraph concern to the impact toughness of DSS, and the effects of secondary phases precipitation on the impact response are discussed.

DSS retain considerable impact toughness values even at low temperatures (*i.e.* -40°C) and the ductile-to-brittle transition (DBT) is more gradual than in carbon steels or ferritic stainless steels. On the contrary, ductility and impact toughness are in general lower than those of austenitic grades (Chapter 1). In fact, whereas the tensile properties of DSS are essentially governed by the BCC ferritic matrix, the good toughness could be ascribed to the presence of the FCC austenite, which easily accomodates plastic deformation, retarding the cleavage fracture of ferrite [4,36].

The materials toughness can be evaluated by means of Charpy-V impact instrument, in which a standard specimen is impacted using a striker mounted on a pendulum; the absorbed energy during the impact gives the impact toughness (KV) of the material. The samples have a V-shaped blunt notch to initiate the crack and, therefore, toughness can be consider as a measure of the difficulty to the crack initiation as well as to the crack

propagation. This test is different from the quasi-static fracture toughness test but, owing to a less expensive cost and rapidity of execution, it is preferred in industry and is still used to evaluate the toughness of metals and to describe their DBT behaviour.

In the next paragraphs, the effects of the secondary phases on the impact toughness behaviour in two DSS grades are presented. The investigated SAF 2205 DSS and Zeron®100 SDSS were already introduced in the previous paragraphs and their chemical compositions are reported in the following Table 2.7. The impact tests were carried out using different Charpy pendulums, as specified in the appropriate section, but the geometry of the specimens and the V-notch shape were all obtained by following the ASTM A370 specifications in the longitudinal plate direction.

Table 2.7 – Chemical composition of the investigated DSS.

Grade	C	Si	Mn	Cr	Ni	Mo	Cu	W	P	S	N
SAF 2205	0.030	0.56	1.46	22.75	5.04	3.19	-	-	0.025	0.0020	0.16
Zeron®100	0.014	0.25	0.88	25.23	6.89	3.67	0.72	0.62	0.023	0.0010	0.28

2.3.1. Impact toughness

The toughness of a material can be defined as its resistance to crack propagation or its ability to absorb energy in the plastic deformation range and represents a measure of the energy to resist to fracture. Secondary phases are structural discontinuities which worsen the mechanical properties, and especially impact toughness, by causing stress intensifications in correspondence of them and thus becoming the preferential cracks initiation sites. Owing to this worsening in mechanical resistance, many standards related to manufacturing of DSS require "no intermetallic phases" in the microstructure [37]. This restriction implies a careful control of the whole manufacturing process, since a reliable and relatively cheap metallographic procedure is not simple to achieve, especially for the quantitative determination of very small (1–2%) dangerous phase contents.

2.3.1.1. Impact toughness of isothermally treated DSS

In the present paragraph, the impact toughness at room temperature of two isothermally heat treated DSS grades is discussed, in order to relate the impact behaviour to the amount

of the secondary phases, with particular emphasis on the early stages of precipitation. The steels were the 2205 DSS and the Zeron®100 SDSS with the chemical compositions reported in Table 2.7. The time-temperature combinations of the isothermal treatments, listed in Table 2.8, were chosen on the basis of previous results [13,14] and were designed with the aim to obtain the precipitation of various amounts of secondary phases. The materials (bars-sized) were treated in a muffle furnace and water quenched; after the treatments, the bars were machined to obtain the Charpy-V specimens.

The impact toughness was investigated by means of an instrumented impact testing machine on Charpy V-notched specimens at room temperature, using an available energy of 300 J. All the obtained load-deflection curves were partially smoothed using the moving average method [38], with a cut-off frequency of 50 Hz.

Microstructures

The as-received materials were composed by a ferritic matrix containing the austenitic grains oriented toward the previous hot rolling direction. In both materials the phases were present in almost equal volume fraction but the isothermal heat treatments gradually lowered the ferrite content giving rise to the formation of secondary phases. However, not all the considered aging times were sufficient to obtain the precipitation of significant amounts of intermetallic phases (Tables 2.8 and 2.9) and this implied different impact toughness responses, depending on their effect on the microstructure.
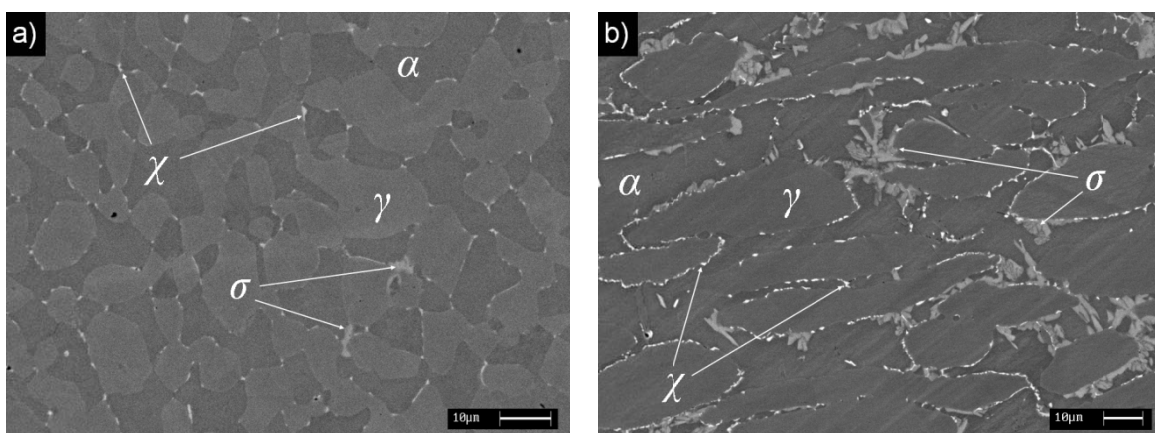

Fig. 2.24 – Microstructure of samples aged at 900°C (SEM-BSE): a) 2205 after 25 min and b) Zeron®100 after 15 min.

As confirmed by other studies [13,14], in both the steels the secondary phases precipitation sequences were the same, but with different kinetics and phases amount. The

χ-phase was the first precipitating one, in correspondence of triple points and grain boundaries and, by increasing the treatment time, its formation was followed by the occurrence of the σ-phase, which grown toward ferrite (Fig. 2.24). The σ particles were coarser than the χ ones and also grown faster, progressively embedding the χ precipitates. As can be seen from Fig. 2.24, the precipitation kinetics was faster in the Zeron®100 DSS owing to its higher alloying element content.

Table 2.8 – Treatments, toughness and precipitates amount for 2205 DSS.

Ageing temperature [°C]	Ageing time [min]	Absorbed energy [J]	Secondary phases [%]
780	20	242.5	not present
	25	231.5	not present
	30	173	< 0.1
	40	141	< 0.1
850	10	229	not present
	15	219	not present
	20	125	<0.1
	25	87.5	<0.1
	30	83.5	0.5
	40	28.5	2.5
900	10	222	< 0.1
	15	181	< 0.1
	20	97	0.6
	25	37.5	1.9
	30	15.5	5.7
	40	14	9.2

The microstructural damage not only depends on the ageing time, but must also be related to local microstructural conditions, because composition differences at a local level may lead to unevenly distributions of the new generated phases and to slight difference in chemical composition of such particles. In agreement with the precipitation kinetics [13,14], which are strictly related to the steel's grade, the treatment times influence the intermetallic content and also the size of the precipitating particles. Therefore, the observed

impact toughness was strictly related to the phases volume fraction and also to particles dimensions and distribution inside the ferritic matrix. Furthermore, the mechanical properties of such phases can be affected by the composition of the parent phase, resulting, for instance, in a greatest hardening of the intermetallic particles in the Zeron®100 DSS due to the presence of W, which can promote their rupture.

The amounts of the detected secondary phases are reported in Tables 2.8 and 2.9, but their dimensions and distribution cannot be considered homogeneous. This was evident in those specimens treated at the same time-temperature conditions which failed at different impact energy values. Besides the distribution of such phases, by increasing the aging time the particles dimensions also increased, promoting the embrittling effect.

Table 2.9 – Treatments, toughness and precipitates amount for Zeron®100 SDSS.

Ageing temperature [°C]	Ageing time [min]	Absorbed energy [J]	Secondary phases [%]
	5	~300	not detected
	8	281	<0.1
850	10	138	0.5
	15	26.5	6.2
	25	4.2	15.3
	3	>300	not present
	5	>300	not present
900	8	55	2.3
	10	50	2.5
	15	11.2	9.5
	3	~300	not detected
	5	237	<0.1
950	8	105	1
	15	10.2	11.9
	25	4.2	15.4

Impact toughness of treated DSS

In the as-received conditions, the room temperature impact toughness was very high in both the steels and, as expected, was greater for Zeron®100 (about 330 J) than for SAF

2205 (about 240 J). The enhanced impact properties of the former DSS can obviously be attributed to the higher alloying element content, which promotes the mechanical strengthening of the phases.

The ageing treatments caused the secondary phases precipitations, leading to a worsening of the impact toughness responses. For each time-temperature condition, the average toughness values are reported in Tables 2.8 and 2.9, while the impact energy values as a function of the content in intermetallic phases are plotted in Fig. 2.25. The effect of the secondary phases is clearly evident starting from 0.5% of the volume fraction, corresponding to the most drastic reductions in impact toughness. The absorbed energy was reduced by more than 50% in both the steels, underlining the severe detrimental effect of these phases, while a further reduction was registered at 1–1.5% of secondary phases, and over the 2% volume fraction a great deterioration in toughness was again observed. In this latter case, small entities of plastic deformations were enough to cause a prevailing brittle fracture mechanism. The relation between impact energy and volume fraction of secondary phases is clearly evident (Fig. 2.25); a very low content was enough to produce very dangerous effects and, by increasing the precipitates amounts, the fracture mechanism showed an ever more prominent brittle behaviour until, for 6–8% of the volume fraction (depending on the considered grade), the ductile component was totally absent.
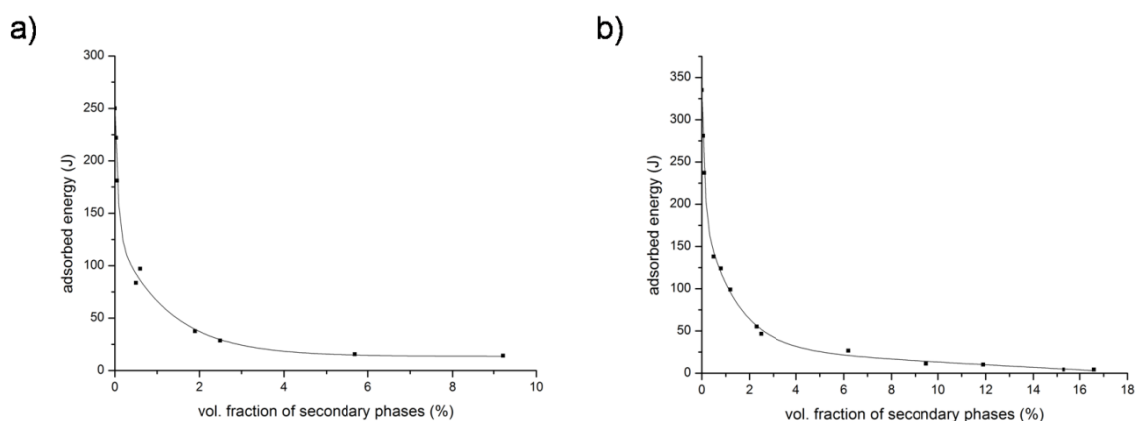

Fig. 2.25 – Effect of intermetallic phases on impact energy reduction: a) 2205 and b) Zeron®100.

As can be seen from Table 2.9, some Zeron®100 SDSS specimens were not completely broken and the registered absorbed impact energies were >300 J (*i.e.* the available energy was totally absorbed by the samples without causing the complete rupture). In these samples the fracture was completely ductile and no secondary phases were detected. A

completely ductile behaviour was also observed in some 2205 DSS specimens aged for the shortest times. In both cases the heat treatments were not sufficient to allow the precipitation of secondary phases.
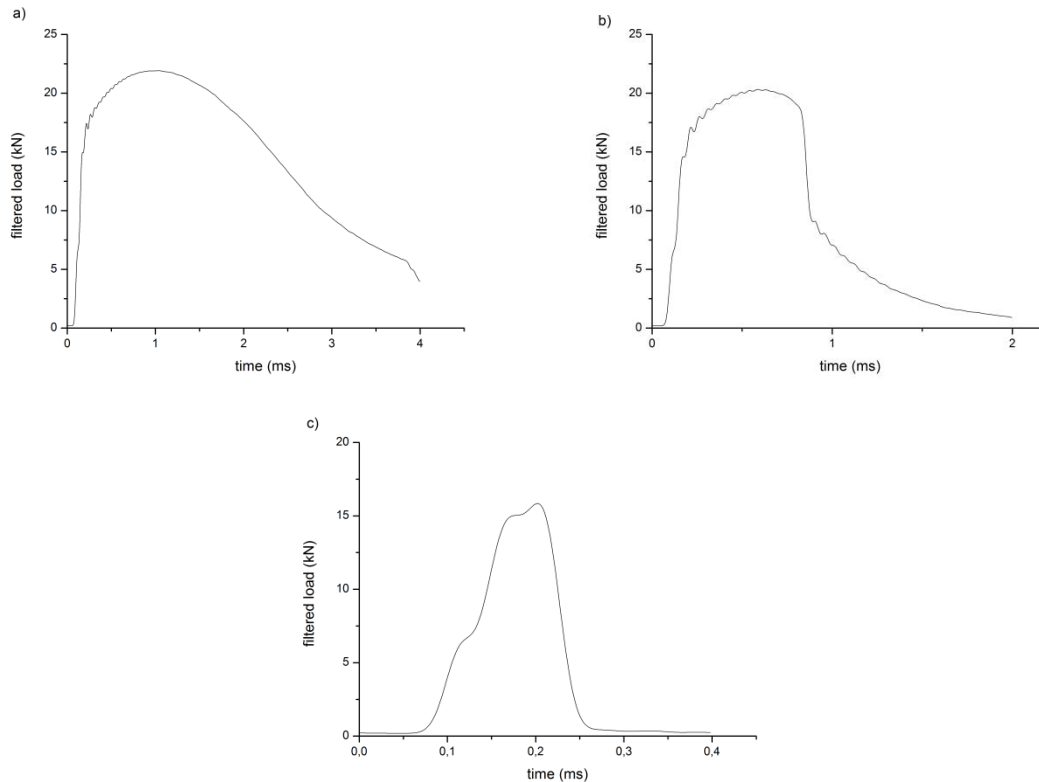

Fig. 2.26 – Load curves of 2205 DSS specimens: a) impact energy >150 J (780°C for 20 min), b) impact energy 50-150 J (900°C for 20 min) and c) impact energy <50 J (900°C for 40 min).

The obtained results were suitable to define a subdivision of the energy plots reported in Fig. 2.25 on the basis of the content in intermetallic phases and the corresponding impact behaviour. The first region comprehends those specimens with an intermetallic amounts lower than 0.5%, while to the third one pertain those samples in which the secondary phases overcomes the 1–2%; the second region is a transient one which lies at intermediate values between the first and the third and whose boundaries depend on the considered grade. Each region is characterized by the similarity of the load curves obtained from the impact test, while different shapes of these curves correspond to different fracture behaviours (Figs. 2.26 and 2.27). It is important to note that the boundaries between the three regions are not well defined and the materials exhibited a transition from the completely ductile to completely brittle fracture mechanism.

In the materials pertaining to the first region, with an intermetallics content <0.5%, the dynamic yieldings were about 15 kN for 2205 DSS and 20 kN for Zeron®100 SDSS, while the absorbed energies were >100 J and >150 J, respectively (Figs. 2.26a and 2.27a). After the yielding, the applied loads increased, owing to the strain-hardening, the fractures nucleated in relation to the maximum loads and the following decreasing can be associated to stable crack propagations, due to the ductile mechanism. A small amounts of secondary phases, identified as mainly χ particles, was detected. In this region, an increasing of the intermetallics content caused a progressively change in the curve slope after the maximum load and a reduction of the fracture propagation time.
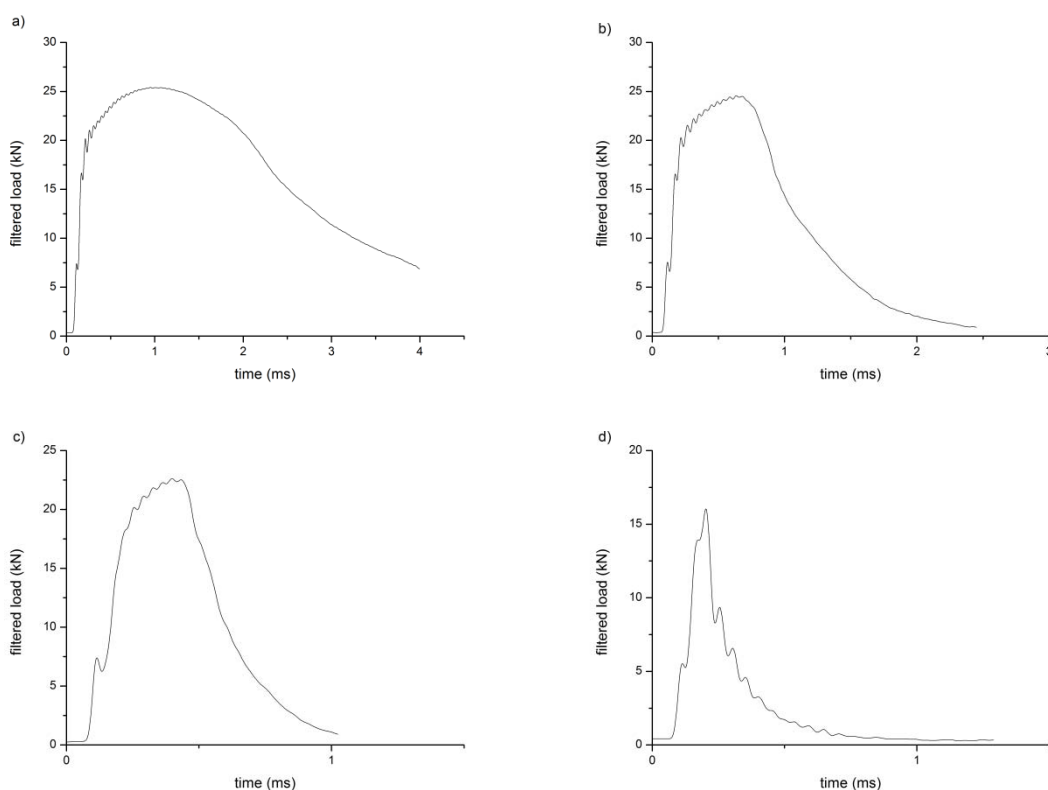

Fig. 2.27 – Load curves of Zeron®100 SDSS specimens: a) impact energy >150 J (850°C for 8 min), b) impact energy 50-150 J (950°C for 8 min), c) impact energy <50 J (900°C for 8 min) and d) impact energy <50 J (900°C for 15 min).

The second region includes the samples with an intermetallics amount of 0.5–1% for 2205 DSS and 0.5–2% for Zeron®100 SDSS, and for which the absorbed energies were in the range 50–150 J. In these specimens the fractures were not completely ductile and the brittle component started to manifest itself. The dynamic yieldings remained almost unchanged for both the steels (Figs. 2.26b and 2.27b) but, after an initial stable crack

propagation, the brittle mechanism took place, causing a changing in curves slope and reducing both the absorbed energies and the propagation times. However, depending on the considered grade, the fracture behaviours were different. The reduction in impact toughness, from the completely ductile mechanism to the prevailing brittle behaviour, was well marked in SAF 2205 (Fig. 2.26b), while in Zeron®100 the transition was more gradual (Fig. 2.27b). In the former case, an abrupt drop in the curve slope was observed (Fig. 2.26b) that can be associated to a higher instability of the crack propagation. Nevertheless, in both cases the greater content in secondary phases strictly affected the fracture behaviour and the brittle mechanism was promoted when the phases amount increased. The hard intermetallics, which in this region were identified as both σ- and χ-phases, preferentially broke, causing a reduction of the average crack-free-paths and facilitating the crack propagation into the adjacent ferritic phase.

In the third region, the materials were characterized by a secondary phases content which overcame 1–2%, the related absorbed energies were <50 J and the situation was again different depending on the considered grade. After the dynamic yielding, which still occurred at 15 kN (Fig. 2.26c), the 2205 DSS exhibited an consistent drop in absorbed energy and the fracture propagation was completely brittle. On the contrary, the Zeron®100 SDSS showed a progressive changing in fracture behaviour. In this latter steel, even if the fracture was prevailingly brittle, the ductile behaviour was initially not negligible (Fig. 2.27c) and, by increasing the intermetallic content, the brittle component was increasingly pronounced. For Zeron®100 SDSS, the fracture was initially mixed and the rupture only occurred for shorter times with a general yielding still at 20 kN. Greater intermetallics contents reduced the fracture time and the yielding value until the fracture became completely brittle (Fig. 2.27d).

In all the materials pertaining to the third region, a small amount of plastic deformation at the notch root was enough to reach the critical brittle fracture conditions, the fracture propagation was very rapid and the absorbed energies were low. The intermetallics allowed an easy crack nucleation and contributed to determine an energy-favoured path for the crack propagation. For secondary phases volume fractions greater than 6–8% the fracture behaviour was completely brittle and no plastic deformations at the notch roots were observed in both the steels. The results showed that when the phases amount was below the 2–3%, the microstructural damage had no influence on the dynamic yielding and

on the overall yielding behaviour, even though it occurred for shorter times and the following strain-hardening contribution was smaller.

Fractography

Deformation and fracture behaviour were strongly influenced by the secondary phases and an examination of both fracture morphology and microstructure close to the notch root can reveal the distinguishing features.
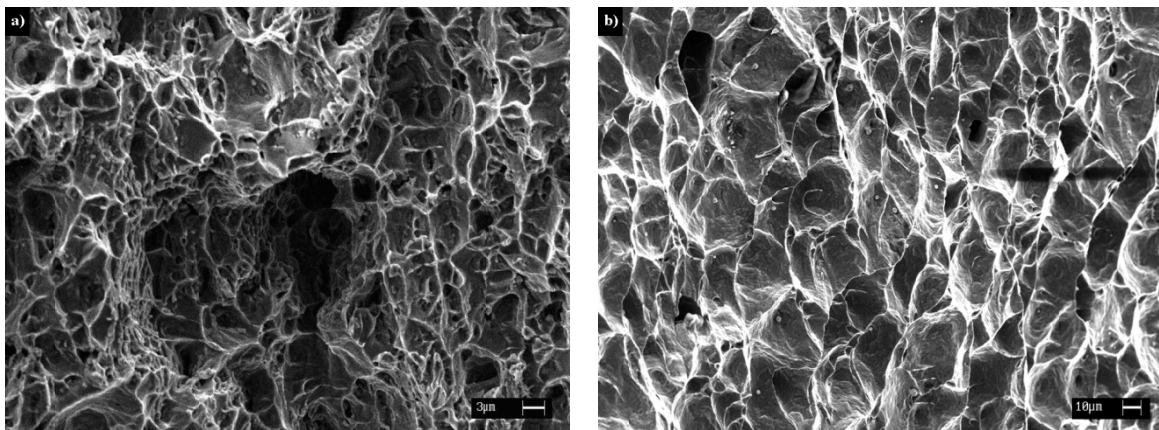

Fig. 2.28 – Samples failed in the first region (ductile behaviour). Fracture surfaces (SEM-SE): a) 2205 (high magnification) and b) Zeron®100 (low magnification).
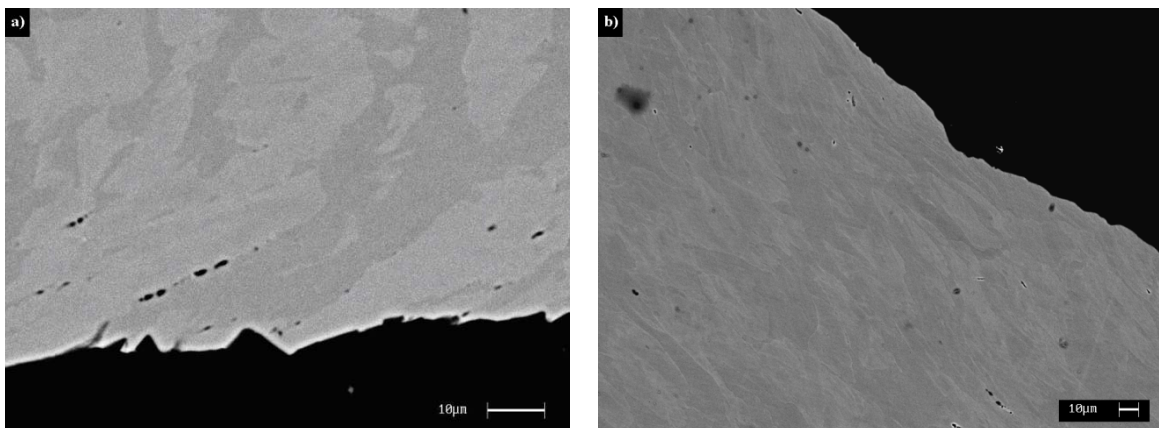

Fig. 2.29 – Samples failed in the first region. Grain shearing near the notch root (SEM-BSE): a) 2205 and b) Zeron®100.

In the first region the materials failed in a completely ductile manner after a large plastic deformation and the fracture morphology showed the characteristic dimpled surface (Fig. 2.28). In both the steels, the low volume fraction of secondary phases was not enough to promote the brittle fracture and the intermetallics acted as nucleation sites for the ductile

rupture. The presence of a large plastic deformation was confirmed by the grain shearing close to the notch root (Fig. 2-29). Nevertheless, the presence of some micro-voids at the triple points and at the grain boundaries near the fracture surface can be attributed to the original presence of small particles which were broken during the impact.

On the contrary, the materials pertaining to the third region failed in a brittle manner. For both the steels, although the fracture was completely brittle when the secondary phase's amounts reached the 6–8%, the approaching to the brittle rupture was different. In the 2205 DSS (Fig. 2.30), the 2% of volume fraction was enough to cause the brittle failure and the fracture surfaces were characterized by the presence of quasi-cleavage facets. Moreover, a high density of micro-cracks was detected at the notch root, which were formed before the occurrence of the final fracture and were oriented parallel to the main crack. In the Zeron®100 SDSS (Fig. 2.31), the same behaviour was observed in the samples with a secondary phases amount >4% and where cleavage and quasi-cleavage facets were detected. On the contrary, in the range 1.5–4% the fracture of the Zeron®100 was mainly mixed, the dynamic yielding gradually decreased and the ductile component gradually disappeared. In the third region, a small plastic deformation was enough to reach the critical conditions for the brittle fracture. The density of such micro-cracks was large and their size was also big, owing to the large content of the secondary phases which allowed an easier nucleation of the brittle fracture.
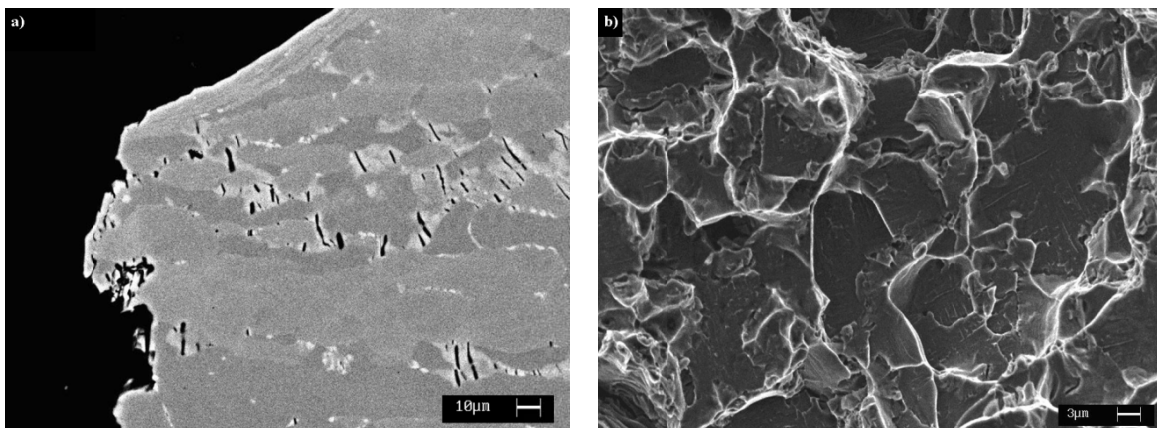

Fig. 2.30 – 2205 DSS failed in the third region: a) micro-cracks close to the notch root (SEM-BSE) and b) fracture surface (SEM-SE).

Finally, the materials in the second region were characterized by a large plastic deformation before reaching the critical conditions at the notch root, density and size of the micro-cracks are intermediate between the first and the third region and lower amounts of

embritteling secondary phases were detected. This is a transient region and the behaviour of the material changed when considering the upper and the lower energy limits, showing an increasingly pronounced brittle fracture mechanism and an ever smaller plastic deformation as the intermetallic amount increased. For both the steels, the fracture was mixed and the morphology exhibited the characteristic features of both brittle and ductile fracture, shifting toward the first or the second depending on the precipitated secondary phases amount.
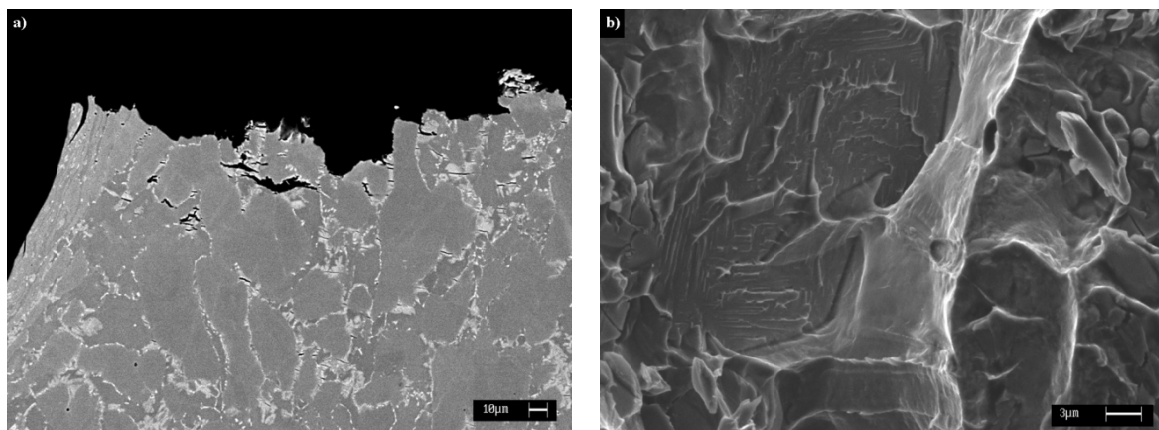

Fig. 2.31 – Zeron®100 SDSS failed in the third region (prevailing fragile behaviour): a) micro-cracks close to the notch root (SEM-BSE) and b) fracture surface (SEM-SE).

Regression analysis: iso-toughness surfaces

As previously reported, almost any time-temperature combination caused the precipitation of a certain amount of secondary phases, quantified through image-analysis procedure on the SEM micrographs, but which cannot be considered uniform within the samples. The intermetallics amounts in the previous Tables 2.8 and 2.9 are, in fact, referred to an average value of secondary phases.

The investigation on DSS impact toughness was also suitable for a regression analysis, considering the experiment as a factorial plan in which 3 replicates were carried out for each temperature-time combination. Temperatures and times of treatment can be considered as the two main factors, while the measured energy absorbed by the material during the impact is the response variable. A not negligible – and not controllable – factor is the distribution of precipitates inside the samples, which was not homogenous. Thus, depending on the position on the treated bar from which the impact sample was machined, different toughness responses were observed. Moreover, another not-controllable factor is

the original presence of defects in the samples, which can cause a more or less accentuated intrinsic defectiveness of the material and which can affect the registered impact toughness. It was therefore decided to merge the influence of the distribution and intrinsic defects of the to a "material covariate factor" by associating to each specimen a discrete value, depending on the measured toughness value and on its deviation from the most probably fair value, because basing on the average value would not be correct.

From the statistic test it was seen that the two main factors (time and temperature), their interaction and the "material covariate factor" were all highly significant against the toughness response; among these, the time appeared to be the most determining factor. The most interesting informations achieved from such analysis was given by the so-called contour plot (Fig. 2.32). This plot shows the time-temperature combinations at which the toughness value is maintained at a constant value, allowing the identification of such areas where the toughness is within an acceptable range. It then provides useful information about possible isothermal heat treatment conditions which can ensure a toughness value of 50 J, the minimum toughness value usually required in many practical applications. However, it must be notice that, besides this kind of approach can to give an assessment of the expected toughness resistance after the heat treatments, it does not takes into account that different microstructures can lead to different responses and thus the obtainable information are only of qualitative character.
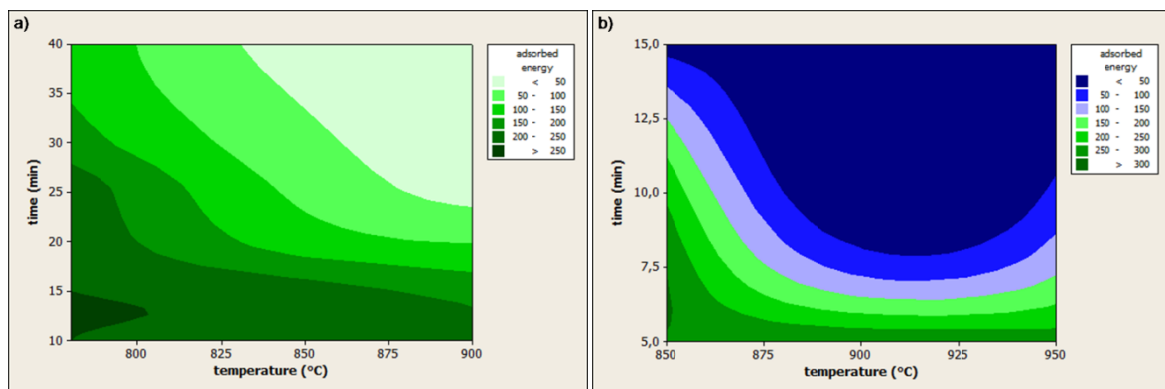

Fig. 2.32 – Contour plots of iso-toughness surfaces: a) 2205 DSS and b) Zeron®100 SDSS.

Fracture Tuoghness

The obtained data were suitable in order to get an estimation of the fracture toughness (K_{mat}) of the steels for a (partial) structural integrity assessment. Although the tests were

not carried out with a direct dependence from the temperature (*i.e.* the tests were all performed at room temperature after the aging treatments), the material showed a ductile-to-brittle transition that is somehow possible to relate to the transition obtained by decreasing the testing temperature. In fact, even though the shape of the curves was not similar to the transition temperature trend – which is sigmoidal – the material exhibited a gradual decreasing of the impact toughness due to the increasing content of secondary phases that can be associated to the decreasing in ductility when the temperature is lowered. Thus, it is possible to relate the steel behaviour to the so called *Master Curve Approach* where the secondary phases, randomly distributed inside the microstructure, can be associated to low toughness regions as in the "weakest links" hypothesis [39].

For the ductile regime (first region) the correlation between the Charpy data (KV) and the fracture toughness is given by [40], resulting in a conservative prediction.

$$K_{mat} = (0.54) \cdot KV + 55 \tag{2.1}$$

Although the previous equation is recommended when the Charpy energy is greater than 60 J, it is however not usable for the transition regime (second region) in the two DSS – for which the transition occurred in the range 160–50 J – because to the presence of the brittle mechanism that begins to manifest itself in an increasing extent. Furthermore, the so called *Master Curve Equation*, suitable for the transition regime, is not even usable due to the fact that a real transition temperature does not exist in the performed experimentation (the method needs the definition of the *Charpy 27 J temperature*) and the equation should be rearranged for the specific case.

Finally, for the brittle regime (third region) the correlation could be given by [40]:

$$K_{mat25} = 12 \cdot \sqrt{KV} \tag{2.2}$$

$$K_{mat} = \left[(K_{mat25} - 20) \cdot \left(\frac{25}{B} \right)^{\frac{1}{4}} \right] + 20 \tag{2.3}$$

where the estimated fracture toughness of the material, *K_{mat25}*, must be corrected for the appropriate thickness *B*.

A note must be done on the *Charpy 27 J* critical impact toughness value: this value is relevant to material testing standards, which frequently require a minimum Charpy impact energy of 27 J. In [4] the TTT diagram for a SAF 2507 SDSS showing the curve corresponding to the 27 J impact toughness are reported. In the investigated SAF 2205 and Zeron®100, a full analysis on the effect of the isothermal treatments on the impact toughness in the whole temperature range 700–1000°C has not been done, but is it possible to say something about the time-temperature combinations which allowed a significant secondary phases amount and which leaded to an impact toughness value of about 27 J. From the impact test results, it can be seen that for Zeron®100 SDSS the critical value of secondary phases is reached after aging the material at 850°C for 15 minutes, while for the others two temperatures it is only possible to say that the critical value is reached after 10–15 minutes at 900°C and after 8–15 minutes at 950°C. Similar conclusions can be derived for the 2205 DSS, in which the critical value of secondary phases was reached after ageing the material at 850°C for 40 minutes and at 900°C for 25–30 minutes. The higher content of alloying elements in Zeron®100 makes the steel more prone to secondary phases precipitation, lowering the treatment times for which the critical values are reached.

Concluding remarks

Small amounts of secondary phases were enough to severely compromise the toughness of the materials, which instead was very high in the as-received conditions. The impact testing results showed that for about 0.5% of intermetallic phases the impact toughness was reduced by over 50% in both the steels and for contents <0.5% the main effect was a reduction of the absorbed energy by facilitating the ductile fracture. Up to 1–1.5% of volume fraction the fracture was mixed and for greater amounts the fracture was mainly brittle. For greater volume fractions of intermetallics the impact toughness was further reduced and small entities of plastic deformations were enough to cause a prevailing brittle fracture mechanism until, for 6÷8% of volume fraction, the ductile component was totally absent.

The plastic deformation caused the secondary phases breakage with the formation of a high density of micro-cracks, inducing an easy nucleation and a fast propagation of the final fracture crack. Both σ- and χ-phase was found to be responsible for the embritteling

of the examined DSS and the observed impact toughness can mainly be addressed to phases amount, dimensions and distribution in the Duplex microstructure.

2.3.2. Transition Temperature

At low temperatures some metals, notably steels, become brittle and, since they are ductile at room temperature, this transition to brittle cleavage behaviour has led to several engineering catastrophes. In general, brittle cleavage can occur in metals with BCC and HCP crystal structures under appropriate conditions, while in FCC materials it does not. The most important factors linking these three different structures are the Peierls-Nabarro stress and the way the yield stress varies with temperature.

Generally, in FCC metals, the force required to move dislocations is not strongly temperature-dependant, therefore dislocation movement remains high even at low temperatures and the material remains relatively ductile. On the contrary, the yield stress of BCC materials is markedly affected by temperature, causing a change in the failure mode from plastic flow at high temperature (upper shelf) to brittle fracture at low temperature (lower shelf), while the intermediate region is characterized by the presence in different proportion of both mechanisms (ductile-to-brittle transition or DBT). However, some FCC high-nitrogen austenitic steels exhibit DBT because the addition of N can cause a strong temperature dependence of the yield strength [41]. Conversely, the presence of a suitable amount of Cu allows for a greater austenite stability which improves the low-temperature toughness due to an increasing of the stacking fault energy of the phase [41]. DSS and especially SDSS contain significant percentages of N (up to 0.3%) and sometimes Cu. Nitrogen is fundamental for the γ-phase stabilization, it allows the interstitial solid-solution mechanical strengthening at room temperature and improves the corrosion resistance, while copper is added to improve the corrosion resistance in sulphuric environments and to minimize the erosion damage. However, despite its beneficial aspects, the high nitrogen content in these steels can negatively affect the austenite behaviour at the lowest temperatures, while the presence of a suitable amount of copper can in some extent counteract this effect.

In two-phase alloys the crack nucleation is easy to occur by piling up dislocations at grain boundaries and the presence of secondary phases inside the matrix increases the

number of the interfaces, leading to a worsening the mechanical behaviour. Since χ- and σ-phases are hard structural discontinuities, their presence causes a stress intensification in correspondence to them, making these particles the preferential initiation sites for the cracks and reducing the overall impact properties. Thus, in the study of the DBT behaviour on DSS, the situation is aggravated when secondary phases are present, and the structural stiffening of lattice due to temperature decreasing is further accentuated by localized stress intensifications phenomena caused by secondary phases.
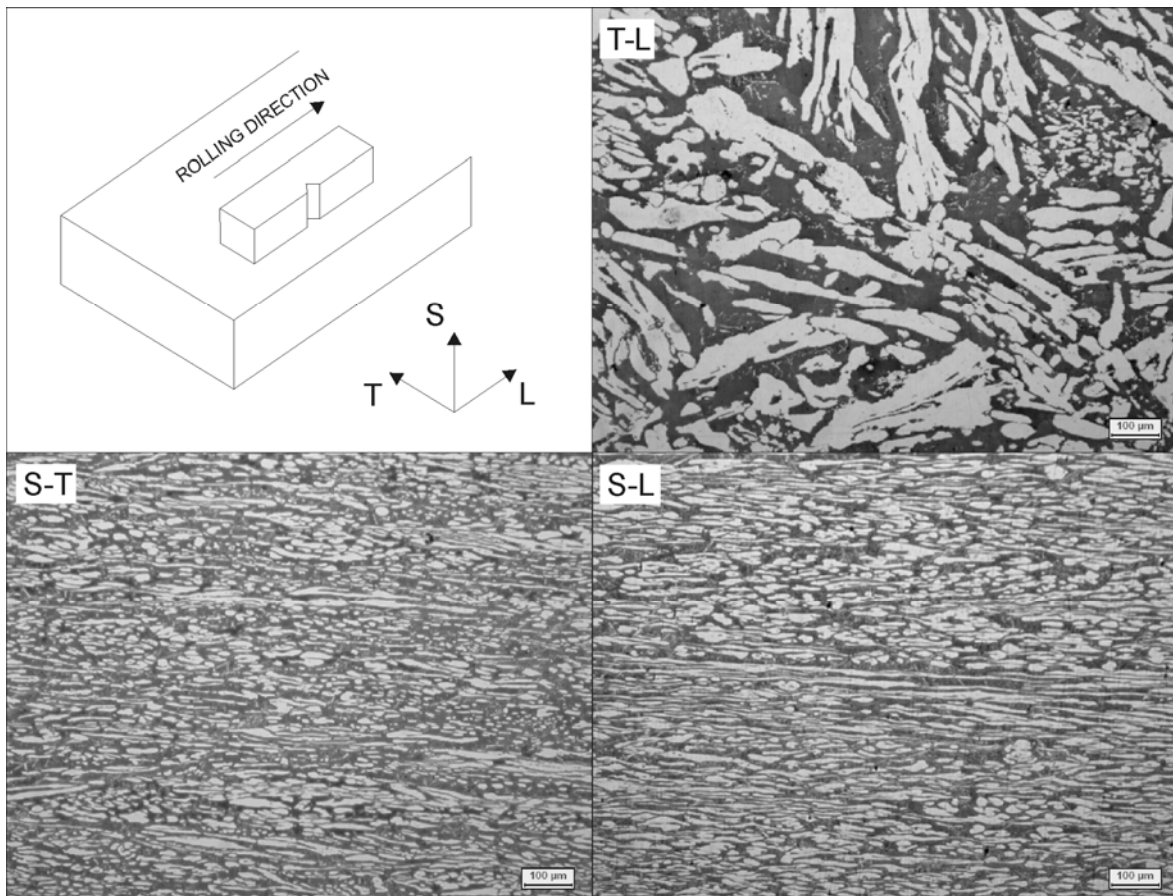

Fig. 2.33 – Orientation and microstructure of the tested specimens (OM, Beraha's reagent): ferrite (dark) and austenite (white).

2.3.2.1. Ductile-to-Brittle Transition in a Zeron®100 SDSS

In this paragraph, the impact toughness of the Zeron®100 SDSS (chemical composition in Table 2.7) is presented by considering two different microstructural conditions. The tests were performed on the material in the as-received state (hereinafter called "wrought") and after an isothermal heat treatment of 8 minutes at 850°C [34], aimed to damage the

microstructure by allowing the precipitation of a slight amount of intermetallic phases (< 0.5%). From what was reported in Paragraph 1.2.4.4, this amount of secondary phases strongly affected the toughness properties of the material, leading to a decreasing of the impact toughness by over 50% at room temperature.

The impact energy was evaluated on the T-L direction of the wrought material plate (Fig. 2.33), initially in a temperature range from -100°C to 20°C and then followed by a further test at -120°C only on the wrought material, in order to obtain a better description of the transition. The impact tests were carried out by means of an automatic impact pendulum, with an available energy of 450 J, according to ASTM E23 standards. Moreover, for all the tested specimens the lateral expansion was also evaluated, by measuring the width of the specimens opposite to the V-notch before and after the tests, in according to ASTM A370 standards, in order to achieve a further parameter to characterize the plastic deformation of the samples.
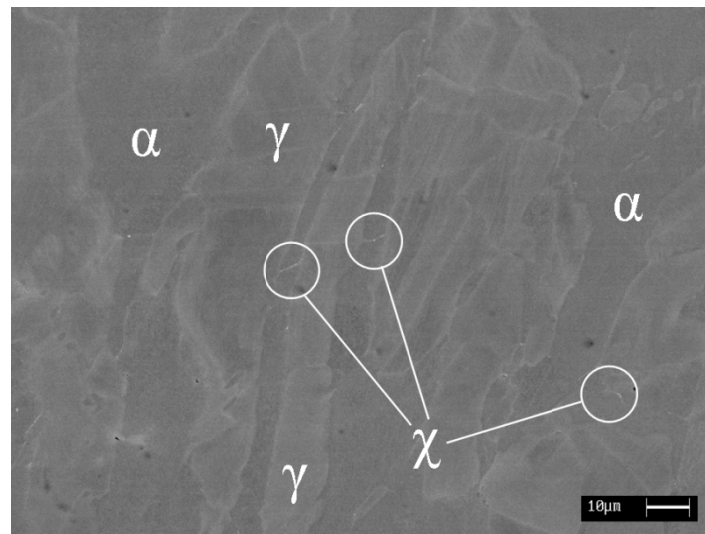

Fig. 2.34 – Microstructure of the aged sample (SEM-BSE):
ferrite (α), austenite (γ) and χ-phase.

Microstructure

The as-received material was composed by almost equal volumes of phase fraction (about 48% austenite and 52% ferrite) and no secondary phases were detected. The chosen experimental temperature was within the critical temperature range and the isothermal heat treatment caused the eutectoidic decomposition of the ferritic matrix, with the formation of secondary phases. As expected, the precipitation in the treated sample was very slight and

the soaking time mainly allowed for the formation of χ-phase. As can be seen in Fig. 2.34, the secondary phases were mainly χ particles located at the grain boundaries, even though some σ islands were also observed. The χ particles sizes were in the order of few micrometers or less, while the rare σ particles were little coarser, and the evaluated total amount was estimated to be lesser than 0.5%, even though in these conditions an accurate quantification is not simple.

Ductile-to-Brittle Transition

The presence of both BCC ferrite and FCC austenite imply that the resulting transition curve for the tested steel may appear as a combination of the two different behaviours pertaining to the single-phase materials and the characteristic "S-shaped" curve was expected to be quite smoothed. Due to the discrete character of the test, a mathematical model is required to describe the material behaviour and the obtained data were then fitted by using the hyperbolic tangent function (*tanh*) [42]:

$$Y = A + B \cdot tanh\left[\frac{(T - T_0)}{C}\right] \tag{2.4}$$

where Y is the KV energy, T is the test temperature and A, B, T_0 and C are adjustable parameters estimated by regression procedure. T_0 is a location parameter which provides the inflection point of the curve and, in the present work, it was considered to be the transition temperature (T_{trans}), A+B corresponds to the upper shelf energy (USE) and A-B to the lower shelf energy (LSE).

Table 2.10 – Results of *tanh* fitting and extrapolated data.

Condition	A	B	C	T_0 (T_{TRANS})	USE	χ^2	R^2	T_{27J}
wrought	180.75	153.55	53.36	-73.23	334.30	1.20	0.99	-158
aged	143.27	113.03	44.36	-49.82	256.30	2.58	0.97	-120

Note: T_{TRANS} from regression analysis [42] and T_{27J} from extrapolation [40].

The average impact test values and the *tanh* fittings are plotted in Fig. 2.35, while the results of the regression analyses are reported in Table 2.10 and will be discussed later. It is evident that the two materials did not reach the completely brittle fracture conditions in

the chosen temperature range and, on the contrary, the wrought samples exhibited a relative good impact toughness down to -100°C. Only for the wrought material, a further test at -120°C was performed and for both the materials the completion of the transition curve was obtained by the extrapolation of the critical value T_{27J}, using the empirical relations given in [40].
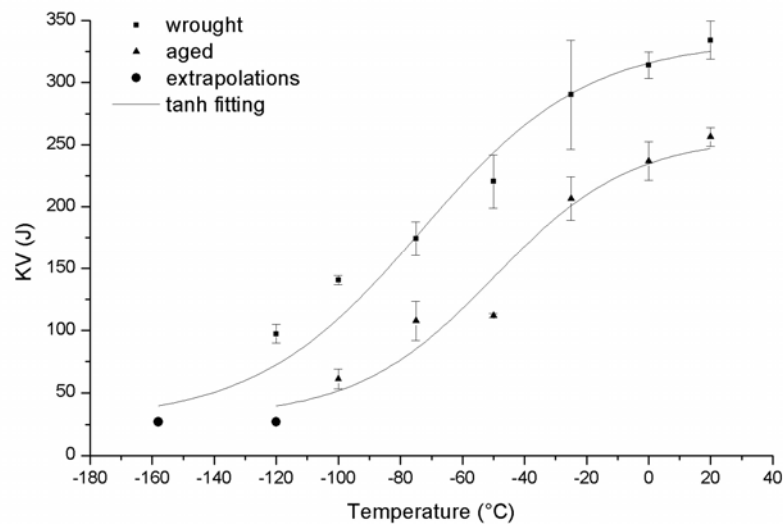

Fig. 2.35 – Transition curves of the tested materials (*tanh* fitting).

As can be seen from the plot, the *tanh* fitting is a good representation of the materials behaviour as the temperature decreases and, as expected, the curves do not evidence a drastic drop in toughness in the transition region. This behaviour can obviously be ascribed to the presence of the FCC austenitic phase, which retards the cleavage fracture of the material.

The Charpy impact toughness at room temperature in the wrought samples was very high (about 335 J), but a slight precipitation of secondary phases affected the toughness behaviour by lowering the absorbed energy of about 80 J. It is interesting to note that this difference in toughness was almost constant for all the experimental temperature range, and the shape of the two transition curves highlight a shifting of the wrought material behaviour toward lower toughness values and higher temperatures, especially in the upper shelf region. Thus, it is reasonable to assume that the secondary phases only acted as crack

initiation sites, while the plastic deformation behaviour was determined by the Duplex matrix and remained similar in both the examined materials, as reported in [43].

The *tanh* fitting is widely used to describe the DBT of steels, especially for nuclear pressure vessel subjected to neutron irradiation, but no data concerning the regression coefficients on DSS are available in literature. However, if compared to the 2205 DSS [44], the Zeron®100 SDSS exhibited a better overall toughness response and the observed impact toughness reduction in the transition region was more gradual. The estimated transition temperature was substantially lower and the brittle fracture took place for more severe temperature conditions, underlining the enhanced properties of this steel achieved by the addition of a major content of alloying elements. Moreover, a comparison with the 2507 SDSS [45], points out again a better response in the considered temperature range, which can be probably ascribed to a greater content of copper and to the presence of tungsten in solid solution.
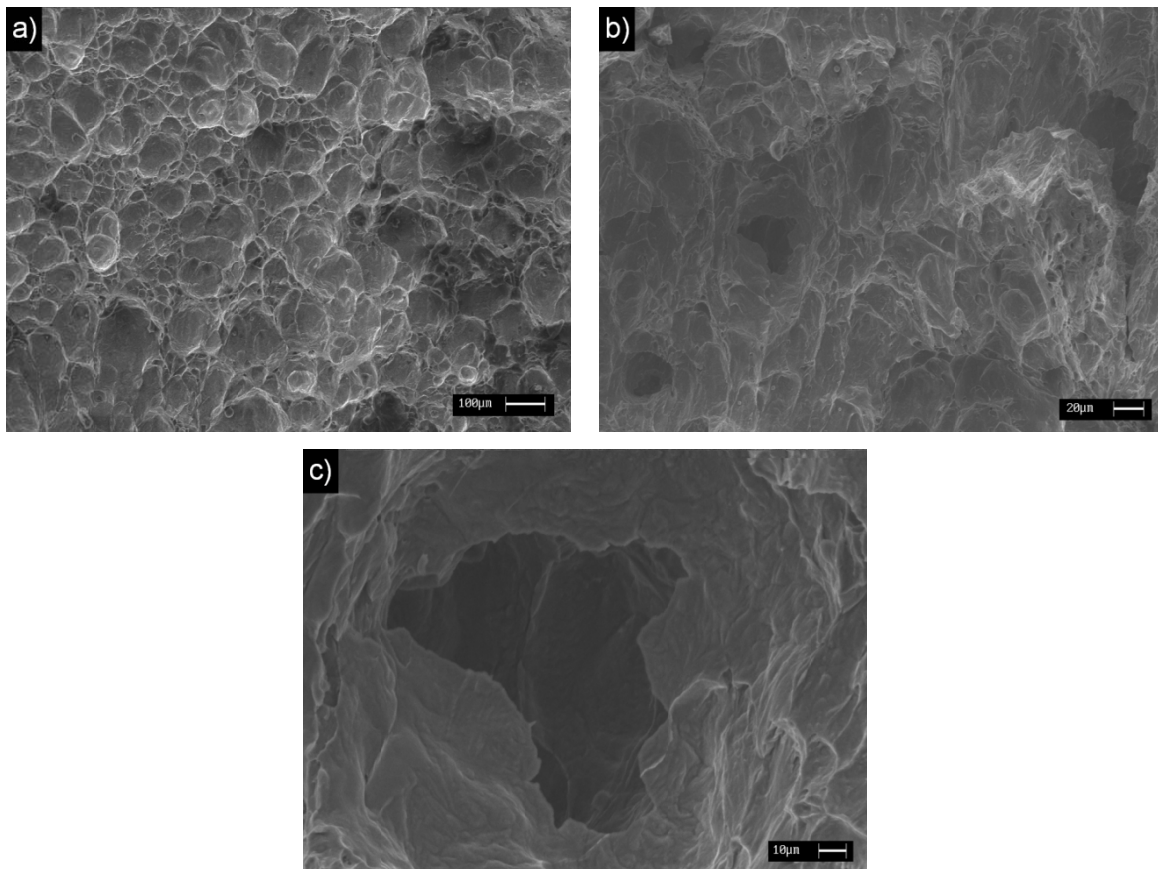

Fig. 2.36 – Fracture surfaces at 20°C (SEM-SE): a) wrought material, b) aged material and c) detail of (b).

Fracture Behaviour

At room temperature, the wrought material failed in a completely ductile manner, the fracture surfaces had the typical fibrous character and the fracture morphology showed the typical dimpled surface (Fig. 2.36a). In the aged material, although at room temperature the ductile mechanism was the prevailing one, the presence of the secondary phases lowered the absorbed energy, enhancing the brittle cleavage and allowing the reduction of the cracks free-paths. As can be seen from Fig. 2.36b – taken from the centre of fracture surface – the intermetallic sites are clearly visible, although some of them could be attributed to pre-existing cavities, and are considered responsible for the formation of the quasi-cleavage micro-facets in their vicinity (see detail in Fig. 2.36c). However, in both cases the plastic deformation in correspondence of the notch root was very high (Fig. 2.37), even though in the aged material the microvoids coalescence was more pronounced, due to the secondary phase particles which acted as preferential nucleation sites. The presence of the intermetallics in the aged material clearly lowered the absorbed energy, but the specimens still retained an appreciable toughness.
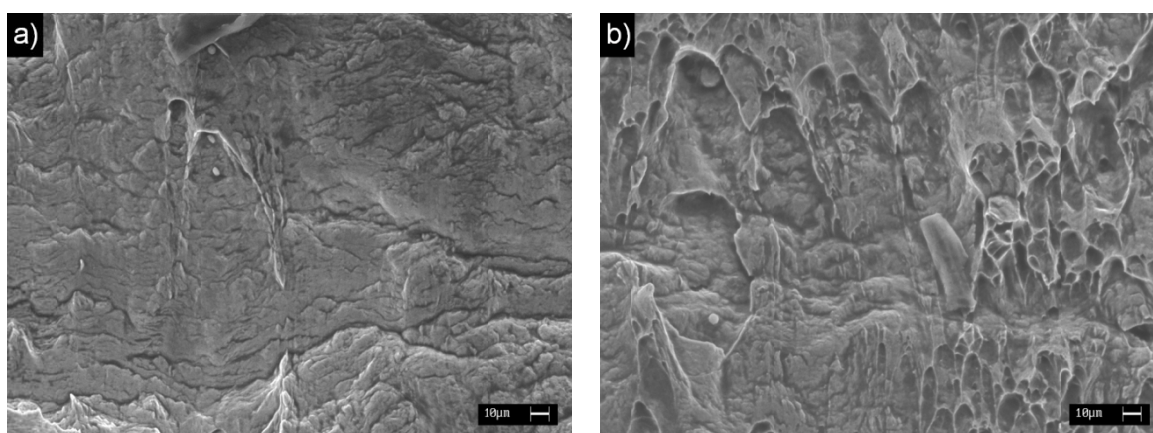

Fig. 2.37 – SEM-SE images of the notch root at 20°C: a) wrought material and b) aged material.

The macroscopic analysis of the fracture surfaces (Fig. 2.38) revealed the distinguishing features of the fractures associated to temperature decreasing. By coupling the observation with a microstructural investigation and considering the obtained impact toughness values, it was possible to assign the boundaries to the both shelves (upper and lower) and thus define the temperature range associated to the transition region. From the available data, it is reasonable to assume that the transition began between 0°C and -25°C for the wrought material and at around 0°C for the aged one, when significantly extended macrocracks

appeared on the fracture surface and when the surface started to be substantially damaged. Secondary phases affected the steels behaviour by increasing the transition start temperature and by promoting the initiation of the brittle rupture, even if also in this case the fracture was prevailing ductile and the plastic deformation was still very high.
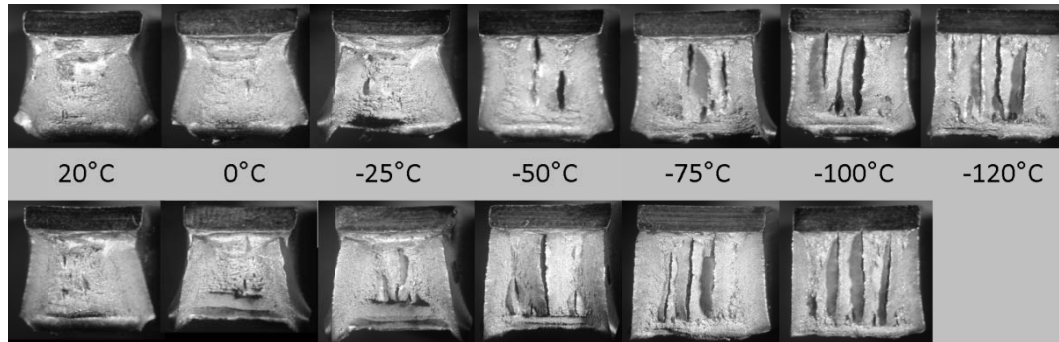

Fig. 2.38 – Fractures of wrought (up) and aged (down) materials.

In the wrought material, the fracture behaviour at -25°C (*i.e.* after the hypothesized transition beginning) was mainly ductile but, despite to the high recorded impact toughness value, the brittle fracture started to manifest itself and cleavage facets appeared both nearby and in correspondence of the macrocracks (Fig. 2.39a), even if a large plastic deformation at the notch root was still observed (Fig. 2.39b). Likewise, in the aged material the impact toughness at 0°C was also high, but the quasi-cleavage areas in the fracture surface were more extended than in the wrought one at the same temperature (Fig. 2.40a) and the microvoid coalescence at the notch root was more pronounced (Fig. 2.40b) due to the presence of the intermetallics.
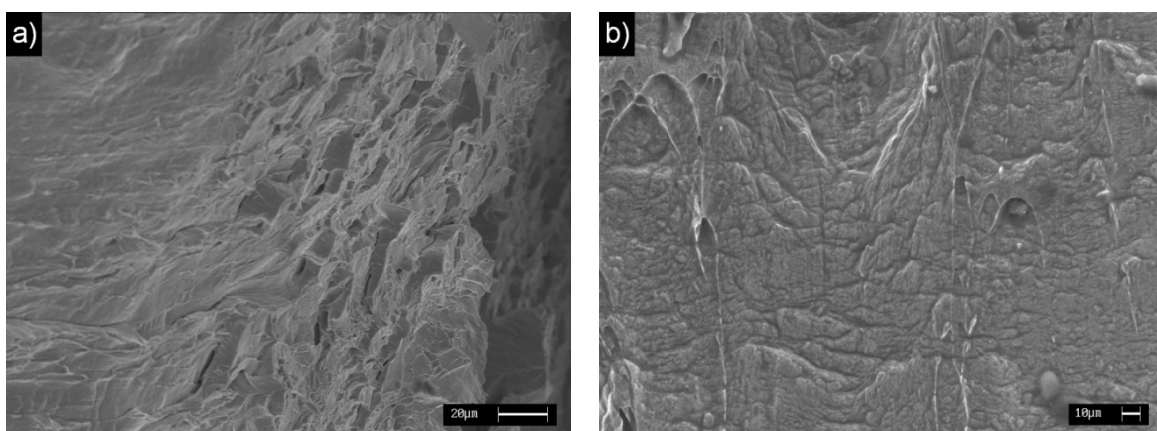

Fig. 2.39 – Wrought material failed at -25°C (SEM-SE): a) cleavage nearby a macrocrack and b) notch root.
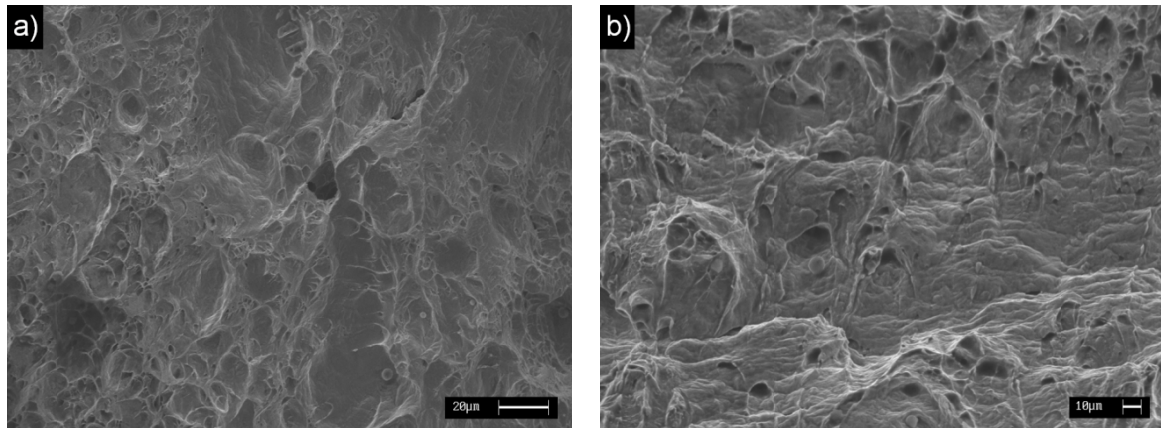
Fig. 2.40 – Aged material failed at 0°C (SEM-SE): a) cleavage in the lower part of the surface and b) notch root.

Lowering the temperature, a mixed ductile/brittle fracture mode was observed in both materials and the delamination phenomenon started to manifest itself, clearly visible from Fig. 2.38. The presence of these splits (or walls) is associated to an unstable crack propagation which occurred at the ferrite/austenite interfaces in a direction parallel to the rolling plane, along the most elongated grains [46]. Between two neighbouring walls, whose number increased as the temperature decreased, the material was failed in a mixed mode, depending on the testing temperature, while in correspondence of them the failure has occurred by decohesion of the crystallographic planes, with a completely brittle fracture mode.
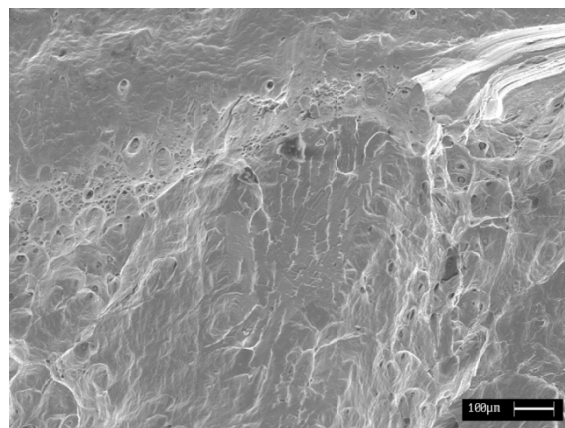

Fig. 2.41 – Cleavage in the wrought material failed
at -100°C (SEM-SE): notch root.

In the wrought material, at -75°C the firsts cleavage micro-facets were observed at the notch root and passing from -100°C to -120°C the extension of these areas was enhanced (Fig. 2.41). The same behaviour at the notch root was observed in the aged material by

passing from -75°C to -100°C, highlighting again the shifting of the transition behaviour – and therefore of the shelves – toward higher temperatures.

During the transition, cleavage facets with river patterns and tongues were increasingly pronounced in the whole fracture surface (Fig. 2.42), even though an appreciable ductile component was still observed. The plastic deformation at the notch root remained very high in both materials, but the presence of the secondary phases worsened the aged material, allowing an easier microvoid formation.
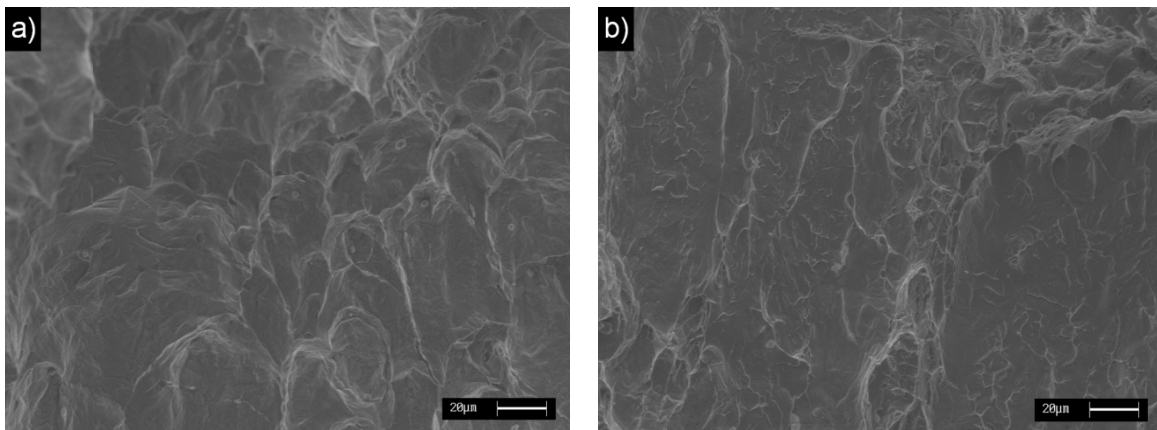

Fig. 2.42 – Fracture surfaces at -100°C (SEM-SE): a) wrought material and b) aged material.

As a result of the investigation, it is reasonable to assume as lower boundary for the transition a temperature lower than -120°C for the wrought material and nearby -100°C for the aged one. However, even though a significant toughness reduction has been observed in both materials, the completely brittle mechanism is not evident in none of them and several ductile areas was instead observed in the fracture surface, even at the lowest testing temperatures.

Extrapolations and Regression Analysis

In the experimental temperature range, none of the tested materials has reached the critical condition for the so-called *Charpy 27 J Temperature* (T_{27J}) and the completely brittle behaviour was not observed, even though a progressive drop in impact toughness was recorded. The definition of the T_{27J} value is relevant to material testing standards, which frequently require a minimum Charpy impact energy of 27 J and its determination can be useful for the different industrial applications. If the T_{27J} is not directly observed, it is possible to estimate it from Charpy values at other temperature by means of the empirical

relation given in [40], in which the impact toughness value of a single test is related to the difference between the relative test temperature T and the unknown T_{27J}. However, because of the wide range of shapes of the Charpy transition curves, this relation and the recommended values for the extrapolation are applicable only if the tests result in an impact energy range of 5-101 J. The obtained impact values were suitable for the application of this approach and the results are reported as circles in Fig. 2.35.

As previously reported, for the fitting of the Charpy impact data the hyperbolic tangent (*tanh*) model proposed by Oldfield [42] was taken into account. This model provides a fitting curve that is symmetric respect to the inflection point, it works well with large data sets and quite well with sparse but reasonably well distributed data. The parameters in the *tanh* function were adjusted by the Levenberg-Marquardt method, which is a standard technique used to solve non-linear least squares problems [47]. The chosen fitting function is, in fact, not linear in the parameters and thus a non-linear least squares method is required to improve the parameter values by an iterative procedure, in order to reduce the sum of the squares of the errors between the function and the measured data points. A more accurate representation of the material behaviour can be obtained if the method is improved by introducing a weighting of the observed values. The chosen weighting method was the so-called "instrumental" one, which considers if unequal errors have been introduced into the data by the measuring device, and for each observation it was defined as the reciprocal of the variance.

As expected, nominally identical specimens were failed with different Charpy impact energies at the same temperature. The variance is not constant from point to point in the whole temperature range and, due to the randomness, such distribution leads to a strong unequal weighting, forcing the curve to pass near the points with the smallest deviation from the mean value. Thus, the data were pooled after the fracture surfaces investigation in order to get a statistically accurate description of the transition. The presence of the secondary phases in the aged material suggested to separately consider the available data for the two materials because the variance of the mean values strongly depended on the microstructural conditions. For the pooling procedure, the three different regions – upper and lower shelves and transition region – were considered and an analysis of the variance (one-way ANOVA [48]) was carried out in order to assign a kind of "average variance" for

each region, while the boundaries of each region were chosen on the basis of the fractography observations.

In Table 2.10 the statistical parameters of Equation (2.4) are reported. Comparing the two regression curves, it is possible to note that the fitting of the data for the wrought material is better than for the aged one. The analysis of the residuals confirms the agreement of the transition curve estimation for the first case, while in the latter one the fit is not as well good, both in terms of reduced-χ^2 and adjusted-R^2. This difference can be explained considering that the mean impact toughness values in the aged material are more sparse, due to the fact that the precipitation of the secondary phases is not homogeneous in the entire microstructure. The σ- and χ-phase nucleation sites are randomly distributed, so there could be some areas with a higher density of secondary phases, which is closely related to the local composition of the parent phase and to the initial microstructure of the tested material.

Lateral Expansion and Plastic Deformation

The evaluation of the lateral expansion, measured on the opposite side of the notch in the broken specimens, identifies another parameter which can represent the toughness of the material. Indeed, it characterizes the amount of plastic deformation of the sample (*i.e.* the ductility of the material) at a macroscopical level and can be related to the strength properties of the material.
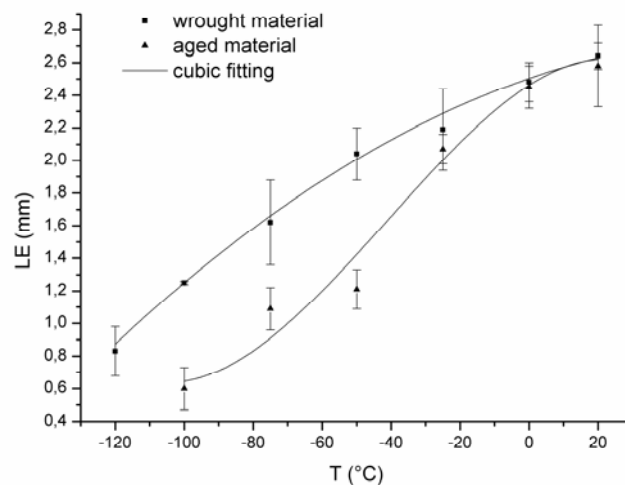

Fig. 2.43 – Lateral expansion (LE) of the specimens vs. testing temperature (T).

The graph in Fig. 2.43 shows the variation of the lateral expansion as function of the temperature and points out the combined effect of secondary phases and temperature on the material ductility when the temperature is lowered. As can be seen from the figure, down to -25°C the overall ductility of the aged material is not strongly influenced by the secondary phases, but can be instead considered comparable to that of the wrought samples. Only a reduction in absorbed energy was observed and the material was still satisfactory in terms of strength properties. Conversely, for temperatures below -25°C the registered drops in toughness and lateral expansion in the aged material were very marked and the material behaviour was highly worsened, due to the synergistic effect of secondary phases and temperature reduction. In the aged material, the presence of such discontinuities inside the matrix determined a reduction of the average crack-free-path which, combined with a microstructural stiffening caused by the low temperatures, leaded to a reduction of the overall deformability of the material, affecting the observed ductility. On the other hand, the worsening of the properties in the wrought material was more gradual in the entire experimental temperature range because the damage was only induced by the temperature decreasing.

Fig. 2.44 – SEM-BSE fracture surfaces close to the notch root: (a) wrought and (b) aged materials failed at 20°C.

Nevertheless, an examination of the microstructure close to the notch root confirmed that the plastic behaviour of the matrix at a fixed temperature can be considered the same in both the materials and the presence of the secondary phases didn't affect the plasticity at a microscopical level, which instead was only determined by the temperature reduction. As can be seen from Figs. 2.44 and 2.45, the plastic deformation of the two materials can be considered comparable, since was of a comparable entity, and only depended by the testing

temperature. The secondary phases influenced the aged material response by facilitating the cracks initiation and causing a reduction of the absorbed energy, while the subsequent propagation was fragmented due to the increasing of the embritteling sites.
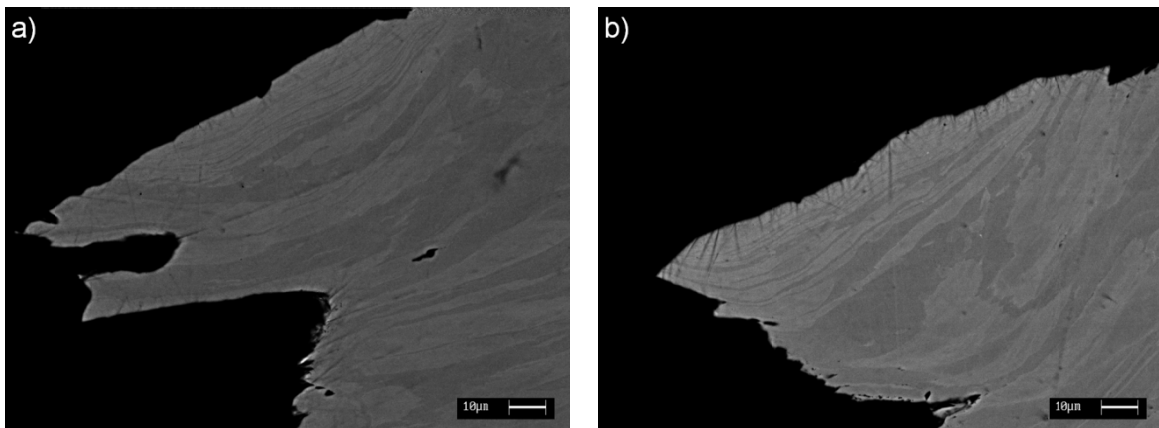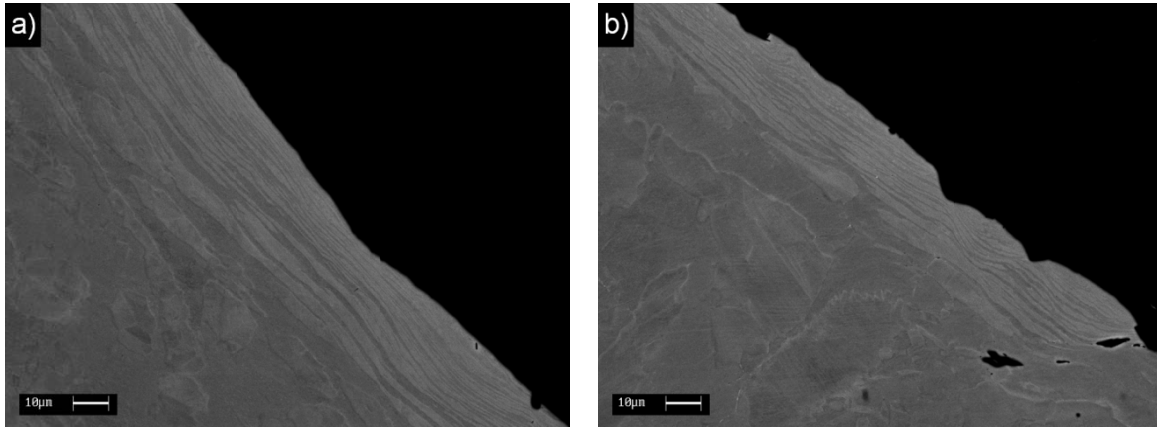

Fig. 2.45 – SEM-BSE fracture surfaces close to the notch root: (a) wrought and (b) aged materials failed at -100°C.

Furthermore, in both the materials, the formation of delamination walls considerably alter the observed ductility because avoided a complete expansion of the material. These walls were oriented in the same direction of the main crack (*i.e.* from the notch root to the opposite surface, see Fig. 2.38) and propagated inside the sample in a direction which was parallel to the rolling plane. Such delaminations caused a subdivision of the fracture surface allowing the formation of regions characterized by completely different fracture behaviours. As previously reported, the fracture inside the splits and in correspondence of them was brittle, while the areas between two consecutive walls retained a certain amount of ductility, depending on temperature. This deformation energy remained confined between the splits and cannot be unloaded in the entire sample cross-section, causing the reduction of the overall ductility. Thus, the overloading at which that areas were subjected altered the plastic behaviour of the material, making them more prone to the brittle failure. This fact was more evident in the aged material, where the areas between the walls exhibited more extended brittle regions, due to the presence of the intermetallics which promoted the brittle rupture.

Concluding remarks

The Zeron®100 SDSS provided a very high impact toughness at room temperature (about 335 J) and its behaviour in the transition region did not exhibit an abrupt drop. The

material in the wrought conditions consistently passed the Charpy test specification of 40 J minimum and 0,38 mm lateral expansion at -120°C [49] and, as a matter of fact, it showed more than twice of these values. The mechanical properties of this steel are improved if compared to the widely employed 2205 DSS and the similar grade 2507 DSS, the impact toughness behaviour was always better in the whole transition region and the transition temperature is considerably higher.

Nevertheless, a slight secondary phases precipitation (<0.5%) lowered the impact energy of about 80 J at room temperature and this difference in impact toughness can be consider almost constant within the whole transition region. The ductility of the aged material fell considerably for temperatures below -20°C, highlighting that the presence of the intermetallic phases acts as preferential cracks nucleation site and reduces the average crack-free-path, lowering the overall ductility, while the matrix plastic behaviour can be considered comparable to the wrought material and is strictly related to the reduction of temperature.

Any toughness requirement must be valid where intermetallic precipitates are present [50], thus, for this reason, the material in the aged conditions in not suitable for the normal applications and cannot be consider reliable for exercises in temperature ranges below zero.

REFERENCES

[1]   D. A. Porter, K. E. Easterling and M. Y. Sherif. *Phase transformations in metals and alloys*. CRC Press, Taylor&Francis Group, USA (2009).

[2]   B. Sundman, B. Jansson and J. O. Anderson. *CALPHAD* 9 (1985).

[3]   L. Kaufman and H Bernstein. *Computer calculation of phase diagrams*. Man. Labs. Inc. Cambridge, Mass/Academic Press, New York (1970).

[4]   J. O. Nilsson. *Mater Sci Tech Ser* 8 (1992) 685.

[5]   J. O. Nilsson, G. Chai. Proc. Conf. *Duplex 2007 International Conference & Expo*. Grado, Italy (2007).

[6]   J. O. Nilsson, P. Kangas, T. Karlsson and A. Wilson. *Metall Mater Trans* A 31A (2000) 35.

[7]   I. Calliari, M. Breda, M. Pellizzari and E. Ramous. *The χ-phase in duplex stainless steels* (in press).

[8]   L. Duprez, B. C. De Cooman and N. Akdut. *Steel Res* 72 (2001) 311.

[9]   M. Pohl, O. Storz, T. Glogowski. *Mater Charact* 58 (2007) 65.

[10] M. Pohl, O. Storz, T. Glogowski. *Int J Mater Res* 99 (2008) 1163.

[11] J. Charles. *La Metallurgia Italiana* 2 (1995) 83.

[12] S. Wessman, R. Petterson and S. Hertzman. *Steel Res Int* 81 (2010) 337.

[13] I. Calliari, M. Zanesco, E. Ramous. *J Mater Sci* 41 (2006) 7643.

[14] I. Calliari, M. Pellizzari, E. Ramous. *Mat Sci Tech Ser* 27 (2011) 928.

[15] I. Calliari, K. Brunelli, M. Zanellato, E. Ramous, R. Bertelli. *J Mater Sci* 44 (2009) 3764.

[16] I. Calliari, M. Pellizzari, M. Zanellato, E. Ramous. *J Mater Sci* 46 (2011) 6916.

[17] I. Calliari, M. Zanesco, E. Ramous and P. Bassani. *J Mater Eng Perform* 16 (2007) 109.

[18] I. Calliari, P. Bassani, K. Brunelli, M. Breda and E. Ramous. *J Mater Eng Perform* 22 (2013) 3860.

[19] D. M. Escriba, E, Materna-Morris, R. L. Plaut and A. F. Padilha. *Mater Sci Forum* 636–637 (2010) 478.

[20] S. B. Kim, K. W. Paik, Y. G. Kim. *Mat Sci Eng A* A247 (1998) 67.

[21] Z. L. Jiang, X. Y. Chen, H. Huang, X. Y. Liu. *Mat Sci Eng A* A363 (2003) 263.

[22] T. H. K. L. Weng, J. R. Yang. *Mat Sci Eng A* A338 (2002) 259.

[23] C. S. Huang, C. C. Shih. *Mat Sci Eng A* A402 (2005) 66.

[24] S. Hertzman, R. Petterson, K. Frisk, T. Jerwin. Proc. Conf. *Duplex 2000 6th World Conference & Expo*. Venice, Italy (2000).

[25] K. T. Kim, Y. H. Lee and Y. D. Lee. Proc. Conf. *Duplex Stainless Steels '97 International Conference & Expo*. Maastricht. The Nederlands (1997).

[26] I. Calliari, K. Brunelli, M. Zanellato, E. Ramous, R. Bertelli. *J Mater Sci* 44 (2009) 3764.

[27] J. Li, Z. Ma, X. Xiao, J. Zhao, L. Jiang. *Mater Design* 32 (2011) 2199.

[28] I. Calliari, M. Dabalà, E. Ramous, G. Straffelini. *Mater Sci Forum* 604-605 (2009) 419.

[29] A. Weisbrodt-Reisch, M. Brummer, B. Hadler, B. Wolbank, E.A. Werner. *Mat Sci Eng A* A416 (2006) 1.

[30] N. Sathirachinda, R. Pettersson, S. Wessman, J. Pan. *J Corr. Sci* 52 (2010) 179.

[31] Z. Weia, J. Laizhua, H. Jinchenga, S. Hongmeia. *Mat Charact* 60 (2009) 50.

[32] B. Deng, Y.M. Jiang, J. Gao, J. Li. *J Alloy Compd* 493 (2010) 461.

[33] P. Johansson, M. Liljas. *Avesta Polarit Corros Manag Appl Eng* 24 (2001) 24.

[34] I. Calliari, M. Breda, E. Ramous, K. Brunelli, M. Pizzo and C. Menapace. *J Mater Eng Perform* 21 (2012) 2117.

[35] J. Hamada and N. Ono. *Mater Trans* 51 (2010) 635.

[36] R. N. Gunn. *Duplex Stainless Steels: Microstructure, Properties and Applications.* Abington Publishing, Cambridge, England (1997).

[37] R. B. Johansen, B. H. Leinum, S. Karlsen, H. A. Trandem, G. Valdø, A. O. Tjernæs and T. Helgesen, Proc. Conf. *Duplex 2000 6th World Conference & Expo*. Venice, Italy (2000) 405.

[38] G. Straffelini. *Metall Mater Trans A* 31A (2000) 1443.

[39] K. Wallin. *Innovative approaches to irradiation damages and fracture analysis* (1989) 170.

[40] A. C. Bannister. *Structural Integrity Assessment Procedures for European Industry (SINTAP)*. British Steel plc. (1997).

[41] B. Hwang. *Mater Sci Forum* 654-656 (2010) 158.

[42] W. Oldfield, *ASTM Standardisation News* 3 (1975) 24.

[43] I. Calliari, G. Straffelini and E. Ramous. *Mater Sci Tech Ser* 26 (2010) 81.

[44] H. Sieurin and R. Sandström. *Eng Fract Mech* 73 (2006) 377.

[45] G. Chai. *Struct Dur Hlth* 3 (2007) 191.

[46] E. Erauzkin and A.M. Irisarri. *Fatigue Fract Eng M* 15 (1992) 129–137.

[47] D. W. Marquardt. *J Soc Ind Appl Math* 11 (1963) 431–441.

[48] D. C. Montgomery. *Design and Analysis of Experiments*. Wiley&Sons, USA (2008).

[49] R. Francis, G. Byrne, G. R. Warburton. Proc. Conf. *Stainless Steel World '99*. SSW99-007 (1999) 613.

[50] C. S. Wiesner. Proc. Conf. *Stainless Steel World '97*. D97-107 (1997) 979–990.

CHAPTER 3

EFFECTS OF COLD ROLLING

3.1. INTRODUCTION

This chapter deals with the effect of cold rolling in DSS, a particular cold working process associated to plain-strain conditions (*i.e.* where two direction are mainly interested by deformation), in which the resulting strain can be considered approximately homogeneous in the deformation plane [1]. In technological terms, "cold" means that the operations are carried out at or below room temperature; in metallurgical terms, a metal is said to be "cold-worked" when it is deformed at temperatures and strain rates resulting in a negligible contribution of diffusional processes to the strain, conventionally when a metal is deformed at temperatures below $0.3 \cdot T_M$, being T_M the absolute melting temperature. Changing the shape is the primary aim of cold working; hence, deformations imparted during such processes tend to be large. This process alters the mechanical properties of the materials, and these changes correspond in variation of structure and textures which accompany the plastic deformation [1].

Low temperatures plastic deformation of a polycrystalline metal essentially consists of grains deformation, being negligible the contribution of either grain boundary migration or sliding. Since DSS are biphasic materials, diffuse strain heterogeneities (*i.e.* different strain states inside the same subdivided grain and influences exercised by neighbouring grains on each other) can arise from the concomitant deformation of grains of a different strength (austenite and ferrite) and from the tendency to change into a specific strain state that partially accommodates the imposed macroscopic strain state. A specific feature of the deformed state in heavily strained metals is the increasing "structural damage", *i.e.* such structural events which cause degradation of the mechanical properties and eventually lead to ductile fracture (void formation, void coalescence leading to cracks, etc.) [1], intimately related to the crystal disorder induced at the microstructural level.

Heavily cold worked metals are subdivided by grain boundaries and dislocations boundaries, which are arranged in lamellar or subgrain structures and whose frequency and distribution determine the properties of the deformed metal, including flow stress, textures, recrystallization behaviour and formability. These boundaries originate not only from pre-existing boundaries in the undeformed metal, but also from dislocation boundaries which form during the deformation process, dividing the grains into sub-regions that are smaller than the original grain size [2]. Many metals develop a cellular substructure – also after moderate strains – which can gradually evolve in a subgrained structure as the deformation becomes more pronounced, and the dislocation density is the fundamental average parameter of these cold worked substructure [1].

DSS possess a two-phases microstructure, composed by austenitic grains dispersed within a ferritic matrix, and the phases behaviours during plastic deformation depend on the mechanisms associated to the crystallographic relationships between the phases (Chapter 1). The phases behaviour during cold working is conditioned by the interphase distance, which for austenite is the grain size itself. When this distance is thinner than the free-slip distance, a cell substructure develops, whereas dislocations mainly form transverse walls connecting the interfaces when the interphase distance is of the same order – or less – than the free-slip distance [1]. In DSS, the grain sizes of the phases are of the same order of magnitude and austenite is confined by the surrounding ferritic matrix; hence, the deformation mechanisms and the developed substructure suffers from the restraints that the phases impose to each other, as discussed in the present chapter.

Moreover, cold plastic deformation can cause a martensitic transformation in austenite, especially if the phase is not well stabilized (Chapter 1). This kind of solid-state induced process give rise to the so-called Strain-Induced – or α' – Martensite (hereinafter called SIM), extensively observed in metastable austenitic stainless steels [3-17].

The aim of this chapter is to study the effects of cold rolling in various DSS grades, not only in terms of strain-induced phase transformation, but also considering the involved deformation mechanisms and discussing the associated changes in properties.

Cold rolling

The materials were subjected to cold rolling at different deformation degrees, from 3% to 85% of thickness reduction, by using a manual reversing mill. The various reduction

grades were achieved through discrete deformation steps (*i.e.* not continuously) which, owing to the rolling mill capabilities, were at the maximum of 0.5 mm each. The rolling process was free of constraints in the transverse direction, thus allowing the deformation of the material in all the directions. Note that even if at small deformation degrees (3–15%) the transverse contribution can be neglected, it assumes relevance by increasing the thickness reduction and an equivalent strain must be considered, as reported in the specific section (Paragraph 3.3.2).

Materials

The investigated DSS and their chemical compositions are reported in Table 3.1. The steels were the same examined in Chapter 2, but for the present study it was decided to limit the experimental to the more representative materials (two Lean DSS, a Standard grade and a SDSS), in order to point out the differences among different grades pertaining to different categories.

Table 3.1 – Chemical composition of the investigated Duplex Stainless Steels.

Grade	C	Si	Mn	Cr	Ni	Mo	Cu	P	S	N	PRE_N
SAF 2101	0.028	0.69	3.82	21.72	1.13	0.10	0.34	0.028	0.0025	0.16	25
SAF 2304	0.030	0.56	1.43	23.17	4.29	0.18	0.16	0.027	0.0010	0.13	26
SAF 2205	0.030	0.56	1.46	22.75	5.04	3.19	-	0.025	0.0020	0.16	36
SAF 2507	0.015	0.24	0.83	24.80	6.89	3.83	0.23	0.023	0.0010	0.27	42

Investigation methods

The as-received (AR) and the cold rolled (%CR) DSS samples were prepared following the standard procedure for the metallographic investigation (mechanical grinding and polishing) and etched with the Beraha's reagent, a common tint etchant employed in DSS to reveal the biphasic microstructure. A further investigation was only performed on SAF 2205, for which a supplementary set of deformed samples was firstly subjected to an electrochemical etching at 6 V in oxalic acid and then re-etched using a solution composed by 0.10 g of $Na_2S_2O_5$, 5 ml of HCl and 1 ml of HNO_3 in 60 ml H_2O.

Hardness tests (HV_{10}) were performed in order to measure the overall effect of the deformation on the materials in terms of global hardening, whereas SAF 2205 was also

subjected to micro-hardness tests ($HV_{0.025}$), with the aim to follow the work-hardening evolution of the phases during to the plastic deformation.

The etched microstructures of the samples were observed using a Leica Cambridge Stereoscan 440 Scanning Electron Microscope (SEM), operating in backscattered-electron mode (BSE) at 29 kV. A Leica DMRE Optical Microscope (OM) was employed to investigate the AR materials after the Beraha's etching, and both SEM-BSE and OM micrographies were edited on an image-analysis software for an estimation of the volumetric percentage of the phases.

Electron Back-Scattering Diffraction (EBSD) analyses were only performed on SAF 2101 subjected to 10%, 50% and 80% thickness reduction, after metallographic preparation. In this material, the rolling direction plane of the sheets was considered. Observations were performed using a LEO 1430 SEM at 20 kV, equipped with an IncaCrystal 300 system and coupled with a 1330x1024 CCD camera. EBSD maps were measured on a square grid and the step size (2.5–0.125 μm) was selected according to the magnification of the scan field.

In SAF 2205, a deeper investigation on the effects of cold working was performed using a Jeol JEM 200CX Transmission Electron Microscope (TEM), operating at 160 kV. The thin foils samples were firstly mechanically thinned and polished, and then electrochemically polished on a Struers TecnoPol at –20°C and 35 V, employing a solution composed by 5% percloric acid, 25% glicerol and 75% ethanol.

All the samples were analyzed by X-Ray Diffraction (XRD) on a Siemens D500 diffractometer, using CrKα radiation ($\lambda = 2.2909$ Å) in the angular range $2\theta = 60–140°$ (step size of 0.05° and 3 seconds of counting time for each step), in order to investigate the phases displacement in the solution-annealed and cold worked conditions. The same instrument was employed to achieve the patterns for the SFE calculations in SAF 2205, limiting the analysis to the angular range $2\theta = 60–85°$ (step size of 0.025° and 6 seconds of counting time for each step). All the XRD measurements for both phases displacement and SFE calculations were performed on the rolling plane, with the samples oriented toward the rolling direction (RD). Moreover, a slightly deeper description of textures development in SAF 2205 has also involved measurements on the orthogonal plane (ND) to the rolling one, whereas a more detailed study on texture formation will be given in a further publication.

Since SIM is a ferromagnetic phase while austenite is not, magnetic measurements allow to identify and quantify the martensite amount in the %CR samples, if present. The saturation polarization is linearly proportional to the amount of ferromagnetic phase in alloys [18,19] and the quantification can be achieved by a direct comparison with the saturation polarization obtained by the magnetic tests on the as-received materials. For the present work, specials AC and DC magnetometers was developed and applied for testing the bulk samples. The AC device consists in a close circuit composed by a "U" shaped Fe-Si iron yoke, with a driving coil connected to a function generator and a power amplifier, capable to measure different values by applying a maximal effective field of 2458 A/m. The DC Stäblein-Steinitz magnetic equipment is a close circuit designed to reach higher coercivity and magnetization field than the AC magnetonmeter, consisting in two E-shaped soft iron yokes placed opposite one another and with an air-gap between each of the three pairs of transverse limbs. These techniques are both based on the reaching the magnetic saturation from hysteresis loop and the adopted measuring set-up are especially suitable for testing structural steel and medium hard magnetic samples.

Anodic potentiodynamic polarization tests were conducted for testing the corrosion behaviour of as-received and deformed DSS, using an AMEL 568 potentiostat and immerging the samples in a pH7 electrolyte solution composed by 35 g/l of NaCl in deionized water (artificial sea water). All tests were performed at room temperature using as reference a calomel electrode (SCE) and platinum as counter-electrode. For all tests, a scanning rate of 0.8 mV/s was applied.

For the determination of the Critical Pitting Temperatures (CPT) of the materials, the ASTM G150 standard was followed, using a potentiostat/galvanostat AMEL 7060. The system included two cells containing the same aqueous solution (1 Molar of NaCl) and electrically connected by means of a salt bridge. In the first cell, maintained at room temperature, the reference electrode (calomel) was immerged, while the second, a thermostated bath, included the counter-electrode (platinum) and the sample. The ASTM standard states the evaluation of the CPT by maintaining a constant potential of 700 mV and increasing the temperature of the thermostated cell at the rate of 1°C/min. The CPT is then defined as that temperature at which a current of 100 $\mu A/cm^2$ is absorbed by the sample.

The cold rolled SAFs 2205 and 2101 DSS were also analyzed by means of the Neutron Time-of-Flight Diffraction (ToF-ND) technique, in the Italian Neutron Experimental Station (INES) located at the pulsed neutron source ISIS (Didcot, UK). The INES diffractometer is equipped with 9 banks of ^{3}He detectors, covering an angular range of 2θ=11–170° and lying on a circle of 1 m radius from the diffraction centre [20]. Each bank provides a diffraction pattern which resolution depends on the angular position of the bank itself, according to the derivative of the Time-of-Flight equation, thus leading to a higher resolution in the backscattering one (*i.e.* bank-1). For the measurements, the samples were mounted on aluminium tape, which has a small scattering length such that allowed avoiding undesired reflections from the support device, and were oriented in order to achieve the diffraction patterns pertaining to the rolling direction.

The ToF-ND spectra were refined using the Rietveld method on the GSAS software [21], which allowed to provide accurate information on lattice parameters variation, phases fractions, texture indexes and microstrains evolution during the deformation process. In all the Rietveld analyses, the peak profile function number 4 [22] was taken into account for a proper estimation of the phases microstrain, and both the overall and the phase-related parameters were refined.

3.2. EFFECTS ON MICROSTRUCTURES AND PROPERTIES

Cold rolling modifies the microstructure by refining and orienting the grains as the thickness reduction increases, causing the formation of a heavily banded microstructure at high degrees of deformation and making DSS strongly anisotropic. The microstructural damage induced by cold working assumes ever more relevance as the deformation proceeds; grains shapes macroscopically change and an increased number of defects is introduced within the crystal lattices, leading to the formation of sub-structures. Therefore, also owing to the possible occurrence of the strain-induced martensitic transformation, a variation of DSS properties is expected.

3.2.1. Microstructures

The OM and SEM micrographies obtained on the AR samples revealed that the solution-annealed microstructures were intermetallics-free and by image-analysis it was possible to

evaluate the related phases fractions, reported in Table 3.2. The AR microstructures were well balanced, with a content of both phases close to the 50/50 optimal value, except in SAF 2101, for which it was estimated a ferrite content of about 76%. The unbalanced phase ratio in this latter steel can alter in some extent the involved deformation mechanisms during cold working and can affect the observed properties, also in the AR conditions.

Table 3.2 – Austenite and ferrite volume fractions from image analysis [%].

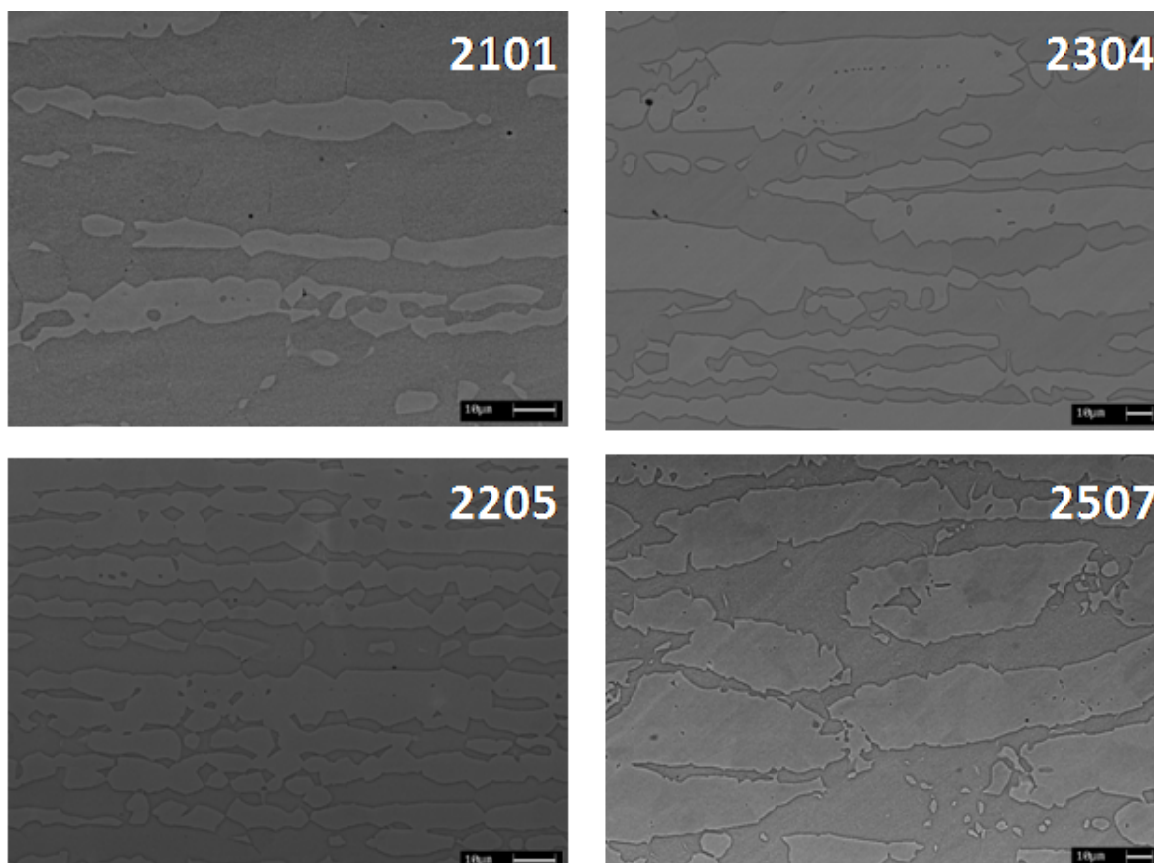|	2101	2304	2205	2507
Ferrite (α)	76	47	45.5	45
Austenite (γ)	24	53	54.5	55

Fig. 3.1 – As-received microstructures of the investigated DSS (SEM-BSE, Beraha's etching).

As can be seen from Fig. 3.1, the various AR microstructures were different. Size and shape of the constituent phases are closely related to the previous thermo-mechanical process (hot rolling and solubilisation), leading to possible different responses to cold

rolling, especially in the early stages of deformation. From Fig. 3.1, it is possible to identify different types of starting microstructures. In SAFs 2304 and 2507, although obtained through different manufacturing processes, the shapes of austenitic grains were quite similar and coarser respect to the other two grades, and the classical banded DSS microstructure is not well evident. An increased grain fragmentation and the presence of small austenitic islands can be notice in SAF 2507, mostly owing to the strong cross-rolling process employed to achieve the final shape of this steel.

Conversely, SAFs 2101 and 2205 were both from similar final products, and the austenitic grains were heavily elongated toward the direction of the previous hot rolling process, evidencing the pancake grain displacement of the DSS microstructure. In SAF 2205, austenitic grains were highly polygonalized, owing to a particular combination of process parameters (such as thickness reduction and annealing time) which eased recrystallization in austenite during solubilisation. In SAF 2101 such polygonalization was not evident as well and its microstructure can be addressed to an intermediate type between SAFs 2205 and 2304.
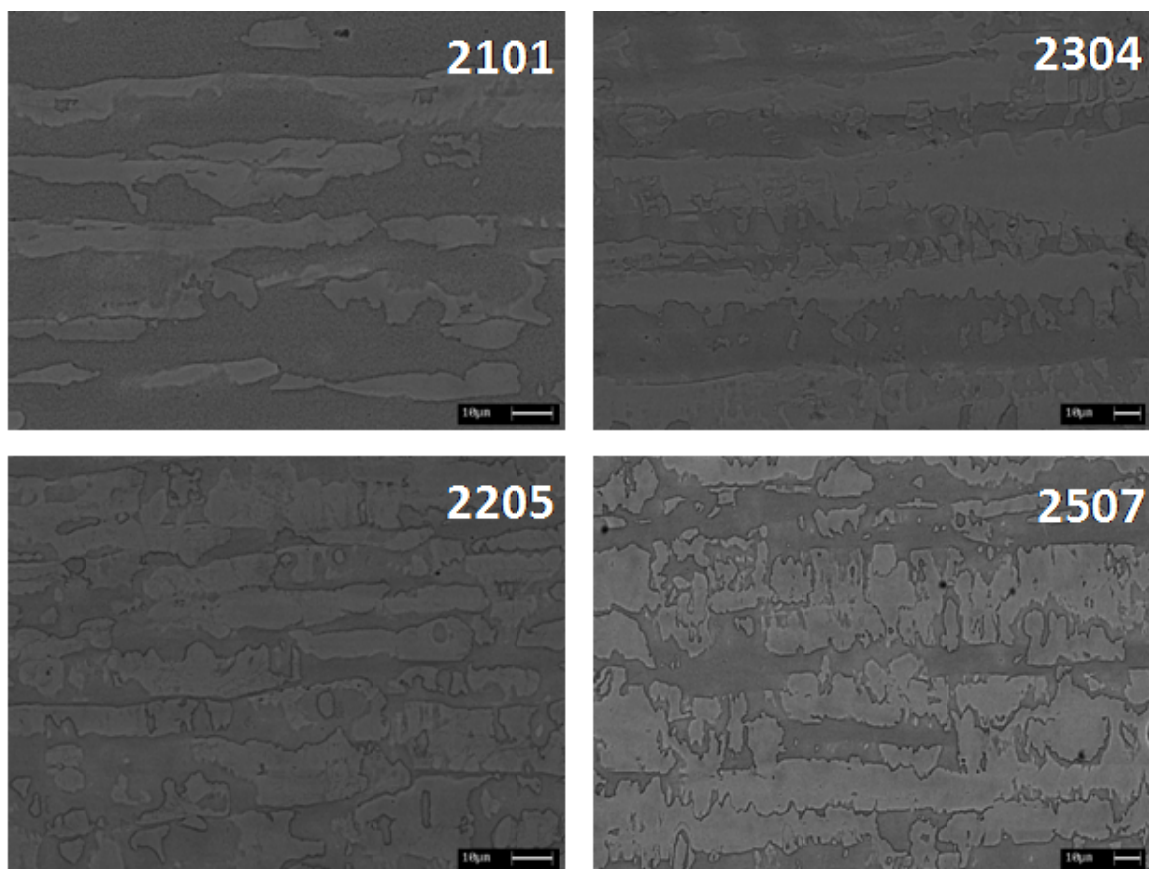

Fig. 3.2 – DSS microstructures after 85% of thickness reduction (SEM-BSE, Beraha's etching).

Cold rolling changes the microstructure by fragmenting and refining the microstructural constituents. In DSS, the grains shape was progressively changed and thinned in the orthogonal direction respect to the rolling plane, causing the formation of a strongly-oriented banded microstructure at 85% of thickness reduction. On the rolling plane, the grains were increasingly deformed as thickness reductions proceeded and considerably fragmented at the higher deformation degrees (Fig. 3.2).
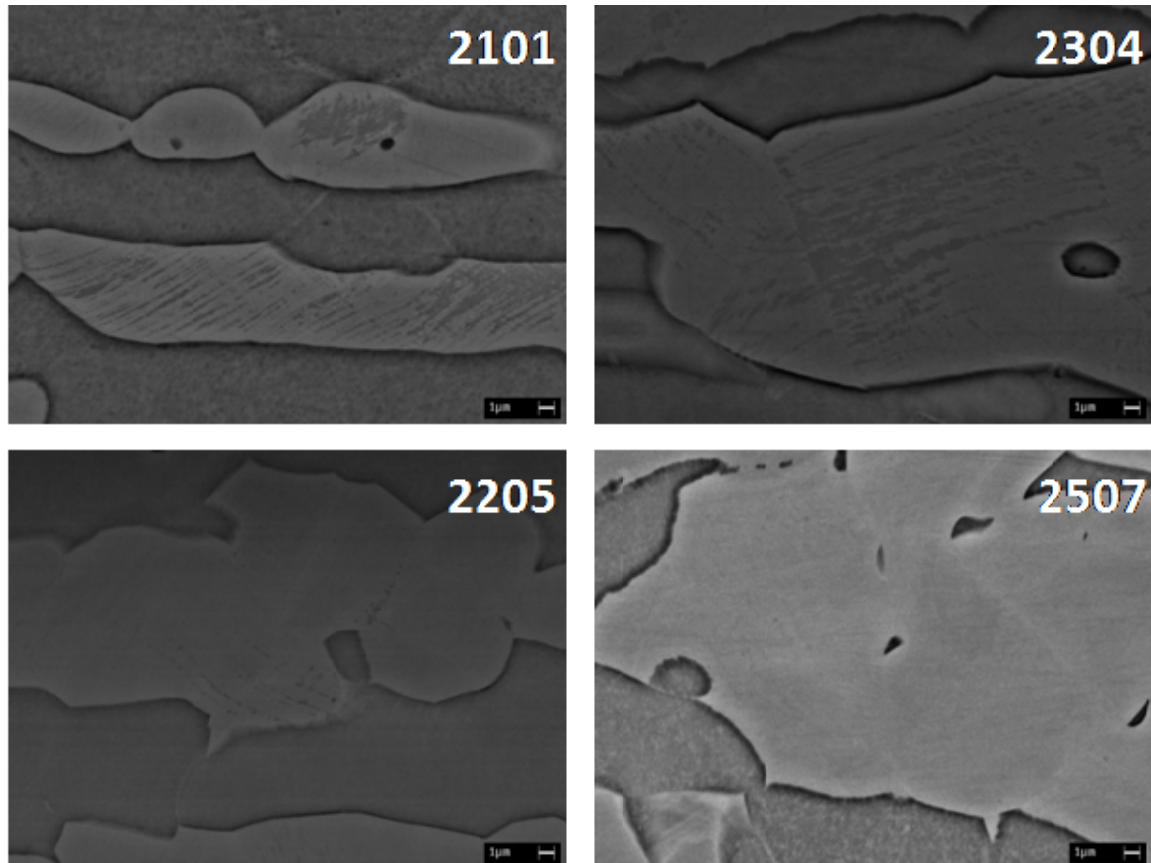

Fig. 3.3 – Structural modifications in austenite at 35% of thickness reduction (SEM-BSE, Beraha's etching).

The cold plastic deformation may also cause the formation of SIM, as already observed in metastable austenitic stainless steels [3-17]. In addition to the steel composition, the initial microstructure can play an essential role on the material stability and, therefore, the previous thermo-mechanical processes can affect the observed behaviour of the phases after the plastic deformation [11,17]. SIM is not easily detectable in DSS and its quantification is difficult by classical metallographic techniques because it occurs with no changes in chemical composition, owing to the diffusionless character of the transformation. Nevertheless, the boundaries between austenite and SIM must be

considered as areas with high interfacial energy and the different orientations of the phases may produce a detectable metallographic contrast. As a matter of fact, the investigation on the Beraha's etched samples revealed some features which pointed out the possibility of such transformation. Above 15% of thickness reduction (Fig. 3.3), the employed reagent highlighted some recurring structural modifications inside the austenitic regions, which tended to expand inside the whole grain as the deformation proceeded (Fig. 3.4). These faulted regions were also seldom detected in the 15%CR samples of SAFs 2101 and 2304 Lean DSS, whereas in SAF 2507, the higher-alloyed – and more stable – grade, the interior of the austenitic grains remained always unchanged at any thickness reduction.
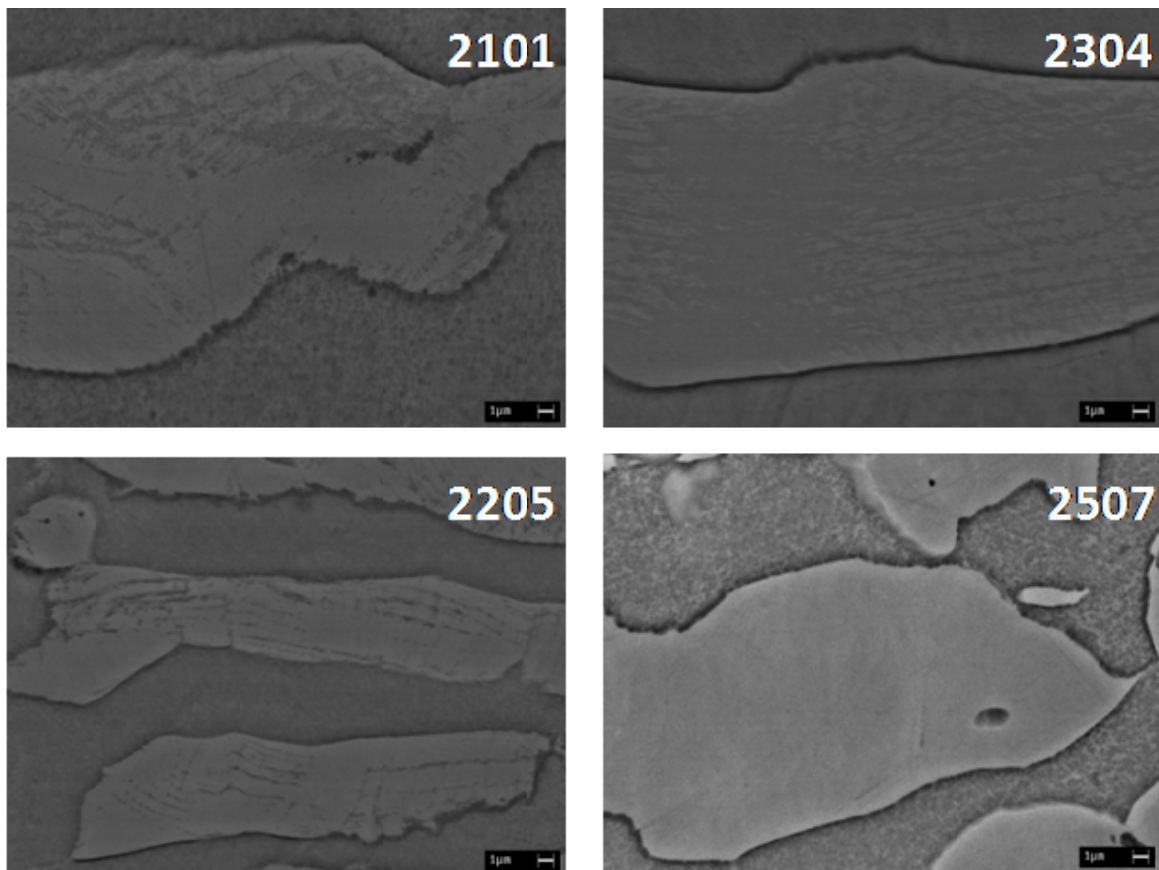

Fig. 3.4 – Structural modifications in austenite at 65% of thickness reduction (SEM-BSE, Beraha's etching).

It is well known that, in a solution-annealed DSS, the Beraha's tint etchant preferentially acts on ferrite, owing to the selective character of the reagents, and leaves the austenitic phase unaffected. This behaviour is ascribed to the different anodic potential of the phases and, in a biphasic microstructure, the etched phase is the one which is anodic with respect to the other (*i.e.* ferrite in DSS). Cold working has been found to render a

deformed area more anodic, owing to the increasing of the active anodic sites on the surface [23] and, therefore, leading to different corrosion behaviours inside the same phase as a consequence of the plastic deformation. Hence, after cold rolling, the faulted regions detected inside the γ-grains clearly gained a more anodic potential respect to the surrounding austenite but, unfortunately, cannot be strictly related to SIM laths because, between them, there could be some austenitic regions which did not transform into martensite but which gained a different anodic potential with respect to other parts of the same grain. These features have been already observed in a 2101 DSS [24] (Paragraph 3.3.1) where the martensitic transformation was investigated by means of EBSD and, also in this case, a direct attribution to SIM formation was not possible.

The presence of the faulted region in Lean DSS at very low thickness reductions (15%) can be addressed to a more proneness to SIM formation of austenite in such materials or, at least, to a increased plasticity of these materials. Indeed, in Lean DSS, austenite is less stable than in the other grades, due to the lack of γ-stabilizing elements, and therefore the martensitic transformation can more readily occur. On the contrary, the absence of structural modifications in SAF 2507 highlights the great stability of this material if compared to the other grades.

3.2.2. Hardness

The same increasing trend in Vickers Hardness (HV) was observed in all DSS. The work-hardening of the biphasic steels is modified respect to the characteristic single-phase behaviour, and the presence of austenite gave rise to a macro-hardness increment which is conditioned by the high strain-hardening rate of the FCC austenitic phase in the first stages of deformation (Fig. 3.5). At low thickness reductions, up to 15% of deformation, a rapid increase in hardness was observed in all DSS, due to the strain-hardening, whereas the subsequent cold working leaded to an almost linear rising in HV. In Lean DSS, the greater relative hardness increment was observed, owing to the minor amount of alloying elements in these grades which caused less important effects due to solid solution strengthening mechanisms, making the phases more prone to deformation. This was particularly evident in SAF 2304, in which the compositional effect, combined to a coarser structure of the steel, eased the highest strain-hardening, especially in austenite.

The concurrent presence of different crystal structures alters the micro-mechanisms of deformation and the single phase behaviours are constrained by the presence of the other phase, because neighbouring grains imposed restraints on each other. As previously reported, austenite can be thought as the "second phase" in form of elongated aggregates confined by grain boundaries, and its deformation is restricted to an area which is limited by the surrounding ferrite. On the contrary, the ferritic matrix less suffered of such restrictions, and the imposed strain can find easier deformation paths as the thickness reduction proceeded, allowing the activation of a considerable number of slip systems at higher deformation degrees and causing a greater thinning respect to austenite.
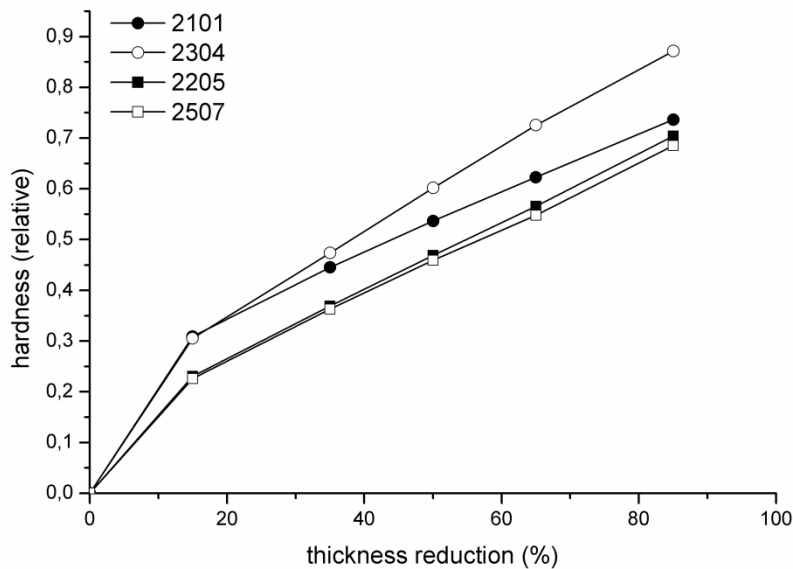

Fig. 3.5 – Hardness variation as a function of the deformation degree.

In DSS, it was shown that the deformation in each phase takes place homogeneously and that the strain is transmitted through the interfaces by common slip systems [25]. However, as the number of dislocations in a boundary increases, the effectiveness of the boundary as an obstacle to the movement of dislocation also increases. In the case of low and medium thickness reductions (up to 50%) ferrite well accommodates the deformed austenitic grains while, as the applied strain increases, grain boundaries become harder by dislocations piling up. This behaviour highly constrains the deformation of austenite, causing the observed grain fragmentation at the highest thickness reductions (Fig. 3.2). Thus, as a consequence of these different behaviours, a banded-like microstructure is developed during cold working, resulting in a heavier fragmentation of austenite at the

highest thickness reductions and in a concentration of deformation in ferrite, which is instead more thinned in the orthogonal direction to the rolling plane.

The above described mechanisms must be considered valid in well-balanced DSS, having an almost equal volume fractions of the phases, where austenite readily strain-hardens at the early stages of deformation, causing a greater thinning of the ferritic bands at the higher deformation degrees. In SAF 2101, containing a not negligible surplus of ferritic phase, this phenomenon does not occur and, even if the ferritic bands are in any case reduced, cold working mainly affects the austenitic phase, which is more refined and fragmented. In this steel, the gross presence of the hard ferritic matrix overcaome the strain-hardening effect occurring in austenite, thus causing the observed different deformation behaviour at a microstructural level.

3.2.3. Textures and x-rays diffraction

In this paragraph, XRD measurements on AR and %CR samples were employed to investigate the grains reorientation as a consequence of the plastic deformation. However, the phases displacement described here is only of qualitative character, and a full description of grains rearrangement after cold rolling requires deeper investigations. A slightly detailed description of texture development in SAF 2205 is given in Paragraph 3.3.2, and the observed behaviour may be in some extent considered valid for the other grades when heavy deformations are involved, even though different starting microstructures can alter the intermediate reorientation phenomena and the development of the final textures.

The formation of texture in DSS and single-phase stainless steels is reported in several literature works [26-32], where phases orientations after hot-deformation, annealing and cold-working are extensively discussed. In these studies, the investigated DSS can be compared to SAFs 2205 and 2507 analyzed in theis thesis, but the presented results are not free of discrepancies. Nevertheless, it emerges that the hot rolling manufacturing process causes the formation of Cubic textures in both DSS phases and, in addition, typical FCC deformation textures – mainly the Brass-type component – are developed in austenite.

The Brass component is typical in hot-rolled materials having low SFE, such as austenite in DSS, and for which the conditions for extensive dislocations cross-slip are

difficult to reach. Conversely, the development of the Copper-type texture in austenite seems to be not possible in DSS, owing to its low SFE value and therefore to the impossibility to achieve sufficient reductions at room temperature [33], even though it was observed in a hot-rolled high-alloyed DSS [30]. On the other hand, the development of FCC cubic textures can be associated to the dynamic recrystallization process occurring during high-temperature deformations, especially during the roughing stage, where the higher thermal regimes do not inhibit its formation. Finally, for what concerns ferrite, the observed major component is the Rotated Cubic {001}<110>, caused by dynamic recovery during hot rolling, especially after the finishing operations.

The solubilisation of DSS, which follows the forming operations, is performed at temperature higher than 1050°C, and the required soaking times are enough to allow the formation of annealing textures, more or less pronounced in relation to the entity of previous hot-working. Annealing textures can be substantially different from deformation textures – and are generally more pronounced – and are known to be affected by several factors, such as rolling reduction, chemical composition, grain size, annealing temperature and time, heating rate and many others. In DSS, austenite was found to develop a dominant Cubic texture, whereas ferrite exhibits a dominant Rotated Cubic with a weak Cubic component [27]. It is however possible that other types of textures may take place during annealing as a consequence of the previous hot-working. After rolling, owing to the BCC structure, ferrite can develop Cubic and Goss-type components, whereas the presence of a not negligible Goss-type component in austenite can be either formed during rolling and retained in the annealing stage, or directly formed during solubilisation, as it is a typical recrystallization texture occurring in FCC materials. However, it must be taken into account that a description with ideal components is always inadequate, and this is especially valid for alloys. Rather, textures (deformation and annealing) can be better described as a spread of orientations, among which certain are better developed and more pronounced than others. Moreover, the thermo-mechanical history of the material and the hot-working process parameters are responsible for the particular texture developed in the annealing stage, since are part of the variables affecting grains displacements.

For what was previously reported, XRD patterns are characteristic of the manufacturing process and the phases orientations in the AR state can substantially affect the behaviour during cold working. In the present study, XRD measurements were only performed in the

rolling direction (RD), and cannot be considered exhaustive for a texture analysis. However, some information can also be achieved and a qualitative description of the phases rearrangement can be made.
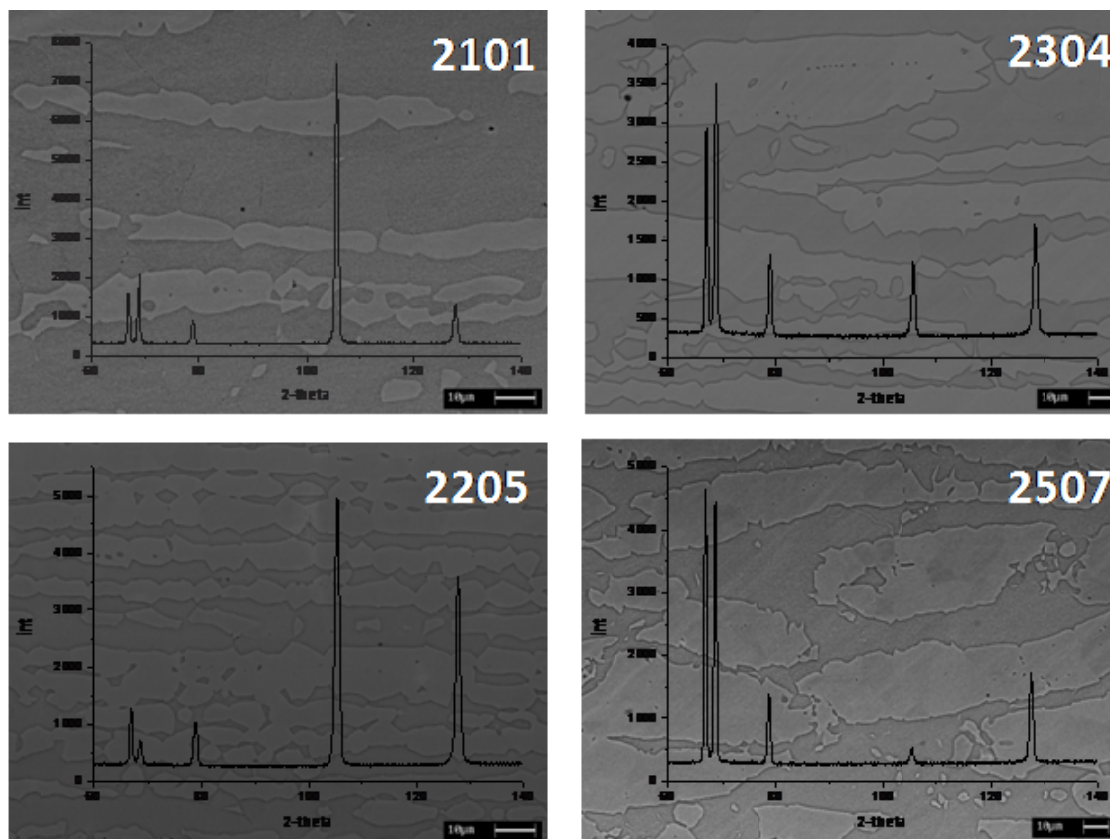

Fig. 3.6 – As-received microstructures and corresponding diffraction spectra.

The AR diffraction spectra along RD were characterized by very narrow peaks, because to the solubilisation, but different features arise from different grades. As can be seen in Fig. 3.6, SAFs 2304 and 2507 had similar starting microstructures (Paragraph 3.2.1) and the height of α(110) and γ(111) principal peaks suggested a nearly-random grains orientation in both phases. This fact, in addition to a greater plasticity of the γ-phase achieved by a coarse microstructure, can justify the greatest relative increment in hardness observed in SAF 2403 (Paragraph 3.2.2). In this latter Lean DSS, the randomness of the austenitic grains caused a more favourable orientation to the rolling force, leading to a higher strain-hardening rate respect to the other grades.

On the other hand, in SAFs 2101 and 2205, the heights of both α(200) and γ(220) reflections respect to the α/γ principal peaks underline a strong initial texture of the AR

materials (Fig. 3.6). In these steels, the huge signal from α(200) planes in the RD revealed the presence of a strong cubic orientation in the AR-ferrite, achieved after the previous hot-rolling and recrystallization processes, since both are responsible for the development of cubic textures. In SAF 2101, the heights of the γ-peaks, if compared to those of ferrite, underlined its unbalanced microstructure and cannot fully reveal the presence of initial textures in the FCC phase. On the contrary, in SAF 2205, the AR-austenite texture was found to be mainly composed by a combination of recrystallization textures – {110}<100> Goss-type and {100}<001> Cube components – and other remnants of deformation textures pertaining to the hot rolling process, as explained in the next Paragraph 3.3.2.
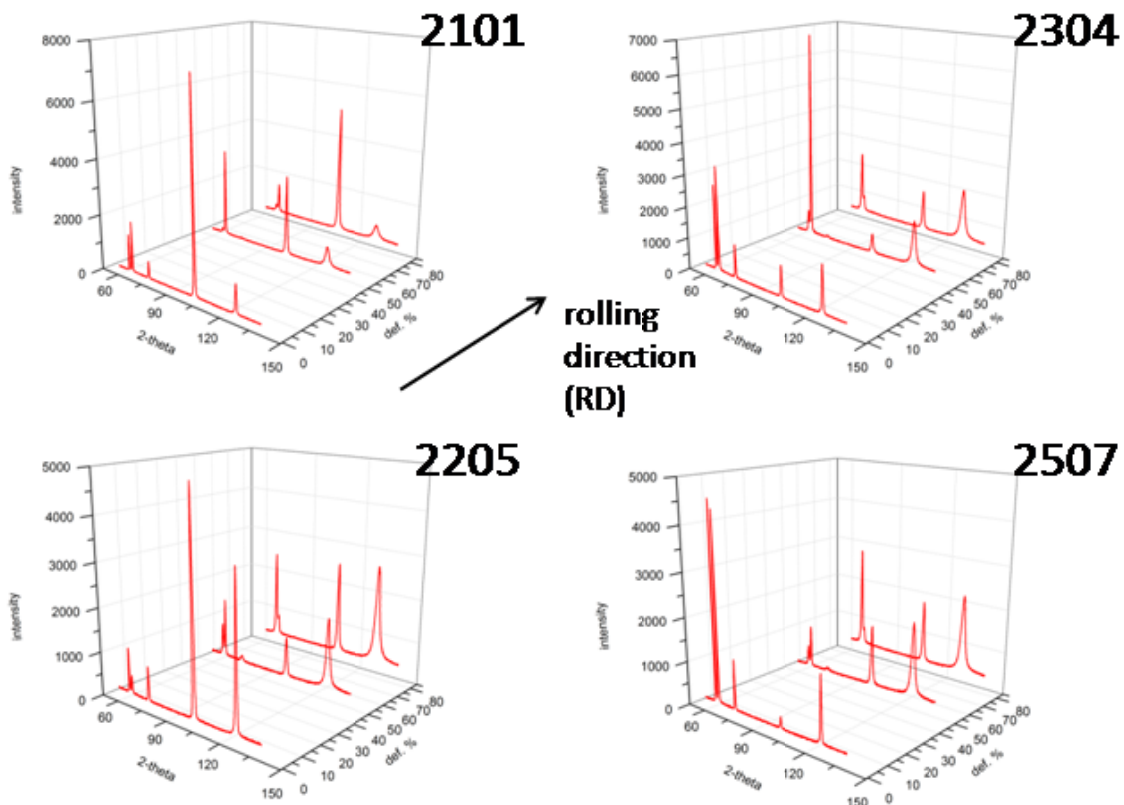

Fig. 3.7 – Diffraction spectra of AR, 50%CR and 85%CR materials (3D view).

Cold deformation caused a rearrangement of the grains, and such orientations-redistribution process strongly depended on the initial microstructure. Previous works on cold deformed DSS [26-32] point out that cold rolling up to 90% of thickness reduction mainly causes the development of the {001}<110> Rotated Cubic texture component in ferrite. From these works also emerges that austenite is interested by an alloy-type texture

development since the early stages of deformation and, at the higher deformation degrees, the {110}<112> Brass-type texture is accompanied by a spread in orientations; moreover, austenite was found to be also characterized by the presence of a more pronounced {110}<100> Goss component than in single-phase austenitic stainless steels.

Concerning the present work, after intermediate reorientations, in correspondence of the highest thickness reduction both phases in all DSS tended to displace toward what appeared to be the main rolling textures directions, and the huge peak broadening revealed a heavy grains refinement as a consequence of the cold-working (Fig. 3.7). In the 85%CR samples, the strong $\alpha(200)$ reflections in RD underlined that ferrite mainly displaced toward a cubic orientation (BCC rolling texture), whereas in the 85%CR-austenite the strong presence of both $\gamma(111)$ and $\gamma(220)$ suggested the presence of typical FCC rolling texture. This is not so evident in SAF 2101, owing to the scarce presence of γ-phase in the starting microstructure and also to the possible formation of SIM. However, in all DSS, a full description of deformation textures requires deeper investigations.

XRD measurements are also widely employed to detect SIM in austenitic stainless steels, since it appearance can be easily revealed. However, if the martensitic transformation occurs, SIM and ferrite peaks will be superimposed, making a pattern analysis difficult to be performed. In the cases under study, the strong initial texture in SAFs 2101 and 2205 and the heavy phases orientations acquired at high deformations make the XRD direct-comparison procedure not reliable, since is based on a random grain distribution, and also hindered the full-pattern refinements performed by the Rietveld method. Nevertheless, the presence of the $\gamma(220)$ peaks at the higher thickness reduction in all the investigated DSS underlined that if the martensitic phase was formed, it did not replac the whole austenitic phase. Moreover, no HCP ε-martensite was detected; its absence could be ascribed to either the possibility of a direct $\gamma \rightarrow$ SIM transformation through dislocations reaction [34] or a too low amount of the metastable hexagonal phase.

3.2.4. Pitting corrosion resistance

Several studies have highlighted the unclear role of cold working on the resistance to localized corrosion of stainless steels [35-37], but the occurrence of residual stress and the formation of SIM can substantially affect their pitting resistance, because the number of

the active anodic sites in the surface are increased [23,37,38]. Thickness, composition and uniformity of the passive layer are modified in different extent by plastic deformation [39,40] and the increasing in dislocation density favours the film dissolution, due to the presence of lower binding energy regions, if compared to a perfect crystal [41]. However, cold plastic deformation induces distortions within the microstructure, creating sub-structures inside the grains (dislocations networks, twins, deformation bands), thus increasing the crystalline disorder and the number of interfaces. This may affect the formation of a less effective passive film on the surface and, moreover, the presence of distorted interfaces and defects must be considered as high energy sites which may provide further trigger points for the localized corrosive attack [42,43].

In this section, the pitting resistance of the four selected DSS grades in as-received conditions and after cold rolling is discussed, with the aim to highlight the effects of cold plastic deformation on the corrosion behaviour. The investigated steels were the SAFs 2101, 2304, 2205 and 2507 reported in Table 3.1. All the steels, in solution-annealing and water-quenched conditions, were cold rolled at various degrees of deformation, from 15% to 85%. Since surface roughness can affect the measured CPT value [44] and with the aim to correctly compare the results on different materials, the surfaces of the tested samples were prepared in the same manner, with a finishing as uniform as possible.

Table 3.3 – Results from potentiodynamic tests.

	2101			2304			2205			2507		
	TQ	50%	85%	TQ	50%	85%	TQ	50%	85%	TQ	50%	85%
E_{cor} [mV]	-230	-140	-175	-245	-200	-235	-180	-130	-230	-130	-200	-160
I_{cor} [A/cm^2]	2.8 E-08	2.4 E-08	8.5 E-08	3.8 E-08	2.3 E-08	3.3 E-08	1.1 E-08	1.5 E-08	2.1 E-08	1.0 E-08	1.5 E-08	2.5 E-08
E_{break} [mV]	140	80	50	505	550	450	1170	1180	1160	1170	1150	1175

Note: test performed in pH7 solution (35 g/l of NaCl in deionized water – artificial seawater)

Potentiodynamic tests at room temperature

The main data obtained from the potentiodynamic tests performed at pH7 in aqueous solution are summarized in Table 3.3, where I_{corr} was obtained by Tafel extrapolation from the free corrosion potential. As expected, a comparison between the as-received samples of

different grade revealed the excellent behaviours of SAF 2205 and 2507 DSS in artificial seawater, significantly higher than the SAF 2304 and 2101 Lean DSS (Fig. 3.8 and Table 3.3). Although the absorbed current density in passive condition were roughly comparable for all steels, the corrosion potential increased with PRE_N index, and the range of potentials which characterizes the passive behaviour was considerably wider for the high-alloyed grades, for which the breakdown potential was almost ten times higher than in SAF 2101.
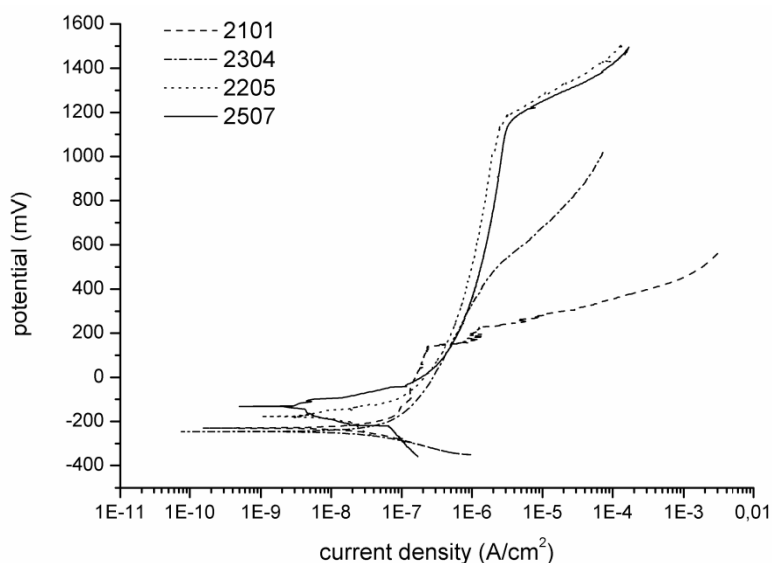

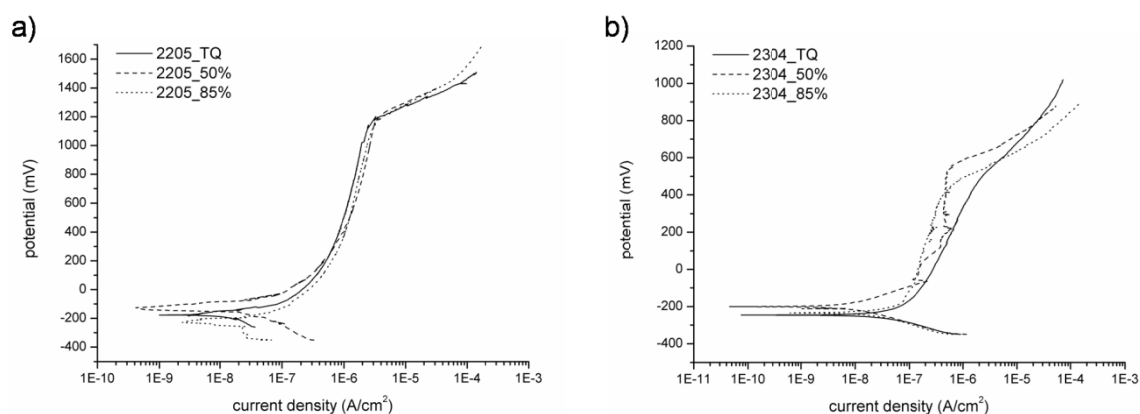Fig. 3.8 – Anodic polarization curves of the AR materials.

Fig. 3.9 – Anodic polarization curves of AR, 50%CR and 85%CR materials:
a) SAF 2205 and b) SAF 2304.

A comparison between the two SAF 2101 and 2304 Lean DSS revealed a higher overall behaviour of the latter DSS respect to the former, and the best response to pitting corrosion of SAF 2304 in marine environment is clearly visible from the curves in Fig. 3.8. Free

corrosion potentials and currents were similar for the two steels but the SAF 2304 exhibited a greater stability in passive conditions, with a wider passive range and a breakdown potential three times higher than SAF 2101. Although in SAF 2304 the highest content of Cr and Mo resulted in a negligible increase in terms of PRE_N, the presence of higher amounts of such elements provided this steel an enhanced resistance to pitting corrosion, owing to the beneficial effect of both elements on the stability of the passive film. Furthermore, the higher content of Mn in SAF 2101, added to stabilize the austenitic phase, may be responsible for a further destabilization of the passive film at potential next to breakdown.
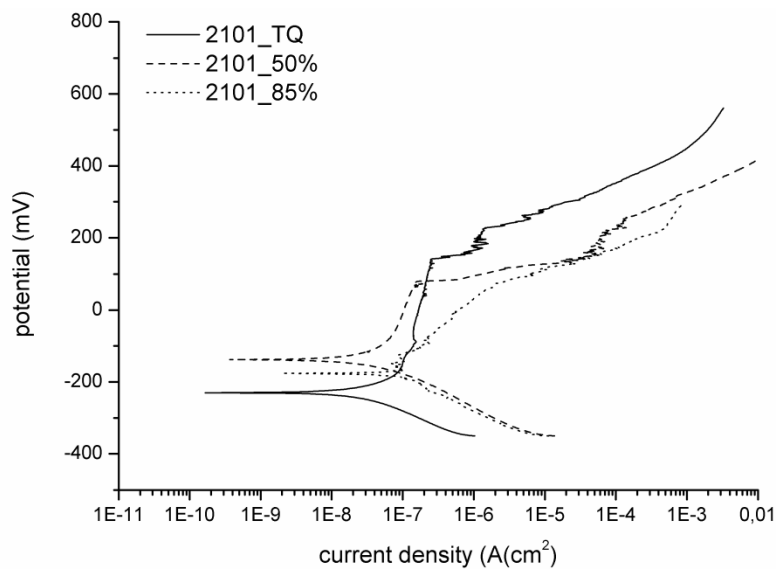

Fig. 3.10 – Anodic polarization curves of SAF 210, as-received and deformed.

Cold working did not substantially alter the pitting resistance in SAF 2304, 2205 and 2507. The tests on the deformed materials didn't reveal significant variations and the curves didn't exhibit specific variation trends by increasing the deformation. In these DSS both the free corrosion and breakdown potentials in the deformed state were very close to each other (Fig. 3.9), even though in SAF 2304 a decreasing in transpassivity potential at the highest deformation degree was observed. Nevertheless, the curves remained almost unchanged even after cold working and the oxide film appeared to be stable in any case. In SAF 2205 and 2507 the best responses as a consequence of deformation were registered. In these materials, the curves are virtually superimposed (see Fig. 3.9a for SAF 2205, while SAF 2507 exhibited a similar behaviour), underlining the very high stability in aggressive environments even after heavy plastic deformation.

On the other hand, the corrosion behaviour of SAF 2101 was different from the other grades (Fig. 3.10). Although the plastic deformation implied a progressive decreasing in the breakdown potential, the passive film was found to be almost stable up to 50% of deformation. Conversely, the highest thickness reductions caused a great instability of the protective layer, highlighted by a progressive rising in absorbed current density by increasing the scanning potential, and for which the variation was about of an order of magnitude before reaching the breakdown conditions. The lower pitting resistance of this steel, coupled with the microstructural damage induced by cold working, determined the achievement of the critical conditions for the oxide layer breakage for ever more lower potential as the deformation degree increased.

Table 3.4 – DSS critical pitting temperatures in as-received conditions.

	2101	2304	2205	2507
CPT [°C]	13	27	54	85

Critical pitting temperatures (CPT)

The determination of the critical pitting temperature allows to ascertain a very useful parameter in the evaluation of materials for applications in heavily chlorinated environments. The rising in temperature causes a decrease of the breakdown potential and thus introduces an additional variable for the assessment of the DSS resistance in an aggressive environment, which must be added to the possible contribution introduced by plastic deformation. The decreasing in the breakdown potential can be explained by the greater chemi-absorption of chloride ions on the passivated surface, which allows for the breaking of the protective film. As the temperature increases, the passive layer enriched in chromium becomes increasingly thin – and more prone to localized attack – due to the higher dissolution rate of the oxide if compared to the possibility of a new layer formation by chromium diffusion from metal to the surface [45]. Another work [46] has also shown that at high temperatures in some stainless steels the passive film becomes thicker and at the same time more porous, and thus less protective. In any case, the higher the temperature the weaker the protective properties of the passive film.

The SAFs 2304, 2205 and 2507, in the as-received conditions, exhibited CPT values which were within the expected corresponding ranges (Table 3.4), approaching – and

sometimes overcoming – the upper limits. The same statement was instead not valid in SAF 2101, for which the measured CPT was very close to the lowest limit established for its category. In this latter steel, although an increase of ferrite content may lead to an improved performance of the austenitic phase, the content of such elements which characterize the stability of the passive layer (Cr and Mo) is lower than in other grades. Moreover, as previously explained, the presence of a too high amount of manganese can contribute to the worsening of its pitting resistance, destabilizing the protective layer.
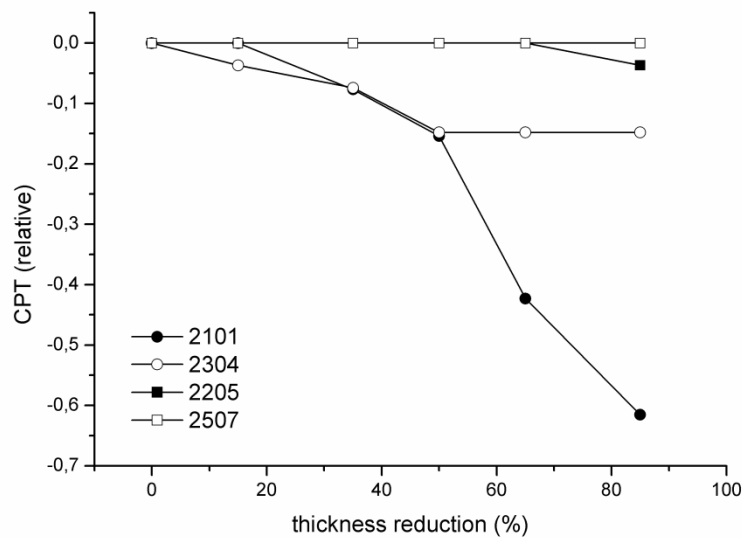

Fig. 3.11 – Critical Pitting Temperatures (CPT) as a function of the deformation degree.

Generally, the microstructural changes induced by cold working affect in some extent the corrosion behaviour of stainless steels. Composition and thickness of the passive layer are altered by the presence of residual stresses and crystalline disorder [39-42], and also the possible presence of SIM can further worsen the steel resistance in aggressive environments. As can be seen from Fig. 3.11, in SAF 2507 there wasn't any change in critical temperature at any thickness reduction, while in SAF 2205 only a decreasing of 4% at the highest deformation degree was registered. The corrosion resistance and microstructural stability of these two steels was very high, owing to the increased content of alloying elements which ensured an adequate stability of the passive layer (Cr, Mo and N) and the stabilization of the austenitic phase (Ni, N). However, the causes of the slight reduction in CPT observed in SAF 2205 (lower alloyed than 2507) could be addressed not only to the disorder induced by plastic deformation, but also to the formation of the martensitic phase, as reported in previous studies [47] and discussed in Paragraph 3.3.2.
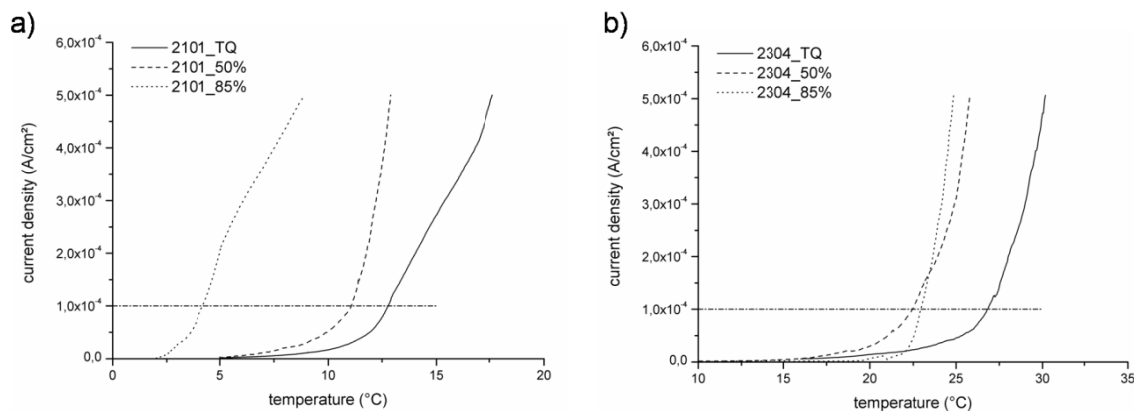
Fig. 3.12 – Critical Pitting Temperatures (CPT) variation: a) SAF 2101 and b) SAF 2304.

The situation was different in the two Lean DSS and, also in this case, SAF 2101 was more affected by the effects of plastic deformation. By comparing equal thickness reductions, the 2101 is more prone to SIM formation, since the content of the strongly γ-promoting elements (Ni and N) is very low and therefore the austenite phase is not sufficiently stable at room temperature. Austenite is also the weakest phase against pitting resistance and the occurrence of SIM would further compromise its corrosion behaviour. The formation of SIM in this steel is discussed in Paragraph 3.3.1 [24], and was found to form for deformations exceeding 20–30% of thickness reduction. This findings are reflected in the progressive decreasing in CPT observed in SAF 2101 (Fig. 3.12a), for which a reduction of 70% in CPT at the higher deformations was measured. The situation observed in the other Lean DSS was similar to that of 2101 (Fig. 3.12b). For 2304, the intermediate deformations caused a lowering in CPT of about 15%, while for higher thickness reduction no further reductions were observed. In this steel, the effect of plastic deformation against pitting resistance is definitely smaller than in SAF 2101, owing to a higher microstructural stability. However, the possible formation of SIM in SAF 2304 must not be excluded and the registered decreasing performances in corrosive environments could be indeed attributed to the formation of this new phase, although the verification of its genesis requires further study .

Concluding remarks

DSS possess excellent resistance to corrosion in a wide range of corrosive environments, particularly against pitting attacks. The performances of SAF 2101, 2304, 2205 and 2507 in as-received conditions were superior than the common AISI 316 austenitic stainless

steel in artificial seawater (pH7). The excellent behaviour of the two higher-alloyed SAF 2205 and 2507, both as-received and cold-worked, makes these steels more suitable for applications in heavily chlorinated respect to Lean DSS, where the higher cost is justified by the extraordinary pitting resistance.

On the contrary, the performances of SAF 2101 were significantly lower than the other grades, making the steel not particularly suitable for applications in marine environment, especially if subjected to cold deformation. In 2101, the presence of high manganese contents and the SIM formation after cold working caused a great destabilization of the passive layer and global deterioration of the corrosion resistance characteristics. The characteristics in SAF 2304 were instead intermediate between SAF 2101 and the higher-alloyed grades, having breakdown potential close to that of 2101 but with a passive layer more stable – even after plastic deformations – owing to its higher content of alloy elements such as chromium and molybdenum.

The CPT determination underlined the findings revealed by the potentiodynamic tests. SAF 2507, as expected, possessed the highest CPT value in the as-received conditions (85°C) and exhibited the greatest microstructural stability even after heavy cold deformation, owing to its higher content of alloying elements. In SAF 2205 only a slight decrease in CPT at the highest deformation degree was registered, caused by the onset of little amount of SIM (Paragraph 3.3.2) and by the increasing in active anodic sites which promoted the localized attack. In Lean DSS, plastic deformation caused a decreasing in CPT but, while in SAF 2304 this reduction was mild (15%) and there were no further reductions over 50% of deformation, in SAF 2101 a marked reduction in CPT was observed, reaching the 25% of the initial value at the highest deformation degree. In both cases, the deterioration of the corrosion behaviour can be attributed not only to compositional factors and to the disorder induced by plastic deformation, but also to the formation of SIM, which was attested in SAF 2101 (Paragraph 3.3.1) and which requires further investigations in SAF 2304.

3.2.5. Magnetic properties

As DSS contain about 50% of ferrite, they exhibit a certain degree of magnetism, which however is not sufficient to avoid mechanical clamping during machining [48]. As

reported, cold working can cause the formation of the ferromagnetic SIM from austenite, therefore increasing the amount of magnetic phase. The austenitic regions which undergo martensitic transformation act as small ferromagnets and are magnetized when an external magnetic field is applied, influencing the magnetic properties of the material. This change in magnetic properties as a consequence of plastic deformation can be detected by means of the AC and DC magnetometers presented in Paragraph 3.1.

All the AR and %CR DSS were firstly demagnetized and then subjected to magnetic tests, but they were not all tested using the same technique. SAFs 2304 and 2205 were only examined by means of AC measurements, owing to a scarce availability of material in the deformed state; in these steels, both the well-balanced microstructure and the discrete magnetic level of ferrite have permitted to obtain representative magnetic hysteresis loops, since both materials have reached the saturation level. On the contrary, the AC method wasn't able to saturate the SAFs 2101 and 2507, owing to the higher ferrite content in the former steel and to the high magnetic level of ferrite in the latter; thus, in these cases, the DC magnetometer was employed. Unfortunately, the results provided by AC and DC measurements are of different type and the obtained saturation values reported in Table 3.5 are not directly comparable. Nevertheless, in both cases, if the SIM transformation took place in the deformed DSS, an increasing of the saturation magnetic field (B_{max}) is expected.

Table 3.5 – DSS saturation magnetic field in as-received conditions.

	2101	2304	2205	2507
B_{max} [T]	0.75**	0.63*	0.55*	0.59**

(*) AC magnetization
(**) DC magnetization

As can be seen from Fig. 3.13, in SAFs 2101 and 2304 a strong increase of B_{max} was observed by increasing the deformation degree; in SAF 2205, only a little variation toward higher B_{max} values was registered at the highest thickness reduction, whereas in SAF 2507 the saturation field remained almost unchanged. These findings reveal that cold rolling caused a strong increase of the magnetic phase amount in Lean DSS, which can be ascribed to the SIM formation. Is it known that the saturation magnetic field is linearly proportional to the amount of ferromagnetic phase [18,19], allowing a determination of the SIM amount. Unfortunately, a quantification of the strain-induced phase is not even

possible, because these measurements need the knowledge of the total amount of transformed austenite at the higher deformation degree, in order to set the limits of the calibration curve, thus only qualitative considerations can be made.
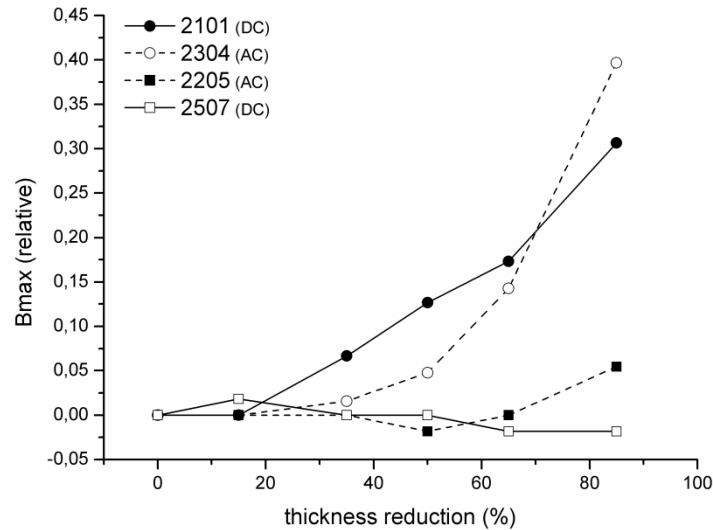

Fig. 3.11 – Saturation magnetic field (B_{max}) as a function of the deformation degree.

SIM also formed in SAF 2205 and, from the magnetic results, it seems that it only occurred at the highest thickness reduction, in significantly lower extents respect to Lean DSS. In this case, the steel is more stable than Lean DSS and a reduced SIM amount was expected. However, as described in the next Paragraph 3.3.2, deeper analysis revealed that in SAF 2205 the SIM transformation took place after 15% of thickness reduction and this discrepancy with the magnetic results can be ascribed to the very low amount of SIM formed during low and intermediate deformation stages, making not possible its observation by means of AC test, owing to its detection limits. Conversely, SAF 2507 was found to be highly stable, and the saturation magnetic field only exhibited some fluctuations arising from local microstructural inhomogeneities.

3.3. STRAIN-INDUCED MARTENSITE IN DSS

As already reported, DSS are characterized by a high content of alloying element and can undergo significant microstructural modifications as a consequence of either thermo-mechanical treatments or plastic deformation (Chapter 1). In the previous sections of this chapter, the possibility of a strain-induced martensitic transformation in the steel under

study was hypothesized. Various experimental evidences was presented and all the performed measurements point toward such direction. In this section, the onset of SIM in DSS after plastic deformation is discussed, by analyzing two cold rolled DSS grades (SAF 2101 and SAF 2205).

In Chapter 1, SIM formation is described as a diffusionless process, which occurs in metastable austenitic stainless steels as a consequence of cold working [3-17]; throughout this process, austenite evolves toward the thermodynamically more stable SIM, owing to the shear bands intersection mechanisms. Austenite stability depends on the microstructure developed after the processes to which the steel was subjected, and on the Staking Fault Energy (SFE) of the phases, related to the steel chemical composition at a fixed temperature [3]. The SIM formation, whose tendency increases with the decrease of the SFE value [5], is frequently associated to the appearance of an intermediate phase, the ε-martensite, whose formation is not necessary for the SIM process, especially in low SFE materials [6]. This transformation has been already suggested in a cold rolled SAF 2205 [47], although the austenite in that DSS was found to be less metastable than in the austenitic grades, and a further analysis of the SIM phenomenon in discussed in the present section.

3.3.1. Characterization of a cold rolled SAF 2101

SAF 2101 is one of the lower-alloyed DSS grade in which the amount of both substitutional and interstitial elements is rather low if compared to other grades; therefore, the stability of austenite is expected to be lower than other DSS, and also lower than austenitic stainless steels. The chemical composition of the investigated steel is reported in Table 3.6. This steel was subjected to cold rolling from 10% to 80% of thickness reduction and the as-received (AR) and cold rolled (%CR) samples were subjected to a deep characterization, in order to understand if the SIM transformation can also occur in this class of steels.

Table 3.6 – Chemical composition of the investigated SAF 2101 DSS.

	C	Si	Mn	Cr	Ni	Mo	Cu	P	S	N
SAF 2101	0.028	0.69	3.82	21.72	1.13	0.10	0.34	0.028	0.0025	0.16

Microstructure

The starting microstructure of SAF 2101 and the modifications induced by cold rolling were already presented in the previous Paragraph 3.2. As reported, the analyzed SAF 2101 DSS is not well-balanced, having a ferrite content which was estimated at about 76%. Hence, cold working mainly caused the deformation of the austenitic phase, which was substantially thinned and fragmented.

After cold rolling, the high-magnification SEM investigations only revealed some gray contrasts inside the austenitic grains which could be associated to the recurring structural modification discussed in the previous Paragraph 3.2.1. As reported, these features could represent martensite laths, but cannot be immediately addressed to the new phase (Fig. 3.14).
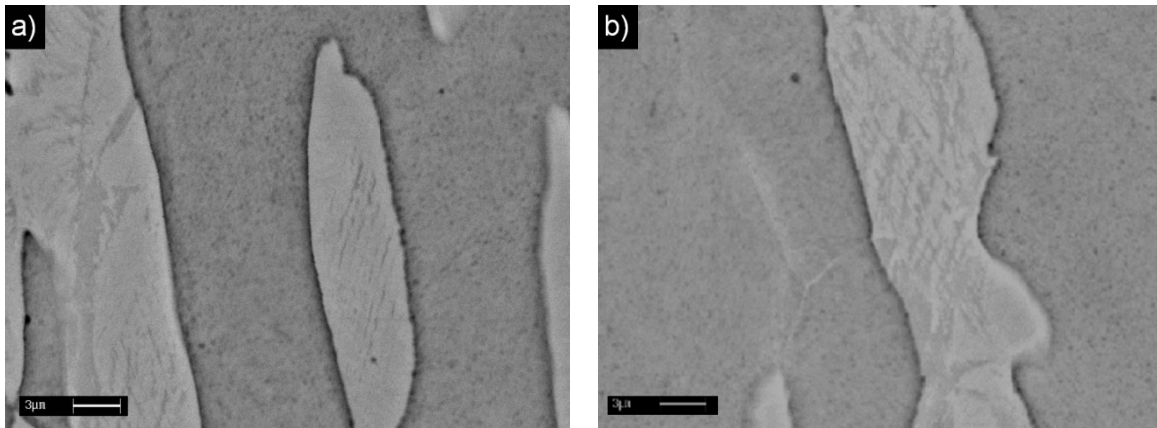

Fig. 3.14 – Micrographies of CR samples (SEM-BSE, etched): a) 50% and b) 60%.

X-Rays Diffraction

As reported in Paragraph 3.2.3, XRD was not helpful to reveal if the SIM formation occurred in SAF 2101, but a relevant decreasing of the FCC austenitic peaks intensity was observed. If SIM transformation took place, it not interested the whole austenitic phase, since γ-peaks are still visible after the higher thickness reductions. Moreover, no HCP ε-martensite has been detected in the cold rolled samples.

EBSD investigation

A first set of analyses were performed on the 10%CR sample at low magnification on the longitudinal section (step size of 2.5 and 1.25 mm). In a first attempt, austenite, ferrite and ε-martensite were used as reference phases, while SIM cannot be considered as a reference

pattern, since its crystal structure and lattice parameters are very similar to those of ferrite. The minimum acceptable difference of lattice parameter for automatic indexing is considered to be about 2–3% [13] but this value is below the EBSD resolution limit. On the 10%CR sample, a mean content of 22% austenite and 78% ferrite was estimated, no ε-martensite was detected (as also observed through XRD analyses) and the non-indexed points were less than 0.5% in all examined fields.
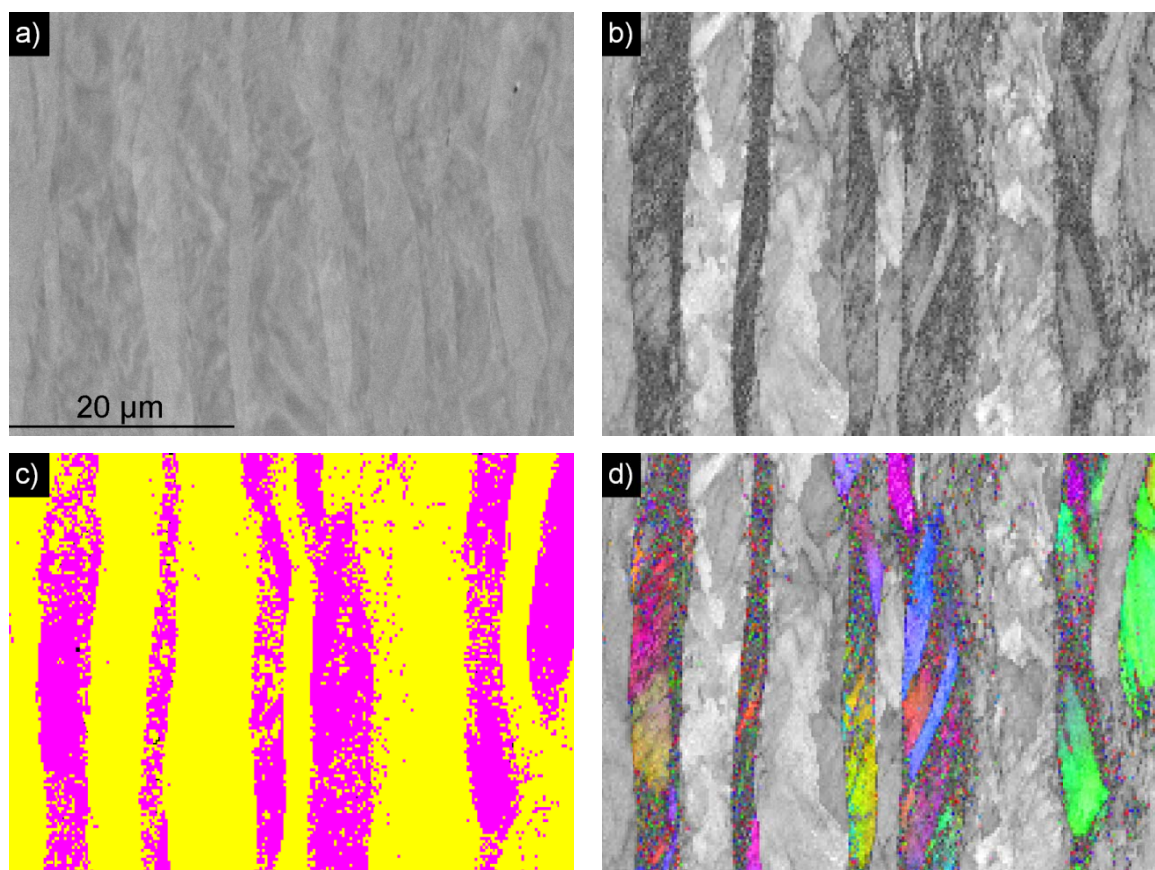

Fig. 3.15 – EBSD analysis on 50%CR sample, longitudinal section. Step size 0.2 μm. No cleanup. a) FBSE image, b) pattern quality image, c) phase map: yellow/ferrite, pink/austenite, black/not indexed and d) orientation map for austenite phase superimposed to the pattern quality map.

The EBSD analyses performed on 50%CR sample revealed that the deformation was mainly concentrated in the austenitic phase. A comparison between the Forward-Backscattered Secondary Electrons (FBSE) image and the pattern-quality image clearly points out that the darker regions in the FBSE image (which correspond to the ferrite grains) are characterized by a higher pattern quality and therefore by a lower deformation (Fig. 3.15). On the contrary, the brightest areas are also characterized by residual subgrains of austenite and portions with a low pattern quality. These latter regions were partially

recognized as austenite, partially as ferrite and partially were non-indexed. For the 50%CR sample, the degree of correctly indexed austenite, estimated considering the ratio between the total area of dark and bright regions of the FBSE images, was evaluated as about 80%, which correspond to about 17.6% of untransformed austenite in the sample. Therefore, it was assumed that the low pattern quality regions pertain to transformed austenite, and eventually heavily deformed austenite, with crystallite size below the resolution limit. A similar approach was previously used in literature to discriminate different phases [49,50].
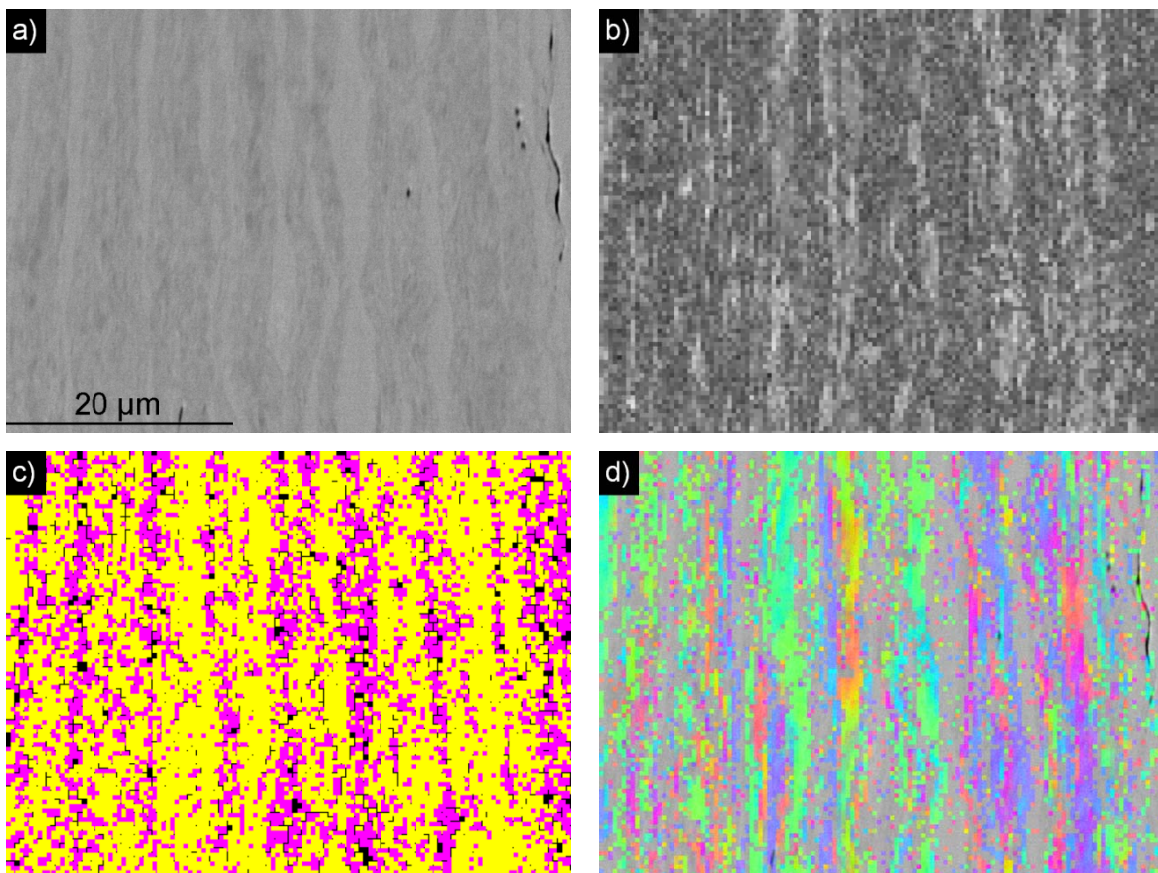

Fig. 3.16 – EBSD analysis on 80%CR sample, longitudinal section. Step size 0.2 μm. No cleanup. a) FBSE image, b) pattern quality image, c) phase map: yellow/ferrite, pink/austenite, black/not indexed and d) orientation map for ferrite phase superimposed to pattern quality map.

Finally, the EBSD analyses carried out on the 80%CR revealed that in these conditions, besides austenite, ferrite is also interested by subgrain formation and deformation bands (Fig. 3.16). At higher magnifications (Fig. 3.17) residual austenite was more evident, with a width size in the order of micron or less, hindering the austenite quantification, since particle size was closer to observation limit [51]. Nevertheless, an estimation of the residual austenite using a similar approach employed for the 50%CR sample was

performed; a value of about 2% of the volumetric fraction can be estimated, even though in this case the error is of the order of 1%, since in many cases very few pixels per grain are detected, causing a strong decreasing in accuracy of the performed evaluation [52]. Nevertheless, from such measurements, it is possible to assert that almost all austenite in 2101 DSS transformed to SIM.
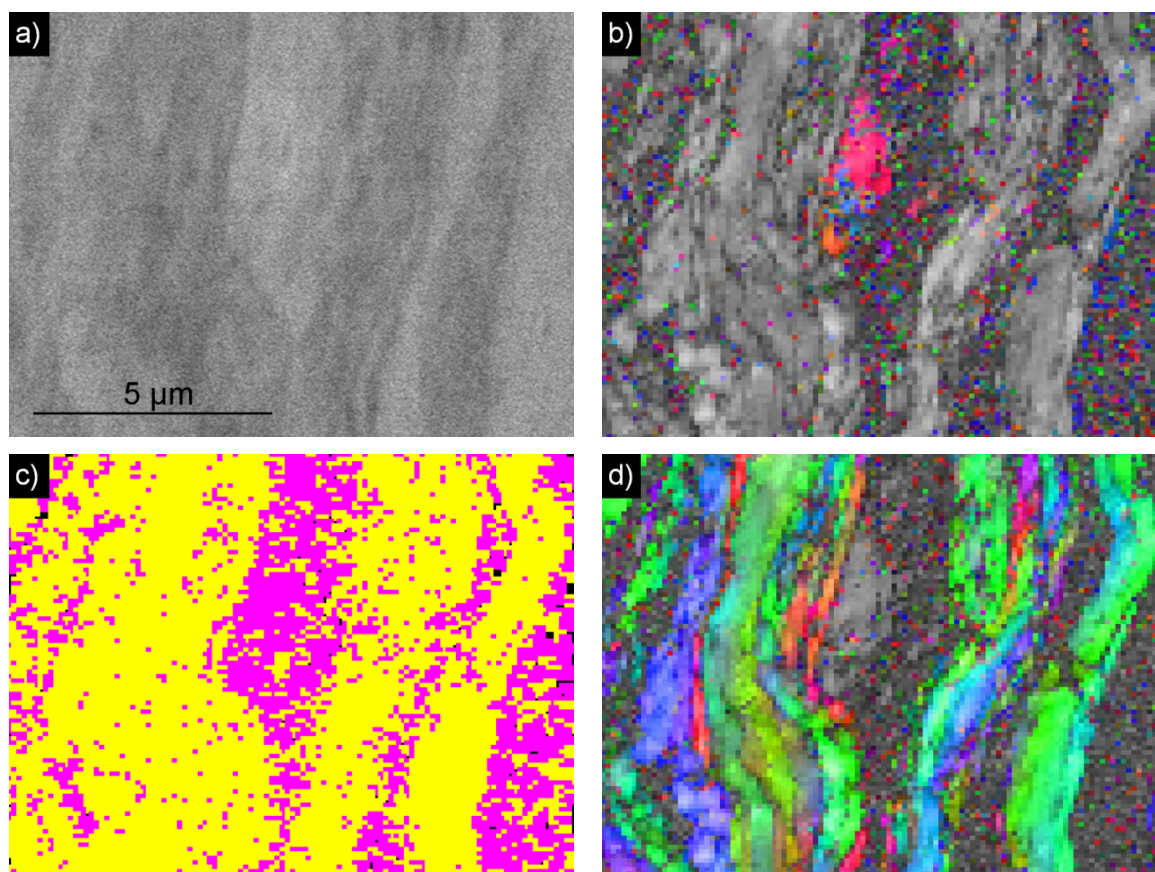

Fig. 3.17 – EBSD analysis on 80%CR sample, longitudinal section. Step size 0.12 μm. No cleanup. a) FBSE image, b) orientation map for austenite phase superimposed to pattern quality map, c) phase map: yellow/ferrite, pink/austenite, black/not indexed and d) orientation map for ferrite phase.

Magnetic measurements

It is well known that the saturation polarization is linearly proportional with the amount of ferromagnetic phase in alloys [18,19], allowing for a quantification of the amount of ferromagnetic SIM in the CR samples by a direct comparison with the saturation polarization obtained by the magnetic tests.

The first magnetization curves and the saturation hysteresis loops were measured a double-yoke magnetometer on the completely demagnetized samples; the maximum external field applied was about 2250 A/cm, which was absolutely sufficient for the

magnetic saturation of the samples. As can be seen in Fig. 3.18a, the saturation polarization values gradually increased with the plastic deformation, passing from 0.752 T in the AR material to 0.94 T in the 80%CR sample, as a result of the SIM formation. The amount of SIM can be calculated from the following eqiation:

$$\mu_0 M_s^{sample} = R^\delta \mu_0 M_s^\delta + R^{martensite} \mu_0 M_s^{martensite} \qquad (3.1)$$

where: M_s^{sample}, M_s^δ and $M_s^{martensite}$ are the saturation magnetization values of the tested sample, δ-ferrite and SIM respectively. R^{delta} and $R^{martensite}$ are instead the relative ratios of ferrite and SIM. The determined saturation polarization values of ferrite and SIM are 0.95 T and 0.92 T respectively.
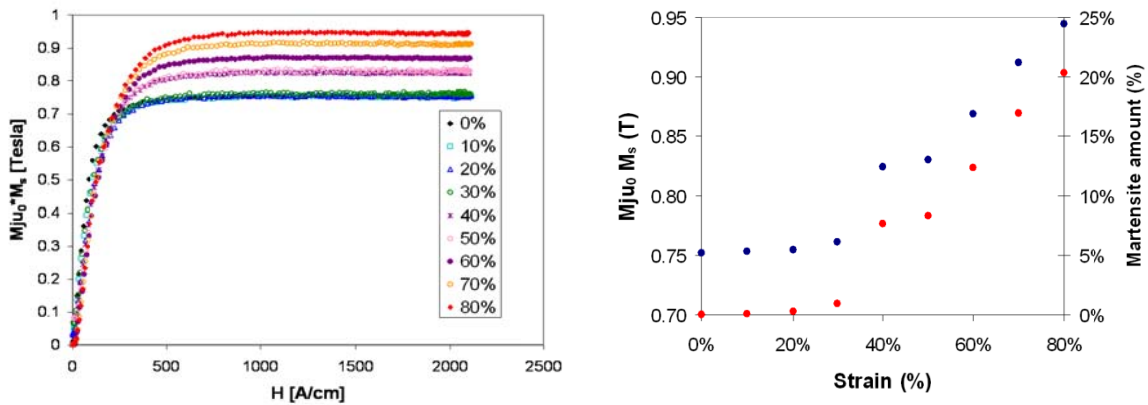

Fig. 3.18 – a) First magnetization curves on AR and CR samples and b saturation polarization values and the quantified amount of martensite vs. strain).

The saturation polarization values and the quantified amount of SIM are plotted together in Fig. 3.18b. The saturation polarization (blue points) seems to be almost the same at the lower thickness reduction, up to 30%. A further increase in cold deformation leads to a stronger and gradual increase in magnetic saturation field, which reaches the highest value of 0.94 T at 80% of thickness reduction. The estimated amount of SIM by Equation (3.1) at each thickness reduction is reported in Fig. 3.18b as red points.

Hardness test

The results of Vickers hardness test HV_{10} and the amount of SIM estimated by magnetic measurements are plotted together in Fig. 3.19. At low strain rates, up to 20% of thickness

reduction, the hardness increases rapidly due to the high strain-hardening rate of austenite, which affects the overall hardening behaviour, while for further deformations a reduction in the increase of hardness was observed. Above 20% of thickness reduction, the hardness increases quite linearly with the amount of SIM. In the low deformation range the hardening process can be associated with a substantial increase of dislocation density and to an increased number of shear band intersection, mainly owing to the high plasticity of austenite. Comparing the hardness results to the trend of SIM formation, it can be supposed that exceeding the 20%, the energy associated to deformation process is mostly spent for the SIM formation.
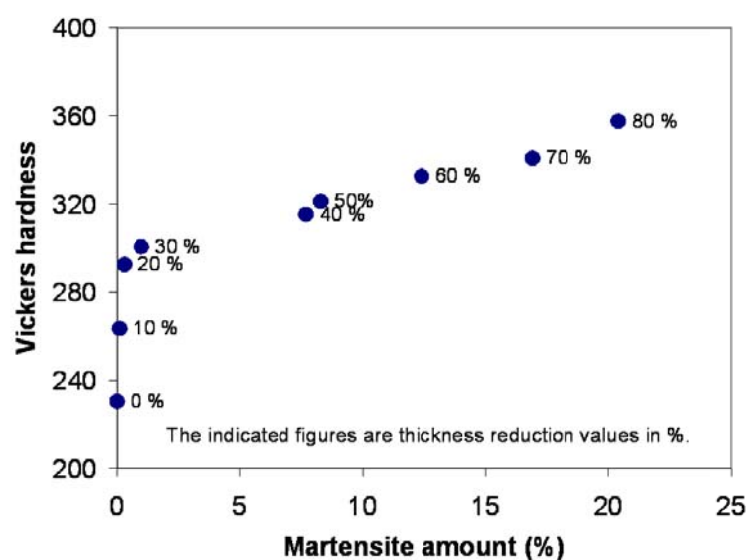

Fig. 3.19 – Vickers hardness vs. estimated amount of strain-induced martensite.

Concluding remarks

This investigation has pointed out that, during cold rolling, in SAF 2101 the austenitic phase was transformed into the so-called Strain-Induced Martensite (SIM), whose amount increased as the deformation proceeded. In 20%CR samples the transformation started to take place; in 50%CR only about 20% of the initial austenite underwent SIM formation; and in 80%CR samples almost all the austenite was transformed.

In this steel, up to 20% of thickness reduction the deformation energy was mainly spent on the strain-hardening of the material, leading to a rapid increase of the dislocation density inside the grains and therefore to an increase in hardness. Above 20% of deformation the hardness increased slightly, because the energy was thought to be mostly

employed for the SIM formation, whose amount seemed to be linearly related to the thickness reduction, and only in a minor part for a further strain-hardening of the material. Magnetic and EBSD measurements are in agreement each other, highlighting the formation of SIM in this DSS grade.

However, it must be notice that EBSD was of discrete character and has only involved the investigation of 10%CR, 50%CR and 80%CR samples, thus without any information on the first stages of the SIM formation. Moreover, as reported in Paragraph 3.2.5, the sensibility of the magnetic measurement does not allow to detect magnetic variations inside the samples when the phase content is very low (<10%). Thus, it is highly probable that SIM transformation can also occur at lower deformation degrees than 20% of thickness reduction, but more sensible techniques are required in. For this purpose, SAF 2101 (as-received and cold rolled) was subjected to Neutron Time-of-Flight Diffraction, but the data are still under analysis, in order to fully describe such transformation.

3.3.2. Effects of cold rolling in SAF 2205 DSS

From the results presented in the previous Paragraph 3.3.1, is evident that the SIM transformation could reasonably take place in SAF 2101 DSS as a consequence of cold rolling, even though there were no direct observations of the new phase and only the magnetic consequences of such transformation were detected. In the present section, the effects of cold rolling on another DSS grade, the SAF 2205, were investigated using deeper investigation techniques, such as Neutron Diffraction (ToF-ND) and Transmismion Electron Microscopy (TEM), in order to unambiguously characterize the onset of such transformation.

In SAF 2205, since the amount of the γ-promoting elements is low, the austenitic phase is in any case lower-alloyed respect to that of austenitic stainless steel, but its stability can be conditioned by the biphasic microstructure. As a matter of fact, a comparison with a metastable AISI 304L austenitic steel – for which the SIM transformation have been extensively studied [3-17] – is presented, in terms of austenite stability and Stacking Fault Energy (SFE) associated to the FCC phase.

Nevertheless, the steel under examination in this paragraph differs from the SAF 2101 previously presented and, since SAF 2205 is characterized by a greater amount of γ-

promoting elements (see composition in Table 3.7), the austenite stability is higher. Thus, if the SIM transformation takes place, a lower extent of SIM is expected. Moreover, as previously reported, the DSS microstructure, owing to its biphasic character, can play a not negligible role in such phase transformation, modifying the mechanisms of deformation and the kinetics of SIM formation.

Table 3.7 – Chemical compositions of SAF 2205 and AISI 304L [wt.%].

	C	Si	Mn	Cr	Ni	Mo	P	S	N
SAF 2205	0.030	0.56	0.89	22.75	5.04	3.19	0.025	0.002	0.18
AISI 304L	0.033	0.53	1.59	18.11	7.96	0.64	0.026	0.002	0.07

Preliminary considerations

As reported in Paragraph 3.1, the SAF 2205 DSS was cold rolled at room temperature in a not continuously manner, involving thickness reductions in the range 3–85% and using a manual reversing mill free of constraints in the transverse direction. This latter fact implies that the transverse contribution at medium-high thickness reductions cannot be neglected and an equivalent strain must be considered. As pointed out by Hecker *et al.* [7], a change in deformation mode from mono- to bi-axial has certain influence on the martensitic transformation, delaying the kinetics at the first steps of deformation and causing an increase of the SIM content at medium-high strains. Hence, the effective strain criterion considered in the present work was that of von Mises, given by the following relation:

$$\varepsilon_{VM} = \frac{\sqrt{2}}{3} \sqrt{(\varepsilon_1 - \varepsilon_2)^2 + (\varepsilon_2 - \varepsilon_3)^2 + (\varepsilon_3 - \varepsilon_1)^2} \tag{3.2}$$

This criterion typically provides a better correlation between plastic flow and stress state [7] and gives a better description of the effective strain developed during the rolling process. Table 3.8 relates the various thickness reductions to the effective strains at which the samples were subjected.

Table 3.8 – Correlation between thickness reduction and effective strain.

thickness reduction	3%	5%	15%	35%	50%	65%	85%
von Mises effective strain (ε_{VM})	0.032	0.054	0.170	0.451	0.726	1.099	1.987

The stacking fault probability of the austenitic phase was estimated considering the Warren-Averbach approach [53], founded on γ(111) and γ(200) peaks displacement after plastic deformation. The DSS samples were deformed to 3% of thickness reduction in order to produce a suitable number of stacking faults [54] and resulting in a detectable shifting of the diffraction lines positions. The calculations were performed comparing the annealed (AR) and the 3% cold worked (3%CR) spectra, using the following expression [3]:

$$\Delta 2\theta = (2\theta_{200} - 2\theta_{111})_{3\%CW} - (2\theta_{200} - 2\theta_{111})_{AR}$$

$$= -\frac{45\sqrt{3}}{\pi^2}\left[tan\,\theta_{200} + \frac{1}{2}\,tan\,\theta_{111}\right]\alpha \qquad (3.3)$$

The SFE of austenite was determined using the formula developed by Schramm and Reed [3] and which was already employed for the analysis of several austenitic stainless steels:

$$\gamma = \frac{K_{111}\,\omega_0\,G_{(111)}\,a_0\,A^{-0.37}}{\pi\,\sqrt{3}}\,\frac{\langle\varepsilon^2\rangle_{111}}{\alpha} \qquad (3.4)$$

In expression (3.3) the 2θs are given in degrees and were achieved by a Gaussian fit of the diffraction peaks, while α denotes the stacking fault probability, which increases with the density of the generated stacking faults. In equation (3.4), $K_{111}\,\omega_0$ is a proportionality constant found to be 6.6 [55], a_0 is the austenite lattice parameter, $G_{(111)}$ is the share modulus for the γ(111) planes – assumed $7.39 \cdot 10^{10}$ N/mm^2 for the 2205 DSS [56] –, A is the Zener anisotropy $2C_{44}/(C_{11} - C_{12})$ – calculated considering the C_{ij} given in [57] – and $<\varepsilon^2>_{111}$ is the mean square strain, estimated from the XRD peak broadening after the cold deformation. For a verification of the SFE results, the same calculations were performed on an AISI 304L austenitic stainless steel (composition in Table 3.7), as-received and 3% cold rolled, whose SFE is extensively reported in literature (~17–20 mJ/m^2 [3,58-62]), assuming a shear modulus $G_{(111)} = 6.5 \cdot 10^{10}$ N/mm^2 and a Zener anisotropy $A = 3.43$ from a previous work [3].

Stacking Fault Energy

The susceptibility to SIM formation via non-diffusive phase transformation from austenite is strongly connected to the stability of the austenitic phase and therefore to its SFE. The microstructural stability depends on the amount of the solubilised alloying elements into the phase, but also can be related on the microstructure itself. Several empirical relations link the SFE values to the chemical composition of the steel [3,54,63], but were developed for austenitic stainless steels and cannot be considered reliable for DSS, since the amounts of alloying elements are substantially different. The low Ni content of DSS, if compared to that of austenitics, mainly affects the calculations, leading to negative values and pointing out the inapplicability of these relations. Furthermore, it was also highlighted that the validity of these formulae is restricted to a limited range of compositions for the austenitic steels as well [64].

The calculated SFE and stacking fault probability of 2205 DSS and AISI 304L are reported in Table 3.9. For the austenitic stainless steel, the results are strictly in agreement with the values reported in literature, assuring the reliability of the employed XRD method for this class of steels, while the obtained value for the DSS approaches the 10 mJ/m^2 determined by direct measurements of extended dislocation nodes [56]. Therefore, the results confirmed the 2205 DSS as a low SFE material, owing to its lack of γ-forming elements, and underlined the susceptibility of this material to SIM formation.

Table 3.9 – XRD parameters and SFE of the steels under analysis.

	$10^6 <\varepsilon^2>_{111}$	$10^3 \alpha$	$10^3 <\varepsilon^2>_{111}/\alpha$	SFE [mJ/m^2]
2205	8	18	0.4	8.5
304L	7	8	0.8	17

The obtained SFE for the DSS was lower than the one for the AISI 304L and, since the SIM formation in the austenitic steel is well established, such phase transformation in the DSS is then expected. However, it must be considered that the deformation mode – and the associated strain field – the biphasic microstructure and both initial microstructure and strain state could play a fundamental role on phase transformation and micro-mechanisms of deformation in DSS, leading to a possible different response to cold working.

Microstructure

The effects of cold working on DSS microstructures are reported in the previous Paragraph 3.2.1, in which the observed features pertains to Beraha's etched samples. For the present investigation, a further set of samples was firstly subjected to an electrochemical etching at 6V in oxalic acid and then re-etched using a solution composed by 0.10 g of $Na_2S_2O_5$, 5 ml of HCl and 1 ml of HNO_3 in 60 ml H_2O, to highlight other features respect to those revealed by the Beraha's etchant.
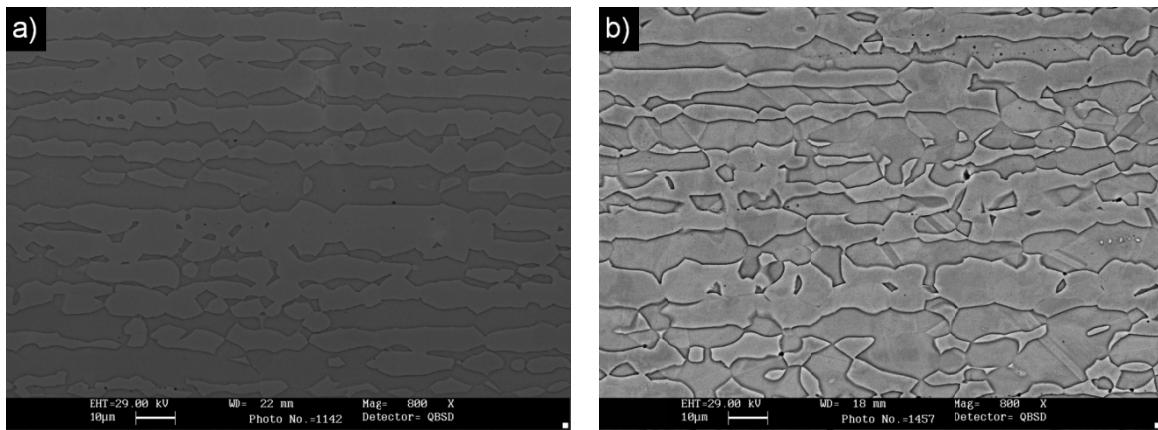

Fig. 3.20 – AR microstructure of SAF 2205 (SEM-BSE): a) Beraha's etchig and b) oxalic acid.

As previously reported, the as-received SAF 2205 DSS exhibited a well-balanced microstructure, composed by almost equal volume fractions of the two phases (Table 3.10), with the austenitic grains (γ) dispersed inside a ferritic matrix (α) and elongated toward the direction of the previous hot-rolling process (Fig. 3.20).

Table 3.10 – Volume fractions, hardness and refined parameters of the phases in the AR samples.

	phase fraction (vol.%)		HV$_{0.025}$	ToF Rietveld parameters (bank 1)			
	OM	ToF		cell dimension a [A]	crystallites size [A]	microstrain S_{400}	texture index J
Ferrite (α)	45.5	43.2	375	2.87906	2425	0.991	9.482
Austenite (γ)	54.5	56.8	345	3.60637	4106	0.177	1.393

As expected, in the solution-annealed material the phases have different hardness, with ferrite slightly harder than austenite (Table 3.10), owing to recovery and recrystallization stages occurred during the solution-annealing treatment. The subsequent cold deformation

caused a different hardening of the two phases, because to their different crystal structures, leading to the observed shapes of the hardness curves (Fig. 3.21).
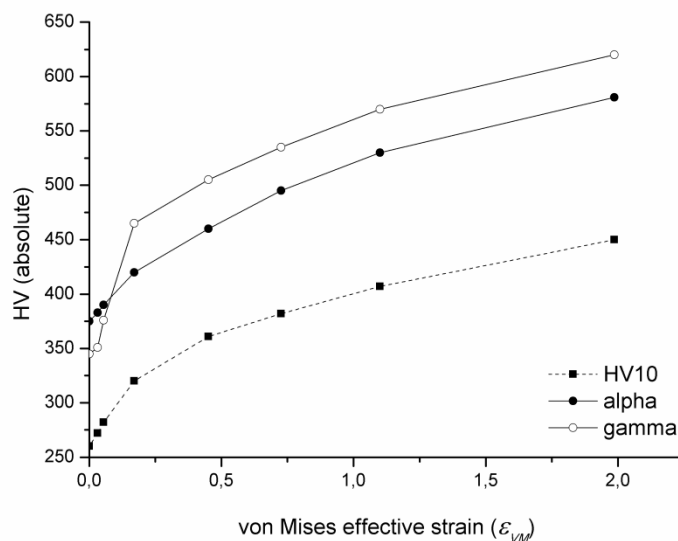

Fig. 3.21 – Ferrite and austenite micro-hardness variation (HV$_{0.025}$), together with the global hardness HV$_{10}$.

In austenite, as a FCC phase, the strain-hardening rate was very high and a significant work-hardened state was reached at 15% of deformation, while the subsequent hardening was found to be more gradual and almost proportional to the thickness reduction (Fig. 3.21). Low thickness reductions (3%CR) allowed an easy deformation of the phase, but not all the grains contributed to this first hardening. From the observations, few traces of slip bands (nearly at 45° from the rolling direction) were mainly found within the annealing twins (Fig. 3.22a), even though a slight hardening also occurred in whole grains. However, not all twins were interested from slip bands, owing to the different orientations developed during the solution-annealing treatment, and the deformation was only concentred in those which developed a favourable orientation of the primary slip systems. It also must be notice that, in the solution-annealed state, austenite was still considerably oriented because to the previous hot-rolling process and the activation of the slip systems inside the non-twinned parts of grains could be difficult at the lower deformations. In the 5%CR samples the dislocation density was substantially increased, dislocations extensively started to interfere each other and hardness reached values comparable to that of ferrite at the same deformation degree. Again, twins were mainly interested to shear bands intersections and slip especially occurred in those twinned parts which grew acquiring a nearly-cubic

150

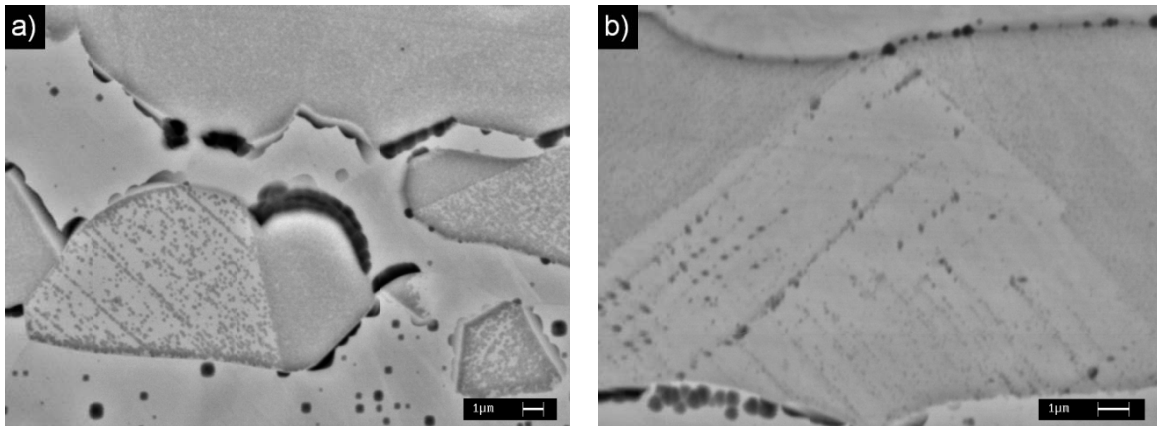symmetry, and for which a favourable orientation to the rolling force was achieved (Fig. 3.22b).

Fig. 3.22 – Traces of slip bands in austenite: a) 3%CR and b) 5%CR.

At 15% of deformation, several slip systems were activated and a great increase in hardness was measured, causing a considerable plastic flow and dislocation motion inside the grains, and almost all portions of the grains contributed to the deformation. In the 15%CR samples, a wide number of the shear bands intersections were observed (Fig. 3.23), justifying the substantial austenite hardening. Greater thickness reduction (from 35% to 85%) caused a progressive rising in hardness, shear bands were increasingly pronounced and all grains contributed to the deformation process, and a heavy grain fragmentation at the highest thickness reductions was observed.
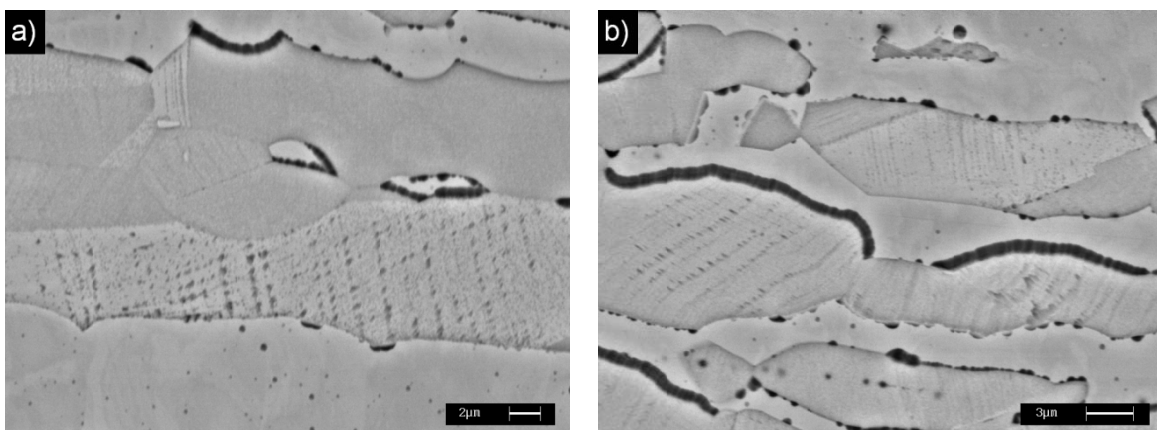

Fig. 3.23 – Shear bands intersections in austenite after 15% of thickness reduction.

Owing to its BCC structure, the activation energy of the primary slip system in the ferritic matrix is higher than in austenite, leading to a different response to cold working.

The observed increment in HV was indeed nearly regular in the whole deformation range (Fig. 3.21) and hardening was found to be almost linear with the thickness reduction. In the rolling plane, ferrite was elongated toward the rolling direction but, if compared to austenite, a greater thinning of the grains in the orthogonal direction was observed in the 85%CR samples, due to the activation of a considerable number of slip systems which allowed a greater deformation of the grains.

X-Rays Diffraction

The diffraction patterns depend on the microstructure achieved during the manufacturing process and the phases orientations can substantially affects the behaviour during the subsequent cold working. The XRD measurements were performed in only two directions respect to the rolling plane (RD and ND) and cannot be considered complete for a quantitative texture analysis. However, the presence of preferred orientations can be revealed and a qualitative description of the phases rearrangement can be made.
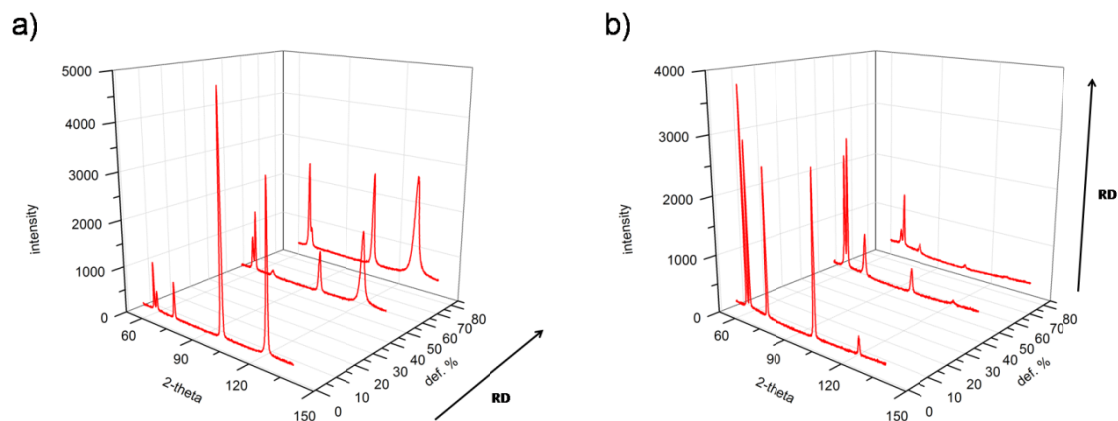

Fig. 3.24 – Diffraction patterns of SAF 2205 (AR, 50%CR and 85%CR):
a) rolling plane (RD) and b) normal plane (ND).

In the SAF 2205 DSS under study, the spectrum of the AR material along RD was characterized by very narrow peaks, because to the solubilisation, and the height of both $\alpha(200)$ and $\gamma(220)$ reflections respect to the α/γ principal peaks underlined a strong initial texture in the material (Fig. 3.24). For the AR material, the strong huge from the $\alpha(200)$ planes in the RD correlated to the spectrum obtained in ND, revealed that ferrite mainly had a {100} Cubic orientation, almost equally spread toward both <110> and <100> directions and which can be respectively ascribed to the previous hot-rolling process and to

the recrystallization occurred during solubilisation. In the AR-austenite, the dominant signal from the γ(220) planes in RD, coupled with the γ(200) reflections in ND, revealed the presence of a strong {110}<100> Goss-type texture component, which usually occurs during recrystallization in FCC metals and in the solution-annealed austenite in DSS [27]. Moreover, the huge signal from the γ(111) orientations along ND suggested the concurrent presence of a strong initial FCC rolling texture in austenite. After hot-rolling, considering the low SFE characterizing austenite in SAF 2205, the {110}<112> Brass-type component is more likely to be formed, but the presence of γ(111) in ND could be more correctly addressed to the {112}<111> Copper-type. If very strong hot deformations are involved, the development of this latter texture in austenite could be probable, as observed by [30] in a SAF 2507 DSS; hence, the achievement of the 10 mm thickness in the SAF 2205 bar under study may have required enough thickness reductions such that leading to the development of the pure metal texture. However, owing to grains restraints imposed by the biphasic structure, the possibility of incomplete textures development must be taken into account, and the effective texture developed cannot be exactly defined by the performed analysis.

Cold deformation caused a rearrangement of the grains, and such orientations-redistribution process strongly depended on the initial microstructure. After intermediate reorientations, at the highest thickness reductions both phases seemed to displace toward the main rolling textures directions and the huge peak broadening revealed a heavy grains refinement (Fig. 3.24). In the 85%CR samples, the strong α(200) reflections in RD and the quasi-absence of the α(200) signal in ND underlined that ferrite mainly displaced toward the {100}<110> Rotated Cubic orientation, but the slight presence of the α(110) reflections in the RD denoted that such orientation was not developed in the whole matrix. In the 85%CR-austenite, the low signal from γ(200) in ND suggested that the Goss-type component, achieved after the solubilisation, was almost disappeared because to the cold working and the strong presence of both γ(111) and γ(220) contributions in the RD suggested the presence of typical FCC rolling texture.

The deformation process and the texture development in austenite depend on the level of the internal stress and, as previously discussed, also to the inter-phase mechanisms, which can restrain the grains rotations. A strong correlation exists between the stacking fault frequency and the type of texture developed after heavy deformation and, in low SFE

materials, the stresses imposed by rolling and the presence of low amounts of cross-slip preferentially lead to the development of a Brass-type texture [33,65,66]. The Brass-type becomes increasingly effective as the deformation proceed, while a spread in orientations – and eventually the Copper-type texture – are dominant when extensively cross-slip occurs [33]. For low SFE materials – as the 2205 DSS – the Copper-type texture is difficult to achieve after cold deformation at room temperature, because it is not possible to get sufficient reduction for its development, and thus the Brass-type is generally the dominant one [33]. In the 85%CR-austenite, the absence of the $\gamma(200)$ reflections in RD revealed that any type of cubic orientation were lost after the cold working and the low amount of the $\gamma(111)$ in ND suggested that no – or very few – Copper component was formed. Thus, the strong contribution of both $\gamma(111)$ and $\gamma(220)$ planes in RD can be addressed to a Brass-type texture, already observed in different DSS grades [26,27] and in austenitic stainless steels [67], probably accompanied by incomplete grains rotations owing to the biphasic microstructure.

As previously pointed out, the assurance of these hypotheses requires a careful investigation, but it can be assured that both the inter-phases mechanisms of deformation and the band-like structure strongly influence the phases rearrangement, leading to restrained lattice rotations and thus to the possible occurrence of incomplete textures developments. Austenite, being the "second phase", is more prone to such restrictions, owing to the presence of the ferritic matrix, and the development of harder boundaries could avoid the complete grains reorientation.

The use of XRD is helpful to reveal SIM in fully austenitic stainless steels but, due to the presence of ferrite and also to the similarity of its lattice parameter to that of SIM [13], in DSS this kind of analysis cannot clearly reveal if the transformation took place. If such transformation occurred, SIM and ferrite peaks will be superimposed, making a pattern analysis difficult to be performed. The strong solution-annealed and cold-rolled textures in SAF 2205 hindered the full-pattern refinements performed by the Rietveld method, making a phases quantification not estimable and making XRD unhelpful for a SIM investigation. Moreover, it must be considered that XRD, being a surface technique, could be influenced by the strain-hardening occurred on samples after the grinding/polishing procedures, leading to a misrepresentation of the results.

Nevertheless, the presence of huge γ-peaks at the highest thickness reduction underlined that, if the martensitic transformation occurred, it would not interested the whole austenitic phase and, moreover, no HCP ε-martensite was detected. The absence of ε-martensite could be ascribed to either the possibility of a direct $\gamma \rightarrow$ SIM transformation through dislocations reaction [34] or a too low amount of the metastable hexagonal phase. In this latter hypothesis, the registered signal couldn't have reflected the real microstructure of the samples because, since x-rays are conditioned by the electron cloud surrounding the atoms bonds, the resulting background signal could be too much high, causing the hiding of small peaks which would be confused into it.

Neutron Time-of-Flight Diffraction

ToF-ND measurements can overcome the limits imposed by the XRD analysis method, owing to the high penetrating power of neutrons. Neutron diffraction patterns can indeed represent the real bulk conditions of the samples because for neutrons the atoms nuclei are real point-scatterer, resulting in a real description of the microstructure inside the samples. As previously reported, the Rietveld refinements of the diffraction patterns were carried out using the GSAS code and the more significant phases parameters are reported in Table 3.10.

As can be seen from Table 3.10, the phases fraction in the solution-annealed material is very close to that estimated by the image-analysis procedure on the optical micrographies, reflecting the well-balanced microstructure. The volumetric fractions were determined by a multi-pattern refinement, considering the average value provided by GSAS after the analysis of all the diffraction banks, except the forward-scattering one due to its poor resolution. Since ferrite and SIM have the same lattice parameters [13], the two phases cannot be readily distinguished – due to a superimposition of the diffraction peaks – but, if such transformation occurred, an increment of the BCC phase volume fraction with thickness reduction is expected. From the refinements, it can be assured that cold rolling caused a change in the phases fraction (Fig. 3.25a) and, specifically, a decreasing in austenite volume content was observed as the deformation proceeded, pointing out that the SIM transformation took place in the DSS under analysis. This increasing in volume fraction of the BCC phase was observed from the 35%CR samples ($\varepsilon = 0.451$), underlining that the austenitic phase in the 2205 DSS under analysis is more stable if compared to the

austenite in AISI 304L. In the austenitic steel, the SIM transformation at room temperature occurs since the early stages of deformation, also in plane strain conditions [7,47], while no variation in phase fraction was registered at the lower thickness reductions in the DSS under study.
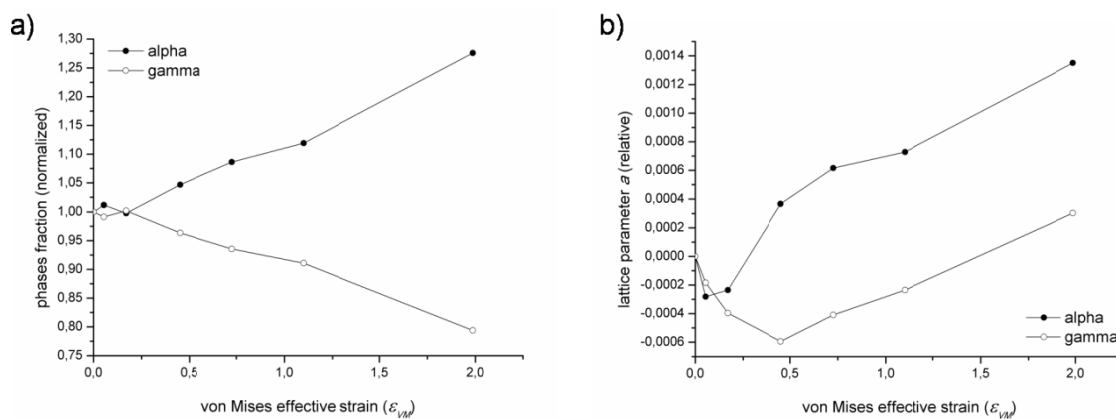

Fig. 3.25 – Effects of deformation in SAF 2205: variation in a) phases fraction and b) lattices parameter.

The lattice parameters of the phases are reported in Table 3.10 and the relative lattice parameter variation as a consequence of the plastic deformation is shown in Fig. 3.25b. It is known that cold working causes a progressive increment in the number of defects, due to the strain-hardening, and also induces residual stresses which depends on the applied load (strain). The results evidenced that at low strains the plastic deformation caused a reduction in the unit cell edge in both phases, and this was especially evident in austenite. In ferrite, after an initial contraction of the lattice parameter (5%CR sample), a subsequent inversion of the trend was registered, while in austenite the edge reduction has proceeded up to 35% of deformation before the occurrence of such inversion. The observed initial reduction in both lattices can be ascribed to the presence of residual compression stresses caused by the rolling process and which were more pronounced in austenite, owing to the greater deformability of the FCC phase. Generally, an increasing in dislocation density and defects lead to localized lattice distortions which can cause an increasing of the measured lattice parameter, because the number of vacancies and extra-planes inside the lattices are increased. In the case under study, the first stages of deformation were characterized by a higher effect of the residual stress respect to the generation of new defects and thus a reduction in lattice parameters was registered. When the formation of vacancies and dislocations was sufficiently high, the local distortions overcame the stress effect and an

inversion of the decreasing trends was observed. The generation of a great amount of defects caused the expected increasing in the relative lattice parameter variation, which occurred in different extent in the two phases due to their different plastic behaviour.

As suggested by the broadening of the x-rays diffraction peaks, the cold deformation caused a heavy grains refinement. The crystallites size of the phases can also be estimated from the broadening of the neutron peaks and must be intended as the average size of the phase volume which is free of defects (such as dislocations and stacking faults). The average crystallites size for both phases in the AR samples are reported in Table 3.10 and, from a comparison with the observed microstructure, the obtained values were smaller than expected. This is due to an instrumental upper limit on the correctly detectable size, which is in the order of 100 nm [20], whereas smaller values can be reliably determined. Hence, in the solubilised samples, the reported average sizes must be only considered from a qualitative point of view, being the real value bigger than the refined one; conversely, the refined sizes as a result of the plastic deformation are the effectively achieved ones. Thus, the solution-annealed grains, although of the same order of magnitude, were coarser in austenite than in ferrite, owing to the greater recrystallization grade achieved by the FCC phase during solubilisation, as also confirmed by the SEM observations. In Fig. 3.26a the crystallite sizes evolution is shown as a function of the applied equivalent strain, and both phases globally exhibited similar trends as the thickness reduction increased. Low deformations (5%) caused the strongest reduction in defect-free areas, which was more evident in austenite, underlining the greater increase in dislocation density occurring in the FCC phase at low strains and justifying the measured increment in hardness. Further thickness reductions caused a progressive reduction of the crystallite size in both phases, reaching a plateau after 35% of deformation, with the defects density more concentrated in austenite (smaller grain size). The global trend is in agreement with several results reported in literature [1,68], even though both phases reached constant size values which are shifted toward very low levels of strain respect to other materials, and were also interested by a heavier grain fragmentation. This strong and readily grain fragmentation can be addressed to compositional factors and also to the biphasic microstructure. As a matter of fact, the increased amount of substitutional alloying elements lowers the SFE of the phases, leading to a more effective resistance to dislocation motion and inhibiting extensive dislocations cross-slip; thus, the formation of dislocation boundaries and the achievement of smaller

mean cell sizes were favoured. Similarly, the peculiar DSS microstructure allowed to determine a reduction of the dislocations average free paths, contributing to a more rapid formation of cells and subgrains.
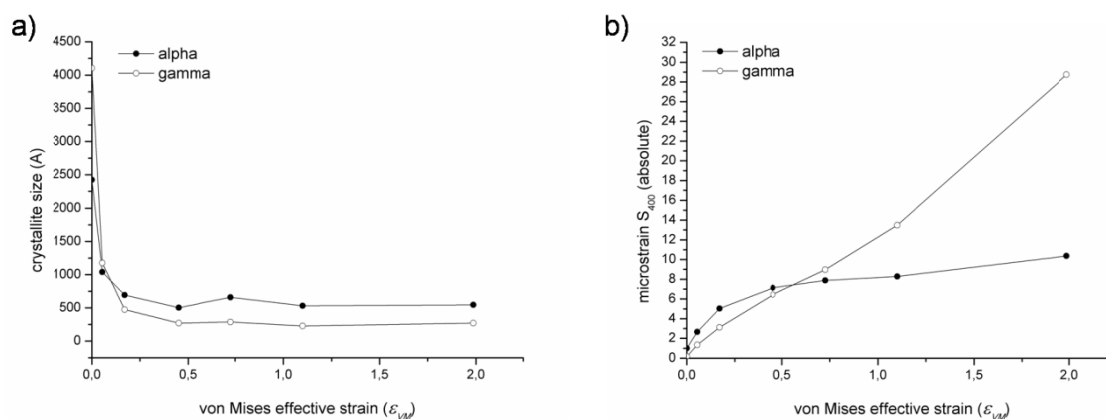

Fig. 3.26 – Effects of deformation in SAF 2205: variation in a) crystallites size and b) microstrain indexes.

The microstrain of the phases was evaluated by means of the S_{400} parameter, which is usually employed for microstrain determination in cubic crystals, together with the S_{220} coefficient [22]. In the case under study, the S_{220} parameter was found to be negative – and thus with not associable physical meanings – therefore, only the S_{400} parameter was refined. The microstrain indexes of the phases in the AR samples (in microstrain units [22]) are reported in Table 3.10 and, as expected, were found to be low, due to the solution-annealing treatment which restored the microstructure in terms of lattice strains. The absolute increase in microstrain indexes as a result of cold rolling is reported in Fig. 3.26b and revealed an increment in the strain field in both phases as the thickness reduction increased, but with different trends. Austenite was subjected to a ever increasing microstrain field, while in ferrite the measured strain nearly approached a saturation value at the highest deformation degree. These different behaviours can again be addressed to the Duplex structure and therefore to the constrained-state of austenite, which caused a progressive intensification of the strain field in the FCC phase. On the contrary, owing to its continuous character, the ferritic matrix was more free to deform, thus resulting in a minor intensification of the developed stress field. Moreover, it must be notice that the S_{400} parameter is associated to a spherical representation of the strain field at which the phases are subjected, and therefore is conditioned by the deformation mode. In the case under study, austenite underwent severe plastic deformation, especially in the rolling plane, and

the measured relative increment of the longitudinal stress field was substantially higher than in ferrite, which instead was more reduced in the orthogonal direction (greater thinning). These different deformation states changed the phases strain fields, which were no longer spherical, forcing the values of the S_{400} parameter to assume different values for the phases. Austenite was more deformed in the rolling plane than ferrite thickened in the orthogonal direction, leading to the observed difference in the estimated microstrain parameters.
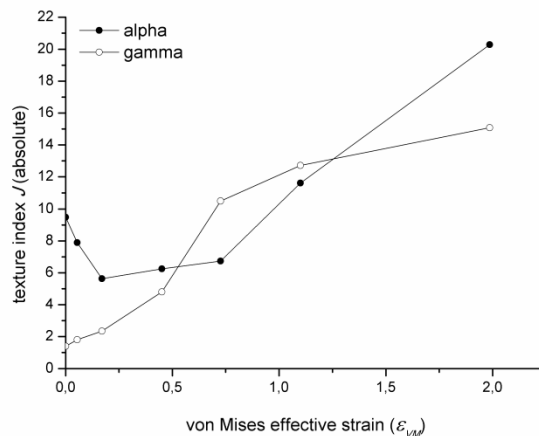

Fig. 3.27 – Texture indexes variation as a function of the effective strain.

Refinements also provided an estimation of the texture index J, defined as the ratio between the total volume of grains divided by the volume of the non-oriented grains [22]. This type of analysis was performed only on the first diffraction bank (bank-1), taking into account the spherical-harmonic approach [22], and thus without any information on which would be the specifics preferred orientations assumed by the phases, but was useful to evidence the orientation and re-orientation processes developed during rolling. The texture indexes in the AR samples are reported in Table 3.10, while their evolution during the cold working is shown in Fig. 3.27. As can be seen, in the solution-annealed conditions ferrite was still strongly oriented, as also revealed by XRD, while the texture in austenite was maintained within typical values for the medium-textured materials. Clearly, the recovery and recrystallization stages in the phases took place at different time during the solubilisation and the measured texture indexes in the AR sample were affected by these different responses. Comparing Figs. 3.24a and 3.27, the reorientation of ferrite is clearly evident. Cold working caused a rearrangement of the grains and, starting from a (double) cubic texture in the AR conditions, ferrite passed through intermediate rotations, reaching a

heavily rolling-oriented state at 85% of thickness reduction. The situation is different in austenite, since recrystallization and rolling textures are different and are not both cubic. The texture index always increased during the whole deformation process due to the rolling texture development and to the concurrent disappearance of the Goss-type component. However, a change in the curve slope in Fig. 3.27 can be noticed after the 50% of deformation, which can be ascribed either to a saturation of the texture development, due to the restraints imposed by the biphasic structure, or to the incomplete reorientation of grains, as discussed in the previous XRD section.

TEM investigation

Neutron diffraction revealed the possibility of the martensitic transformation in SAF 2205, but the estimated volume fractions were rather low, also after the maximum thickness reduction (see next section); thus, only the 85%CR samples were subjected to electrochemical preparation for TEM observations. Unfortunately, performing an investigation on heavy cold rolled samples may be difficult, since the presence of a substantially increased number of defects may interfere with the observation, making the detection of the new phase more complicated. However, considering the low SIM amounts developed throughout the entire deformation process, the probability of finding a polished area containing martensite was higher in 85%CR samples than for the others.

Plastic deformation is known to cause the formation of substructures. Dislocations arranges into high-density tangles as the deformation proceeds and grains are progressively subdivided into cells, resulting in the development of a structure composed by cell blocks. Each block is subdivided in defect-free cells by Incidental Dislocations Boundaries (IDBs) and is separated from the neighbouring one by walls originated by the fusion of microbands, called Geometrically Necessary Boundaries (GNBs). Increasing the deformation, this blocks-structure is maintained and tends to assume a lamellar configuration throughout blocks rotations; very high deformations lead to ever finer microstructures with blocks separations in the order of few thousand of nanometers, but it is not clear if a saturation limit is reached. In low-SFE materials, the features generated by cold-working may be very complex, owing to the simultaneous presence of dislocation substructures, microtwins and, frequently, large proportion of shear bands; moreover, if the

material possess a Brass-type texture, large strains can cause a rapidly rise in dislocation density and a cellular structures may eventually develop [1].
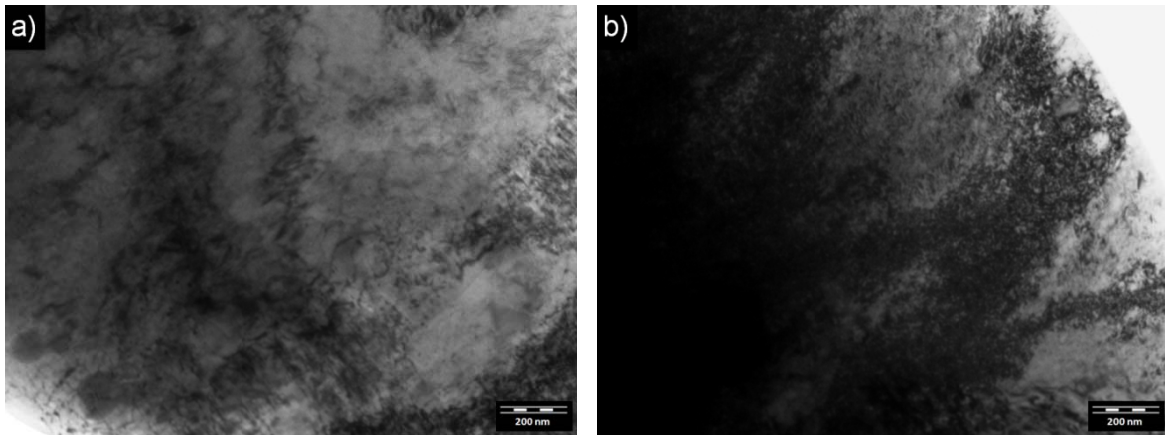

Fig. 3.28 – Deformed microstructures: a) austenite and b) ferrite.

As expected, the deformed microstructures in the 85%CR samples were characterized by a high density of dislocations (Fig. 3.28). Despite the very low SFE, the highest thickness reduction determined the generation of a cellular structure in austenite, with cell blocks separated by GNBs (Fig. 3.29a) and where the IDBs developed within them exhibited traces of the double cross-slip mechanism, as already observed in DSS [69]. As previously reported, the cell formation was eased by the biphasic structure, and therefore by the existing more complex interaction mechanisms than in single-phase steels, causing the observed grains fragmentation and substantially lowering the mean defect-free cell size, as revealed by neutrons (Fig. 3.29b).
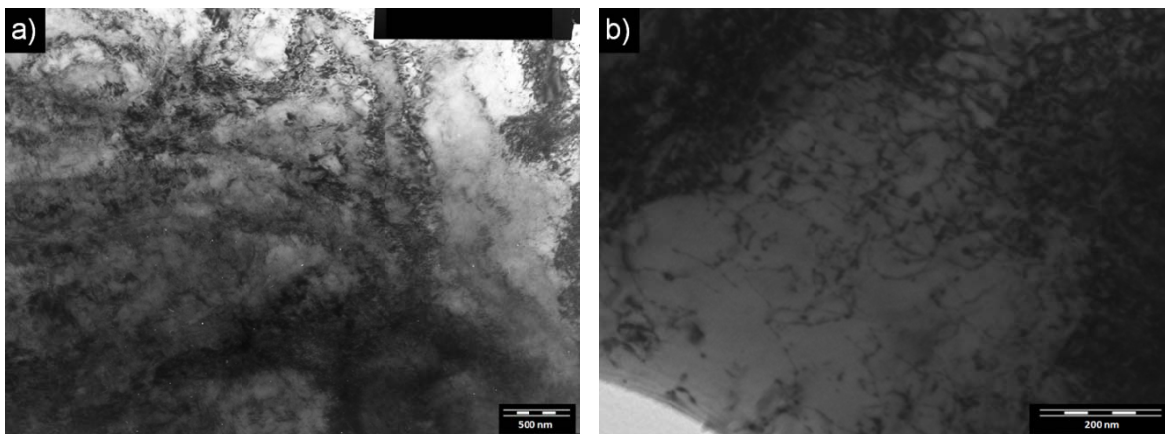

Fig. 3.29 – Cellular structure in austenite: a) cell block separated by GNBs
and b) defects-free cells separated by IDBs.

Besides the effects of deformation on microstructure, the TEM investigation was mainly aimed to reveal the presence of SIM within austenite, as suggested by the ToF-ND refinements. As a matter of fact, the observations confirmed the presence of the strain-induced martensite, even though the significant microstructural disorder in the 85%CR sample hindered an immediate detection of SIM, being able to be confused with other microstructural features. As can be seen from Fig. 3.30a, SIM can be revealed such as regions having a deep dark contrast inside the austenitic grains and surrounded by dislocations agglomerates, but without assuming the characteristic lath-like shape, owing to the increased deformation degree, as also observed by [11] for a fairly grown SIM. However, the pertaining diffraction pattern clearly revealed the presence of the martensitic BCC-structure within the FCC austenitic grains (Fig. 3.30b).
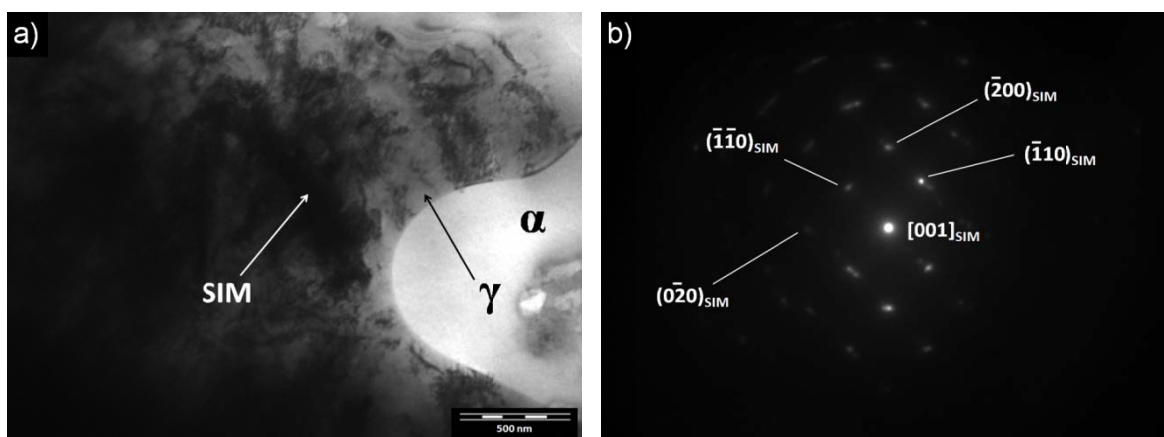

Fig. 3.30 – Strain-Induced Martensite in austenite: a) transformed region
and b) corresponding diffraction pattern.

Strain-Induced Martensite quantification

The martensitic transformation took place in the SAF 2205 DSS and, despite the low SFE value of austenite, it occurred in a significantly lower extent respect to metastable austenitic stainless steels. The estimated volume fraction of SIM from neutron diffraction data was below 14% at the highest deformation degree, underlining the greater stability at room temperature of DSS-austenite, if compared to the austenitic steels. In Fig. 3.31, the volume fraction of SIM obtained from ToF-ND refinements is reported as a function of the applied equivalent strain, together with the estimated quantity from the SEM micrographies. As pointed out in the previous Paragraph 3.2.1, the investigation on the Beraha's etched samples suggested the presence of SIM, and the estimated volume

fractions by image-analysis on the SEM micrographies were in very good agreement with the data from neutrons, confirming the reliability of the performed metallographic quantification. Notice that the slight difference in phases content observed in the 5%CR samples was in the same order of magnitude of the estimated error and could be ascribed to local inhomogeneities, which are always present in these types of materials.
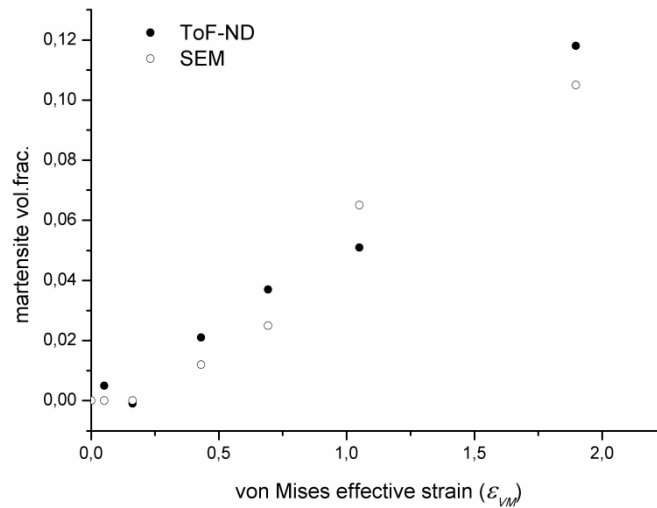

Fig. 3.31 – Estimated amount of Strain-Induced Martensite in SAF 2205 (ToF and SEM data).

SIM transformation is strongly temperature-dependent and all the data concerning austenitic stainless steels evidenced the tendency to reach a saturation value in martensite volume fraction, especially at low temperatures. The strain level at which this saturation occurs depends on the testing temperature and is ever lower as the temperature decreases. The results of the present work confirmed the investigation performed by Tavares *et al.* [47], since the investigated materials and the SIM volume fractions are strictly comparables, highlighting the different behaviour of the SAF 2205 at room temperature respect to that of austenitic steels. In SAF 2205, austenite was increasingly transformed within the considered deformation range and any martensite saturation was not observed, as also reported in [47] even for thickness reductions up to 96.6% and from which the kinetic of such transformation seemed to follow an exponential relation. However, the work presented by Reick *et al.* [56] on a similar DSS grade reported a saturation in SIM formation after 60% of thickness reduction. Probably, this difference could be ascribed to the analysis method, which was not free of errors due to the crystal disorder occurred after the deformation, as pointed out by the authors.

An attempt was made to fit the obtained data by using the equation proposed by Olson and Cohen [12], which is currently employed to model the kinetics of SIM in austenitic stainless steels:

$$f^{SIM} = 1 - \exp\{-\beta[1 - exp(-\alpha\,\varepsilon_{VM})]^n\} \qquad (3.5)$$

In this equation, the volume fraction of SIM (f^{SIM}) is related to the effective plastic strain ε_{VM} by the two temperature-dependent parameters α and β. The former constant is related to the path of shear bands formation, while the latter is proportional to the probability that an intersection will form a SIM embryo. The value of the exponent n was found to be 4.5 for austenitic stainless steels and was determined considering the best overall agreement between the model and the experimental result in the temperature range -188–50°C [12]. In austenitic steels this fitting curve is generally sigmoidal and its S-shape is emphasized at the lower strains as the temperature decreases, underlining a saturation in the martensite volume fraction at the higher deformation degrees.
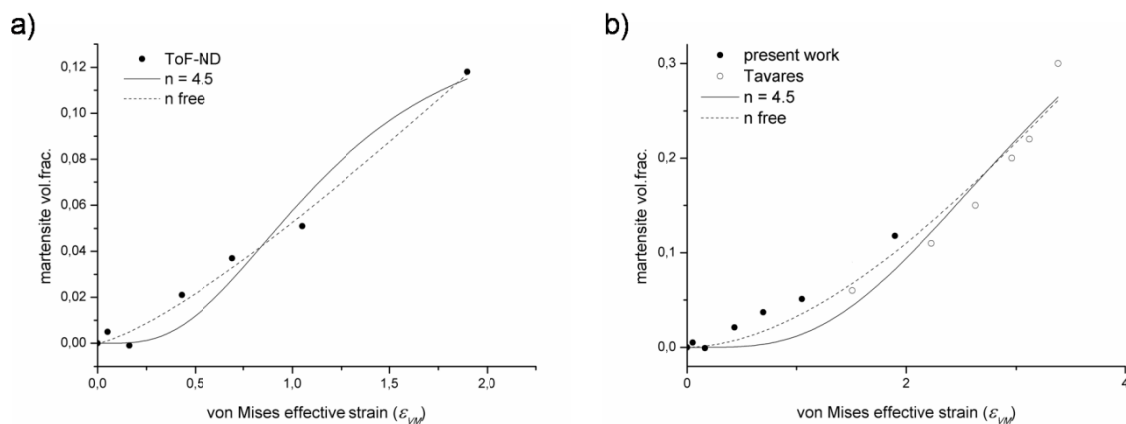
Fig. 3.32 – SIM transformation kinetics. Application of the Olson&Cohen model [12] to:
a) Neutron ToF data (present work) and b) adding the results in Tavares *et al.* [47].

Nevertheless, since in the steel under study the saturation wasn't reached and considering the results presented in [47], it can be supposed that the model cannot provide a reliable description of the SIM kinetics in DSS. As a matter of fact, using the results achieved by neutrons (Fig. 3.32a), the value $n = 4.5$ forced the regression curve to acquire a sigmoidal shape, resulting in a poor fitting in terms of R^2 (0.95) and causing the other parameters assume values comparable to that of austenitics at the higher temperatures

(about 50°C in [12]). On the contrary, letting the exponent free to vary caused a collapse of the regression curve into a nearly-exponential type (Fig. 3.32a), without any meaningful values of the regression parameters. Another attempt was made by adding to the results of the present investigation the martensite amounts estimated by [47] (Fig. 3.32b); however, it is evident that the trend of SIM formation is better described by an exponential law, rather than a sigmoidal curve. In fact, trying to fit the entire dataset with the proposed model always caused a collapse of the regression curve into an exponential-type, pointing out the inapplicability of such regression analysis to DSS. Thus, in order to describe the kinetics of SIM formation in this class of steels, a deeper analysis must be carried out, considering various DSS grades and taking into account both the effect of temperature and the possible contribution of different microstructures.

Concluding remarks

The results presented in this section has evidenced the occurrence of the strain-induced martensitic transformation in SAF 2205 DSS. SIM was found to form in the low-alloyed DSS grades, such as SAF 2101 [24], and its appearance in SAF 2205 was not completely unexpected. The presence of a low amount of γ-promoting elements, although greater than in SAF 2101, makes austenite in any case unstable at room temperature, and therefore more prone to undergo this diffusionless process after cold plastic deformation.

However, the present investigation underlined the greater stability of DSS-austenite in SAF 2205 at room temperature if compared to austenitic stainless steels, as also evidenced by Tavares *et al.* [47], and the amount of SIM was estimated below 14% of the volume fraction at the highest thickness reduction. Moreover, the transformation kinetics were different. In SAF 2205, the estimated amount of SIM was ever increasing in the whole deformation range and any saturation in martensite amount wasn't reached, as also reported by [47] for further thickness reductions. Thus, the model proposed by Olson and Cohen [12] to describe the SIM transformation kinetics is not applicable in DSS and a deeper study is required, considering different DSS grades and taking into account other variables such as temperature and microstructure.

Nevertheless, the presence of SIM in SAF 2205 did not affect its extraordinary combination of properties. The mechanical stiffening induced by cold working will probably lead to a reduction in impact toughness in the transverse direction respect to the

rolling plane, but the corrosion properties did not suffer of the martensitic transformation. As reported in Paragraph 3.2.4, cold working – and therefore the presence of SIM – did not substantially alter the corrosion behaviour of SAF 2205, and especially its resistance against localized pitting attacks. As a matter of fact, a slight reduction in Critical Pitting Temperature was found to occur only after 85% of deformation, whereas the pitting resistance at room temperature was not influenced by cold deformation.

REFERENCES

[1]   J. Gil Sevillano. *Prog Mater Sci* 25 (1981) 69.
[2]   D. A. Hughes and N. Hansen. *Acta Mater* 45 (1997) 3871.
[3]   R. E. Schramm and R. P. Reed. *Metall Trans A* 6A (1975) 1345.
[4]   R. E. Schramm and R. P. Reed. *Metall Trans A* 7A (1976) 359.
[5]   P. Seetharaman and J. Krishnan. *J Mater Sci* 16 (1981) 523.
[6]   G. B. Olson and M. Cohen. *J Less-Common Met* 28 (1972) 107.
[7]   S. S. Hecker, M. G. Stout, K. P. Staudhammer and J. L. Smith. *Metall Trans A* 13A (1982) 619.
[8]   R. Lagenborg. *Acta Metall* 12 (1964) 823.
[9]   P. L. Mangonon and G. Thomas. *Metall Trans* 1 (1970) 1577.
[10]   F. Lecroisey and A. Pineau. *Metall Trans* 3 (1972) 387.
[11]   K. Spencer, M. Véron, K. Yu-Zhang and J. D. Embury. *Mater Sci Tech Ser* 25 (2009) 7.
[12]   G. B. Olson and M. Cohen. *Metall Trans A* 6A (1975) 791–795.
[13]   P. Haušild, V. Davydov, J. Drahokoupil, M. Landa, P. Pilvin. *Mater Design* 31 (2010) 1821.
[14]   A. Das, S. Sivaprasad, M. Ghosh, P. C. Chakraborti, S. Tarafder. *Mat Sci Eng A* 486 (2008) 283.
[15]   J. Talonen, H. Hänninen. *Acta Mater* 55 (2007) 6108.
[16]   A. Hedayati, A. Najafizadeh, A. Kermanpur, F. Forouzan. *J Mater Process Tech* 210 (2010) 1017.
[17]   J. M. Diani and D. M. Parks. *J Mech Phys Solids* 46 (1998) 1613.
[18]   F. Fiorillo. *Measurements and characterization of magnetic materials*. Elsevier Publishing Company, Amsterdam, The Nederlands (2004).
[19]   I. Mészáros and P. J. Szabo. *NDTE Int* 38 (2005) 517.
[20]   S. Imberti, W. Kockelmann, M. Celli, F. Grazzi, M. Zoppi, A. Botti, A. Sodo, M. Leo Imperiale, M. de Vries-Melein, D. Visser and H. Postma. *Meas Sci Technol* 19 (2008).
[21]   A. C. Larson and R. B. Von Dreele. *General Structure Analysis System (GSAS)*. Los Alamos National Laboratory Report LAUR (1994) 86.
[22]   A. C. Larson and R. B. Von Dreele. *GSAS Manual* (2004).
[23]   G. F. Vander Voort. *Metallography: Priciples and Practice*. ASM International (2007).
[24]   P. Bassani, M. Breda, K. Brunelli, I. Mészáros, F. Passaretti, M. Zanellato and I. Calliari. *Microsc Microanal* 19 (2013) 988–995.
[25]   B. Verhaeghe, F. Louchet, B. Doisneau-Cottignies, Y, Bréchet. *Phil Mag* 76 (1997) 1079.
[26]   J. A. Jimenez, M. Carsi, O. A. Ruano. *J Mater Sci* 35 (2000) 907.
[27]   J. Ryś, M. Witkowska. *Arch Metall* 55 (2010) 733.
[28]   J. Keichel, J. Foct and G. Gottstein. *ISIJ Int* 43 (2003) 1781.

[29]   J. Keichel, J. Foct and G. Gottstein. *ISIJ Int* 43 (2003) 1787.

[30]   J. Hamada and N. Ono. *Mater Trans* 51 (2010) 635.

[31]   C. H. Shek, G. J. Shen, J. K. L. Lai and B. J. Duggan. *Mater Sci Forum* 157–162 (1994) 853.

[32]   L. Duprez, B. C. De Cooman and N. Akdut. *Steel Res* 73 (2002) 531.

[33]   I. L. Dillamore and W. T. Roberts. *Acta Metall* 12 (1964) 281.

[34]   I. Altenberger, B. Scholtes, U. Martin, H. Oettel. *Mat Sci Eng A* A264 (1999) 1.

[35]   Z. Szaklarska-Smialowska. *Corrosion* 27 (1971) 223.

[36]   D. C. Cook. *Metall Trans A* 18A (1987) 201.

[37]   A. Randak, F. W. Trautes. *Werkstoffe und Korrosion* 21 (1970) 97.

[38]   K. Elayaperumal, P. K. De, J. Balachandra. *Corrosion* 28 (1972) 269.

[39]   S. V. Phadins, A. K. Satpati, K. P. Muthe, J. C. Vyas, R. I. Sudaresan. *Corr Sci* 45 (2003) 2467.

[40]   F. Navai. *J Mater Sci* 30 (1995) 1166.

[41]   N. D. Greene, G. A. Saltzman. *Corrosion* 20 (1964) 294.

[42]   A. Barbacci, G. Cerisola, P. L. Cabot. *J Electrochem Soc* 149 (2002) B534.

[43]   P. K. Chiu, S. H. Wang, J. R. Yang, K. L. Weng, J. Fang. *Mater Chem Phys* 98 (2006) 103.

[44]   N. J. Laycock, M. H. Moayed, R. C. Newman. *J Electrochem Soc* 145 (1998) 2622.

[45]   R. Qvarfort. *Corr Sci* 40 (1998) 215.

[46]   J. H. Wang, C. C. Siu, Z. Szaklarska-Smialowska. *Corrosion* 44 (1988) 732.

[47]   S. S. M. Tavares, M. R. da Silva, J. M. Pardal, H. F. G. Abreu, A. M. Gomes. *J Mater Process Tech* 180 (2006) 318.

[48]   R. N. Gunn. *Duplex Stainless Steels: Microstructure, Properties and Applications.* Abington Publishing, Cambridge, England (1997).

[49]   A. Wilson and G. Spanos. *Mater Charact* 46 (2001) 407.

[50]   R. Petrov, L. Kestens, A. Wasilikowka and Y. Houbert. *Mat Sci Eng A* A447 (2007) 285.

[51]   V. Randle. *Mater Charact* 60 (2009) 913.

[52]   F. Humpreys. *Scripta Mater* 51 (2004) 771.

[53]   B. E. Warren. *Prog Met Phys* (1959) 147.

[54]   C. G. Rhodes and A. W. Thompson. *Metall Trans A* 8A (1977) 1901.

[55]   R. P. Reed and R. E. Schramm. *J Appl Phys* 45 (1974) 4705.

[56]   W. Reick, M. Pohl and A. F. Padilha. *Steel Res* 67 (1996) 253.

[57]   N. Jia, Y. D. Wang and R. Lin Peng. *J Phys-Condens Mat* 20 (2008) 1.

[58]   J. Talonen, H. Hänninen. *Acta Mater* 55 (2007) 6108.

[59]   M. J. Whelan, P. B. Hirsh, R. W. Horne and W. Bollmann. *Proc Roy Soc A* 240 (1957) 524.

[60]   L. E. Murr. *Thin Solid Films* 4 (1969) 389.

[61]   J. F. A. Borges, A. F. Padilha and K. Imakuma. *Rev Brasilera de Fisica Aplicada e Instrumentaçao* 1 (1986) 335.

[62]   H. J. Kestenbach. *Metalurgia* 32 (1976) 181.

63]   F. B. Pickering, Proc. Conf. *Stainless Steels '84*. The Institute of Metals, London (1984) 12.

[64]   K. H. Lo, C. H. Shek, J. K. L. Lai. *Mat Sci Eng R* 65 (2009) 39.

[65]   H. Hu, S. R. Cline and R. S. Goodman. *J Appl Phys* 32 (1961) 1392.

[66]   R. E. Smallman and K. H. Westmacott. *Phil Mag* 2 (1957) 669.

[67]   D. Raabe. *Acta Mater* 45 (1997) 1137.

[68]   G. A. Malygin. *Phys Solid State* 48 (2006) 693.

[69]   U. Messerschmidt, M. Bartsch. *Mater Chem Phys* 81 (2003) 518.

APPENDIX A

Industrial applications of Duplex Stainless Steels

Duplex Stainless Steels (DSS) are very interesting materials and their employment in aggressive environments is presently of increasing interest. The beneficial properties and limits of these steels are presented throughout the present thesis, discussing the various difference arising from different composition and after both isothermal heat treatments and cold working. But what about their real industrial applications? Some of them are listed in Chapter 1, covering a wide range of possibilities where the choice of DSS in particular environment is preferred. As evidenced in this thesis, these steels must be handled with extreme care, in terms of specific use, especially if thermal cycles are involved and also if cold plastic deformation is needed to acquire peculiar shapes or sizes. As a matter of fact, the production of big pipes requires manufacturing welding operations on steel plates or sheets, and frequently the materials must be cold worked to reach the final product dimensions. Thus, the effective employment of DSS must be accurately chosen, considering all the possible situations which can alter their microstructure, in order to avoid undesired effects.

In this appendix, two examples of DSS employment in seawater applications are discussed, concerning their usage for pipelines production in off-shore platforms and for armouring wires in subsea cables.

A.1 Characterization of UNS S32760 welded joints for Off- Shore applications

The UNS 32760 is a Super Duplex Stainless Steel (SDSS), also known as Zeron®100, which can be thought as an improved version of the SAF 2507, containing W and a greater amount of Cu to enhance the corrosion resistance. This grade is a high-alloyed DSS, reaching very high values of mechanical properties combined to excellent resistance to

stress corrosion cracking (SCC) and intergranular corrosion in marine environments. Hence, in Off-Shore engineering, its use permits to design components having smaller thicknesses – and therefore lighter – without compromising the corrosion resistance and avoiding the use of expensive anti-corrosion coatings.

From the welding point of view, SDSS must be managed as austenitic stainless steels but using dedicated devices, in order to limit the occurrence of corrosion caused by the formation of undesired structures. As reported in Chapters 1 and 2, DSS – and especially SDSS – are very sensitive to secondary phases precipitation (σ- and χ-phases, nitrides) if subjected to improper thermal cycles in the temperature range 850–950°C, even for very short times. The formation of the two intermetallic phases χ and σ is essentially due to the instability of ferrite at high temperatures, whereas the formation of nitrides is associated to the low solubility of nitrogen in ferrite at room temperature and to specific heating/cooling conditions at which the steel is subject. These phases must be avoided, since they severely worsen the good performances of these steels by lowering their toughness and making them more prone to corrosive attack [1].

In this first part of this section, the development of a welding procedure for joining a UNS S32760 SDSS (commercially F55) is described. The particularity of the examined case consists in the requested combination of mechanical and microstructural features of the weldment, at the limits for a reproducible welding procedure, suitable to be used as manufacturing process compatible to production requirements. Therefore, it was necessary to carefully design the welding procedure, choosing the best process parameters in order to achieve the required results.

The whole process was monitored and controlled throughout the quality management system of special welding process in *De Pretto Industrie* company, according to the ISO 3834-2 standards.

Welded joint requirements
The F55 SDSS is systematically and industrially welded around the world, including Italy. In the past 5 years, the requests coming from various contractual specifications for the realization of welds have became much more restrictive, especially for those parts intended for Off-Shore applications. Increasingly restrictive ranges of impact toughness values at low temperature and ferrite content, and the required corrosion resistance have caused not

negligible implications on the realization of final products, both for manufacturers and filler materials producers. Moreover, the obtainment of the expected features must be intimately connected to an accurate control of the welding parameters, such as voltage, current intensity, welding speed, interpass temperature and heat input. Therefore, the achievement of the desired final characteristics must be necessarily accompanied by a proper design of the welding procedure.

Table A.1 – Welding joint requirements.

Test	Requirements
Transversal sections [ASME IX Ed.10 QW462.1(b)]	Ultimate tensile strength 750 MPa
Prova di piega laterale [ASME IX Ed.10 QW462.2]	[ASME Sec. IX]
Charpy impact toughness (-46°C) [ASTM E 23-07 ae1] welding zone – fusion line fusion line + 2 mm – fusion line + 5 mm	45 J average 35 J minimum on single specimen
Hardness HV_{10} [EN ISO 6507-1:2006]	Maximum 350 HV_{10}
Macrographic examination [EN 1321:1997 and EN ISO 15614-1:2012 par. 7.5]	[ASME Sec. IX]
Micrographic examination at 0° and 180° [ASTM E 3-11]	At 100x and 500x magnification on base material heat affected zone (shielding) – heat affected zone (root) welding zone (shielding) – welding zone (root)
Ferrite content (%) [ASTM E 562-11 and ASTM E 1245-03]	Admitted values 25–65% base material heat affected zone (shielding) – heat affected zone (root) welding zone (shielding) – welding zone (root)
Corrosion (40°C for 24 hours) [ASTM G48-11 Method A]	no pitting admitted maximum weight loss of 4.0 g/m^2
Chemical analysis of the welding (optical spectrometry)	$PRE_N > 40$

The additional restrictions on welding techniques and the related tests aimed to their qualification have further limited the feasible welding operations. These constraints, in fact, impose the use of the Gas Tungsten Arc Welding (GTAW) process for the first welding passes, exclude the use of both Flux-Cored Arc Welding (FCAW) and Submerged Arc Welding (SAW) processes, and also impose very low limits on the usable heat input.

Moreover, the mandatory use of specific shielding gases and the additional technological restrictions have further limited the welding procedure design.

For the qualification of the procedure, the welded joint must comply with the combination of mechanical and microstructural features reported in Table A.1, depending on the demands of the design code (ASME BPVC). All joints must be subjected to non-destructive tests (Table A.2), according to ASME standard and to additional requests from customer and end user.

Table A.2 – Non destructive tests.

Test	Extent
Visual examination	100%
Penetrating-liquids examination	100%
Radiologic examination	100%
Ultrasonic examination	100%

As-received material

The UNS S32760 base material employed in the bead welding execution for the process qualification has been provided by the customer in form of sheet, which will be longitudinally welded to obtain the metal pipes (ASME SA928). The chemical composition and mechanical properties of the material (evaluated at room temperature, except where otherwise noted) are listed in Tables A.3 and A.4, respectively.

Table A.3 – UNS S32760 chemical composition [wt.%].

C	Mn	Si	P	S	Cr	Ni	Mo	N	Cu	W	PRE$_N$
0.02	0.642	0.359	0.0211	0.0007	25.173	6.886	3.585	0.2292	0.54	0.6414	40.67

Table A.4 – UNS S32760 mechanical properties.

$R_{p0.2}$ [N/mm^2]	R_m [N/mm^2]	A%	KV -46 °C [J]	Ferrite (%)	Hardness (HV$_{10}$)
695	863	31.5	118 (average)	44.87	max 302
	ASME. IX Ed.10 QW-150		ASTM A 370-11a	ASTM E 562-11	ASTM E 384-11
	transverse to the welding		welding zone and heat affected zone	minimum from welding zone and heat affected zone	maximum from base material, welding zone and heat affected zone

Design of the welding procedure

After a careful analysis of construction drawings, contract specifications and qualification ranges stated by the reference code, and by evaluating the assessment of time and methods concerning the production capabilities of the *De Pretto Industrie*, it was decided to execute the joint through the Gas Tungsten Arc Welding (GTAW) and Shielded Metal Arc Welding (SMAW) processes. The GTAW manual welding was chosen for the first passes (about 6 mm of deposited material), and for the subsequent filling the SMAW process was adopted. The choice of the qualifying position along the joint was determined by the effective position of the welding that will be actually used in production, resulting in a plane-frontal bead welding position (PB/2G).

The considered welding processes have different characteristics, that are reflected on the achievable final microstructure. The GTAW process, owing to its high heat input, involves the formation of coarser dendritic structures in the molten zone (ZF) than the SMAW method, but at the same time a reduced microporosity level in ZF can be obtained. Typically, SMAW DSS weldments exhibit a low toughness, which is not directly attributable to the presence of intermetallic phases but can also be caused by oxygen embrittlement [2] or by the higher microporosity level.

Particular attention should be paid to the proper choice of both filler material and shielding gas. As concerns the filler, one must considers that UNS S32760 differs from UNS S32750 (SAF 2507) for a higher content of Cu and for the presence of a significant amount of W. Therefore, to ensure the required characteristics, the filler must contains a proper amount of such elements. On the other side, for the choice of the shielding gas there are different schools of thought within the users and producers communities of base and fillers materials. The more conservative and traditional approach is that to use pure argon as a shielding gas on the obverse and reverse of the weldment; conversely, the use of mixtures of argon and nitrogen were found to have beneficial effects on the final joint microstructure and on the toughness values [2-4]. The current and most progressive approaches [2-4] instead suggest the use of argon and nitrogen mixtures – containing 2–4% of N_2 – as shielding gas, and the use of either pure nitrogen or mixtures nitrogen/hydrogen as backhand gas. These suggestions have a limited literature support, but the internal know-how of the filler material producers for borderline applications precisely recommend the use of these mixtures; however, the technical literature [2] does not counsel the use of

H_2 as shielding gas, owing to the possibility of hydrogen embrittlement and hydrogen cracking in ferritic structures. Finally, ternary and quaternary mixtures can be used for the DSS weldings, but they are suitable for automatic and concentrated-energy welding processes; the employment of these particular shielding mixtures allows to guarantee a correct execution of the weldment, limiting the formation of inclusions and ensuring a correct phase balance, a critical point for DSS.

As previously mentioned, the UNS S32760 SDSS is characterized by the precipitation of secondary phases, which may form even for very short exposure times; hence, the welding operations performed on this DSS grade always involve the precipitation of a certain percentage of such phases. Therefore, the welding procedure must be designed to limit the formation of detrimental compounds, mainly acting on heat input and thermal gradients during cooling, and taking into account solutions that are compatible with timing and costs..

The DSS weldments, as for austenitic stainless steels, do not require any preheating, but the weld edges must be carefully cleaned. Regarding the interpass temperatures, an analysis of literature and specifications [2,5] has highlighted the preference for the lowest possible value, consistent with needs and traditional industrial costs. This is because the realization of dedicated forced-cooling equipments for the areas close to the joint are not industrially feasible, considering the number of different types of joints which can be realized. In DSS, a maximum interpass temperature of 150°C is generally accepted, although it may sometimes not be enough; on the other hand, the maximum heat input is generally set between 1.5 and 1.8 kJ/mm, and must be carefully controlled throughout the entire welding procedure, particularly during the first (root) pass.

Execution of the welding procedure

A first qualification procedure (first bead) has involved the adoption of a welding procedure identical to that used for standard DSS grades (as SAF 2205), whose main process parameters are listed in Table A.5. However, the execution of the first bead has led to unsatisfactory results in terms of mechanical properties and microstructural requests. Therefore, the procedure was re-designed by changing the process parameters, as reported in Table A.5, and using the "hot-pass" technique.

Table A.5 – Process parameters for the qualification procedures.

Parameter	Value	
	First qualification procedure	Second qualification procedure
Process type (firsts passes)	GTAW	
Process type (filling)	SMAW	
Joint type	Head-head on pipe – V-joint	
Dimensions	$\varnothing_{ext}$ 324 mm, thickness 12 mm	
Welding position	2G/Frontal	
Filler material	ER 2594 + E 2595-15	
Interpass temperature	150°C	100°C
Shielding gas	Argon + N_2	
Backhand gas	Argon + N_2	$N_2 + N_2$
Maximum heat input (first pass)	1.8 KJ/mm	1.7 KJ/mm

In both qualifications, the welding parameters were continuously monitored and recorded, paying particular attention to electrical variables and feed rate; the oxygen content was also constantly monitored in the reverse shielding gas chamber ($O_2 < 0.05\%$).

Table A.6 – Results on the qualification beads.

Test	Values	
	First qualification procedure (bead 29090A)	Second qualification procedure (bead 29316)
Tensile test (transversal to the welding)	-	minimum 833 MPa
Lateral bending	2 satisfactory 2 failed	4 satisfactory
Charpy impact toughness (a) Welding zone – (b) Fusion line (c) Fusion line + 2 mm (d) Fusion line + 5 mm	(a) average 84J – minimum 63J (b) average 39J – minimum 33J	(a) average 59J – minimum 51J (b) average 84J – minimum 76J (c) average 128J – minimum 110J (d) average 162J – minimum 156J
Hardness HV_{10}	-	maximum 326 HV_{10}
Macrographic examination	satisfactory	satisfactory
Ferrite content (%)	-	47–62
Corrosion	Pitting and weight loss (8.0 g/m^2)	no pitting and no weight loss
Chemical analysis of the welding	PREN = 41.1	PREN = 41.0

Mechanical tests of the qualification beads

All the non-destructive tests for both beads were performed in accordance with the acceptability criteria reported in Table A.2 and all the results were satisfactory. However, according to the contractual requirements, the results of the mechanical tests performed on the first qualification bead (29090A) were classified as "not satisfactory" (Table A.6). On the contrary, as a result of the redesigned welding procedure, the mechanical tests on the second qualification bead (29316) were found to be in compliance with the customer requirements (Table A.6).

Microstructural characterization

Overall microstructure

In both the qualification beads, the optical micrographies revealed the typical welding structure and the biphasic microstructure exhibited the classical dendritic morphology achieved after the melt cooling. In the first bead (Fig A.1), the presence of the intermetallic σ-phase is clearly evident in correspondence of the α/γ interfaces. The formation of this compound is conditioned by many factors such as chemical composition, temperature and heat treatments, and the temperatures which are normally reached in both welding (ZF) and heat-affected (HAZ) zones fall within the critical range for its formation. On the contrary, the observations of ZF and HAZ in the second qualification bead has not revealed the presence of any intermetallic phases, both in the coverage area (Fig. A.2) and in the root zone (Fig. A.3).
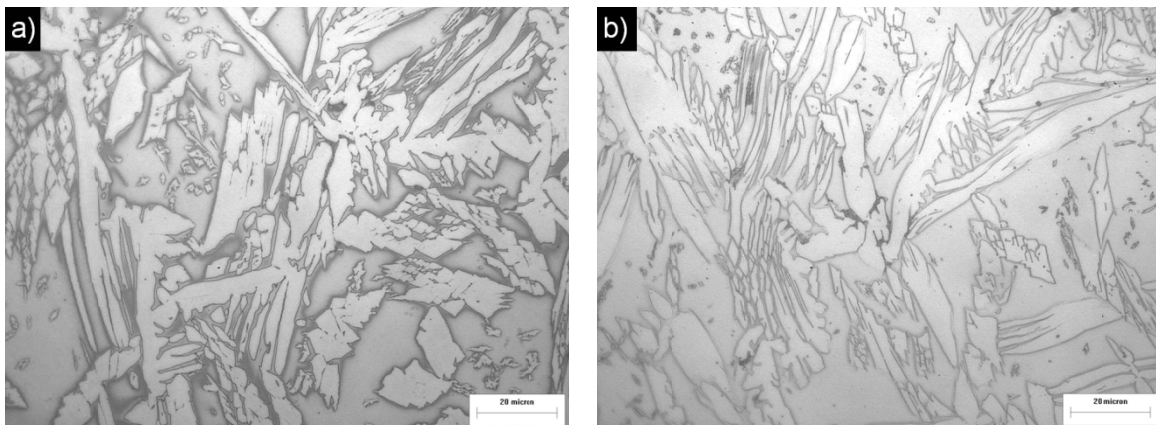

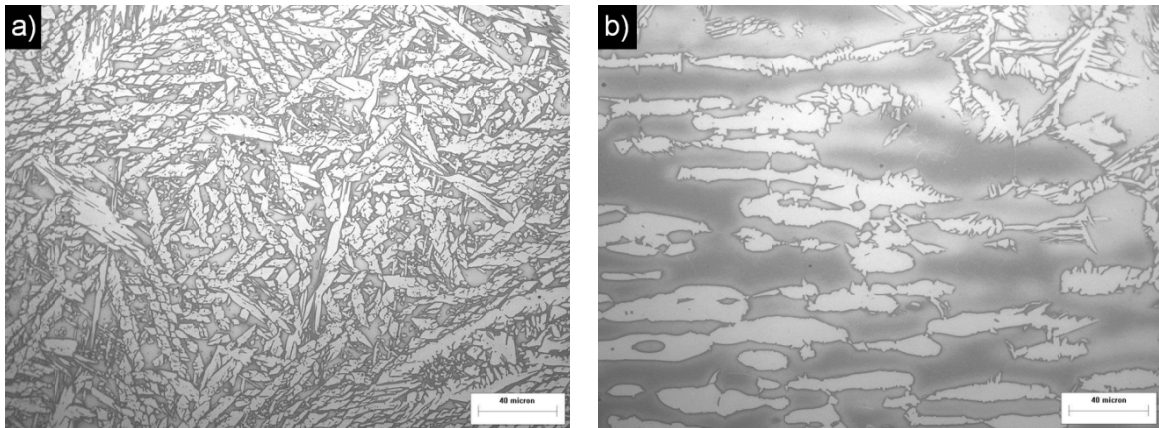Fig. A.1 – Welding zone in bead 29090° (OM, NaOH).

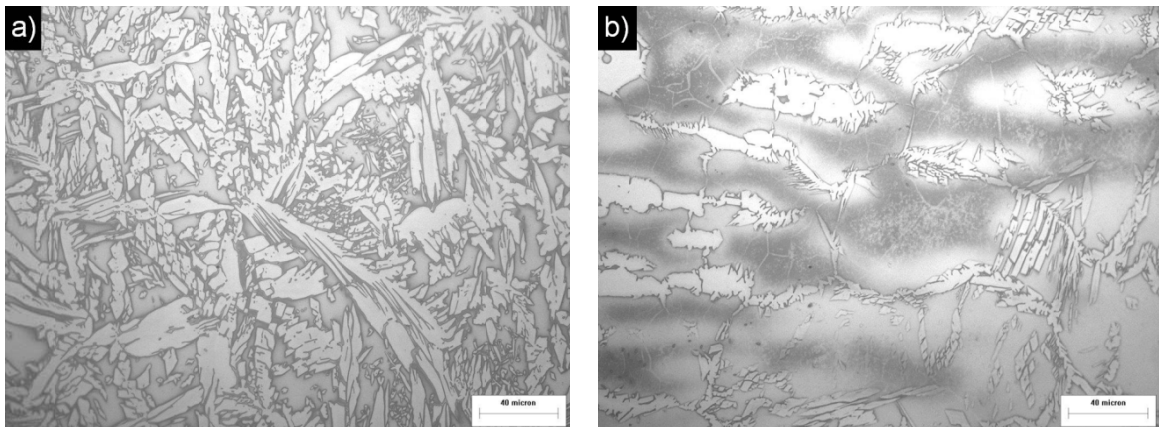Fig. A.2 – Welding joint (shielding) in bead 29316 (OM, NaOH): a) welding zone and b) heat affected zone.

Fig. A.3 – Welding joint (root) in bead 29316 (OM, NaOH): a) welding zone and b) heat affected zone.

GTAW welding area

The first passes of the two qualification beads 29090A and 29316 were obtained by the same GTAW welding procedure, differentiated in the parameters above mentioned, and both porosity and inclusion contents were almost comparable. In bead 29090A, a significant amount of secondary phases, such as σ- and χ-phases, was observed in the vicinity of the centreline of the weld (Fig. A.4). In this bead, the formation of small precipitates in ZF occurs from the first pass at the bead root, about 1 mm from the bottom of the weld. After the subsequent passes, an increased content of secondary phases was observed, maintaining the central position and extending up to the last pass, due to the low cooling rate affecting this area. The central location of the precipitation sites highlights the criticality of the GTAW process on welding this type of steel; in addition to the high heat input that distinguishes this method, the centreline position was found to be the most

favoured precipitation area, since the time in the critical temperature range was enough long for the formation of intermetallic phases.
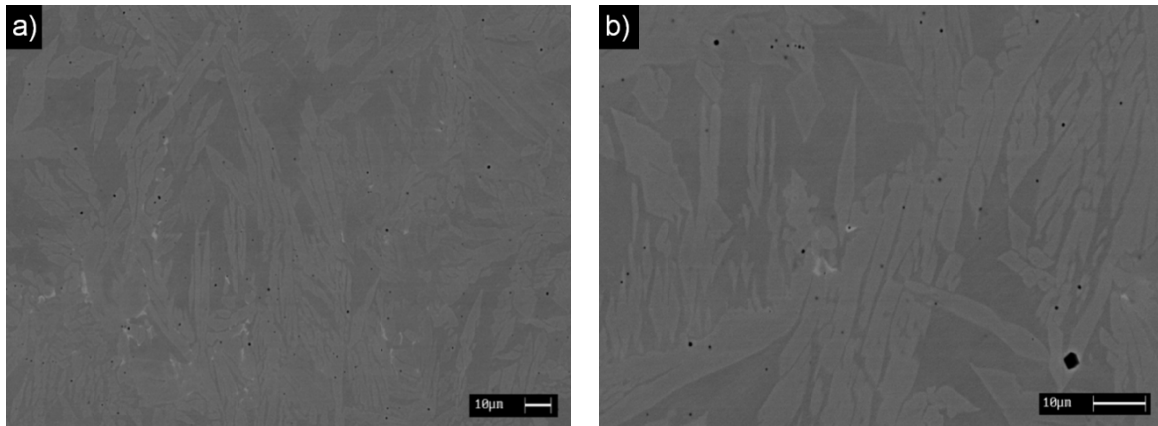

Fig. A.4 – Bead 29090A: σ- e χ-phases in the GTAW welding centreline.

Table A.7 – Chemical composition of σ-phase in bead 29090A [wt.%].

Si	Mo	Cr	Mn	Fe	Ni
0.92	6.00	26.87	0.64	58.24	7.33

The average composition of the σ-phase detected in bead 29090A is reported in Table A.7. On the contrary, in bead 29316, the use of an appropriate protection gas mixture allowed a better yield in obtaining a "clean" microstructure, limiting the formation of σ-phase. Despite the use of suitable procedures, the intermetallics precipitation was not completely avoided (Fig. A.5), even if it occurred in significantly lower extent than in bead 29090A. Nevertheless, the dangerousness of very low secondary phases amounts within the microstructure must not be neglected; in fact, as evidenced by previous studies [6], the 0.5% of volume fractions of such phases is enough to cause a reduction in toughness of about 50% at room temperature. Due to the small size of the precipitates, it was not possible to carry out a composition analysis, but the micrographies in Fig. A.5 show the unequivocal presence of σ-phase, which appears brighter than austenite and ferrite, owing to its higher average atomic number. These findings again revealed that the GTAW process must be considered highly critical for these steels, and especially for the high-alloyed UNS S32760 SDSS, in which the precipitation kinetics are favoured by the high content of such elements which render the material more prone to intermetallic formation [7].
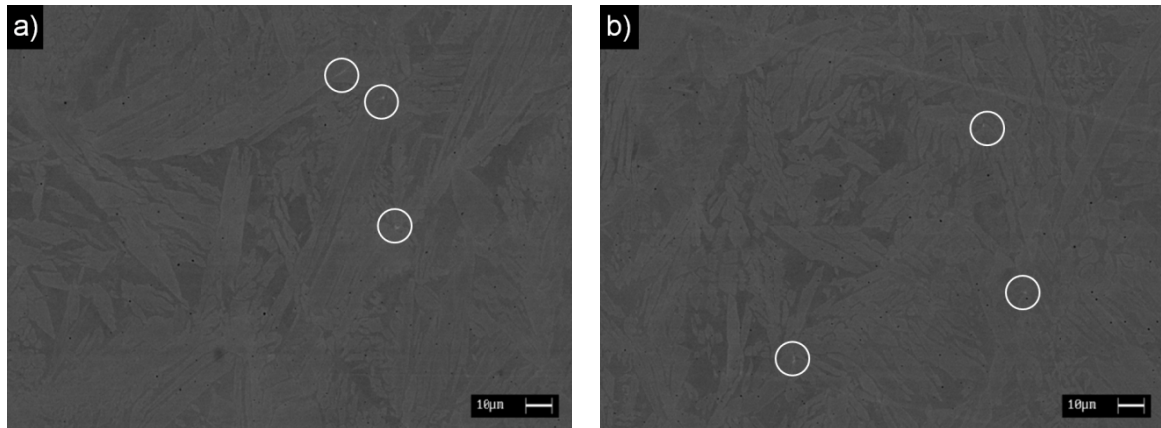
Fig. A.5 – Bead 29316: σ-phase in the GTAW welding centreline.

In both the beads, the base material next to the HAZ of the GTAW process, was instead interested by the precipitation of Cr_2N chromium nitrides of globular form, observed in intergranular position (Fig. A.6a). These particles, which are visible in the micrographies as small blacks particles at the ferritic grain boundaries, can be attributed to a too slow cooling rate in these areas, and hence to a prolonged exposure of the material within a thermal regime which cannot be consider negligible for nitrides formation, but which was not high enough for intermetallics formation. However, it cannot to be excluded that the presence of such phases in the vicinity of the HAZ was not due to high temperatures exposure, but that nitrides were already present in the base material, since some of these particles were observed in a bead zone sufficiently far from ZF and not affected by critical thermal cycles (Fig. A.6b).
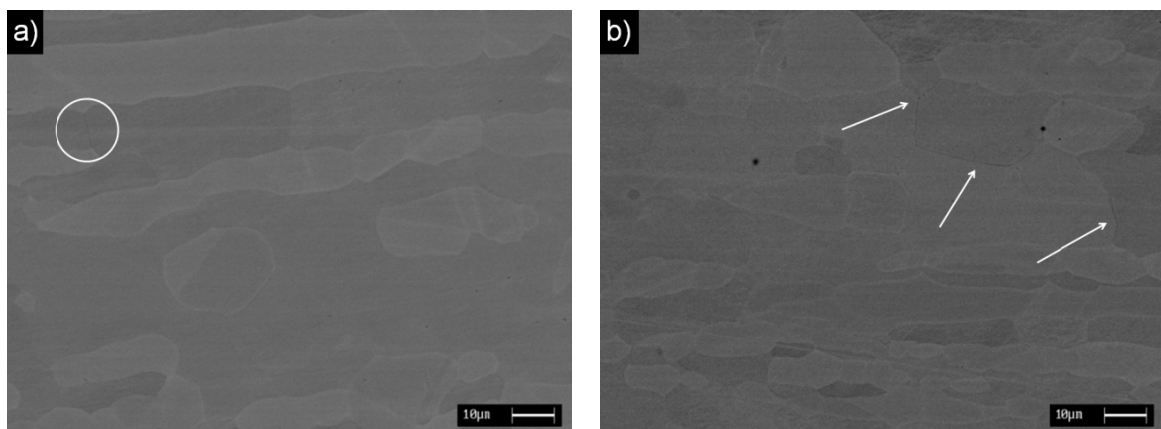

Fig. A.6 – Chromium nitrides in the base material: a) heat affected zone and b) bead end.

SMAW welding area

The SMAW method, characterized by a lower heat input than the GTAW process, was employed for filling the upper part of the beads. The higher cooling rate in ZF allowed the formation of an averagely finer dendritic structure than that obtained using GTAW, but which was found to be affected by a higher porosity. The porosity level in both beads was evaluated by image analysis on the SEM micrographies; in bead 29090A the estimated porosity was about 1.4%, while in bead 29316 was 0.9% (Fig. A.7). This difference in porosity also explains the registered toughness values which, albeit in a lower extent than σ-phase, contributed to the deterioration of mechanical properties in the beads.
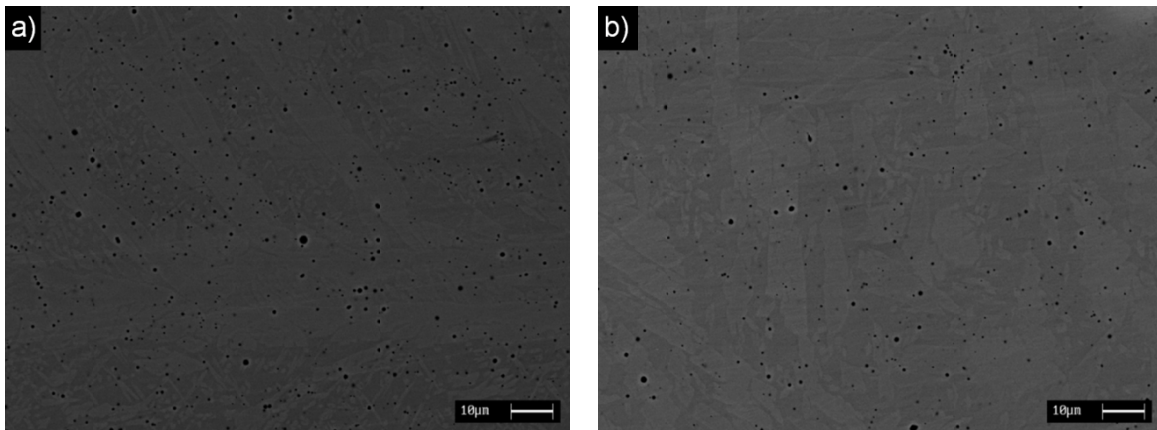

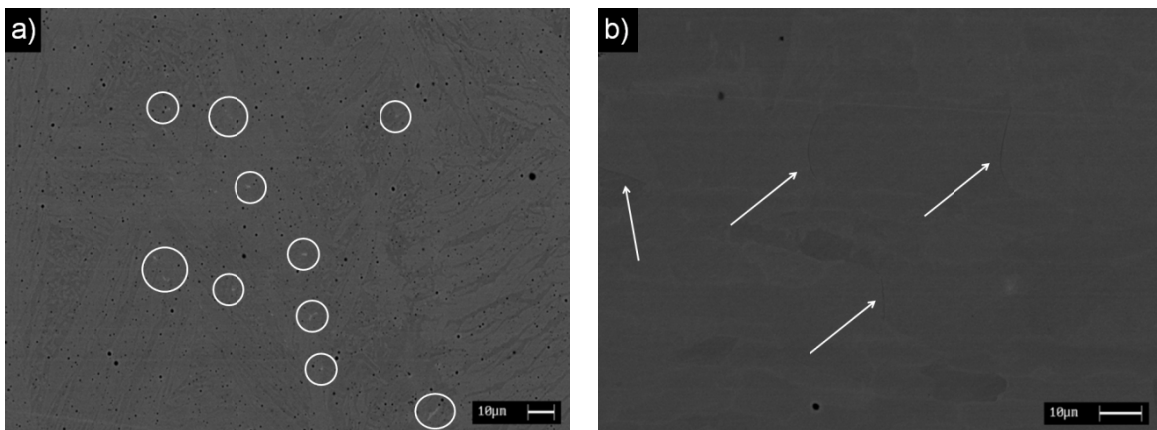Fig. A.7 – Porosity in SMAW welding zone: a) bead 29090A and b) bead 29316.

Fig. A.8 – SMAW welding: a) σ-phase in bead 29090A and b) intergranular nitrides in heat affected zone.

Owing to the lower precipitation of σ-phase in the GTAW-ZF, the bead 29316 was free from intermetallics precipitation in the SMAW-ZF, whereas the first SMAW passes performed on bead 29090A were affected by the presence of secondary phases, originated

from the last GTAW pass and dragged in ZF because to the subsequent SMAW welding process (Fig. A.8a).

The HAZ of SMAW process in both beads was instead affected by intergranular chromium nitrides precipitation (Fig. A.8b), and the highest cooling rates also caused the formation of nitrides in transgranular position (Fig. A.9). In these latter zones, the heating caused a dilatation of the crystal lattices, bringing ferrite in nitrogen-supersaturated solid solution conditions, and the subsequent cooling was too fast to allow nitrogen diffusion and redistribution in austenite, causing nitrides precipitation within the ferritic grains.
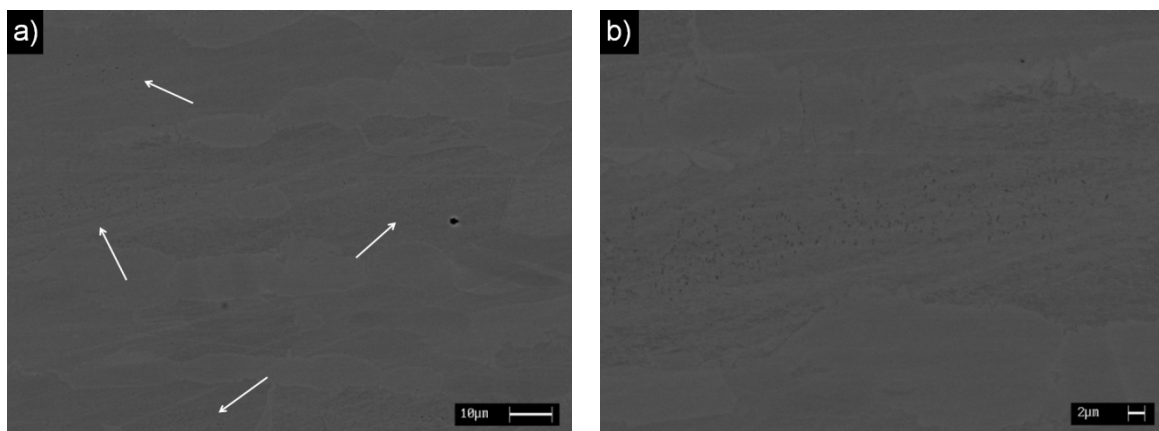

Fig. A.9 – SMAW welding: a) transgranular nitrides in heat affected zone and b) detail of (a).

Concluding remarks

In this section, the development of a suitable welding procedure for UNS S32760 SDSS was presented. The procedure was realized by coupling GTAW and SMAW processes, paying extreme attention to the process parameters and carefully taking into account the shielding gas mixture, in order to obtain the desired combination of mechanical properties, microstructure and corrosion resistance properties. Considering the criticality of the welded material, the results were very positive and encouraging, since the re-design of a first-attempted procedure has permitted the achievement of very satisfactory issues.

Even if it is almost impossible to weld this type of steels without the formation of a certain percentage of secondary phases, the precipitated quantities can be limited by a correct assessment of welding parameters. However, an unavoidable embrittlement of the joint occurs in any case.

This work also revealed the already known limits of the standard metallographic investigation techniques (such as optical microscopy) in revealing the precipitation of

secondary phases. It is rather common that a microstructure stated as "clean" in reality it is not, since the real microstructural conditions can be only observed through high magnification investigation (SEM rather than OM). However, the use of advanced techniques is not even possible and is also somewhat expensive, making difficult a reliable microstructural characterization of the welded joints.

A.2 Characterization of SAF 2205 armouring wires

Historically, submarine (or subsea) power cables were introduced to link shore-based power grids across bays, estuaries, rivers, straits, etc. and, at the present day, the number of these cables being installed world-wide is rapidly increasing. In fact, subsea cables are now employed to carry power between countries and to offshore installations (oil/gas platforms and ocean science observatories), to transfer power from offshore renewable energy schemes to shore (wind, wave and tidal systems), and to transfer power from energy sources to consumers, thus interconnecting different regional electrical transmission networks to allow global trading of energy, also in remote areas. Advances in subsea cables technology, the fast rate of return on investments compared to power stations construction, and the ability to import power from hydroelectric or wind generating systems have combined to make the installation of submarine cable links attractive [8].

Subsea cables (Fig. A.10) can mainly subdivided in two categories, HVAC and HVDC cables. The former are aimed to transfer Alternating Current, transmitted down each of three conductors, whereas in the latter the Direct Current is transmitted down a primary conductor and requires a return path provided via another conductor or via seawater using an anode/cathode. Both single- and three-core subsea cables are normally produced and the progresses in subsea technology has recently advanced to allow the manufacture of cables for bulk power transmission in continuous length up to 100 km. These cables are designed to satisfy specific mechanical and corrosion-resistance requirements and, with growing reliance on offshore-based renewable energy schemes, many countries now classifies submarine power cables as critical infrastructure [8].

The installation of subsea cables present many challenges in the fields of mechanical and marine engineering. Cables, in fact, must withstand the significant mechanical forces that are generated during installation, due to their own weight and the action of tidal

currents; the installed cable is also at risk from damage by anchors, fishing activities, vessel impact and movement of the cable or seabed terrain. To protect the cable during laying or in service, metallic armour wires are applied in one or two layers to the construction as part of the manufacturing process; however, additional protection can be offered by burying the cable in the seabed using a variety of jetting, ploughing or trenching techniques, which are unfortunately not even applicable, as in rock seabed [8]. Failure statistics on submarine cables show that the most frequent causes of failure is external damage (anchors and heavy fishing tools), whereas failures of internal origin are not very probable, and no failures have occurred when the cables have been buried into the seabed. Therefore, subsea cables must be adequately protected in such areas where the risk for mechanical impact is high.

1 – Conductor (usually copper)

2 – Conductor screening (usually extruded)

3 – Insulation (XLPE or EPR)

4 – Insulation screening (semi-conductive)

5 – Screen

6 – Laminated sheath (aluminium tape and polyethylene)

7 – Optical fibres (optionally used for telecommunications)

8 – Fillers (as needed)

9 – Binder tapes

10 – Armour Bedding (polypropylene strings)

11 – Armouring wires

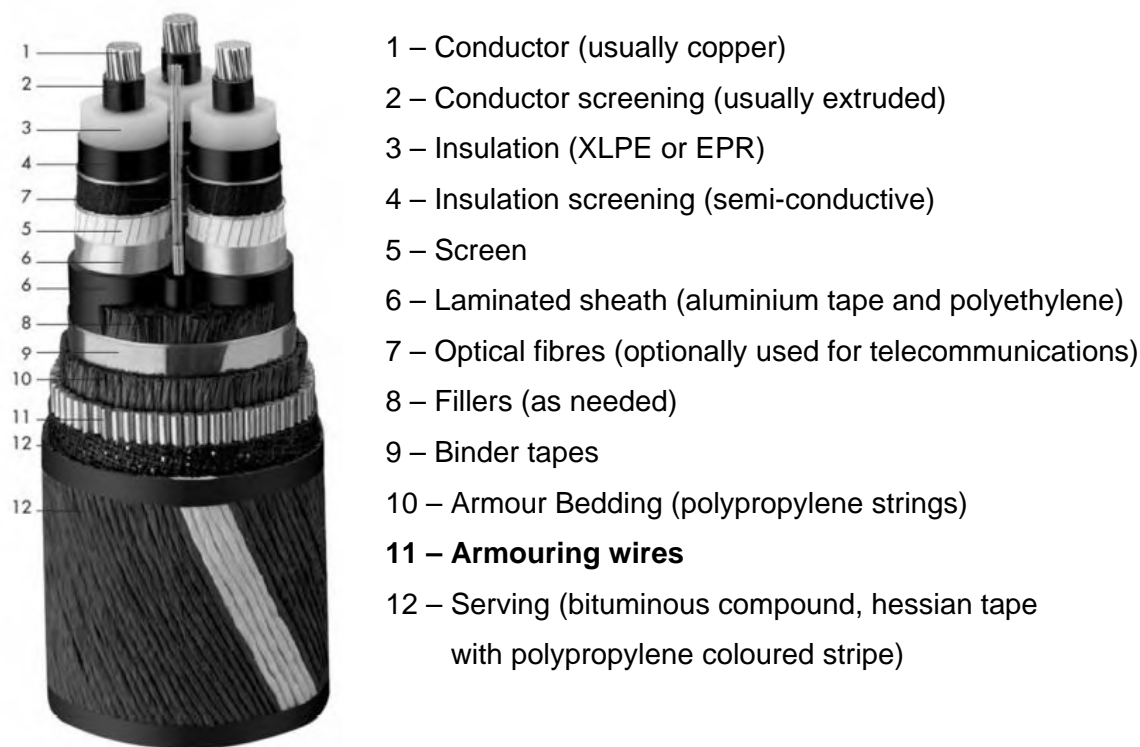12 – Serving (bituminous compound, hessian tape with polypropylene coloured stripe)

Fig. A.10 – Principal parts of subsea cables.

As previously reported, the protection of subsea cables is achieved by steel armouring wires, which must withstand several requirements: bending, twisting and coiling without deterioration, external water pressure without significant deformation, external impact damage, adequate resistance to corrosion hazards and adequate flexural fatigue life. Generally, these wires are made of patented low-carbon steel subjected to galvanization,

in order to achieve high mechanical properties and an adequate resistance to corrosion attacks. However, in the last years, the improved combination of mechanical and corrosion-resistance features have shifted the choice toward the more interesting stainless steels, both austenitic and duplex grades. As a matter of fact, these stainless steels have high mechanical properties, also in sub-zero conditions, and possess a low permeability, allowing the reduction of energy losses by the cable's magnetic field and consequently significantly increasing its efficiency, without needing to interfere with the cable design. Moreover, the enhanced resistance to crevice and pitting corrosion, makes these grades very suitable in subsea applications. In some cases, stainless steels are galvanized in order to offer excellent corrosion performances because, when the zinc layer gets damaged, the surrounding zinc will sacrifice itself serving as a sacrificial anode and protecting the underlying stainless steel.

Duplex armouring wires

The interesting combination of properties in aggressive environments makes DSS particularly suitable for submarine applications, where the high initial cost is justified by the extraordinary performances throughout the product lifecycle. In the present section, a characterization of SAF 2205 DSS armouring wires is presented, both in terms of mechanical and corrosion-resistance properties, aimed to prove the performances of differently produced wires, originated by different manufacturing processes, in order to determine an achievable cost-saving by reducing the number of forming operations.

As previously reported, armouring wires must possess high mechanical properties to satisfy the required strength and must be suitable against corrosion; moreover the electrical resistivity must be as higher as possible, because the induced current in the armour can be high, up to the same values as in the conductor, thus leading to considerable ohmic losses. Hence, the choose of SAF 2205 DSS seem to be favourable, owing to its corrosion properties, but the achievement of sufficient strength and electrical resistivity requires plastic deformations at room temperatures.

The manufacturing cycle of DSS armouring wires is composed by subsequent wire-drawing and annealing steps, in order to determine the proper combination of properties. For the purpose of this section, products deriving from two similar production cycles were investigated. The processes are reported in Fig. A.11 (denoted with the numbers 2 and 3,

whereas 1 is a pre-forming process), both involving wire-drawing and annealing operations by starting from 6 mm diameter wires (B) and reaching the final diameter of 3 mm (F and H); in process 2, the final diameter is achieved after an intermediate step (D, diameter 4.5 mm). Note that all the annealing treatments are, in fact, solubilisations at 1050°C (Chapter 1 and 2).
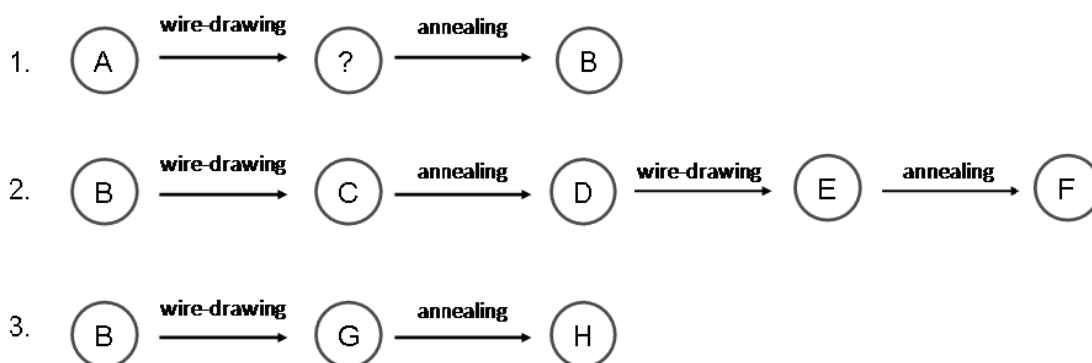

Fig. A.11 – Wire production processes.

The wire properties were tested after each step, in order to understand their variation as a function of the cold plastic deformation induced by wire-drawing and as a consequence of the following solubilisations. It is well known that cold-working causes a change in mechanical properties. In wire-drawing, DSS are highly strain-hardened, leading to the formation of a banded ferrite/austenite structure and making them strongly anisotropic; hardness and mechanical strength are increased, whereas the impact toughness in the transverse direction is reduced. On the other hand, the subsequent solution-annealing steps are aimed to restore the microstructures in terms of plastic strains, making DSS further workable by partially (or totally) regenerating the starting characteristics. In Table A.8, a summation of the measured mechanical, physical and corrosion properties pertaining to each manufacturing step is reported. As expected, process 3 (B-G-H sequence) was the most critical one, because it involves the maximum cold reduction in wire diameter (50%).

It must be noticed that wires have to satisfy a combination of properties. They must be strain-hardened, in order to achieve sufficient mechanical strengthening and electrical resistivity, but at the same time they must possess an adequate corrosion resistance in seawater, since are aimed for application in marine environments. The combination of such properties is obtained by properly designing the annealing treatments after each

deformation step. In fact, the treatments must be long enough to partially restore the microstructure and excessive soaking times must be avoided, because they can cause a full recrystallization of the phases, leading to a loss in the necessary mechanical and physical properties.

Table A.8 – Wires properties after each manufacturing step.

Sample	Diameter [mm]	State	Reduction [%]	Rm [MPa]	Rp0.2 [MPa]	A5 [%]	Resist. [μΩm]	$HV_{0.5}$	$HV_{0.015}$	CPT [°C]
A	6.5	WD	-	871	707	24	0.7824	354	378	54.5
B	6.0	ANN	8	799	616	30	0.7830	291	355	51.0
C	4.5	WD	25	1278	989	6	0.7842	364	475	-
D	4.5	ANN	25	820	594	32	0.7854	279	333	-
E	3.0	WD	33	1403	1142	4	0.7956	377	476	53.0
F	3.0	ANN	33	838	578	29	0.7921	277	358	51.5
G	3.0	WD	50	1480	1203	4	0.8125	415	617	51.0
H	3.0	ANN	50	851	593	27	0.7867	282	351	53.5

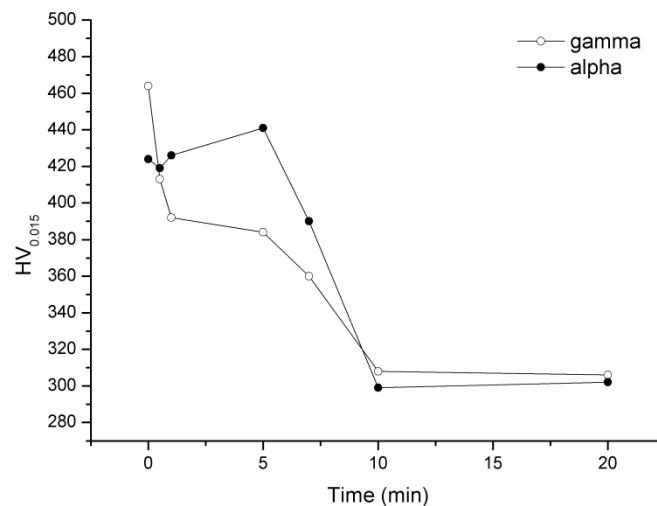WD = wire-drawn
ANN = annealed

Fig. A.12 – Effect of soaking time at 1050°C on ferrite
and austenite hardness in the A-state sample.

As a matter of fact, in Fig. A.12 is reported the effect of the soaking time at 1050°C on the phases hardness in the A-state wire. As can be seen, low solubilisation times cause a

ready recrystallizzation of austenite (γ), whereas ferrite (α) is mainly interested by recovery processes. However, after 10 minutes treatment, the phases reach comparable hardness values, thus getting ineffective the strain-hardening achieved by cold-working. Moreover, the effect of solubilisation on restoring the microstructure is strongly dependent on the previous deformation degree, since different reductions in diameter cause a energy storage of different entity. This energy is released during annealing, leading to the restoration of the microstructure. Therefore, owing to these high-temperature phenomena, the soaking time must be properly chosen, also considering the previous deformation step.

Microstructures and properties

The microstructures of the wire-drawn samples depended on the deformation degree and were increasingly fragmented as the diameter reduction increased, with the maximum distortion in the 50% deformed sample (Fig. A.13a); the subsequent annealing treatments caused a partial recrystallization of the austenitic grains, underlined by boundaries polygonalization (Fig. A.13b). As confirmed by the results presented in Table A.8, the mechanical and electrical properties significantly vary considering the two different wire states (deformed/annealed) and are closely related to the microstructure of each sample.
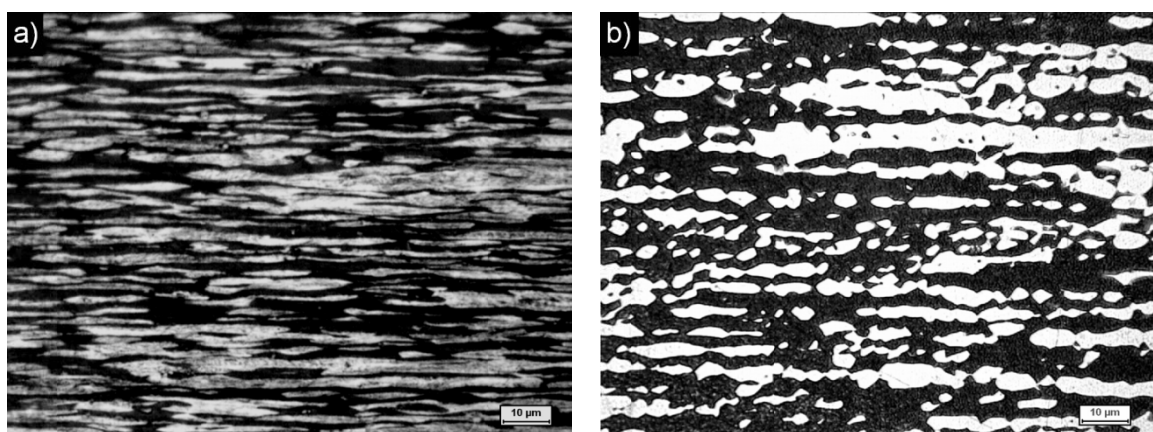

Fig. A.13 – Wire microstructures: a) 50% deformed sample (G-state) and b) annealed (H-state).

The $HV_{0.015}$ micro-hardness tests on both phases were performed on a diametrical-longitudinal section and, as expected, the profiles showed a similar trend. In all samples, the hardness values decreased from the wire surface towards the wire centre, in agreement with the deformation mode at which wires were subjected.

In all the wires, the micro-hardness $HV_{0.5}$ was also measured, in order to better determine the actual (global) hardness, and the values are reported in Fig. A.14 together with the mean micro-hardness $HV_{0.015}$, calculated by averaging the values measured in each phase. The difference in HV achieved by the two methods must be ascribed to the employed testing load, because the micro-hardness values increase by decreasing the testing load, leading to errors in excess. However, besides these differences in absolute values, the variation trends are similar and denotes the work-hardening to which the drawn wires are subject. As can be seen, the greater diameter reduction leaded to the major increment in hardness, whereas HV settled around an almost constant value in the solution-annealed samples .
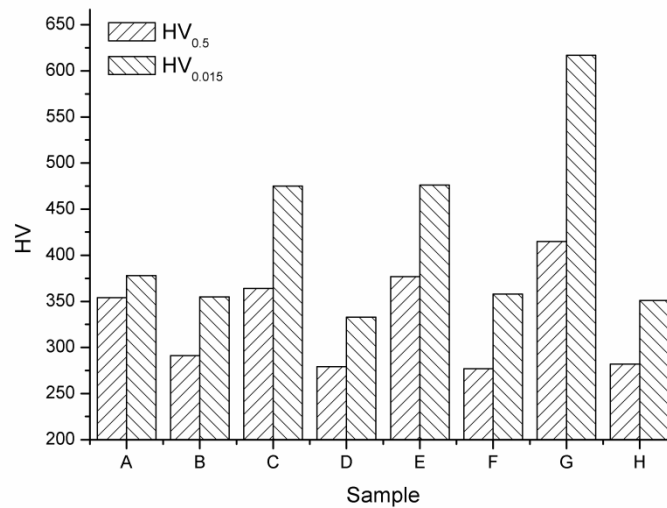

Fig. A.14 – Hardness and micro-hardness variation after each production step.

The hardness variation was quite similar to that of the other mechanical and physical characteristics (Fig. A.15). As expected, further reductions in wire diameter leaded to a progressive increment in tensile and yield strength, due to the work-hardening of the material, and the increased number of vacancies induced by cold deformation caused an increase in electrical resistivity. On the other hand, the solubilisation treatments restored the materials properties. This latter fact was more evident in the mechanical strength, for which the annealing caused a complete recover of the initial value. However, the electrical resistivity globally exhibited a more irregular trend, with the highly deformed state interested by a greater variation, the observed can be addressed to the solubilisation process parameters, underlining that annealing must be properly designed.
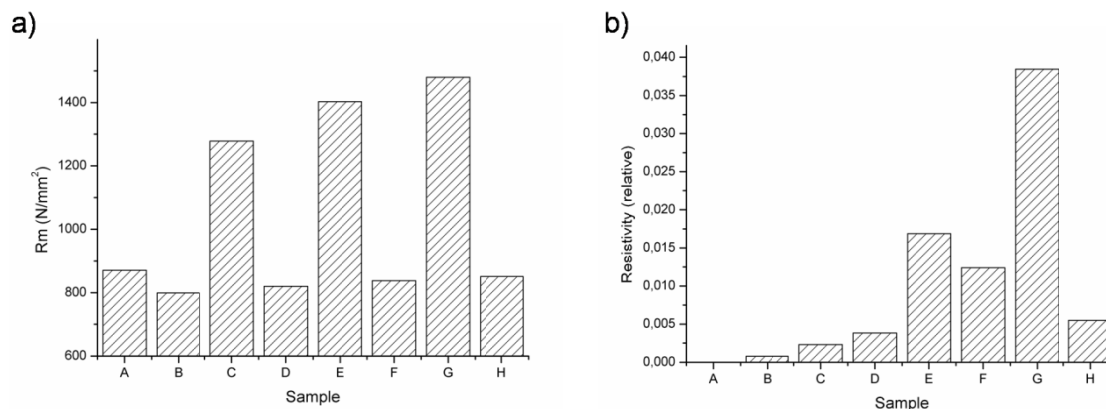
Fig. A.15 – Properties variation after each production step: a) tensile strength and b) electrical resistivity.

Critical Pitting Temperature

The Critical Pitting Temperatures (CPT) determination was carried out by following the ASTM G150 standards (1 mol NaCl solution), using the same apparatus described in Chapter 3, and the results are reported in the previous Table A.8.

In all the states (A to H), the material exhibited CPT values always above 50°C, which is a temperature close to the lowest limit pertaining this steel (Chapter 3), but no particular variation trends were evidenced. The slight variations (in the order of few degrees), can be instead attributed to sample size effects – in particular to the area exposed to the corrosion test, which varied from 0.28 to 0.70 cm^2, depending on the considered sample – and to the geometry of the electrical circuit (electrode arrangement). In fact, as discussed in Chapter 3, SAF 2205 is a rather stable DSS grade and its variation in CPT, measured on significant testing surfaces, was found to be in the order of 10% at the maximum thickness reduction of 85%. Hence, the CPT values must be considered as affected by geometrical and electrical variables, rather than microstructural phenomena.

Concluding remarks

The present investigation confirmed the reliability of employing SAF 2205 as armouring wire for subsea cables. The results pointed out that an intermediate step in the manufacturing cycle is not necessary, as the properties after solution-annealing were almost equivalent, leading to cost-savings in the production of wires maintaining suitable characteristics.

Moreover, the results also suggested the possibility to employ SAF 2205 in the as-deformed state (very high mechanical strength an electrical resistivity without any loss in corrosion performances), even if in this case a full characterization is required, including magnetic tests and impact toughness and fatigue properties determination.

REFERENCES

[1]   J. O. Nilsson. *Mater Sci Tech Ser* 8 (1992) 685-700.

[2]   TMR Stainless. *Linee guida pratiche per la lavorazione di acciai inossidabili austeno-ferritici*. International Molybdenum Association (2011).

[3]   M. Frodigh. *High alloyed duplex stainless steels – Aspects on welding and fabrication*. Giornate nazionali di saldatura 7 (2013).

[4]   C. O. Pettersson, P. Stenvall, Z. Zhou. *High alloyed duplex & austenitic stainless steels – Aspects on welding and fabrication*. Eurojoint 5 & Giornate nazionali di saldatura 5 (2009).

[5]   IIS. *Saldatura per fusione – Vol.2*. Istituto Italiano della Saldatura (1996).

[6]   I. Calliari, M. Breda, E, Ramous, K. Brunelli, M. Pizzo, C. Menapace. *J Mater Eng Perform* 21 (2012) 2117.

[7]   I. Calliari, M. Pellizzari, E. Ramous. *Mat Sci Tech Ser* 27 (2011) 928.

[8]   J. R. Attwood. *Cable design for subsea power links*. IEEE Power Engineering Review (2000) 13.

APPENDIX B

Archaeometalurgy

It is rather diffuse that, during his Ph.D. period, the student is involved in other projects, which are not intimately connected to the aim of his final research, but which belong to further activities performed in his department. Despite the various works performed on thesis of different topics, this appendix deals with an important side-project accomplished throughout the three years of Ph.D. – and which is still under development – regarding the archaeometallurgical study of papal coins converted into medals. One can think that there aren't any connections between this topic and the research project, and in part it is true (steels and silver-copper coin alloys are not metallurgically and industrially equivalent), but the involved archaeo-investigations are still of metallurgical character and may provide the author a wider vision of the metallurgical world, in a different form respect to the steels metallurgy, but useful to improve his knowledge and background.

The research presented in this appendix is aimed to systematically study more than 500 coins, minted in a time ranging from 17th to 19th century and subsequently transformed into devotional medals, in order to (possibly) date the period of such conversion. The investigated medals are composed by a wide variety of coins and pegs, and a stylistic classification is needed to subdivide the entire collection in smaller groups with similar aesthetics features. However, this qualitative classification from macroscopical observations cannot be considered exhaustive to achieve reliable information about the conversion period and deeper analyses are required. On the other hand, the analysis of the composition of the brazing alloys can give a better knowledge on the technical skills of the silversmiths who performed the joint, and the amount of the employed alloying elements can be used as discriminating factors for the medallions dating. Particularly, the crucial factor for a possible dating of the coin-to-medal conversion is the presence of zinc in the brazing alloy. In fact, referring to the literature on the use of metallic zinc in Europe (see references in Table B.5), from the composition of the brazing drop it might be possible to

establish a sort of history regarding the analyzed alloys, allowing a dating in respect such conversions into medals.

The transformation of the coins into pendants has involved the joining with proper pegs by means of a brazing procedure. Obviously, the more reliable investigation method is that to directly observe the brazing drop by cutting the coin in two halves. Unfortunately, the medals cannot be damaged and the employment of destructive techniques such as cutting must be avoided, because they cause a loss in the intrinsic value of the artefacts. The particularity of this study consists in the analysis of the various brazing drops compositions in the lowest-destructive possible way, but at the same time suitable to achieve reliable results. For this purpose, a thin layer of metal was firstly removed by micro-milling from each brazing drop, allowing the appearance of the brazing alloy, free from oxides and dirty layers. These areas were then analyzed by a Scanning Electron Microscope (SEM) coupled with an Energy Dispersive Spectroscope (EDS), in order to characterize the brazing alloy from a compositional point of view.

However, this approach needs a validation, because the brazing drop is the result of a strong non-equilibrium solidification process and, therefore, the sampling points on the drop are not all equivalent in terms of alloy composition. Position and depth of the sampling point can affect the obtainable results and a reference sample must be firstly analyzed. Hence, it was of paramount importance the preliminary metallographic study performed on a sample called "expendable", in order to determine the brazing alloy composition and understand in detail the physical metallurgy of the brazing, in terms of resulting microstructures and elements partitioning. The investigations on the expendable medal has evidenced that the brazing drop is composed by a Ag-Cu alloy, charged with other minor elements such as Zn and Pb, and also the semi-destructive analyses on other medals revealed the presence of such elements, in different extent depending on the considered case. Moreover, once the composition of the brazing alloy is known, a cross-linking with the stylistic classification is required in order to determine possible connections and to attribute the conversion works to different sets of artisans. However, the stylistic features are still under classification and the related results are not yet available. From this latter point of view, the research was also extended to the analysis on pegs of similar brand, in order to achieve another correlation parameter regarding similar characteristics.

B.1 Metallurgical study of a XIX century *Scudo* converted into medal

In this first section, the results from the preliminary study on the medallion called "expendable" are presented. This first study was of fundamental importance in order to determine the brazing alloy composition and the solidification microstructures, since different cooling conditions lead to different microstructures inside the same brazing drop, affecting the partitioning of the alloying elements. Therefore, the obtained results were employed to assess the reliability of the employed semi-destructive method on the analyses of the 500 coins.

Moreover, from this preliminary destructive study, it was possible to achieve information on the coin microstructure, allowing a better understanding on the production cycle of the coin itself in the XIX century.

Introduction

In Numismatics, coins provides a lot of information about the social, economical and technological history of the people and territories trends which created them. Numismatics study of the mid 17th to 21st century generally focuses on the research of production methods, use of money and the social context in which the coin was minted. In this regard, metallography is very helpful, as it can be used to link the internal structure of metals and alloys with production processes and to the chemical-physical-mechanical properties.

In the XVIII century, the manufacturing process used in the Papal States to produce coins consisted of several processing stages. First, silver plates of uniform thickness were prepared by rolling mills. Second, blanks were obtained by means of metal punches. Third, the blanks were heated and chemically bleached, in order to obtain a bright surface. Finally, the blanks were coined by a screw press (striking).

Later, after a period of circulation, the coins were recycled as an adornment. This demonetization was recognizable by the presence of a little hole through the coin or the addition of a peg to allow its use as pendant. The sacred subject represented on obverse and reverse side of the Papal silver *Scudo* and its axes transformed the coin into a devotional or a decorative object. A pendant obtained in such way not only had an ideological or religious value, but also emphasized the economic power and the social prestige of those who exhibited it.

In this section, the attention is focused on the metallographic analysis of a silver medal from the 19th century, shown in Fig. B.1, modified by a Ag-surface enrichment. The medal contains a brazing drop, presumably added to hold a peg. The application of widely preferred non-destructive analysis, such as X-Ray Fluorescence (XRF), was not taken into account because the results can be misrepresentative due to the limited depth resolution [1]. On the other hand, in most cases XRF represents the only way to get useful information, especially for analysis of art objects without surface alterations (corrosion and alteration layers, patinas..) and when they cannot be damaged [2].

The coin under study is part of a wider private collection of similar pendants, composed of coins from 17th to 19th century and for which a classification based on non-destructive analysis is currently being undertaken. The sectioning of the coin, as carried out for this work, was necessary for to understand the manufacturing processes involved in the coin's fabrication and its subsequent conversion into a medal. This investigation is part of a the project discussed in this appendix and aimed at supporting numismatic classification with physical analysis. The results obtained from the analyses discussed in this section will be used to confirm the reliability and the validation of other non-destructive analyses.
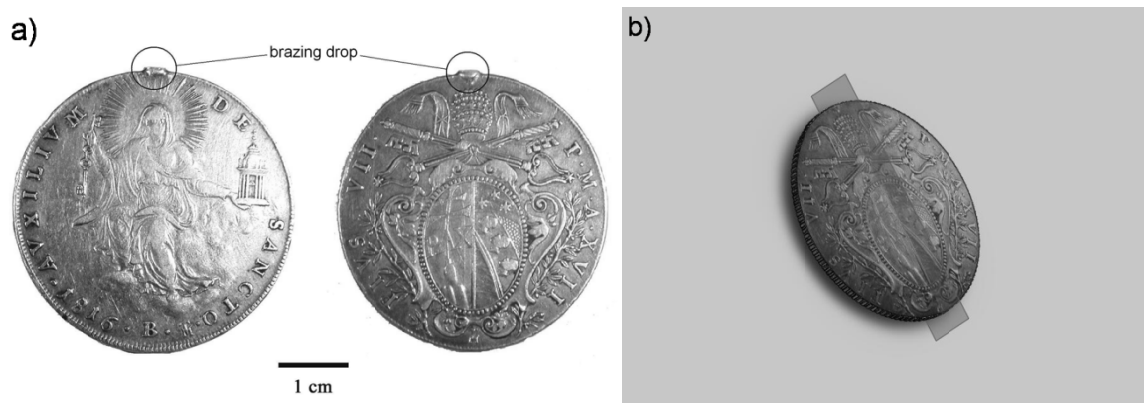

Fig. B.1 – Examined medallion: a) photo of reverse (Papal Shield) and obverse (Madonna seated on clouds with keys and temple) sides of the Pius VII *Scudo* and b) sampling area.

The coin

The investigated sample was a silver *Scudo*, minted by Pope Pius VII in 1816, officially using a Ag-Cu alloy containing 91.7% silver and having a title tolerance of ±0.3%. Concerning the sacred representations, in the obverse of the coin the Church is depicted, sitting on clouds with keys and the temple, while on the reverse side there is the coat of arms in oval frame between two branches of laurel and surmounted by the tiara and

crossed keys (Fig. B.1). The monogram TM stands for the initials of the engraver Tommaso Mercandetti, medalist and engraver of the Papal States.

The SEM-EDS analyses performed on the cross section revealed that the coin consists of a silver-copper alloy. As can be seen from Table B.1, the bulk and surface compositions are different, with a greater content of Ag in the area approaching the surface. The micrograph and the schematic representation in Fig. B.2 provided a better understanding of the differences between the surface and the bulk structure, underlining a silver enrichment on the surface, especially within the first layers.

Table B.1 – Surface and bulk composition of the coin (wt.%).

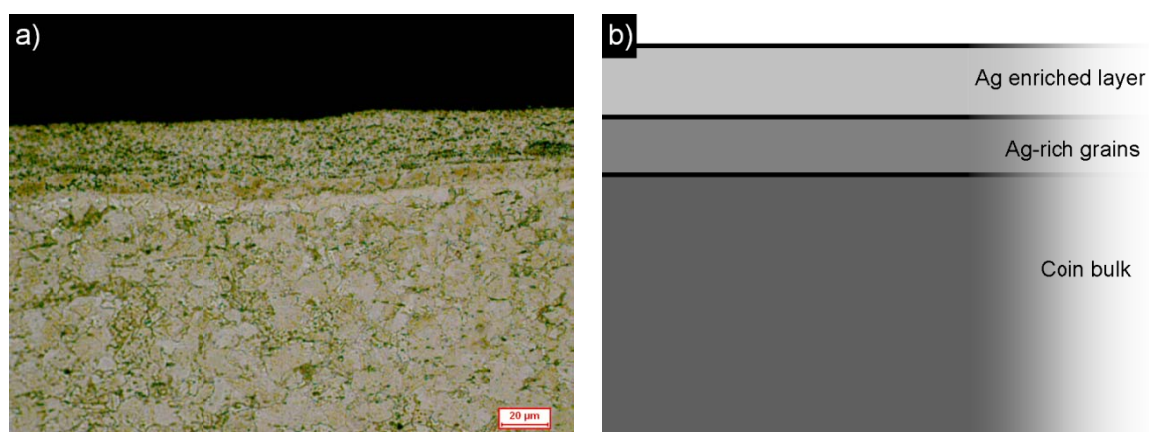|	surface	bulk
Ag	96.8	92.8
Cu	3.2	7.2

Fig. B.2 – Cross-section of the coin surface: a) OM, etched and b) schematic representation.

The schematic presented in Fig. B.2b highlights the different layers. The external one (Ag-enriched) extends to about 20-25 µm in depth and is composed by about 97% Ag; as can be seen, its microstructure is not well-defined. The intermediate layer is characterized by the presence of a single layer of white (Ag-rich) grains. The core (bulk) of the coin is distinguished by the presence of the biphasic (α-β) structure in form of mainly twinned grains, more or less etched in relation to the specific copper content of each. Moreover, a careful observation of the micrograph in Fig. B.2a allows to identify a transient area between the first two layers. This intermediate layer was generated by the natural

solidification of the blank during the fabrication process [3], and certainly has suffered from an additional copper depletion caused by the combined action of electrochemical and wearing processes that may have reduced the content of the less noble metal in the alloy.

The bulk microstructure of the coin, as revealed after chemical etching by chromic acid (H_2CrO_4), can be interpreted considering a process of thermo-mechanical nature [4]. It is known that size, shape and configuration of grains are related to the production process; from the micrographies of the internal layer, it is possible to assert that the blank was mechanically deformed and hammered into sheet, probably by a rolling mill. However, the dendritic structure due to the solidification of the plates is completely absent, excluding a solely cold rolling manufacturing process. Plastic deformation is in any case confirmed by the small size of the grains, appearing in a polygonal shape, and the presence of twins suggests two hypothesis. The slabs, in fact, can be either annealed after the cold rolling or directly obtained from a hot deformation process, since in both cases it is possible to obtain the observed microstructure owing to static or dynamic recristallization stages, respectively.

The obtainment of the starting slabs for the coins production has necessarily involved the melting of the alloy and the casting in suitable forms. Thus, the observed microstructure, modified by the subsequent thermo-mechanical processes, preserves somehow memory of what was obtained during the plates solidification. A deeper analysis of the coin structure in Fig. B.3 allows to hypothesize a different origin of the grains on the basis of the different entities of the chemical etching; chromic acid selectively acts on the copper-based phases (Cu-rich, coloured in red), leaving the silver-based phases unaffected (Ag-rich, white) and etching in different extent those phases containing a suitable amount of copper (intermediate colouring). From these considerations, it is possible to assume that the Ag-rich and the slightly attacked grains are those deriving from the silver-based solidification dendrites, having low coppers content or concentrations close to solid solution saturation limit. On the contrary, the red-coloured grains can be attributed to the Cu-rich secondary dendrites, separated from the melt during the solidification process. Finally, the grains having intermediate colorations probably derived from the eutectic structure, which surrounded primary and secondary dendrites as a result of non-equilibrium solidification conditions. These distinctions allows to suppose which was the microstructural evolution occurred during the manufacturing process of the plates, even if

the high-temperature diffusion may influence the elements distribution within the different phases.
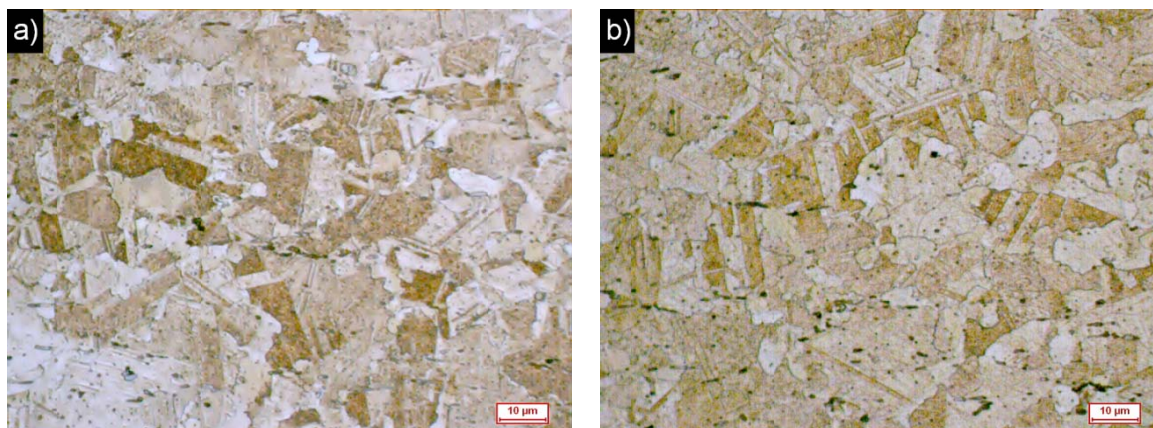

Fig. B.3 – Bulk microstructure of the coin (OM, etched).

Moreover, it is interesting to note that the twinning process mainly interested those grains arising from the secondary solidification dendrites (enriched in copper) and that the twinned areas inside them are composed by almost pure silver. In fact, owing to its lower Stacking Fault Energy (SFE), silver caused the formation of annealing twins by preferentially rearranging within the phases, both in Cu-rich and eutectic grains. Nevertheless, in some (rare) grains deriving from primary dendrites, and in which the copper content is very low, it is possible to observe twins of intermediate copper-silver composition. In these latter cases, the low content of copper in solid solution within the primary dendrites could be influenced by the silver matrix which, probably owing to a high number of lattice vacancies, eased a copper redistribution in solid solution, thus causing the formation of twins characterized by an intermediate copper-silver composition. Despite the observations, this phenomenon is in contrast with what generally happens in face-centered cubic metals (such as Ag and Cu), where the solute content can substantially lower the SFE of the solvent. The presence of copper in the Ag-rich phases, in fact, should favour a nearly-pure silver twinning which, in the case under study, is instead of intermediate composition.

From the observed findings, it is possible to hypothesize the different operations carried out in the mint workshops. Assuming that the goodness of the alloy was subjected to rigorous checks at the beginning and at the end of the production chain, it is plausible that

the blanks were obtained from the plates by punching after the rolling operations. In the following step, the dowel was heated and minted.

The thermo-mechanical processes and environment alter the surface state of metals, especially in absence of protective atmospheres, and the alloy composition may play a fundamental role on the achievable features; in the case under study, the first surface layer of the investigated coin (Fig. B.2) can be attributed to a combination of random and intentional processes. A recent experimental study by Beck *et al.* [3] has shown that, for Ag-Cu alloys containing more than 72% of Ag, the surface enrichment may directly derive from the solidification process. Such alloys undergo phase separation during cooling, leading to the formation of a Ag-rich layer in the outer side of the sample. This layer is characterized by a thickness that varies between 20 and 80 microns whereas, at greater depths, the grains of Ag-rich phase are surrounded by an eutectic matrix. Despite the high silver content in the alloys studied by Beck, it was also noticed that the surface did not appear shiny and bright, owing to the occurrence of oxidative phenomena within the first surface layers, in the order of a few micrometers. Therefore, for this unsightly surface effect, is reasonable to assume that mints intentionally proceeded to a further surface treatment.

The enrichment in silver of the coin surface (silvering), detailed described by Cope [5] and subsequently studied by La Niece [6], provides that the blanks were firstly heated in order to cause the oxidation of the copper in the surface and, in a second stage, washed using a weak acid (probably vinegar, acid derived from citrus fruit, sulfuric acid, etc.) to remove the oxide. This treatment make the surface porous and depleted in copper, while the final strike of the coinage was intended to consolidate the Ag-rich phase, giving a surface appearance as if it were of high quality silver. Hence, the first and second layers described above can be respectively addressed to the silver enrichment procedure and to the Ag-rich layer derived from the phenomenon described by Beck.

Therefore, it was possible to suppose the processes involved in the coin manufacturing, according to the production technologies developed in the 18th century and still employed in the 19th. The plates were brought to the proper thickness by alternating rolling and annealing processes, the blanks were obtained by means of a punching machine and the coins, subjected to silvering, were finally minted by a press [7]. Moreover, the edge of the coin is characterized by a circumferential knurling and by the incision of the Latin word

PAX (peace), evidencing the existence of a further step prior to the coinage in which the blanks were placed between two steel rods, one fixed and one sliding, in order to imprint the knurling design and the legend [7,8].

The brazing drop

The coin under study was devoid of the peg but the brazing drop was still clearly visible; this has permitted to choose the sampling area in order to analyse the brazing itself. The alloy's average composition is reported in Table B.2, while the partitioning of the elements in the solidification microstructure is discussed later in this section.

Table B.2 – Brazing alloy average composition.

	Ag	Cu	Zn	Pb
wt%	75,5	17,9	4,4	2,2
at%	66,1	23,4	6,3	1,0

Considering the previously reported compositions of the coin and the enriched layer, it can be determined that the melting points are about 890°C and 930°C, respectively. Referring to the Ag-Cu-Zn ternary diagram [9,10], if one considers the brazing alloy under study as a "pure-ternary" alloy – *i.e.* without Pb – its melting point can be estimated as between 750°C and 800°C (see the shaded triangle in Fig. B.4) and the presence of lead as alloying element will further lowers this temperature.
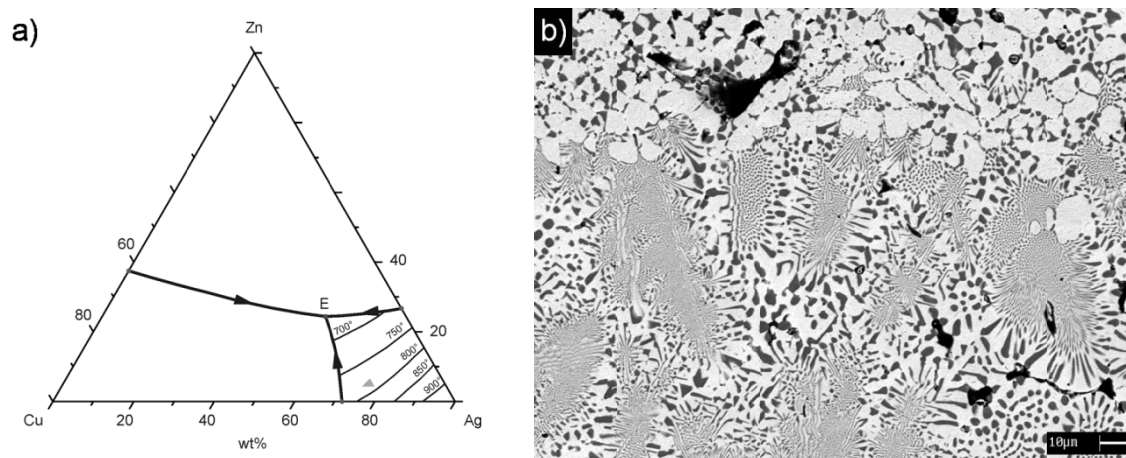

Fig. B.4 – a) composition of the brazing if considered as "pure-ternary" and b) microstructure of the brazing drop (SEM-BSE).

The brazing solidification is a non-equilibrium process, and thus its distinguishing features can be revealed from a microstructural analysis. Due to the different solidification conditions at which the liquid metal is subjected, from a microstructural point of view, the overall microstructure can be divided in two main regions as seen in Figs. B.4b and B.5: a *sideward* eutectic region and a *central* prevailing-dendritic area.
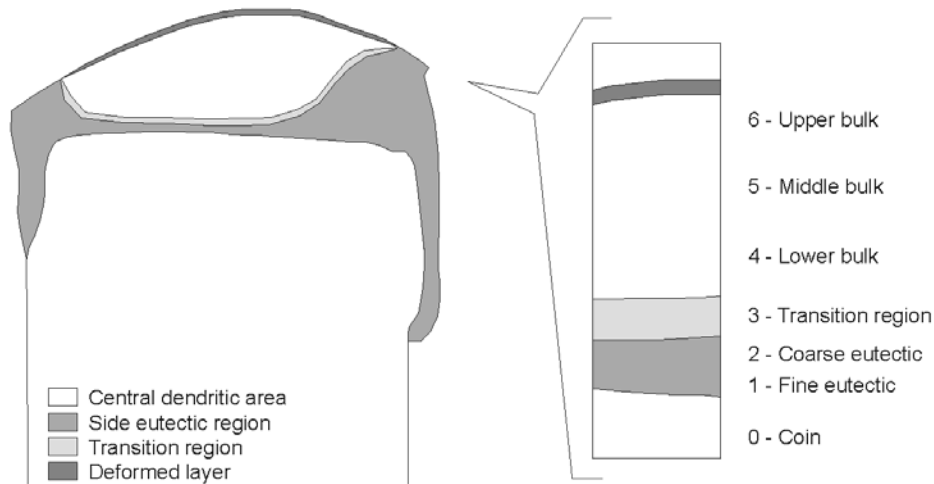

Fig. B.5 – Schematic representation of the brazing.

The eutectic region is mainly composed of a fine eutectic structure that embeds some coarser zones in which, during solidification, the conditions for the formation of the primary dendrites are mainly not reached. The parts of the brazing in contact with the ambient air and with the coin's surface appear fine-structured due to a greater undercooling and therefore to a higher solidification rate, while the liquid metal located between them solidifies a little more slowly, resulting in the formation of a coarser eutectic structure that sometimes involves the growth of the primary (Ag-rich) α-dendrites with a globular shape. In the central region, the cooling rates are still high, but slower than the eutectic areas, and the melt is trapped inside the solidified sideward regions. Such conditions are more shifted towards the equilibrium and allow for the formation of a structure composed by primary (Ag-rich) α-phase in the form of dendrites inside an eutectic matrix. In addition to the dendritic growth of the Ag-rich phase, in this area the separation of the secondary (Cu-rich) β-dendrites also occurs.

It is possible to note that the dendritic zone is not completely surrounded by the eutectic structure, but instead extends up to the top of the brazing, corresponding to the contact

surface between the brazing and the peg. This situation has probably occurred because the peg was heated during the brazing process, and the resulting higher interfacial temperature allowed to dendrites formation. Furthermore, at the top of this region, a 3–10 μm thick substrate of dendrites, which are highly plastically deformed, is also clearly visible, underlining a pressure of the peg against the coin during the brazing process, after the partial solidification of the melt (see Figs. B.5 and B.6)
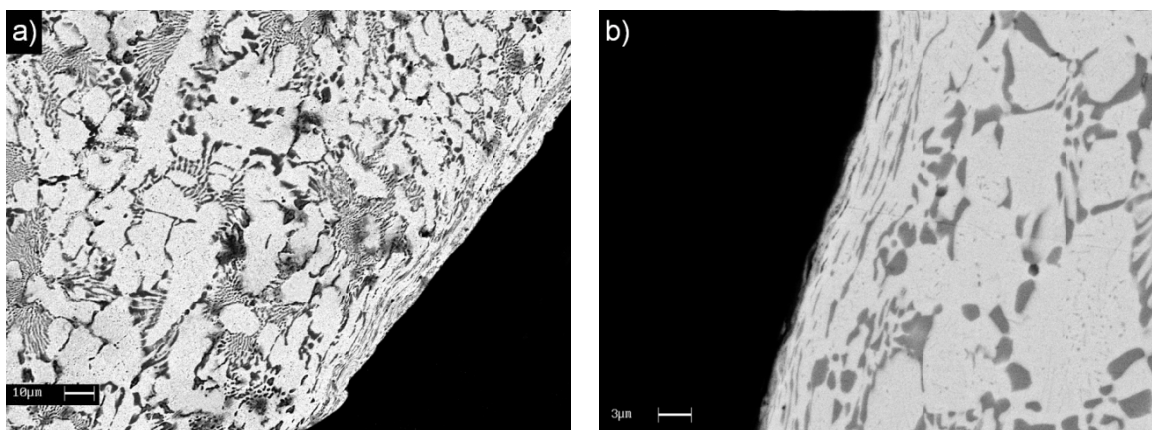

Fig. B.6 – Deformed layer at the top of the brazing (SEM-BSE).

Summarizing, dendrites appear only in the central (and central-upper) region, that is the bulk of the brazing, where the process conditions lead to the maintenance of a greater temperature of the melt. The sides of the brazing and the smears, which protract from the bulk toward the coin's faces, are instead completely eutectic, due to the contact with cooler interfaces and to the smaller volume of metal involved (see the scheme in Fig. B.5).

The mean sizes of the dendrites is greater than 1 μm, thus permitting a local composition analysis of the different phases inside the microstructure: the primary (Ag-rich) α-dendrites, the secondary (Cu-rich) β-dendrites and the eutectic structure, composed by an α(E) Ag-rich phase and a β(E) Cu-rich phase. Referring to the position reported in Fig. B.5, the different phases detected and the relative compositions are listed in Table B.3. In addition to the two previously described main regions, the local analyses have revealed the presence of a kind of transition region between these areas, in which the same phases have an intermediate composition.

As can be seen from Table B.3, it has emerged that in the eutectic structures and in the transition region, the composition range of the different phases is quite narrow, while in the bulk the distribution of the elements inside the same kinds of phase can be very different

from one zone to another. The elements partitioning doesn't follow a particular trend but it depends only to the local thermal conditions reached by the melt during the solidification, which determined the solubilised amount of the elements inside the specific phase.

Table B.3 – Brazing phases composition.

Phase	Position in Fig. B.5	Composition [at.%]			
		Ag	Cu	Zn	Pb
Eutectics					
Fine eutectic (average)	1	56.7	36.0	6.8	0.5
	4 to 6	49.7–62.5	34.8–47.8	1.5–1.6	0.9–1.2
Coarse eutectic (average)	2	44.9	44.2	9.4	1.5
α(E)	1	52.6	40.1	6.1	1.2
	2	83.6	7.5	6.5	2.4
β(E)	1	not executable			
	2	6.8	79.6	13.2	0.4
Dendrites					
α (Ag-rich)	3	81.5	13.0	4.4	1.1
	4 to 6	82.8–88.4	10.7–16.3	0.7–2.3	0.5–2.8
β (Cu-rich)	3	16.9	74.8	8.2	0.0
	4 to 6	8.3–28.5	70.2–88.5	1.5–2.4	0.0–0.6

Focusing on the distribution of the minor elements (*i.e.* Zn and Pb) and considering their atomic percentage (at.%), it can be seen that Zn is mainly distributed inside the secondary (Cu-rich) β-dendrites and inside the eutectic structure (mainly in the eutectic β-phase), while inside the primary (Ag-rich) α-dendrites the Zn atomic amount is comparable to that of Pb. On the contrary, Pb is practically only present in the Ag-based phases.

In the bulk of the brazing, the high cooling rates and the presence of Pb do not allow for the prediction of the final structure by following the Ag-Cu-Zn ternary phase diagram, owing to the formation of non-equilibrium phases and to the total insolubility of Pb in both Cu and Zn, resulting in a different partitioning of the alloying elements. In fact, referring to [9,10], if one considers the brazing alloy as "pure-ternary", the amount of Zn inside the detected phases is expected to be quite high. However, because the brazing composition is shifted towards the higher amounts of silver, the Ag-rich is the first phase to solidifies

inside the bulk, with a very high Ag content (about 90 wt.%). This allows for the solubility of Cu and Pb to increase, and therefore partial rejection of Zn, due to its complete insolubility in Pb. Despite to the high solubility of Zn in Ag, the concurrent presence of Pb causes the rejection of Zn from within the α-dendrites and thus the resulting primary (Ag-rich) α-dendrites are almost free of Zn. Solidification then proceeds with the formation of the secondary (Cu-rich) β-dendrites, containing also Ag and enriched in Zn, due to the great affinity between Cu and Zn. In these dendrites, Pb is nearly or totally absent, because it is rejected by both Cu and Zn, in which it is completely insoluble. Finally, the interdendritic melt undergoes eutectic solidification, by forming a Cu-rich phase that rejects Pb toward the liquid, and the Ag-rich phase, enriched in Pb and containing the remaining Zn. In the whole central region all of the Pb is completely solutionized by the present phases and no pure Pb segregations was detected.
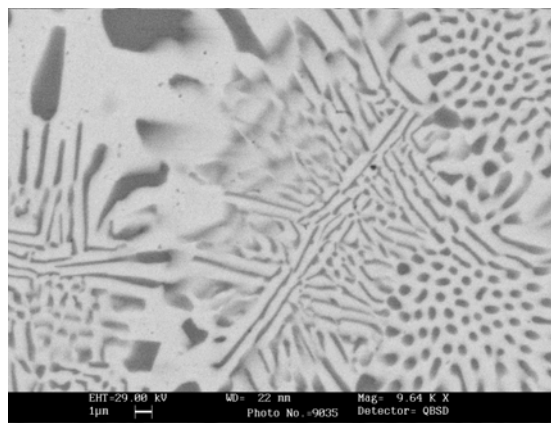

Fig. B.7 – Coexistence of different forms of eutectic (SEM-BSE).

The sides and the smears, as previously reported, solidify as completely eutectic, because they are subjected to a greater undercooling, and the phases analyzed exhibit an average composition more or less comparable to the eutectic in the bulk, except for the Zn content which is substantially higher. The eutectic which is formed in this region is either lamellar or globular (Fig. B.7), whose shape depends on the different diffusion kinetics involved in the solidification process, which are affected by the local thermal conditions reached at the solid/liquid interface. In these regions, the Pb is mostly segregated due to the higher cooling rates and therefore to the absence of the primary (Ag-rich) α-dendrites which preferentially dissolve this element. Thus, as can be seen from Fig. B.8, the

exceeding pure Pb solidifies in areas that appear as big bright spots inside the eutectic matrix, due to the high atomic number.

In the transition region, the established thermal regime leads to a different partitioning of the alloying elements inside the solidifying phases, resulting in an intermediate composition between the previously described regions. This region can be thought as an evolution of the coarse eutectic structure that is moving toward the composition range that pertains to the bulk of the brazing.
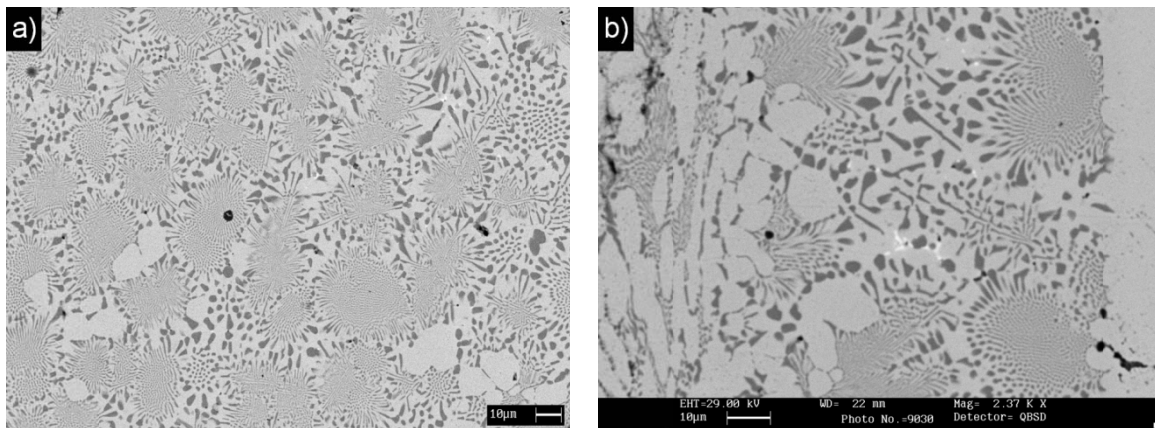

Fig. B.8 – Lead segregation inside the eutectic structure (SEM-BSE).

Concluding remarks

The investigations performed on the expendable coin are in accordance with the innovative technology production started from XVIII century [7], which provides many stages from the manufacture of a blank to the impression of the design. The preparation of the blanks was aided by rolling mills, in order to produce uniformly thick strips from which the blanks of the required size and thickness could be cut by means of metal punches. These blanks were then chemically blanched, subjected to creasing and finally coined by the pressure of two heavy iron screws.

The investigation of the elemental partitioning in the brazing drop will allow for confirmation of less invasive analyses on other similar samples, since the obtainable data reflects the mean composition of the brazing alloy. In fact, an EDS analysis performed after the removal of a thin layer of metal from the sideward regions (sides or smears), reveals that the amounts of Ag and Cu not deviate substantially from the real average composition, while the presence of elements such Zn and Pb is ensured. If the removed layer is too thick, or if the sampling point is located near the contact surface between the

brazing and the peg, the EDS analysis reflects the bulk composition of the brazing and thus the presence of Zn could be underestimated.

B.2 Compositional study of brazing alloys on XVII–XIX century coins converted into medals

In this section, the results obtained from the systematic study of the brazing drops on more than 500 coins converted into medals are presented. For editorial reasons, the compositions of the brazing alloys are not reported in the present thesis and, as previously mentioned, the data are still under analysis because the stylistic classification is not yet complete. However, the compositional results suggested some hypothesis which are discussed in the present section.

The samples belong to a wide private collection of medallions of similar aspect, consisting in coins ranging from 17th to 19th century and subsequently transformed into devotional medals by brazing pegs of different stylistic character. The investigated medals were subdivided into the three following categories.

- Papal coins, numbered in sequence.
- Not-Papal medals, signed with the letter C.
- Papal medals, signed with the letter M.

All the medals were obtained from coins out of circulation by means of brazing, a joining technique which consists in connecting metal pieces using another metal alloy of (mainly) different nature, called filler, without melting the portions to be assembled. The brazing alloy, whose melting temperature should be less than that of the base metals, is interposed between the parts to be bonded; at this temperature the molten brazing alloy wets the metal parts, allowing their joining after cooling.

This study deals with the determination of the brazing drops chemical compositions by SEM-EDS analyses in the least-destructive possible way, in order to date the period of the conversion into medals. As reported in the introduction, the discriminating factor for such dating may be the presence of zinc as brazing alloying element and its relative amount, since the employment of its metallic form by artisans for the realization of brazing alloys and artefacts can be addressed to recent times. Hence, the present section is mainly focused

on the presence of zinc in the brazing alloys and on the introduction in Europe of its production methods.

Sampling areas

The identification of proper sampling areas was carried out taking into account that the volume of each investigated area must be in accordance with the instrumental requirements, and also considering that the sampling points play a key role in accordance with the principles of alteration and representativeness.

The superficial part of an ancient object is always different from the bulk, owing to chemical processes which occur over time causing degradation and corrosion, even though often is the artisan who voluntarily produces patinas or coatings in order to change the aesthetic appearance of the object. Furthermore, some alterations in aspect due to restoration and/or preservation processes cannot be excluded. The representativeness of the sampling points is related to the heterogeneity of the material. Hence, for the planning of a significant sampling strategy, it was of fundamental importance the metallographic analysis presented in Section B.1, taking into account the phases distribution inside the drops during the removal of the brazing material.
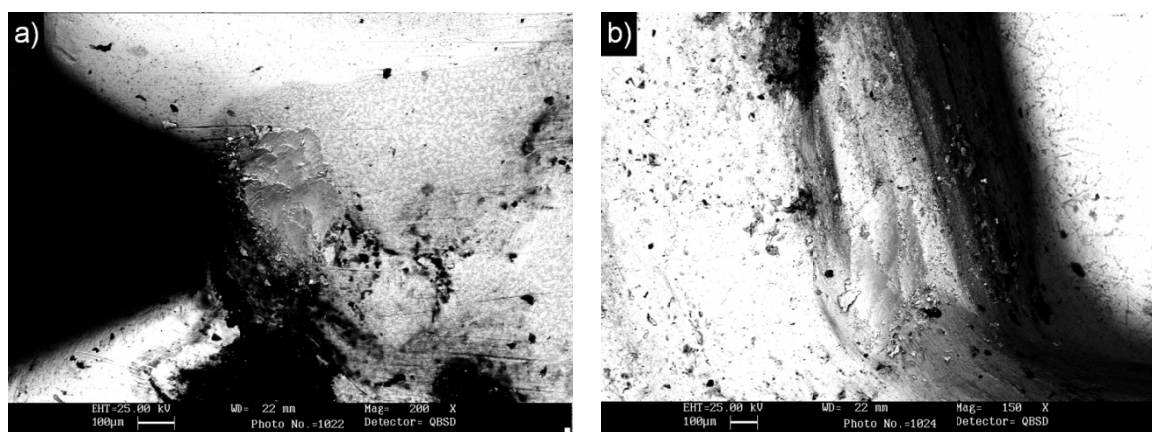

Fig. B.9 – Sampling points: a) massive and b) thin.

The chemical analysis of the brazing was performed after removing a thin metal layer by micro-milling the drop surfaces. The investigation areas were about 100–300 μm^2 and 15–20 μm in depth, in order to assure the detection of the brazing composition, without the interference of deposited oxides on the surface or any dirt layer. Depending on the morphology of the joint, the sampling points can be classified according to the position

relatively to the brazing drop. In "massive" sampling points (Fig. B.9a), depths or position of the metal removal entailed an analysis of the bulk of the brazing, whereas in "thin" sampling points (Fig. B.9b) the investigated areas pertained to side and smears of the brazing drop (see Section B.1 for the brazing drop parts denominations).

Brazing compositions

The brazing alloys were mainly composed by Ag-Cu-Zn, often alloyed with lead and gold and seldom containing other minor elements, as discussed later in this section. Inserting the results in the ternary diagram Ag-Cu-Zn (Fig. B.10a), it is possible to notice that none of the investigated brazing alloys is close to the eutectic composition indicated by the state diagram (*i.e.* 57.3% Ag, 19.4% Cu and 23.3% Zn) and that, by comparison with the ternary diagram reported in [9] (Fig. B.10b), in more than 90% of them the elements balance is such that the liquidus temperature falls within the range 750–900°C.
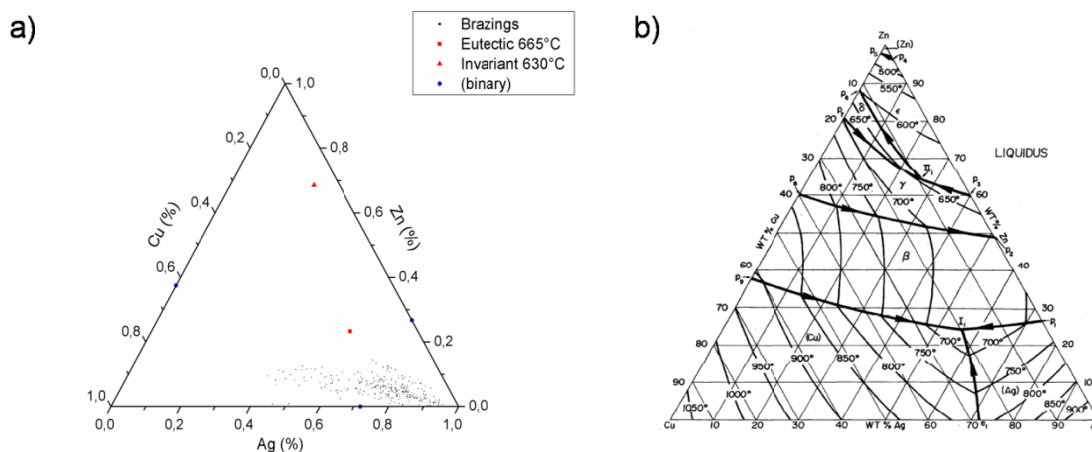

Fig. B.10 – Ag-Cu-Zn ternary diagram: a) compositions of the brazings and b) liquidus surfaces [9].

The diagram in Fig. B.10a includes almost all the investigated alloys, except those in which the content of minor elements is greater than 2–3% and therefore cannot properly be considered as ternary alloys. The presence of trace elements was instead not considered because, although slightly affecting the physical metallurgy of the solidification process, they do not significantly alter the melting temperatures.

As reported in Section B.1, *sterling* silver melts at about 890°C, whereas for the surface enriched layer (about 96% Ag) the liquidus temperature was estimated at 930°C or slightly higher, in relation to the Ag content. Therefore, considering that all the coins were probably enriched in Ag, it can be defined a temperature of about 930°C as limit for the

brazing melting temperatures. From the point of view of the junction between the different parts and referring to ternary diagrams, it is therefore possible to assert that the quantitative determinations performed on the brazing are to be considered reliable. In fact, all the alloys have a melting temperature never higher than 930°C, according to the "thermal constraints" necessary to obtain a brazing joint.

For a verification of the distribution of each element into classes, the obtained data were plotted on frequency histograms (Fig. B.11). These schematics allow to globally view the elements distribution in all samples and the results can be summarized as follows.

- In the most cases, the Ag content is higher than 67.5%, with a more pronounced clustering around 80%.

- Except for few coins, the Cu amounts is always below 35% and manly concentrate in the range 7–22%, with a densification at around 15%.

- Zn is mainly present in levels of 2–7%, with the major number of data between 3% and 6%, and, except for an isolated case, it is always less than 16%.

- Finally, for more than half of the coins, the Cu/Zn ratio falls within the range 2.5–7.5.
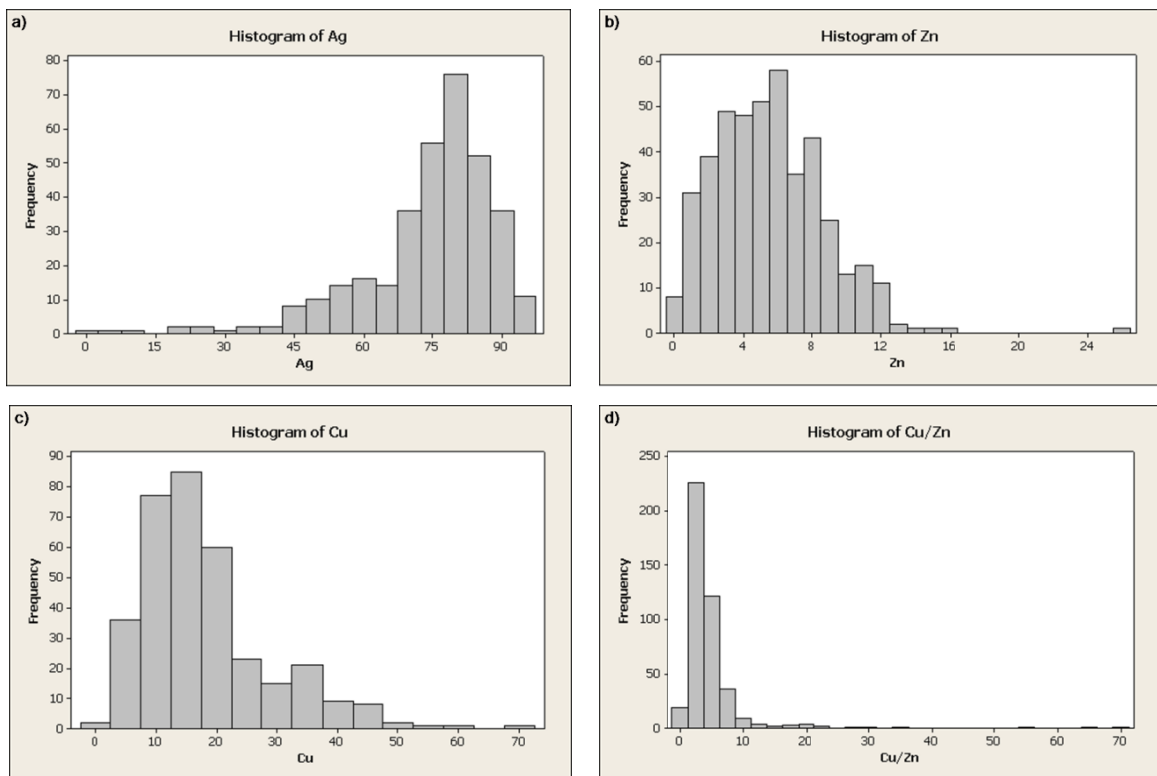

Fig. B.11 – Frequency histograms: a) silver, b) zinc, c) copper and d) Cu/Zn ratio.

Content of zinc

The analyses pointed out that zinc is always present in all the investigated brazing drops and, as can be seen from the frequency histograms, its amount in the alloys is always less than 16%. The phenomenon of zinc segregation and its distribution within the different phases in the brazing microstructure is discussed in Section B.1 and, as above mentioned, it is possible to assert that the obtained results are more or less representative of the bulk brazing composition, in relation to the specific sampling area. If the investigated area pertains to a "massive" sampling point (Fig. B.9a), the detected Zn amount is an underestimation of the bulk zinc content, whereas if the metal is removed from a thinner area (Fig. B.9b), the Zn amount corresponds to that of the bulk composition.

Moreover, it must be considered that the high volatility of zinc can cause a reduction of its amount in those parts of the brazing drop which are in contact with the environment. This depletion in zinc, especially in correspondence of brazing sides and smears, can lead to an underestimation of the true zinc content whenever the removed metal layer was not of appropriate thickness, *i.e.* when the oxide layers were not totally removed. This fact is confirmed by a comparison between the analyses performed before and after the micro-milling operations, and from which the detected zinc content was found to be increased by at least 5 percentage points after the material removal (Table B.4).

Table B.4 – Brazing compositions after and before micro-milling [wt.%].

Coin number	Brazing state	Ag	Cu	Zn
187	as-received	87.5	6.6	5.9
	oxides (as-received) AgO-CuO-ZnO	86.4	7.1	6.5
	milled	69.9	19.4	10.7
217	as-received	92.5	6.9	0.6
	oxides (as-received) AgO-CuO-ZnO	91.8	7.5	0.7
	milled	77.1	16.9	5.9
243	as-received	91.8	7.5	1.7
	oxides (as-received) AgO-CuO-ZnO	91.1	7.1	1.8
	milled	74.1	17.5	8.4

Production of metallic zinc

Since the present study is based on the content of zinc in detected in the brazing alloys, a timetable concerning the employment of zinc as alloying element is reported (Table B.5). These data derived from an extensive literature research about the production of metal artefacts containing zinc and on the evolution of the metallic zinc production process throughout the past centuries.

Table B.5 – Zinc timetable.

Year	Notes	average Zn [wt.%]	Reference
-20–14	Emperor Augustus. Production of brass by zinc cementation.	17	[11]
1–1500	Increase in zinc content in Chinese bronzes. Production in appreciable quantities from year 900 onwards.	3–40	[12,13]
900–1500	Zinc production in India.	-	[12]
1340	Zinc production in Iran.	-	[12]
1368–1644	Ming Dynasty. Zinc is used for the production of coins (1-24% Cu).	up to 97–99	[12]
1520	Europe. Paracelsus claims the knowledge of "zincum", by learning of its existence from Indians.	-	-
1558	Reign of Elizabeth I (1558-1603). Production of brass in England from calamine, containing 20% of Zn and subsequently brought to 24%.	20–24	[13]
1585	Billet production in China containing 98% zinc with lead and iron in traces.	up to 98	[12]
1595	Libavius analyzes a sample of East Indian Zinc, imported from Holland and called "*calaem*" (it was the same material known as "*cadmia*").	-	[14]
1605	Zinc begins to be imported into Europe from the East India Company. Prior to this date was not intentionally produced.	-	[12]
1620	Portuguese ship containing Zinc from the Indies was seized by the Dutch.	-	[11]
1637	Chinese literary source. Alloying procedure consisting in melting 6–7 parts of copper and 3–4 parts of zinc) in order to obtain an alloy having about 30% of Zn (assuming a 25% loss for Zn vaporization).	30	[13]
1718	Stahl realizes that *smithsonite* added to copper a metallic component in the brass production by cementation.	-	[14]
1721	Henkel produces metallic zinc from *smithsonite* in Upper Silesia using an unknown procedure.	-	[14]
1723	British patent for an improved version of the calamine process by using granular copper.	33	[13]
1736	Production of Ni-Ag alloys (*patkong*) in China.	45	[12]
1738	Development in Europe of the first method for the intentional production of zinc from *sphalerite* (ZnS) by W.Champion. Evolved version of the calamine process but laborious and thermically inefficient (24 tons of coal for 1 ton of zinc). Process probably derived from Indian for the type of distillation employed.	-	[12,13]

Table B.5 – (continue).

Year	Notes	average Zn [wt.%]	Reference
1740	Birth of the first European center for the extraction of zinc.	-	-
1745	Ingots of pure Zinc produced in China and brought to Sweden.	98.99	[11]
1746	The German chemist Andreas Sigismund Marggraf obtained zinc from the distillation of calamine in closed containers.	-	-
1760	Between 1760 and 1780, England imported from the east 40t of metallic zinc per year.	-	[13]
1781	British patent for the production of high quality brass by direct compound (the metallic zinc was still too expensive to be used in this process).	-	[13]
1798	Construction of a furnace in Wessola (Silesia). Horizontal process improved in year 1805. Initially, the employed raw material was a by-product of lead and silver. To this was followed the use of *sphalerite* (zinc *blende*), converted in a oxide form by roasting.	-	[11,14]
1800	The beginning of the century was characterized by a large-scale production of zinc in most of Europe.	-	[13]
1800s	First production of zinc castings on an industrial scale by Geiss. Backed by the Schinkel construction company, the foundry founded by Geiss became soon of great importance.	-	[14]
1807	A. Dony improved the zinc production system.	-	[12]
1812	Construction of the first mill in Liege (Belgium).	-	[11]
1830	Gradual elimination of the calamine process.	-	-
1836	Construction of a furnace in Stolberg.	-	[11]

The production of metallic zinc is performed by distillation of *calamine* (zinc carbonate), which is reduced using coal. Since zinc melts at 419°C and the molten metal boils at 918°C, the reduction of calamine involves an immediate distillation of zinc and its subsequent condensation on the upper parts of the furnace. This sublimation is possible only if there is no air inside the furnace, otherwise the zinc is oxidized and then is the oxide to condense on the walls. Therefore, the process is not simple and immediate, but requires continuous modifications and improvements before being economically adopted at an industrial level [15] .

Referring to the previous Table B.5, one can see that the production process of the metallic zinc was introduced on an industrial scale in the early 1700s in England, but not in a favourable manner such as to justify the costs, and it was improved in the subsequent years. At the end of 1700, the horizontal distillation process was introduced and was improved in the following 30 years, making the production of zinc industrially competitive

and only after 1810. In fact, although the metal was widely known and imported from China by some European nations, the spread of the metallic zinc in Europe on a large scale can be dated to a period subsequent to 1810, since in the previous years the manufacturing process was probably still too expensive and not industrially competitive. However, is not to be excluded that the process could be developed for artisanal productions, using the new metal as alloying element for brazing pastes and sold at high cost.

Following its introduction in Europe in the early 1600s, zinc was employed as metallic element in brazing alloys, although not accessible to most people. As a matter of fact, in the late 17st century the word *braze* acquired the meaning of "welding using a copper-zinc alloy" [16] and around the middle of the 18th century there were several attempts in France to use it in place of tin in order to protect iron objects.

Volatility of zinc

Zinc is a transition metal of group 12 and, such as cadmium and mercury, is characterized by a low melting point and a low boiling temperature, due to the bonds weakness in the 4s orbital. Hence, the volatility of this element is not negligible, even at room temperature. This is confirmed by the analyses before and after the metal removal from the brazing drop, revealing a zinc content in the first layers substantially lower than the real one.

An accurate thermodynamic analysis on the volatility of this element can be made by considering that the partial pressure of solid and liquid zinc at the melting point is low ($2 \cdot 10^{-4}$ atm at 419°C). However, this value is high enough to ensure that complete evaporation or sublimation can be effectively reached at temperatures close to the melting point and at a relatively modest degree of vacuum. The vapor pressure of liquid zinc increases rapidly with temperature, reaching the value of 1 atm at 907°C, the zinc boiling point [11] and the theoretical evaporation rate can be predicted from the kinetic theory of gases (Langmuir equation). Therefore, knowing parameters such as process temperature, crucibles size and heating time, it is possible to obtain an estimation of the zinc loss rate for vaporization.

Re-melting of brasses

For the production of the brazing alloys, one hypothesis could take into account the re-melting of brasses, in order to balance the composition. Regardless a deeper analysis

considering the thermodynamic theory, it is possible to notice that the melting temperature of the most common brasses is always higher than 920°C, *i.e.* the zinc boiling temperature, causing a high loss of the metal in the re-melting process, since vaporization already starts at 420°C, the zinc melting temperature.

However, the obtainment of the brazing alloys by brasses re-melting seems to be not realistic. In fact, considering a range of brasses Cu-Zn of variable composition (from 70–85% Cu and 30–15% Zn) and assuming a zinc loss for vaporization of about 25%, the resulting Ag-Cu-Zn alloys, having a percentage of silver within the range of interest (*i.e.* 65–85%), should possess a Cu/Zn ratio between 9 and 22, which is satisfied only by 20 alloys on over 520 analyzed. Therefore, these results lead to reasonably exclude the possibility of a systematic re-melting of brass artefacts in order to produce the investigated brazing alloys, although this type of practice is not to be completely excluded, since if it happened in a small part there are no ways to know it.

Presence of other elements

Several alloys contain important percentages of other elements and, therefore, are no more to be consider as pure ternary Ag-Cu-Zn alloys. However, some considerations on the origin of these elements must be done since, in some cases, they may have been intentionally added by the artisans to fulfill technical or aesthetic requirements, while in other cases they must be interpreted as impurities. Concerning this latter case, it must be considered that impurities are always present in ancient objects, as the manufacturing techniques did not allow to achieve a narrow control of the composition. Hence, the presence of high quantities of impurities deriving from the refining methods of silver and copper is rather expected, and may be originated from processing waste placed in the crucible during the alloying; in some alloys, the impurities level reaches the 10–15%.

Lead

This was the most diffuse element; in most cases it was present in traces or percentages around 2.5–4%, although in some specimens amounts between 5% and 14% were detected. Small percentages of Pb can be related to the process employed for the silver separation from the argentiferous lead *galena* (Pb,Ag)S [17], because the silver obtained by cupellation process would be characterized by a residual lead between around 0.05–2.5%

[18]. On the contrary, massive percentages denote a voluntary addition, justified by the fact that this element allows a lowering of the melting temperature.

Moreover, it should be pointed out that identification and quantification of lead is not trivial, since the principal peak corresponding to the PbM characteristic radiation overlaps with one the Ag L-shell, and an overestimation of the element is not to be excluded.

Gold

This element was found only in brazing of golden coins and its presence may be dictated by a voluntary addition, in order to maintain a certain continuity of colour.

Mercury

Although it is known that mercury is found in nature as impregnation of different rocks, generally in small quantities, the presence of 3–5% in some alloys can be associated to the process of silver extraction by amalgamation. In this ancient process, gold and silver minerals (suitably shredded) are mixed with mercury, originating an amalgam; the precious metals are then extracted by heating the amalgam, which sublimated mercury. This method, in use since 1550, was abandoned in the late 1800 and early 1900 and is now rarely used because of its high cost, low yield and the high toxicity of mercury.

Arsenic

This element, in form of sulphide – *realgar* (As_4S_4) and *orpiment* (As_2S_3) – can be generally found in nature as associated with other metals sulphides, and appeared as an alloys constituent since ancient times. Arsenic was normally used in ancient brazings, even if the year of issue of the coin in which the As was detected suggests a voluntary addition and would lead to a date of the brazing in periods subsequent to 1800. Most likely, the low arsenic percentages can be addressed to the extraction of either silver from *proustite* (Ag_3AsS_3) or copper from *enargite* (Cu_3AsS_4).

Nickel

This element was detected in one case, and its high amount (11.5%) leads to exclude a modern brazing alloy, in which Ni is generally maintained less than 5% if present in the alloy with copper. Given the low percentage of silver detected in the alloy (10.5%), it is

reasonable to think that Ni was employed to save the precious metal, without sacrificing the colour continuity; nickel, in fact, has the property of almost completely whiten the copper, obtaining a metallic gray colour.

Iron

In one sample, Fe was detected in association with Ni; such coexistence could be explained with the use by the silversmith minerals containing both Fe and Ni , such as *bravoite* $(Fe,Ni)S_2$, a gray-silvery variety of *pyrite*.

In the other samples where iron was detected, its presence can be related to the extraction of copper from *chalcopyrite* ($CuFeS_2$) or from *bornite* (Cu_5FeS_4) which, together with *chalcocite* (Cu_2S), are the most important among the many copper ores [19].

Aluminium

The presence in traces of this element may be due to the leaching process (solid-liquid extraction) for the silver separation, consisting in treating the milled minerals (only native metal or silver chloride) with sodium cyanide and recovering the metallic silver by reduction with metallic zinc or aluminium. A similar process, replacing the amalgam method, was introduced in 1800 by using sodium thiosulfate instead of cyanide, but it was soon abandoned.

Other elements

The presence of elements such as *Magnesium* and *Silicon* is not directly correlated to the extractive metallurgy of the principal elements employed in the brazing alloy realization and can be explained by the custom of re-melt objects, in order to meet the needs of material in absence of a strict control of the obtained alloy. Moreover, the use of silica-based fluxes during the alloy preparation is not to be excluded.

Conclusions

The coins were divided into the three main categories previously introduced (Coins/C/M) but, despite the differences in chemical composition, no evidences of any peculiarities characterizing a particular subdivision in macro-class were revealed.

Regarding the compositions, the results did not reveal any correlation in the investigated alloys and also a chronological order based on the year of the coins mint did not give useful information about any grouping of similar alloys. The analyses evidenced that the brazing period cannot be traced only by the elemental composition of the alloys because artisans often used to re-melt objects, without any effective control on the brazing alloy. Hence, a further grouping based on aesthetical features of the pegs is necessary – and is still under development – probably allowing the identification of different groups of artisans. Moreover, to extend these results, it may be also necessary to know what were the most common brazing alloys used in the past, how were prepared (metals and minerals most frequently used, melting methods, temperatures reached in the crucibles, etc.) and the brazing methods; unfortunately, such information are not easily available, since belonged to the artisans know-how.

Considering the emerged results and the previously reported timetable, the detected zinc suggests that such element has been intentionally introduced in the brazing alloys. Its volatility excludes the possibility of brass artefacts re-melting, also because these objects were considered to be of a certain value and therefore not suitable for metal scraps usage. Moreover, the detected amounts revealed that the accidental addition of zinc, associated to ores at which the element is naturally bonded (lead, silver, iron and copper ores), is not a reliable hypothesis. Thus, if the zinc was voluntary added, the brazing alloys should definitely dated post 1810, year when the zinc production process was advantageously introduced in Europe; in fact, in the previous years, the metal was too expensive for a large scale production of brazed medallions and its manufacturing process was still not suitable for a spread in an industrial scale.

REFERENCES

[1]   I. Calliari, M. Magrini, A. Zambon, P. Guerriero, R. Martini. *X-Ray Spectrom* 28 (1999) 86.

[2]   N. Civici, S. Gjongecaj, F. Stamati, T. Dilo, E. Pavlidou, E. Polychroniadis. *Nucl Instrum Meth B* 258 (2007) 414.

[3]   L. Beck, S. Bosonnet, S. Reveillon, D. Eliot and F. Pilon: *Nucl Instrum Meth B* 226 (2004) 153.

[4]   D. A. Scott.. *Metallography and Microstructure of Ancient and historic Metals*. The Getty Conservation Institute (1999).

[5] L. H. Cope. *Methods of Chemical and Metallurgical Investigation of Ancient Coinage*. E. T. Hall, RNS Special Publication (1972).

[6] S. La Niece and P. Craddock. *Metal Plating and Platination*. Butterworth-Heinemann Ltd, London, (1993).

[7] C. Crisafulli. *Uomini e Tecnologie monetarie: la visita di Du Bois alla Zecca di Venezia*, in A. Saccocci (Eds) *Inspecto nummo*. Esedra, Padova, Italy (2001).

[8] A. Finetti. *Numismatica e tecnologia*. La nuova Italia Scientifica, Roma, Italy (1987).

[9] Y. A. Chang, D. Goldberg and J. P. Neumann. *J Phys Chem Ref Data* 6 (1977) 669.

[10] Materials Science International Team (MSIT®). *Numerical Data and Functional Relationship in Science and Technology, Group IV: Physical Chemistry, Vol. 11: Ternary Alloy Systems, Subvol. C: Non-Ferrous Metal Systems, Part 3: Selected Soldering and Brazing Systems*. G. Effenberg and S. Ilyenko, The Landolt-Börnstein series, Springer (2007).

[11] C. H. Mathewson. *Zinc: the science and technology of the metal, its alloys and compounds*. Hafner Publishing Company (1970).

[12] R. F. Tylecote. *A history of metallurgy*. Maney Publishing, London, England (2002).

[13] A. M. Pollard and C. Heron. *Archaeological Chemistry*. The Royal Society of Chemistry, Cambridge, England (1996).

[14] F. Habashi. *Handbook of extractive metallurgy*. Wiley-VCH, Heidelberg, Germany (1997).

[15] R. J. Forbes. *Metallurgy in antiquity: a notebook for archaeologists and technologists*. Leiden, Brill (1950).

[16] D. M. Jacobson and G. Humpston. *Principles of Brazing*. ASM International (2005).

[17] G. Artioli. *Scientific Methods and Cultural Heritage: An Introduction to the Application of Materials Science to Archaeometry and Conservation Science*. Oxford University Press, USA (2010).

[18] C. Giardino. *I metalli nel mondo antico: introduzione all'archeometallurgia*. Laterza, Roma, Italy (1998).

[19] C. Klein. *Mineralogia*. Zanichelli, Bologna, Italy (2004).

APPENDIX C

List of publications

Published papers

BREDA M, Calliari I, Ramous E, Pizzo M, Corain L, Straffelini G (2013). *Ductile-to-brittle transition in a Zeron®100 SDSS in wrought and aged conditions*. Materials Science and Engineering A − Structural Materials: Properties, microstructure and processing, vol. 585, pp. 57–65.

Calliari I, Bassani P, Brunelli K, BREDA M, Ramous E (2013). *Effect of Continuous Cooling on Secondary Phase Precipitation in the Super Duplex Stainless Steel ZERON-100*. Journal of Materials Engineering and Performance, vol. 22, issue 12, pp. 3860–3866.

Bassani P, BREDA M, Brunelli K, Mészáros I, Passaretti F, Zanellato M, Calliari I (2013). *Characterization of a Cold-Rolled 2101 Lean Duplex Stainless Steel*. Microscopy and Microanalysis, vol. 19, pp. 988–995, ISSN.

Calliari I, BREDA M, Ramous E, Brunelli K, Pizzo M, Menapace C (2012). *Impact Toughness of an Isothermally Treated Zeron®100 SDSS*. Journal of Materials Engineering and Performance, vol. 21, issue 10, pp. 2117–2123.

Miranda Pérez A F, Calliari I, Ramous E, BREDA M (2012). *Trattamenti di ricottura dell'acciaio inossidabile duplex 2205 dopo deformazione plastica*. La Metallurgia Italiana, vol. 5 (2012), p. 13–17.

BREDA M, Canovaro C, Miranda Pérez A F and Calliari I (2012). *From Coin to Medal: a Metallurgical Study of the Brazing Drop on a 19th Century Scudo*. Journal of Metals, Minerals and Materials Society, vol. 64, pp. 1350–1355.

Canovaro C, BREDA M, Miranda Pérez AF, Vajna E, Calliari I (2013). *Da moneta a medaglia: caratterizzazione metallografica di uno scudo romano del XIX secolo*. La Metallurgia Italiana, vol. 10 (2013), pp.41–47.

Conference Proceedings

BREDA M, Calliari I, Frigo M, Pellizzari M, Ramous E (2013). *Precipitazione di fasi secondarie in acciai Lean Duplex a seguito di trattamenti isotermici*. In: 24° Convegno Nazionale Trattamenti Termici. Associazione Italiana Metallurgia, Piacenza (IT), October 2013.

BREDA M, Pezzato L, Pizzo M, Mészáros I, Calliari I (2013). *Effects of Cold Deformation in Duplex Stainless Steels*. In: EUROMAT 2013. Federation of European Materials Societies, Seville (ES), September 2013.

Calliari I, BREDA M, Straffelini G, Miranda Perez A F, Reyes Valdes F A (2013). *Impact toughness of isothermally treated Duplex Stainless Steels*. In: XXII International Materials Research Congress. Materials Research Society, Cancun (MEX), August 2013.
BREDA M, Pezzato L, Pizzo M, Calliari I (2013). *Effetto della deformazione plastica a freddo sulla resistenza al pitting negli acciai inossidabili Duplex*. In: Giornate Nazionali sulla Corrosione e Protezione – X Edizione. Associazione Italiana di Metallurgia, Neaples (IT), July 2013.

Calliari I, BREDA M, Ramous E, Straffelini G, Magrini M (2013). *Effect of isothermal heat treatments on Duplex Stainless Steels impact toughness*. In: XXII Convegno Nazionale IGF. Italian Group of Fracture, Rome (IT), July 2013.

BREDA M, Pizzo M, Baldan M, Ramous E and Calliari I (2012). *Transizione duttile-fragile in un acciaio inossidabile Super Duplex Zeron®100 in condizioni di fornitura e a seguito di trattamento isotermico*. In: 34° Convegno Nazionale AIM. Associazione Italiana di Metallurgia, Trento (IT), November 2012.

Ramous E, BREDA M, Miranda Pérez A F, Cardenas J C, Bertelli R (2012). *Gli azoturi negli acciai inossidabili Duplex*. In: 34° Convegno Nazionale AIM, Associazione Italiana di Metallurgia, Trento (IT), November 2012.

Canovaro C, BREDA M, Miranda Pérez A F, Vajna E and Calliari I (2012). *Da moneta a medaglia: caratterizzazione metallografica di uno scudo romano del XIX secolo*. In: 34° Convegno Nazionale AIM, Associazione Italiana di Metallurgia, Trento (IT), November 2012.

Calliari I, BREDA M, Miranda Pérez A F, Ramous E, Bertelli R (2012). *Phase Transformation induced by Heat Treatment in Cold Rolled Duplex Stainless Steels*. In: International Conference & Exhibition on Analysis & Testing of Metallurgical Processes & Materials. The Chinese Society for Metals, Beijing (RC), October 2012.

Carrasco-González L A, García-Vázquez F, Perez-Medina G Y, Calliari I, BREDA M (2012). *Analysis of Discontinuities Generated by GTAW Process in the Manufactoring of Hospital Furniture of AISI 304 Stainless Steel*. In: 34th International Congress of Metallurgy and Materials.

Poster presentations

Bassani P., BREDA M, Brunelli K, Mészáros I, Zanellato M and Calliari I (2012). *Characterization of a Cold Rolled 2101 Lean Duplex Stainless Steel*. In: EMAS 2012 Electron Probe Microanalysis of Materials Today - Practical Aspects.

220

Submitted papers

Basoni J, Calliari I, BREDA M, Toldo F, Meneghini R. *Caratterizzazione meccanica e microstrutturale di giunti saldati in UNS S32760 per applicazioni Off-Shore*. Rivista Italiana della Saldatura (Accepted, pub. on January-February 2014).

Calliari I, BREDA M, Miranda Pérez A F, Pellizzari M, Ramous E. *The Nitrides in Duplex Stainless Steels*. Journal of Materials Science and Technology (Submitted).

BREDA M, Calliari I, Frigo M, Pellizzari M, Ramous E. *Secondary phases precipitation in Low-Ni Duplex Stainless Steels sheets*. Journal of Metals, Minerals and Materials Society (Submitted).

AKNOWLEDGMENTS